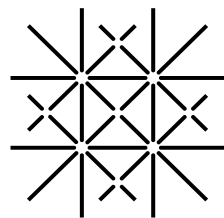


The protein cage Thermosome as versatile delivery platform

**Inauguraldissertation
zur
Erlangung der Würde eines Doktors der Philosophie
vorgelegt der
Philosophisch-Naturwissenschaftlichen Fakultät
der Universität Basel**



**Universität
Basel**

**von
Martin G. Nussbaumer
aus Wallisellen, ZH
Basel, 2015**

Genehmigt von der Philosophisch-Naturwissenschaftlichen Fakultät
auf Antrag von

Prof. Dr. Wolfgang Meier

Prof. Dr. Tanja Weil

Basel, den 17. Februar 2015

Prof. Dr. Jörg Schibler
Dekan

Table of Contents

Table of Contents	III
Acknowledgements.....	VI
Abbreviations	VII
1. Introduction nanomedicine	1
1.1 Nanomedicine	1
1.2 Nano drug delivery systems	1
1.3 Passive and active targeting.....	2
1.4 Cargoes of NDDS and release strategies	4
1.5 Types of NDDS.....	5
1.5.1 Lipid based NDDS	5
1.5.2 Polymer based NDDS.....	5
1.5.3 Protein based NDDS	7
2. Introduction chaperonins.....	12
2.1 Group I chaperonins vs. group II chaperonins.....	12
2.2 Structure of the group II chaperonin from <i>Thermoplasma acidophilum</i> (Thermosome)	13
3. RNA interference.....	15
3.1 Introduction RNA interference.....	15
3.2 RNAi mechanism	15
3.3 siRNA transfection agents.....	17
3.4 PAMAM as siRNA delivery reagent	18
4. Motivation and concept.....	20
5. THS expression and purification.....	22
5.1 Introduction	22
5.2 THS expression	22
5.3 THS purification.....	22
6. THS characterization	26
6.1 Gel electrophoresis	26
6.2 Electron microscopy.....	26
6.3 Mass spectrometry	28
6.4 Stability test	31
7. Modification of THS with cell targeting ligands	34
7.1 THS-Atto647 modification.....	34
7.2 Modification of THS with cell targeting ligands	35

7.2.1 BBN-8/12EG-THS-Atto647	35
7.2.2 Biotin-THS-Atto647	40
7.2.3 FA-THS-Atto647	42
7.2.4 SST-THS-Atto647	44
7.2.5 cRGDFC-THS-Atto647	46
7.2.6 TAT-THS-Atto647	48
7.2.7 VEGF-THS	51
7.3 Conclusions	52
8. Chaperonin-dendrimer conjugates for siRNA delivery	54
8.1 Introduction	54
8.2 THS-PAMAM conjugation	54
8.3 THS-PAMAM-siRNA	58
8.3.1 Binding of siRNA by THS-PAMAM	59
8.3.2 siRNA transfection by THS-PAMAM	60
8.3.3 TAT-THS-PAMAM	61
8.3.4 siRNA transfection with TAT-THS-PAMAM to PC-3 cells	62
8.4 Conclusions	63
9. Reduction sensitive drug release	64
9.1 Introduction	64
9.2 Results and discussions	65
9.3 Conclusions	71
10. THS activity and conformation	72
10.1 Introduction	72
10.2 ATPase activity of THS	72
10.3 Conformational analysis of THS depending on ATP and its analogues	73
10.3.1 Native gel analysis	73
10.3.2 Degradation assay	73
10.3.3 SAXS analysis	74
10.3.4 TEM analysis of the conformational state of THS	76
10.3.5 Conclusions on the THS' conformations	77
11. THS as controllable nanoreactor for biotransformations	79
11.1 Introduction	79
11.2 Results	80
11.2.1 THS-HRP conjugation	80
11.2.2 ATPase activity of THS-HRP	82

11.2.3 HRP activity in THS	82
11.2.4 Influence on the oxidative activity of THS-HRP upon addition of ATP or ATP analogues ..	83
11.2.5 Conclusions	85
12. Gold nanoparticle formation in THS-PAMAM	87
12.1 Introduction gold nanoparticles	87
12.2 Results and discussions	87
12.3 Conclusions	91
13. Conclusions and Outlook.....	92
13.1 Conclusions	92
13.2 Outlook.....	93
14 Experimental sections	95
14.1 Materials	95
14.2 Buffers and broths.....	95
14.3 Methods	95
Bibliography	107
Appendix	117
Curriculum vitae.....	119
Publications.....	121

Acknowledgements

I would like to thank all the people who helped and supported me during these four and a half years of my PhD studies. It was a good, interesting, hard, funny, nerve-wracking, and playful time.

First of all, I want to deeply thank my supervisor Nico Bruns, who supported me in a very pleasant way and gave me lots of helpful advices. During these years he often gave me new ideas, helped me look at a problem from another perspective and gave me some freedom to play around. I profited a lot from his knowledge and kindness. I most graciously thank Wolfgang Meier, who hosted me in his group and offered the opportunity to work in his labs. He lent me his support, whenever I needed it. I also want to thank Tanja Weil to be the Co-Referee of my thesis.

Furthermore, I would like to thank the “Thermosome team”, namely Martin Rother and Kasper Renggli for pushing the thermosome projects, for deeply scientific talks and not so deeply, funny chats. I also like to thank my project students Alessandro Potenza and Christoph Bisig, who performed excellent work on their projects. I would also like to thank Thomas Mindt and his group for helping me with the BBN project and Ingo Muckenschnabel for helping me analyzing the thermosome with UPLC-MS at Novartis. Thanks to Mohamed Chami for performing cryo TEM measurements, Vesna Olivieri for performing TEM measurements, Janine Zankl and Verena Jäggin for helping me with FC and Raphael Urbani for SAXS measurements. I also like to thank Ozana Onaca, from whom I learned a lot in the lab. I kindly thank Danny Tischhauser, Maya Greuter, Jean-Pierre Ramseyer, Gaby Persy, Urs Buser and Sven Kasper, who organized everything in the background. Huge thanks to Jason Duskey for checking and correcting my thesis. Additionally, I would like to thank Jacqueline Bezençon and Adrian Najer for reading and correcting some thesis chapters.

I deeply want to thank all the friends, who were or still are in the Meier or Bruns groups for such a nice time. Special thanks to my former seatmates Daniela Vasquez (I hope we will meet again at the beach with some good Venezuelan rum) and Mihaela Delca. Further thanks to all the office neighbors, especially Patric Bauman (for inspiring talks), Mihai Lomora (always good for a distraction), Adrian Najer (for the funny and intellectual chats), Dalin Wu (the liger team will win), Pascal Tanner (crouch as fast as you can), King Roger (it was a honor to serve you) and Jörg Braun (thank you for forwarding me your seat). I would like to thank Sven Kasper, Severin Sigg, Martin Rother, Fabian Itel, Jason Duskey, Dalin Wu, Thomas Schuster, Stefan Egli, Etienne Cabane, Jörg Braun, Jonas Pollard, Riina Häkkinen, Jagadeesan Sivaraman, Pascal Richard, Adrian Najer, Kasper Renggli and Raphael Urbani to make the time here unforgettable. I also want to thank Thomas “der Panzer” Pfohl and Marc Creus for good chats with and without beer.

Athletic thanks to all members of the glorious and magnificent FC Science United. I would also like to thank the members of the Science Slam Club Basel, where I learned a lot.

A huge “thank you” to all my friends, who supported me during this time and who blow my cobwebs away. The “Nanogang”: Lucas, Luuki, This, Nele, Melanie, Andi, Petz, Dario, Sonja and Su, additionally Böni and Ralph and my “old” friends from Bern: Hugi, Bänz, Zbindä, Sämi, Dave, Äntä, Tschagglin, Ursi, Carmen, Klubi, Tanja, and Michu.

I deeply thank my lovely girlfriend Steffi, who backed me since I have known her and made the whole time easier. Last but not least, I would like to express my deepest thanks to my parents Franz and Rita, who supported me at anytime and any case and believed in me all the years.

Abbreviations

ABTS:	2,2'-azino-bis(3-ethylbenzthiazoline-6-sulfonic acid)
AcN:	acetonitrile
ADP:	adenosine diphosphate
ATP:	adenosine triphosphate
ATP- γ -S:	adenosine 5'-(gamma-thiotriphosphate)
AuNP:	gold nanoparticle
AuNP-Mal:	1.4 nm monomaleimido nanogold
AuNP-NHS:	1.4 nm mono-sulfo-NHS-nanogold
BBN:	bombesin
BBN-8/12EG:	bombesin with 8, respectively 12, ethylene glycol units at the C-terminus
CCK-8:	cell counting kit-8
CCMV:	cowpea chlorotic mottle virus
CCT:	chaperonin containing TCP1
CHO-K1:	Chinese hamster ovary cells
CLSM:	confocal laser scanning microscopy
CPP:	cell penetrating peptides
cRGDFc:	cyclo(-Arg-Gly-Asp-D-Phe-Cys)
dhRh6G:	dihydrogen rhodamine 6G
DMEM:	Dulbecco's modified Eagle medium
DMF:	dimethylformamide
DNA:	desoxyribionucleic acid
Dox:	doxorubicin
dsRNA:	double stranded RNA
DTT:	dithiothreitol
eCFP:	enhanced cyan fluorescent protein
EDTA:	ethylenediaminetetraacetic acid
EMSA:	electrophoretic mobility shift assays
EPR effect:	enhanced permeability and retention effect
ESI:	electron spray ionization
eYFP:	enhanced yellow fluorescent protein
FA:	folic acid
FC:	flow cytometry
FCS:	fluorescence correlation spectrometry
FPLC:	fast protein liquid chromatography
GroEL/GroES:	bacterial group I chaperonin and its co-chaperonin
GRP:	gastrin-releasing peptide
GSH:	glutathione
HeLa:	cervical cancer cells
HPLC:	high performance liquid chromatography
HRP:	horseradish peroxidase
HUVEC:	human umbilical vein endothelial cells
HWHM:	half width at half maximum
HyNic:	succinimidyl-6-hydrazinonicotinamide acetone hydrazone

LC:	liquid chromatography
LF:	Lipofectamine 2000
mal:	maleimide
MALDI-MS:	matrix-assisted laser desorption/ionization mass spectrometry
MCF-7:	breast adenocarcinoma cells
MHP:	maleimido-2-hydraziniumpyridine
miRNA:	microRNA
Mm-cpn:	chaperonin from the archaea <i>Methanococcus maripaludis</i>
mRNA:	messenger RNA
MS:	mass spectrometry
MSR:	molecular substitution ratio
MTFB:	maleimido trioxa-6-formylbenzamide
MWCO:	molecular weight cut-off
NDDS:	nano drug delivery systems
NHS:	hydroxysuccinimide
nt:	nucleotide
PAGE:	polyacrylamide gel electrophoresis
PAMAM:	poly(amidoamine) (PAMAM), in the experiments always 4 th generation PAMAM
PAMAM G4:	4 th generation PAMAM
PBS:	phosphate buffered saline
PC-3:	prostate cancer cells
PEG:	poly(ethylene glycol)
PEG ₄ -PFB:	tetra ethylene glycol pentafluorophenyl ester 4-formylbenzamide
PEI:	polyethyleneimine
PITC:	phenyl isothiocyanate
PK:	proteinase K
PMSF:	phenylmethanesulfonyl fluoride
PPI:	polypropylenimine
R _H :	hydrodynamic radius
RISC:	RNA-induced silencing complex
RNA:	ribonucleic acid
RNAi:	RNA interference
S-SS-4FB:	succinimidyl-disulfide-4-formylbenzamide
SAXS:	Small angle X-ray scattering
SD:	standard deviation
SDS:	sodium dodecyl sulphate
SDS-PAGE:	sodium dodecyl sulphate polyacrylamide gel electrophoresis
SEC:	size exclusion chromatography
shRNA:	short hairpin RNA
sHSP:	small heat shock proteins
siRNA:	small interfering RNA or short interfering RNA
SM(PEG) ₂ :	succinimidyl-([N-maleimidopropionamido]-2ethyleneglycol)ester
SPION:	super paramagnetic iron oxide nanoparticles
ssRNA:	single stranded RNA
SST:	somatostatin
TAT:	transactivator of transcription protein from HIV

TAT-HyNic:	6-hydrazinonicotinamide acetone hydrazone-GRKKRRQRRRPPQ-NH ₂
TEM:	transmission electron microscopy
THF:	tetrahydrofuran
THS:	mutated version of the thermosome from <i>T. acidophilum</i>
TIC:	total ion current
TOF:	time-of-flight
TRiC:	TCP1 ring complex
U-87 MG:	glioblastoma cells
UPLC:	ultra performance liquid chromatography
VEGF:	vascular endothelial growth factor
VLP:	Virus-like particles

1. Introduction nanomedicine

M.G. Nussbaumer

1.1 Nanomedicine

Conventional cancer drugs often have a poor pharmacokinetic profile and are distributed non-specifically throughout the whole body, causing toxicity to the patient due to healthy cell death. Additionally, a major fraction of the drug never reaches its target tissue. The aim of nanomedicine is to prevent such side-effects and deliver the drug only to the diseased tissue.^{1,2} The idea of a magic bullet, which delivers a drug only to a targeted location, was framed over hundred years ago by Prof. Paul Ehrlich.^{1,3} With the upcoming discoveries in nanomedicine, we are getting closer to this idea, namely with nano drug delivery systems (NDDS). A perfect NDDS satisfies many different needs: they should protect the drug against degrading enzymes and opsonisation to avoid premature degradation, they should have an adequate stability in the bloodstream, and NDDS should prevent uptake off target cells, thus avoiding side effects. Furthermore, the NDDS should target specific cells, enhance the drug uptake, and release the drug in a controlled manner (*Fig. 1.1*).^{2,4}

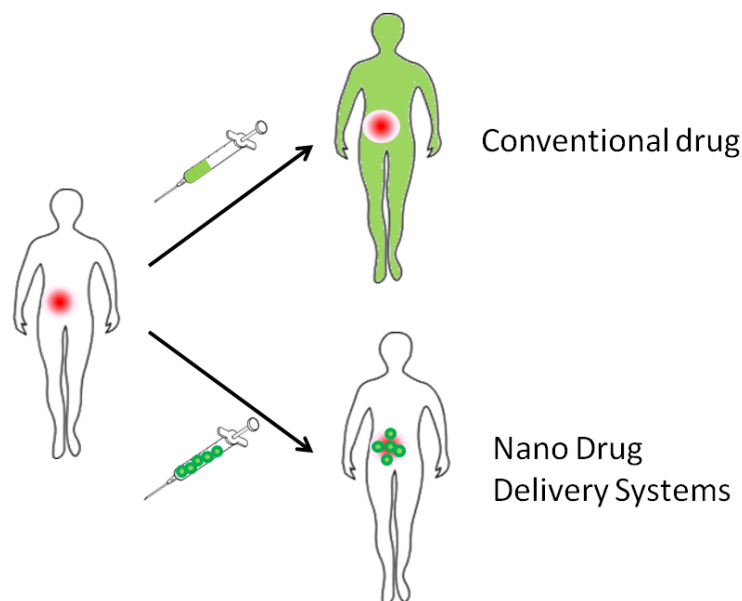


Fig. 1.1: Schematic comparison of the mechanism of action of conventional drug and nano drug delivery systems.

1.2 Nano drug delivery systems

Typically NDDS are macromolecules, or assembly of macromolecules, which are covalently or non-covalently bound to a drug or imaging agent, aiming to protect their cargo from premature degradation. More and more NDDS are now equipped with cell targeting moieties to enhance cell specific uptake and stealthing moieties to hide from the immune system and escape from opsonisation and premature clearance.⁵ Per definition, the size of nano drug delivery systems are between 1 nm and 100 nm.⁶ However, particles up to a size of 200 nm show a similar clearance profile and are often also called “nano”.⁷⁻⁹ Due to the small size of these drug delivery systems, they have high surface to volume ratio. This results in a huge surface for chemical interactions with biomolecules.⁴ However, the real benefit of NDDS are their advantages over free drug. By binding the

drug to a NDDS, their pharmacokinetic and biodistribution characteristics can be altered. Free drugs are often cleared too rapidly from the blood stream by the kidney, liver or spleen, thus a high administered dose is needed to reach the minimum effective dose at the target site. To achieve a high circulation time of the NDDS in the blood, the NDDS has to be larger than 5.5 nm, because this is the cut-off for renal clearance.¹⁰ The upper size limit for NDDS is around 200 nm. Larger objects are removed from the blood circulation by the hepatosplenic filtration process.⁹ A big difficulty of conventional drug delivery represents the administration of hydrophobic drugs, as they may precipitate in aqueous media. Amphiphilic NDDS, meaning NDDS that provide hydrophilic and hydrophobic entities, are able to bind a high quantity of hydrophobic drug while remaining soluble in the blood. Good examples are lipid or polymeric micelles or vesicles (see chapter 1.5 *Types of NDDS*). Beside hydrophobic drugs, hydrophilic drugs can also be incorporated in NDDS to protect them from rapid breakdown in the bloodstream. This protection comes from stopping the drug from coming into contact with degrading environments and substances such as pH, esterases, nucleases, or other degrading substances.⁸ While free drugs have a lack of selectivity for targeted tissue, NDDS can be modified with targeting moieties for active targeting, allowing a higher concentration to accumulate in the diseased tissue and additionally inducing a selective uptake into cells. Some NDDS have mechanisms to release the drug at a desired location (i.e. close to or in the desired cells). These release mechanisms are either triggered systems, which release their cargo upon a stimulus, and/or slow releasing systems, which are able to keep the drug concentration constant over a certain period of time. The combination of tissue targeting and controlled release allows administering a lower dose of drug to the patient, while keeping the drug concentration at the desired tissue at a high level. At the same time the drug concentration in the rest of the body is minimal. Thus, potential side effects can be reduced.^{1, 2, 8}

1.3 Passive and active targeting

A crucial advantage of NDDS over conventional drugs is their improved biodistribution and their longer circulation time in the body due to their size and surface chemistry.⁸ To achieve higher drug concentration at tumor tissue than in healthy tissue, drugs benefit from the so-called enhanced permeability and retention (EPR) effect.^{1, 11} Solid tumors are fast growing and consume a lot of nutrients and oxygen. To guarantee the supply of nutrients, tumors start to recruit new blood vessels and do vascular remodeling. Angiogenic vessels have 600 nm to 800 nm large fenestrations allowing NDDS to extravate into the tumor tissue (*Fig. 1.2*).^{2, 8} These effects result in an up to 10-times higher drug concentration in the tumor tissue compared to the concentration in other tissues.^{8, 12} Furthermore, tumors lack effective lymphatic drainage.^{2, 8} Small molecular drugs also benefit from the EPR effect. However, due to their size, they freely diffuse out of the cancer tissue, whereas NDDS are retained in the tumor due to their size (*Fig. 1.3 A*).¹ Enhanced vascular permeability is also seen in inflammation, making inflammatory tissue another suitable target for NDDS.⁸

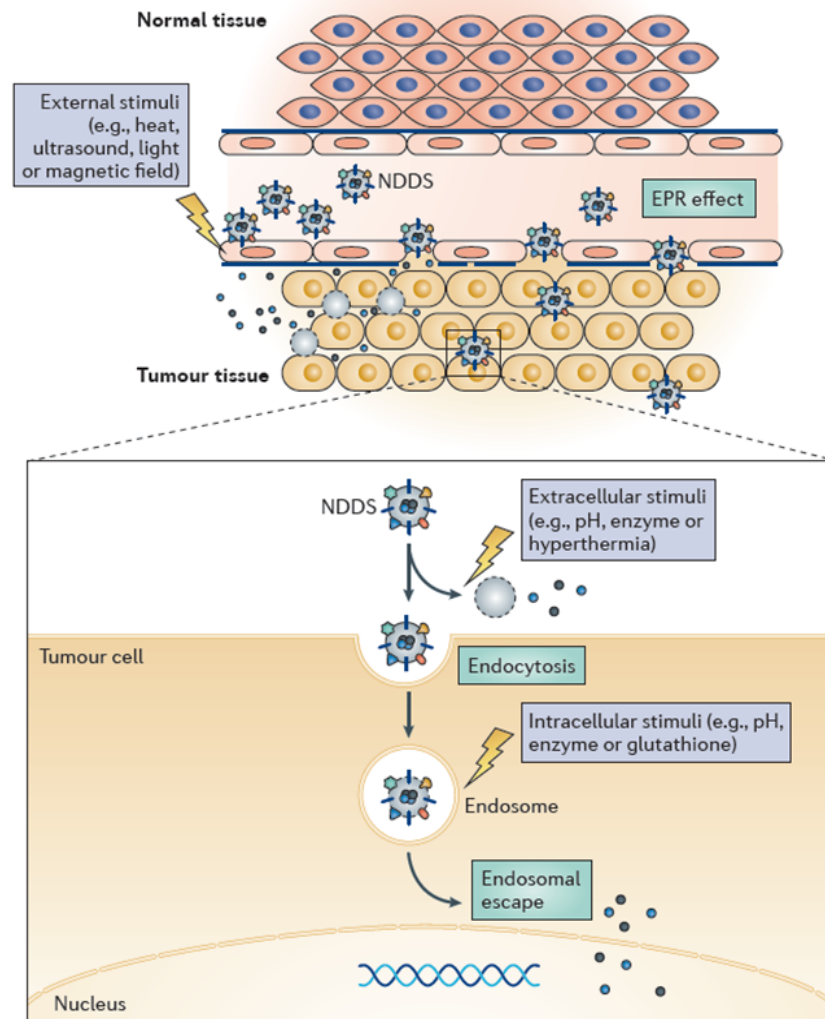


Fig. 1.2: Structure of normal and tumor tissue and the triggered release of cargo from NDSS. By courtesy of Torchilin et al..⁵

There are two classifications of targeting, passive (e.g. EPR effect) and active (e.g. targeting ligands).^{13, 14} However, active targeting depends on passive targeting. In contrast of the implied idea that active targeted NDSS are searching for their target tissue, active targeted NDSS are distributed via passive distribution (EPR effect) to tumor tissue or inflammations. There, active targeted NDSS bind to the targeted cells and promote the uptake of the NDSS into the cells.¹⁴ This increases the NDSS concentration in the specific tissue (Fig. 1.3 B). Active targeting relies on ligands (e.g. peptide sequences, antibodies, aptamers, carbohydrates or nutrition analogues, such as vitamins and growth factors), which bind to cell type specific receptors, concentrating the NDSS at the cell and enhancing their uptake (Fig. 1.3 B). Favored targets are upregulated receptors, which can be specific for a certain cell type. Cancer cells often over express nutrition receptors, such as biotin or folate, which make them interesting for NDSS. By attaching a high number of ligands to a NDSS leads to a multivalent binding effect resulting in a much stronger binding to the cell compared to monovalent binding.^{1, 2, 9, 13} In addition to targeting ligands, NDSS can also be modified with cell penetrating peptides (CPP). CPP's are a powerful tool to transport NDSS into cells. Most often CPP are positively and address the cell membrane by interacting with the negative glycosaminoglycans, but also amphiphatic and hydrophobic CPP's are known. The most prominent representative is TAT, the

transactivator of transcription protein from HIV. A minimal sequence of nine amino acids was found to be the crucial sequence.¹⁵ However, in contrast to targeting ligands, they are not specific for a cell type, but rather penetrating all cell types.^{16,17}

Unfortunately, only 1 % - 10 % of the injected dose of NDDS is eventually found in the tumour.¹² Thus, further investigations have to be conducted to increase this portion and make NDDS more specific for their target.

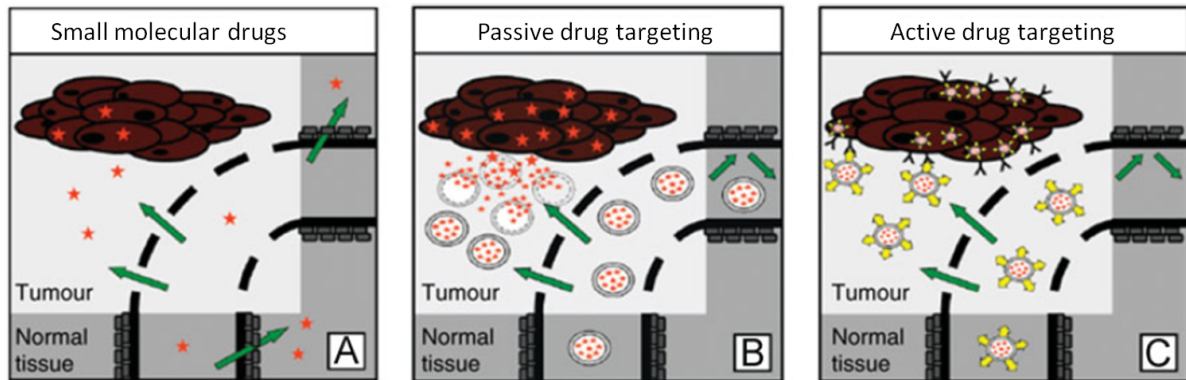


Fig. 1.3: Behavior of small molecular drug (A), untargeted NDDS (B) and active targeted NDDS (C).
By courtesy of MaHam et al..¹⁸

1.4 Cargoes of NDDS and release strategies

Because cancer tissue often exhibits the EPR effect, the majority of NDDS, which are under research or already on market, are related to cancer.⁵ For instance they are loaded with anticancer drugs such as paclitaxel, daunorubicin, or doxorubicin.² However, there are also different other applications for NDDS, namely antibiotics,¹⁹ siRNA,²⁰ DNA,²¹ and contrast agents for MRI, PET or other imaging methods.²² NDDS can also encapsulate enzymes to substitute lacking enzymes in cells or which convert pre-antibiotics into antibiotics.²³⁻²⁵

NDDS protect the drug from premature degradation and release, but when the cargo is at its destination, the NDDS has to release the drug in a controlled way. Either the drug is cleaved from the NDDS or a crucial bond of the NDDS is split, which then destabilizes the NDDS and subsequently releases the drug. Different stimuli in cells or in diseased tissue are used for a triggered release of the drug (Fig. 1.2).^{1,5} Tumors or inflammation sites exhibit a lower pH than other tissue. Additionally, during the endosomal uptake of NDDS, the up taken molecules are acidified to pH 5. Thus, pH-labile systems (e.g. hydrazone bonds) are one of the triggered release strategies.²⁶ NDDS which are held together by electrostatic interactions can be destabilized by changing pH or by high salt concentration, for instance interactions between cationic polymers and nucleic acids.²⁷ Another strategy capitalizes on the higher reduction potential in the cells, which can split reductive sensitive moieties like disulfide bonds.²⁸ In the cell, different enzymes are capable to degrade the NDDS or to cleave crucial bonds, such as esterases or proteases.⁵ A further stimulus is temperature. Normally, the temperature difference between normal and diseased tissue is too small to trigger release. Therefore, the desired tissue could be heated by external sources such as electromagnets (for magnetical NDDS), lasers, or ultrasound.⁵

1.5 Types of NDDS

Different types of NDDS are under investigations or are already applied in medical use. There are lipid-based, such as liposomes and lipidic micelles; polymeric, such as polymeric micelles, polymersomes or dendrimers; peptide-based compartments, e.g. protein cages; metal or silica nanoparticles; quantum dots; carbon nanotubes; fusion proteins or a combination thereof.^{5, 29} Lipid-based, polymer-based and protein-based NDDS will be explained in more details in the next paragraphs.

1.5.1 Lipid based NDDS

The majority of NDDS, which are in clinical trials or on the market, are based on lipids.²⁹ Liposomes have a diameter between 50 nm – 250 nm, show low immunogenicity, have high encapsulation efficiency, and are easy to produce.^{30, 31} There are liposome-based NDDS on the market for drugs against ailments like fungal infections (Amphotericin B), cancer (Daunorubicin, Doxorubicin), or viruses (inactivated hepatitis A virus or hemagglutinine of influenza virus). Additionally, several liposomal drugs are in clinical trials, most of them for cancer treatment.^{5, 8, 30, 32} However, liposomes suffer from low stability and leaking of the encapsulated compound due to the low thickness of the lipid bilayer.^{33, 34} Additionally, liposomes have a reduced circulation time, because they are prone to opsonisation.³⁴ To stabilize liposomes and prolong their circulation time, they are often coated with polymer, e.g. poly(ethylene glycol) (PEG).³¹

1.5.2 Polymer based NDDS

An alternative to lipid based NDDS are polymer based NDDS. Compared to lipids, polymers offer a broader field of application. Polymers are applied in different morphologies to create NDDS (*Fig. 1.4*). Similar to lipids, amphiphilic polymers can form micelles, hollow spherical vesicles, so called polymersomes, or dendrimeric polymers, which are hyperbranched polymers.³⁵⁻³⁷

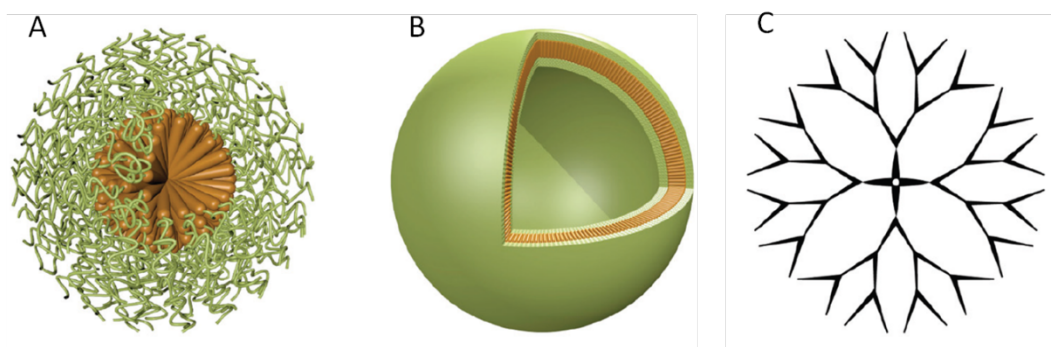


Fig. 1.4: Different morphologies of polymers that are used as NDDS: (A) micelle, (B) polymersome and (C) dendrimer. By courtesy of Gunkel-Grabole et al..³⁸

1.5.2.1 PEG

One of the most employed polymers for NDDS is poly(ethylene glycol) (PEG). PEG is a neutral hydrophilic polymer, which is often used to camouflage NDDS, concealing the NDDS from opsonisation and clearance by the immune system.⁵ Besides its camouflaging effect, PEGylation is also used for increasing the hydrodynamic size of pharmaceutical active proteins or peptides to decrease drug clearing by the kidneys and therefore prolong their circulation time.⁸ Examples for approved PEG conjugates are PEG-asparaginase against acute lymphoblastic leukemia, PEG-adenosine deaminase to treat severe combined immunodeficiency disease, PEG-interferone α 2a

against hepatitis C or PEG-growth hormone receptor antagonist for the treatment of acromegaly.³⁹ However, it has been shown in *in vivo* studies that PEGylated nanoparticles induce PEG specific antibodies, which can induce accelerated clearance of the nanoparticles.^{40,41} PEG is still the gold-standard, but there are other hydrophilic polymers, which are also fulfilling the needs for NDDS, such as poly [N-(2-hydroxypropyl)-methacrylamide], poly(acryloyl-morpholine), poly-N-vinylpyrrolidones, poly(2-methyl-2-oxazoline) and poly vinyl-alcohol.⁵

1.5.2.2 Micelles

Amphiphilic polymers as well as lipids can form micelles, which have a core-shell structure, whereby the hydrophobic part of the polymer/lipid forms the inner core and the hydrophilic part forms the corona.⁴² Polymeric micelles have typical sizes between 5 nm and 100 nm depending on their polymer composition.⁴³ They are attractive to encapsulate poorly soluble drugs and imaging agents, such as doxorubicin and paclitaxel (anti-cancer drugs) or pyrene (hydrophobic fluorescent probe) to make them water soluble.^{42,44} Another polymeric micelle type are the polyion complex micelles. They are composed of ionic polymers with opposing charges and they self-assemble into micelles. PICs are suitable for encapsulation and delivery of charged cargo, such as DNA or siRNA.^{45,46}

1.5.2.3 Polymersomes

Amphiphilic polymers with an increased ratio of hydrophilic to hydrophobic block length tend to form hollow spherical nanoparticles (polymersomes). They have a diameter of 50 nm up to several hundred micrometers for giant vesicles.⁴⁷⁻⁵⁰ During the self-assembly process, they encapsulate the surrounding media and seal it in the vesicles. Normally, the load is hydrophilic and can be inserted in the cavity of the NDDS, but also hydrophobic drugs can be inserted into the hydrophobic part of the membrane. Thus, the NDDS can be load with different drugs simultaneously. Compared to liposomes, polymersomes have several advantages, such as the impermeability for their cargo due to their thicker membrane. Their thicker membrane also has the beneficial effect on their robustness.⁴⁷ Another advantage of polymersomes is their versatile ability to be modified.⁴⁹ Different parameters can be altered, which influence the characteristics of polymer based NDDS, such as length of the polymers, the ratio between hydrophilic and hydrophobic parts, hydrophobicity, shape, and termination of the polymers. In contrast to liposomes, the polymersomes can consist not only of an amphiphilic diblock copolymer AB, but also amphiphilic triblock copolymer ABA or ABC, or even higher order block copolymers. Mixing different polymers makes it possible to easily combine different features. Therefore, many different NDDS functionalizations can be implemented simultaneously. A lot of different polymers have been used to form polymersomes. Prominent polymers for the hydrophilic part are PEG and poly(2-oxazoline)s.^{51,52} For the hydrophobic part, the following polymers are often used: polystyrene, poly(ethylene), poly(lactic acid), poly(dimethylsiloxane), poly(ϵ -caprolactone) and poly(lactide-co-glycolic acid), whereas poly(lactic acid), poly(ϵ -caprolactone) and poly(lactide-co-glycolic acid) are biodegradable esters.²⁹

Polymersomes are often equipped with stimuli-responsive features, such as redox sensitive disulfide bonds or poly(propylene sulfide), pH-responsive polymers (e.g. poly(2-vinyl-pyridine), and polyacrylic acid), UV-labile, or thermo-responsive polymers (e.g. poly([2-diisopropylamino] ethyl methacrylate)). All these polymers fall apart or change their structure upon a specific stimuli resulting in a disintegration of the nanostructure and a release of the drug.⁵³

1.5.2.4 Dendrimers

Dendrimers are hyperbranched uniform spheric polymers with a size range between 1 nm and 10 nm.⁵⁴ In contrast to “conventional” polymers, dendrimers are synthesized stepwise from a multifunctional core, whereas in every step/generation an additional bifurcation is added. Thus their molecular weight and the number of end groups increase exponentially to the number of generation. The step wise synthesis of dendrimers allows achieving polymers with well defined molecular structure and weight, e.g. low poly-dispersity.⁵⁵ To the end groups of dendrimers, a multitude of drugs, targeting, or shielding moieties can be attached. Poly(amidoamine) (PAMAM) is the first synthesized, commercialized, and best characterized dendrimer.^{56, 57} Besides PAMAM, polylysine dendrons, polyester based dendrimers, dendritic polyglycerol or polypropylene imine are also common materials to build dendrimers.^{55, 58} Dendrimers offer the possibility to bind hydrophilic and hydrophobic drugs in their core and drugs or contrast agents can be conjugated to the end groups (Fig. 1.5). Such strategies were used to deliver drugs such as diclofenac, doxorubicin, antibodies, porphyrin or 5-fluorouracil; or imaging agents, such as Gd(III), ^{99m}Tc or Alexa Fluor 594.^{55, 59, 60} Cationic dendrimers, especially PAMAM, are well suited for nucleic acid transfection. With their high density of positive charged end groups, they are able to bind to the negative backbone of nucleic acids (Fig. 1.5).^{38, 61}

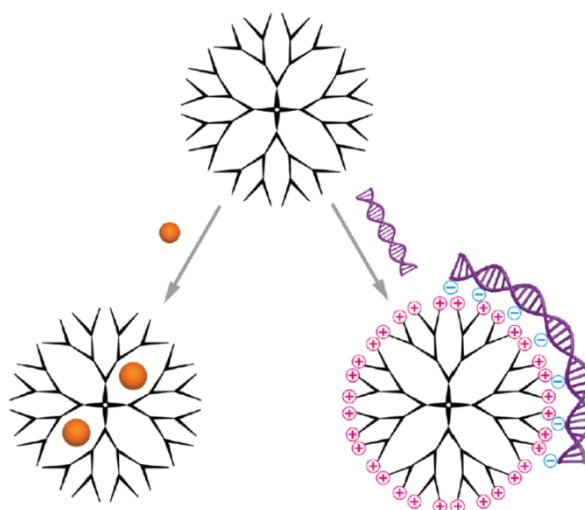


Fig. 1.5: Encapsulation of host molecules (left) and interaction of positive charged dendrimer with the negatively charged backbone of nucleic acids (right). By courtesy of Gunkel-Grabole et al..³⁸

1.5.3 Protein based NDDS

Therapeutic proteins, often in combination with polymers, are already used as NDDS (i.e. Adagen and Oncaspar by Enzon).⁸ In the last years protein cages are under consideration as NDDS. Protein cages are hollow robust nanostructures self-assembled from a multitude of protein subunits that exhibit several symmetrical elements. In contrast to other NDDS, which often lack narrow size distribution, protein cages are well defined in size and morphology. Their typical size between 10 nm and 100 nm is optimal for receptor mediated endocytosis. Protein cages are non-toxic, biodegradable, and exhibit chemical and thermal stability.^{12, 62, 63} However, they can potentially be a source of immune reactions.^{64, 65}

1.5.3.1 Types of protein cages

Protein cage is a generic term for a broad range of proteins, which form a cavity and can enclose guest molecules in their cavity. They belong to different protein families. Virus-like particles (VLP) are

one kind of protein cage. They consist only of the structural proteins of the virus, the so called capsids, without any genetic information of the virus. Examples of VLP protein cages, which were used as NDDS, are following: cowpea chlorotic mottle virus (CCMV),⁶⁶ tobacco mosaic virus (TMV),⁶⁷ cowpea mosaic virus,⁶⁸ bacteriophage MS2 and P22,^{69, 70} adenovirus,⁷¹ or avian sarcoma leukosis virus.⁷² Non viral protein cages, which were studied, are DNA binding protein,⁷³ lumazine synthase,⁷⁴ small heat shock proteins (sHSP),^{75, 76} ferritins⁷⁷ and chaperonins.^{78, 79} In nature, non viral protein cages have diverse roles such as nucleic acid storage, help for protein folding, to protect proteins from misfolding or storage and sequestration of minerals.

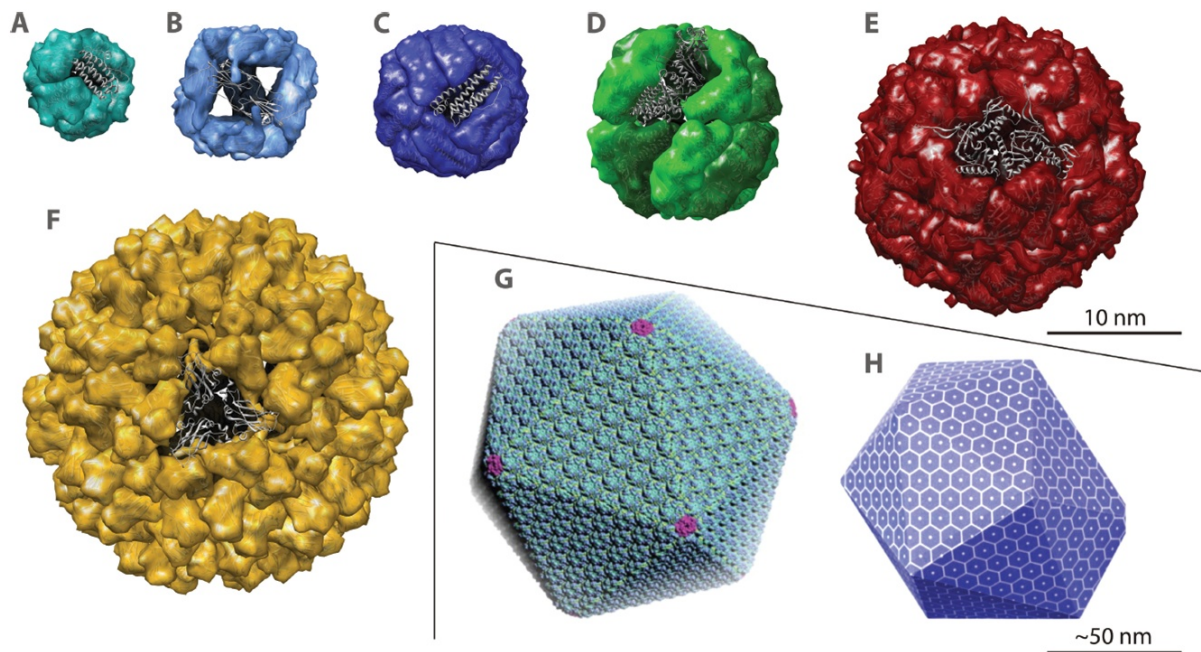


Fig. 1.4: Structures of different protein cages: **(A)** DNA binding protein from starved cells, **(B)** small heat-shock protein, **(C)** apoferritin, **(D)** thermosome, **(E)** encapsulin, **(F)** cowpea chlorotic mottle virus, **(G)** proposed model of carboxysome, **(H)** proposed model of ethanolamine utilization microcompartment. By courtesy of Renggli et al..⁸⁰

1.5.3.2 Biodistribution of protein cages

In a study of T. Douglas, M.J. Young and co-workers,⁸¹ the biodistribution of two protein cages, namely CCMV and Hsp, was analyzed. Even though, CCMV and Hsp differ in size (28 nm vs. 12 nm), in structure (icosahedral vs. octahedral), and in sequence, both protein cages showed a similar biodistribution. This could be because of their similar charge at neutral pH. Within one hour after i.v. injection, the protein cages were rapidly distributed and found in the majority of the organs. The protein cages translocated rapidly and easily through the tissues and extravasated from the circulatory system to the interstitial space, then further to the lymphatic system and eventually again in the vascular system. After 24 hours, the majority of the protein cages were cleared from the mice, without any mortality. In contrast, similar studies with CPMV showed deposition of this protein cage in certain organs up to 72 hours.^{82, 83} CCMV and Hsp showed immunogenicity and induced IgG and IgM response. However, such side effects, which also occur with other NDDS and therapeutic proteins, could be overcome with PEGylation or other shielding of the protein cages.⁶² The biodistribution for both protein cages in immunized mice showed the same results as in naïve ones. In general, protein cages are suggested as safe, non-toxic and biocompatible NCCS.^{81, 84}

1.5.3.3 Modification of protein cages

The subunits of the protein cages can be genetically and/or chemically precisely modified on the inside, outside, and between the subunits, to tune their properties. This characteristic makes protein cages similar to a Lego set.^{63, 85} By genetic engineering of the protein cage's subunits non-native amino acids or cysteines can be precisely inserted at a desired location in or on the protein cages. These point mutations can act as specific attachment points for drugs, imaging agents, targeting moieties or others.⁶² Cysteines, lysines, aspartic and glutamic acids, and tyrosines can be specifically modified with the desired ligands (*Fig. 1.5*).⁸⁶ Modification of the interface between the subunits can be used to tune the stability of the protein cages.

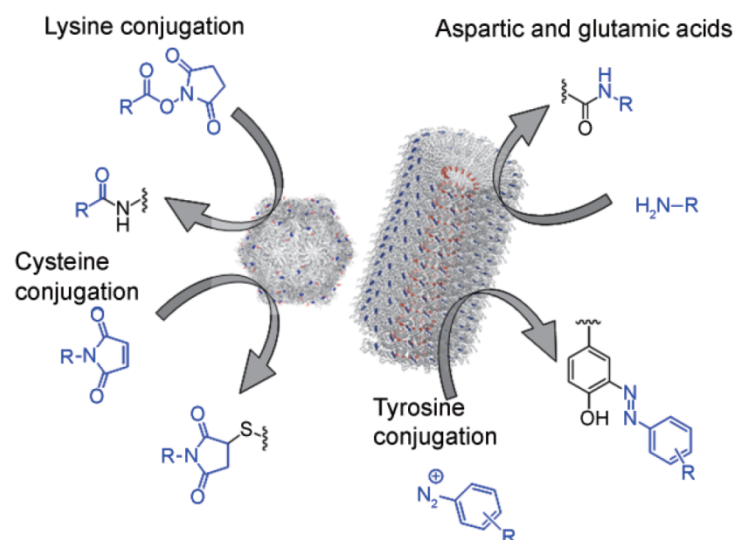


Fig. 1.5: Different amino acids allow a modification of the protein cage with additional functional moieties. By courtesy of Lee et al..⁸⁶

The exterior of the protein cages represent an ideal surface for multivalent ligand display. Both the inner surface and the exterior surface can be genetically or chemically modified. The outer surface was mostly modified with cell targeting and penetrating moieties to enhance specific uptake by the desired cell types. To this end, the tripeptide RGD,^{87, 88} folic acid,⁷¹ biotin,⁷³ aptamer⁸⁹ and others were conjugated to the protein cages and induced enhanced uptake of the protein cages into the specific cell lines.

1.5.3.4 Cargoes of protein cages for drug delivery and imaging purposes

The inside of protein cages creates a protective environment for their cargo. To pack the protein cages with cargo, it is often sufficient to disassemble the protein cages (e.g. by lowering the pH) and let them reassemble in a solution with the cargo present (*Fig. 1.6*).^{63, 87} To increase the loading capacity of the protein cages polymer matrices were polymerized in the proteins' cavities. These polymer matrices act as multivalent anchor for the guest molecules.^{90, 91}

A variety of cargoes were introduced to protein cages for medical applications. Doxorubicin,^{87, 92} paclitaxel,⁷¹ and daunomycin⁷⁷ are representatives of anticancer drugs, which were loaded in HSP, adenovirus, and lumazine synthase respectively. Photosensitizers, i.e. porphyrin or SnCe₆, for photodynamic therapy were incorporated into MS2 bacteriophages⁸⁹ and CCMV.⁶⁶ In other works, the protein cages P22 bacteriophage and ferritin were loaded with Gd(III),^{93, 94} fluorophores^{91, 95} or magnetite⁸⁸ as contrast agents. It was also shown that therapeutic enzymes and even multiple enzymes to achieve an enzyme cascade can be enclosed into protein cages.^{96, 97} Viruses are natural

transfer vehicles for genes. To convert viruses to beneficial vectors, their own genomes were exchanged with beneficial genes for gene delivery.⁹⁸ Not only DNA, but also RNA was encapsulated in protein cages to induce RNA interference.^{74,99}

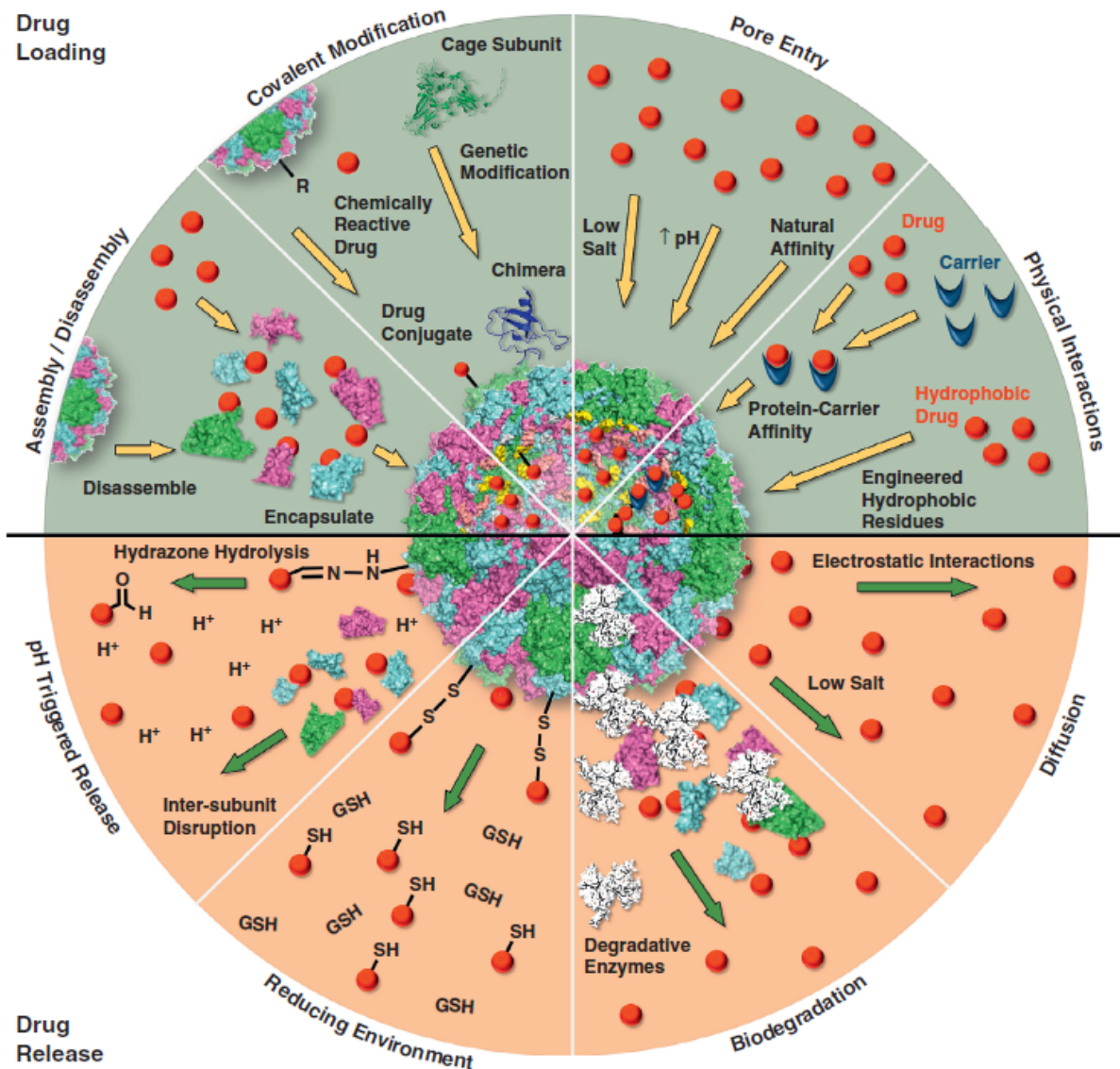


Fig. 1.6: Different ways of loading protein cages with drug and their release. By courtesy of Molino et al.⁶²

1.5.3.5 Pores of protein cages

Some of the protein cages possess pores, where cargo can diffuse through, which can be used for slow release of the drugs. Some of them are “static” and their diameter ranges from 0.4 nm for ferritins¹⁰⁰ to 3 nm for sHSP.¹⁰¹ Other pores change diameter upon a stimulus and can be used for a triggered release of the cargo. Some viral capsids swell upon change of the concentration of metal ions or pH. For instance CCMV changes from a “pore-less” conformation at low pH with metal ions to a conformation with 60 pores, each 2 nm in diameter.¹⁰² There are also some protein cages, which have triggerable small pores, but their stimulus is not known yet.^{103,104} Only small molecules can diffuse through the pores of the above mentioned protein containers. To enclose macromolecules, such as polymers, proteins or siRNA, the protein cages have to be disassembled and reassembled in presence of the macromolecules. In contrast, chaperonins feature one of the biggest pores in the

domain of protein cages (up to ~8 nm). Their pores enable polymers and proteins up to 50 kDa to diffuse into the chaperonin via their pores without the need to disassemble the protein cage structure.^{78, 105} The cavity of group I chaperonins, such as GroEL, is closed by an additional protein complex (GroES) upon addition of ATP, whereas group II chaperonins have a built in lid, which also close the pore upon ATP addition.^{106, 107} Chaperonins and their mechanism are described more in details in chapter 2. *Introduction chaperonins.*

1.5.3.6 Conclusion on protein cages as NDDS

In conclusion, protein cages are highly stable and have very well defined structures and sizes, which fit well in the therapeutic size window for long circulation time. Their cavities can transport, protect and release a variety of cargoes, ranging from hydrophobic small drugs, highly charged macromolecules, to metals as imaging agents and different others. Due to their highly versatile surfaces, single amino acids of protein cages can be modified genetically and chemically, introducing new features, for instance to conjugate cargo to the protein cages on the inner surface or targeting and cell penetrating moieties on the outer surface. Thus, protein cages represent an interesting alternative to other NDDS.

2. Introduction chaperonins

M.G. Nussbaumer

2.1 Group I chaperonins vs. group II chaperonins

Chaperonins belong to the large family of chaperones. They are involved in the protein folding process by stabilizing folding intermediates and preventing proteins from misfolding or aggregating. Their expression is up-regulated in cells upon heat shocks, but also other stress situations, like inflammation.^{107, 108} They are divided in group I chaperonins, found in bacteria and organelles of eukaryotic cells (e.g. chloroplasts and mitochondria), and group II chaperonins, located in the cytosol of eukaryotic cells and archaea.

The most prominent group I chaperonins are the prokaryotic GroEL/GroES and their eukaryotic equivalent Hsp60. GroEL is composed of fourteen identical subunits, which are arranged in two stacked heptameric rings, forming a barrel like structure with an internal cavity in each ring. The co-chaperonin GroES represents the lid for the GroEL. GroES and ATP are needed for proper folding of the protein.¹⁰⁹ Group II chaperonins are also composed of several subunits forming two back-to-back stacked rings. The subunits consist of an equatorial domain that is connected by an intermediate hinge domain to an apical domain. However, there are major structural differences between those two groups (*Fig. 2.1*). In contrast to group I chaperonins, which need a co-protein to close the internal cavity, group II chaperonin subunits feature a helical protrusions at the apical domain, which act as a built-in-lid and close the cavity in an ATP depending manner (*Fig. 2.2*).¹¹⁰ Additionally, the rings of group II chaperonins are mostly built from eight and sometimes nine subunits in contrast to group I chaperonins, where seven subunits form a ring. The subunits of group II chaperonins are not homogeneous. The majority of these chaperonins have two homologous subunits (α and β), which alternating form an eight-membered ring.¹¹¹ One of the most complex chaperonin is the eukaryotic TRiC (TCP1 ring complex) or also called CCT (chaperonin containing TCP1). The rings of TRiC/CCT are composed of eight homologous but different subunits ($\alpha - \theta$).¹¹²

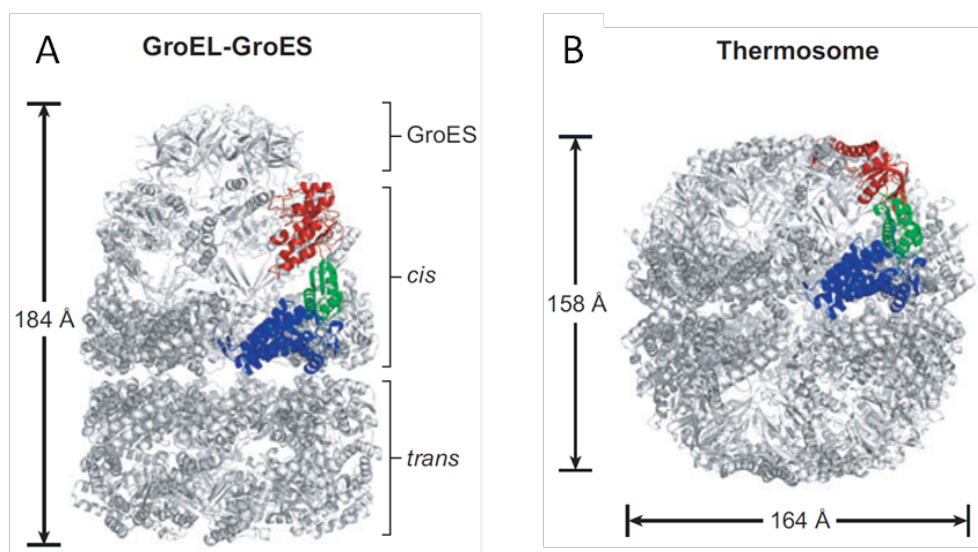


Fig. 2.1: Structural comparison of GroEL-GroES (A), a group I chaperonin, and thermosome from *Thermoplasma acidophilum* (B), a group II chaperonin. By courtesy of Horwich et al..¹⁰⁷

2.2 Structure of the group II chaperonin from *Thermoplasma acidophilum* (Thermosome)

Initially, the group II chaperonin from the extremely thermophilic archaea *Pyrodicticum occultum* was called thermosome, because it was found in large amount in the archaea after accidentally exposure to a heat shock.¹¹³ However, this term became a generic name for all archaeal chaperonins. In this work we focus on the chaperonin from the archaea *Thermoplasma acidophilum* and the term thermosome (THS) will refer to this specific chaperonin.¹¹⁴ The THS is composed of two alternating subunits (α and β) forming two pseudo eight-fold symmetrical rings (Fig. 2.1 B).¹¹¹ The equatorial domains of the subunits, where the N- and the C-termini are located, provide the most inter-ring contacts. In this region, every subunit interacts with only one subunit from the other ring in an α - α and β - β manner.¹⁰⁵ THS in its open conformation has a barrel-like structure with a diameter of about 15 nm in the planar axis and its height is about 18 nm (Fig. 2.2 D).¹¹⁵ The cavities possess a big pore of about 8 nm in diameter, which allows protein substrates to diffuse in and out of the cavity.^{115, 116} During the ATPase cycle of the group II chaperonins, the built in lids close the cavities. In the closed conformation, each ring encloses a cavity with a height of 4.5 nm and an inner diameter ranging from 8.6 nm, between the equatorial domains, and 5.4 nm, at the top of the cavity, resulting in a volume of 130 nm³ per cavity (Fig. 2.2 B). This volume is large enough to provide space for proteins with a molecular mass up to 50 kDa. Even though there are sixteen small windows (max. 2.5 nm) in the wall of the THS cavity in the closed state, the access to the cavity for protein is only possible through the central pore in the open conformation, which has a diameter of about 8 nm.^{105, 116, 117}

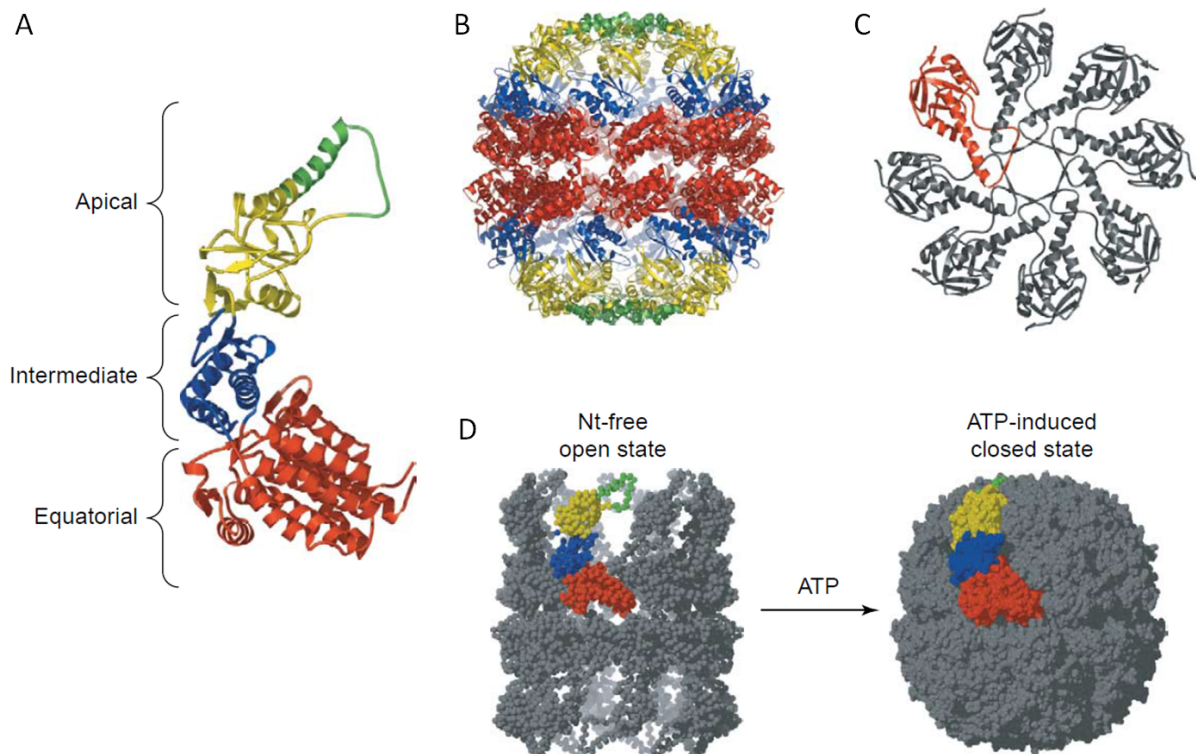


Fig. 2.2: (A) Structure of the group II chaperonin (Thermosome) subunit with its equatorial (red), intermediate (blue), apical domain (yellow) and its helical protrusion (green). (B) Side view of TRiC in the closed conformation. (C) Top view of the closed Thermosome. (D) Conformational change of Thermosome from the open state to the closed state upon addition of ATP. By courtesy of Spiess et al..¹¹⁸

Chaperonins stabilize folding intermediates during the folding process of proteins in an ATP depending manner. This cellular process prevents proteins from miss-folding and agglomeration, thereby increasing the yield of properly folded and functional proteins.¹⁰⁸ Besides actin and tubulin,¹¹⁹ the eukaryotic group II chaperonin TRiC also assists the folding of other substrates including G-alpha transducin, cyclin E, myosin heavy chain, and others.¹¹⁸ The natural substrates of archaeal chaperonins are currently not known.¹²⁰ However, several studies show that these chaperonins bind unfolded proteins and help them properly fold.^{116, 121-125} Additional roles of archaeal chaperonins are also under discussion, such as structural function in archaea or RNA processing.¹²⁶

Improperly folded proteins bind to hydrophobic sites, which are presented in the open apo-state (in absence of nucleotides). These hydrophobic patches are found at the protrusion and at the apical domain pointing into the cavity.^{110, 127} The ATP dependent folding mechanism has been under scientific debate for a long time.^{106, 116, 117, 128-131} Here we review the newest findings, proposing that the binding of ATP drives the apical domains to turn counter clockwise (seen from top to the bottom) partly closing the chaperonin. The subsequent ATP hydrolysis causes the subunits to rock together in a cooperative manner closing the lid completely like an iris-type aperture. During this conformational change the protrusions have an induction and stabilization effect.¹³² Most of the group II chaperonins exhibit positive intra-ring cooperativity. However, the group II chaperonin from *T. acidophilum* (THS) lacks it.¹³³ The conformational change to the closed state causes the hydrophobic binding sites of the subunits to face away from the cavity.^{115, 117, 130} This structural rearrangement leads to the release of the substrate into the cavity, where they can fold properly in an unique chemical environment. The closing of the chaperonin and the release of the substrate into the cavity are crucial for proper folding (Fig. 2.3).¹¹⁶ The release of ADP or Pi triggers the opening of the cavity by a clockwise motion of the subunits and the release of folded protein.¹¹⁶ This episode of the ATPase cycle has been shown as the rate limiting step.¹⁰⁶ The folding mechanism of group II chaperonins is not only dependant on ATP but also magnesium and/or sodium. THS shows magnesium dependence.¹²⁰ Group II chaperonins show a negative inter-ring cooperativity. Thus, only one ring close at a time, whereas the other one is hindered to close and stays open. This conformationation is called bullet conformation. The negative inter-ring cooperativity also results in a “two-stroke” motion, i.e. the two rings close successively.¹³⁴

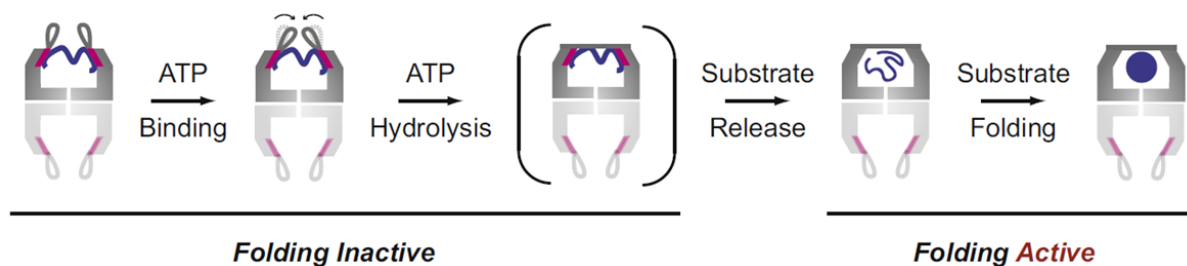


Fig. 2.3: Mechanism of action of group II chaperonins. By courtesy of Douglas et al..¹¹⁶

3. RNA interference

M.G. Nussbaumer

Parts of the chapter 3.3 *siRNA transfection agents* are published in:

T. Schuster, M. Nussbaumer, P. Baumann, N. Bruns, W. Meier and A. Car, in *Subunit Vaccine Delivery*, eds. C. Foged, T. Rades, Y. Perrie and S. Hook, Springer New York, 2015, pp. 181-201.

3.1 Introduction RNA interference

RNA interference (RNAi) is an important cell mechanism to regulate gene expression. It also plays a role in the natural defense against viruses.^{135, 136} This mechanism is present in all eukaryotic cells and is therefore assumed to be a highly conserved evolutionary mechanism.¹³⁷ The discovery of RNAi in 1998 opened the door for novel approaches in medicine and was awarded with the 2006 Nobel Prize in medicine.¹³⁸

3.2 RNAi mechanism

RNAi is induced by a ~20 – 30 nucleotide (nt) long single stranded RNA, which is bound to an Argonaute family protein. This ribonucleoprotein specifically binds the complementary messenger RNA (mRNA) forming the RNA-induced silencing complex (RISC), which enzymatically cleaves the mRNA. Thus the expression of the specific gene that the mRNA codes for is down regulated. The cleavage of mRNA is a catalytic process, where only small amounts of RISC have a big effect on the mRNA concentration in the cytosol.^{135, 139}

There are two main mechanisms, which induce RNAi (*Fig. 3.1*). On one side the endogenous microRNA (miRNA) is involved for gene regulation and on the other side the exogenous small interfering RNA (siRNA) for the defense against viruses or artificially introduced for therapeutic purposes. miRNA are transcribed in the nucleus. They are more than 1000 nt long and possess several hairpin structures. These miRNA are cleaved by the Drosha protein into 65 -70 nt long segments, which are subsequently exported out of the nucleus. In the cytoplasm, the pathways of miRNA and siRNA merge. Exogenous double stranded RNA, originating from RNA viruses, and the endogenous miRNA are cleaved by the Dicer protein into 21 to 25 nt double stranded RNA (dsRNA), which have a two nucleotide overhang at the 3'-end. Therapeutic siRNA are already designed as dsRNA with overhangs. Subsequently, the dsRNA is loaded on the Argonaute, which with some additional proteins form the RNA-induced silencing complex (RISC), where the dsRNA is unwound. Subsequently, RISC with single stranded RNA (ssRNA) binds to complementary mRNA. In case of perfect complementarity, which is often the case in exogenous siRNA, the target RNA is catalytically cleaved. In contrast, the ssRNA coming from miRNA often have some misfits, resulting in a repression of the translation mechanism.^{61, 135, 140}

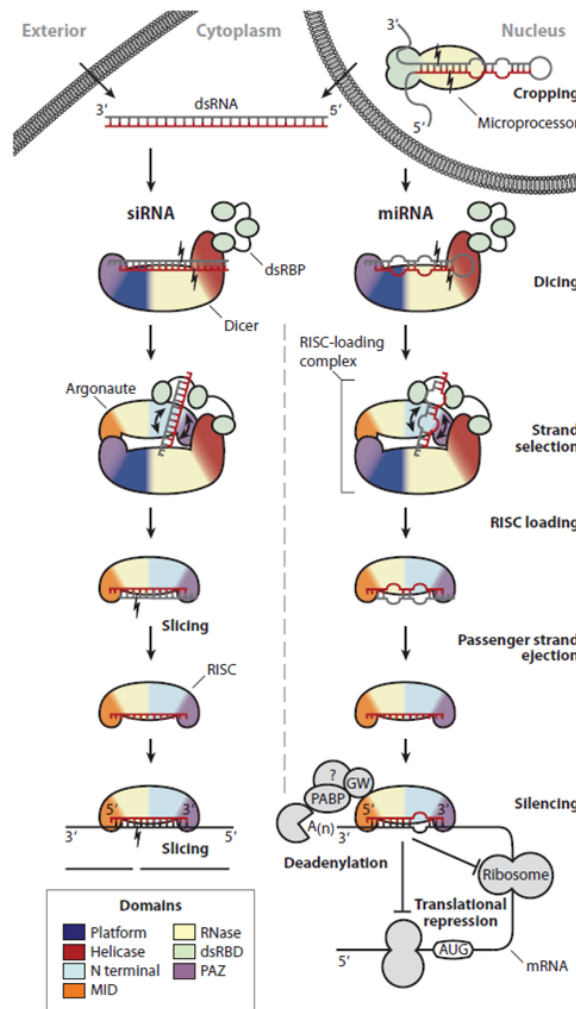


Fig. 3.1: Pathway of RNAi induced by siRNA and miRNA, respectively. By courtesy of Wilson et al.¹³⁵

RNAi is an interesting cellular mechanism for medicinal application. By interfering with the cellular pathway of disease related proteins, it is possible to stop pathologies at their genetic source, e.g. cancer or age-related macular degeneration.¹⁴¹⁻¹⁴³ For experimental use, siRNA (19 – 23nt, double stranded with two nt overhang) as well as short hairpin RNA (shRNA) which are then cleaved into siRNA, are used. However, there are significant barriers to overcome for effective siRNA based therapies.¹⁴⁴ The presence of RNase in the blood serum reduces the half-life of naked siRNA to less than an hour.¹⁴⁵⁻¹⁴⁷ Therefore, siRNA has to be protected from degradation by RNases. One strategy is to chemically stabilize RNA. To this end, the backbone of the siRNA is modified, blocking cleavage by RNases (*Fig. 3.2*). RNA backbone modifications are often performed at the 2'-hydroxyl group by exchanging the hydroxyl group with fluor, O-methyl, or O-methoxy-ethyl. Other variants are to "lock" the sugar ring in the C3'-endo conformation (LNA) by an ether-linkage of the 2' and 4' position or to exchange the phosphate with a thiophosphate on DNA.¹⁴³

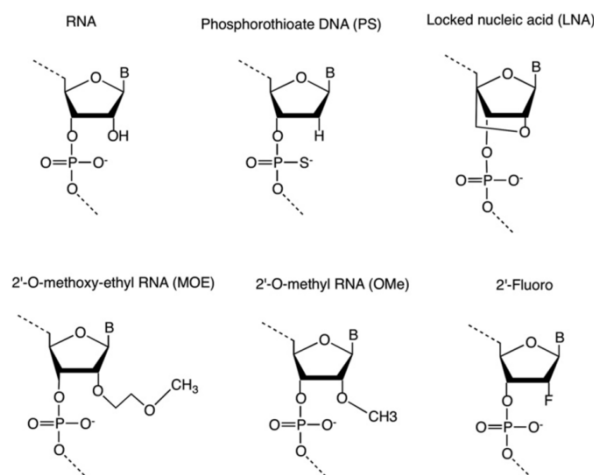


Fig. 3.2: Modified ribonucleic acids to enhance the stability of siRNA. By courtesy of Burnett et al.¹⁴³

The anionic characteristic of siRNA, caused by the ~40 negative phosphate groups, and the molecular size of about 13 kDa make it impossible for siRNA to cross the cell membrane by itself.¹⁴⁰ Thus siRNA needs a delivery system, which protects it from degradation, brings the siRNA to the desired location, transports it into the cell, and releases it in the cytosol. Furthermore, it is crucial to design siRNA carefully and test them for any off target silencing,¹⁴⁵ because poorly designed siRNA can induce unwanted off target effects. Additionally, GU-rich siRNA can stimulate innate immune response.¹⁴⁸

3.3 siRNA transfection agents

The first clinical trials of siRNA were mostly based on local administration of naked siRNA.¹⁴⁹ Nowadays, different siRNA transfection agents have been reported, which can be divided into viral,^{99, 150-152} lipid,^{153, 154} polymer based^{38, 155, 156} or peptide based¹⁵⁷⁻¹⁵⁹ siRNA delivery systems. Most of the siRNA transfection agents complex siRNA by electrostatic interactions between the cationic groups of the transfection agent and the negatively charged backbone of the siRNA. Thus, the transfection agents wrap around the siRNA, protecting them from degradation by RNases. As for other drug delivery purposes, liposomes and lipoplexes are one of the most common transfection agents for siRNA. Different siRNA transfection agents for *in vitro* use are based on cationic and neutral lipids, such as RNAiFect (Qiagen), HiPerFect (Qiagen), Oligofectamine (Invitrogen) and Lipofectamine 2000 (Invitrogen). The latter has become a standard transfection agent for siRNA, although cationic lipids exhibit cytotoxicity.¹⁴⁹ Liposome based stable nucleic acid particles (SNALPs) and lipid nucleic acid particles (LNPs) seem to be less toxic, but they do not efficiently escape the endosomes. Thus, siRNA is stuck in the endosome and therefore not active. Cationic polymers, which represent another class of siRNA delivery reagents, can escape the endosome via the so called proton sponge effect. The amine groups of the polymer buffer the endosomal pH, resulting in an efflux of protons and chloride ions increasing the osmotic pressure. This ruptures the endosomes and releases the siRNA into the cytoplasm.¹⁶⁰⁻¹⁶² One of the first cationic polymers for siRNA transfection was polyethyleneimine (PEI). The branched or dendritic form of PEI is used more for siRNA delivery than the linear form. However, the linear PEI exhibits less toxicity compared to the quite toxic branched and dendritic form.¹⁶² Also other polymers are used for siRNA delivery, namely poly-L-lysine, chitosan, and poly(D,L-lactic-co-glycolic acid). Dendrimers are a third form of polymer used for siRNA and drug delivery.

The word “dendrimer” arises from the greek words dendron, meaning ‘tree.’ and meros, meaning ‘part’. The core in the center of the structure has at least one branching point and three anchoring groups (Fig. 3.3). Thus, in second generation, at least three monomers can be incorporated. With every additional generation, the molecular mass and the number of surface groups increase exponential. The step-wise synthesis allows highly symmetric structures with a well-defined molecular weight to be produced. The branches of the polymer arrange in a way that the dendrimer possesses a globular structure. In contrast to linear or randomly branched polymers, they are spatially structured. Dendrimeric polymers were first reported by Vögtle et al.¹⁶³ In the past years, the synthesis of dendrimers evolved to allow the production of larger molecules.^{56, 164} A high degree of branching leads to high density of functionalities on the surface, and therefore to a multivalent structure. With higher dendrimer generation numbers, the dendrimer properties become dominated by the end groups and its size, while the core is shielded.¹⁶⁵ Additionally, a high degree of functionalities at the end groups allows various modifications, which makes dendrimers attractive as drug delivery systems.¹⁶⁶

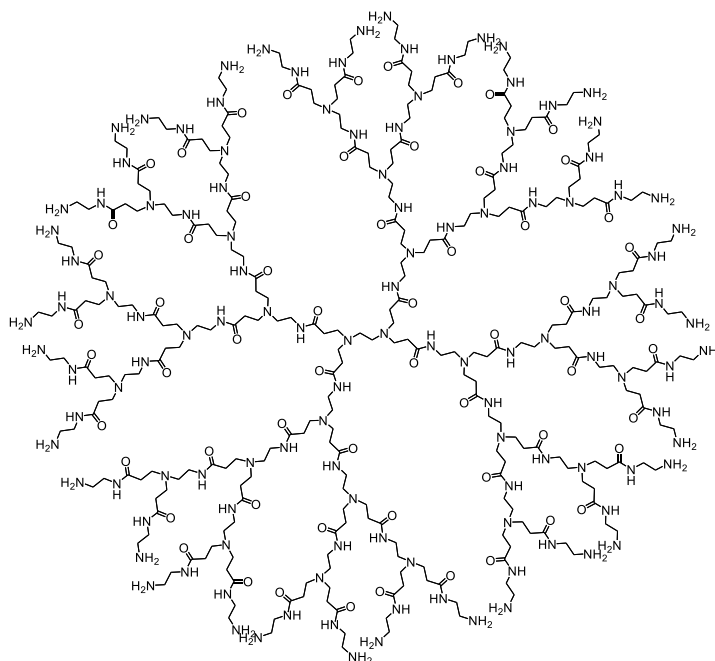


Fig. 3.3: The 4th generation poly(amidoamine) (PAMAM) show the general structure of dendrimers.

3.4 PAMAM as siRNA delivery reagent

The three most prominent cationic dendrimers for nucleic acids are polyethylenimine (PEI), polypropylenimine (PPI) and poly(amidoamine) (PAMAM).⁶¹ In this work we focused on PAMAM (Fig. 3.3), because it shows less toxicity than PEI and PPI. Additionally, generation 6 PAMAM is a commercially available DNA transfection agent for *in vitro* use and is sold under the name Polyfect and SuperFect.^{145, 167} Which generation of PAMAM is most suitable for siRNA delivery has been investigated.¹⁶⁸⁻¹⁷⁰ In a comparison of the different generations of PAMAM, the 4th generation showed optimal charge density for siRNA-complexation (Fig. 3.4).^{58, 171} Therefore, we chose the 4th generation PAMAM (PAMAM G4). It has a molecular weight of 14'215 g mol⁻¹, a diameter of 4 nm, and features 64 primary amine end groups.⁵⁷ The release mechanism of siRNA from PAMAM in the cell is still under investigation. It has been calculated that at low pH, as it is in the late endosome, PAMAM binds siRNA stronger as in neutral pH.¹⁶¹ Thus another effect must be responsible for the

release of siRNA in the cells. From other calculations, it has been shown that high salt concentration can shield the charges of PAMAM and siRNA, weakening the electrostatic interactions. At a salt concentration of 150 mM, which is about the concentration in the cell, the electrostatic interactions are greatly reduced and facilitate the escape of siRNA from PAMAM.²⁷

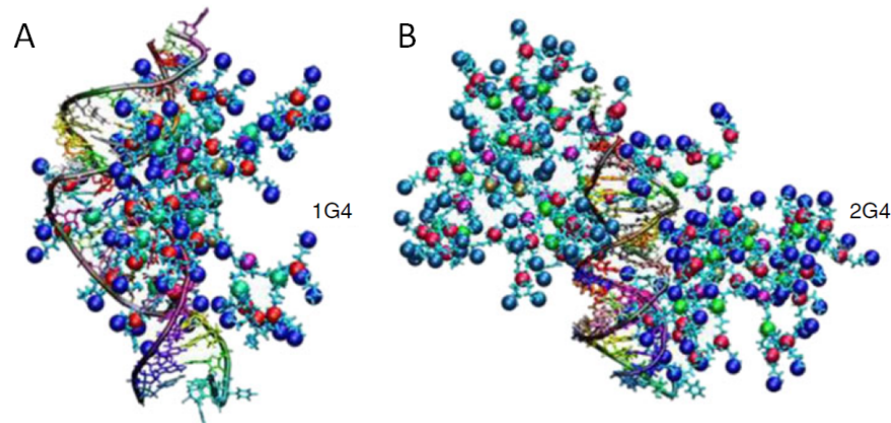


Fig. 3.4: Simulation of the interaction between siRNA and one **(A)** or two **(B)** PAMAM G4 dendrimers. By courtesy of Nandy et al..²⁷

All the cationic polymers as well as the cationic lipids exhibit toxicity. The interaction of the positive charge of the polymers and the negatively charge of the cell surface, can disrupt the cell membranes.⁵⁹ Additionally, the positive charges interact with proteins, resulting in aggregation and therefore, are prone to be opsonized and cleared by the immune system. To encounter these problems, cationic polymers for siRNA delivery have to be shielded from their environment. To achieve this, cationic polymers were modified with PEG, decreasing their interaction with their environment. However, it is always a tradeoff between number of functional group and shielding of the polymer.⁶¹ It was shown that a modification of 20% of the primary amine of PAMAM reduced its toxicity, while maintaining siRNA transfection efficiency.⁵⁸

In conclusion, RNAi based therapies are an emerging and promising strategy to cure different diseases. However, to achieve the full clinical potential, different obstacles have to be overcome. The instability of siRNA in the body, the transport of siRNA into specific cells, and the toxicity of certain transfection agents are some of the problems which have to be faced. Therefore, new NDDS for siRNA delivery have to be developed.

4. Motivation and concept

M.G. Nussbaumer

In recent years, great advances in the field of drug delivery were achieved leading to drug formulations, which have a better release profile and improved pharmacokinetic profiles.^{1, 14} However, drugs still often suffer from inducing unacceptable side effects. Especially in cancer therapies, where patients suffer from drastic hair loss, stomach irritation, and low blood cell counts.¹⁴ This is caused by the distribution of cancer drugs throughout the whole body, where they do not only kill cancer cells, but also other rapidly dividing cells. Hence, the aim is to reduce the drug concentration in the body and to increase the concentration in the diseased tissue. Nano-sized drug delivery systems (NDDS) could overcome these problems in medicine.^{2, 4}

Polymers play an important role in the development of NDDS. Different targeted drug-polymer nano conjugates were developed featuring stimuli responsive release of the drug to reduce systemic toxicity and to prolong the circulation time in blood. Polymers are very interesting for the further development of NDDS because polymers can have diverse characteristics and therefore, they can be customized to specific needs.^{35, 37} However, polymer based NDDS also suffer from drawbacks such as broad size distribution, undefined structure, difficulty of generating multifunctional carriers, and difficulty for site-specific functionalization.⁶²

Protein cages represent a newer approach to create NDDS possessing several advantages over other NDDS such as defined size, well known structure, biodegradability, and a high number of functional groups which can be specifically modified.^{62, 172} Additionally, their low size fits in the therapeutic window in which nano-carriers remain in the systemic circulation and are not affected by clearance.¹⁷³ These features make protein cages promising NDDS.

In my doctoral research study, I wanted to design a carrier that benefits from the best of these two worlds by combining protein cages and polymers to develop novel NDDS. On the one hand, the protein cage has a defined size and structure, and offers the ability to be modified in a site-specific manner. On the other hand the polymer is able to bind and release drugs. To this end, I conjugated the cationic dendrimer poly(amidoamine) (PAMAM) into the cavity of the protein cage Thermosome (THS). An advantage of using THS over other protein cages is that macromolecules can diffuse unimpeded in and out of the THS' cavity without harming the quaternary structure of THS. This protein-polymer conjugate was tested for the ability to serve as a siRNA delivery agent. Thereby, it was crucial to determine if THS-PAMAM is able to bind siRNA and protect it against degradation. A main aspect of my work was to show the uptake of THS by cells. Furthermore, I was interested in the modification of THS' outer surface with cell targeting and penetrating ligands, for enhanced uptake of THS by a specific cell type. Such modification would increase the possible application of THS-PAMAM as a promising NDDS.

To expand the concept of THS as a NDDS, I also modified the THS' cavity with a dye through a reduction sensitive linker, which served as a drug model. In this study cell-internal triggered release of drugs from THS was examined.

Additionally, I examined THS as an ATP-controllable enzyme nano-reactor, which could lead, in the long run, to enzyme replacement therapies. For this purpose, the possibility to freeze THS in its

closed state was of particular interest. Hence, the enzyme is enclosed in the inside of THS and is not active anymore until the ATP concentration inside the cell unlocks the THS again. This could stabilize the enzyme and only activate it, when it is at the side of action.

I wanted to further expand the versatility of THS in the field of nanomedicine. AuNPs show outstanding characteristics for the use in photothermal therapy and imaging.¹⁷⁴ Thus, I was interested in forming gold nanoparticles (AuNP) within the cavity of THS. Thereby, I benefited from the fact that PAMAM serves as scaffold for the formation of AuNP.¹⁷⁵ Combining the ability for THS to transport cargo to the cell while containing AuNP cargo, would make THS interesting in the field of photothermal therapy.

In general, I wanted to illustrate the versatility of THS as a nano drug delivery system. Thereby, the main objective was to show siRNA transfection by the protein-polymer conjugate THS-PAMAM and broaden its field of application by modifying it with cell targeting ligands. Furthermore, I wanted to show that THS can be modified in a way that THS can serve in other fields of nanomedicine, such as enzyme activity control, triggered drug release and photothermal therapy (*Fig. 4.1*).

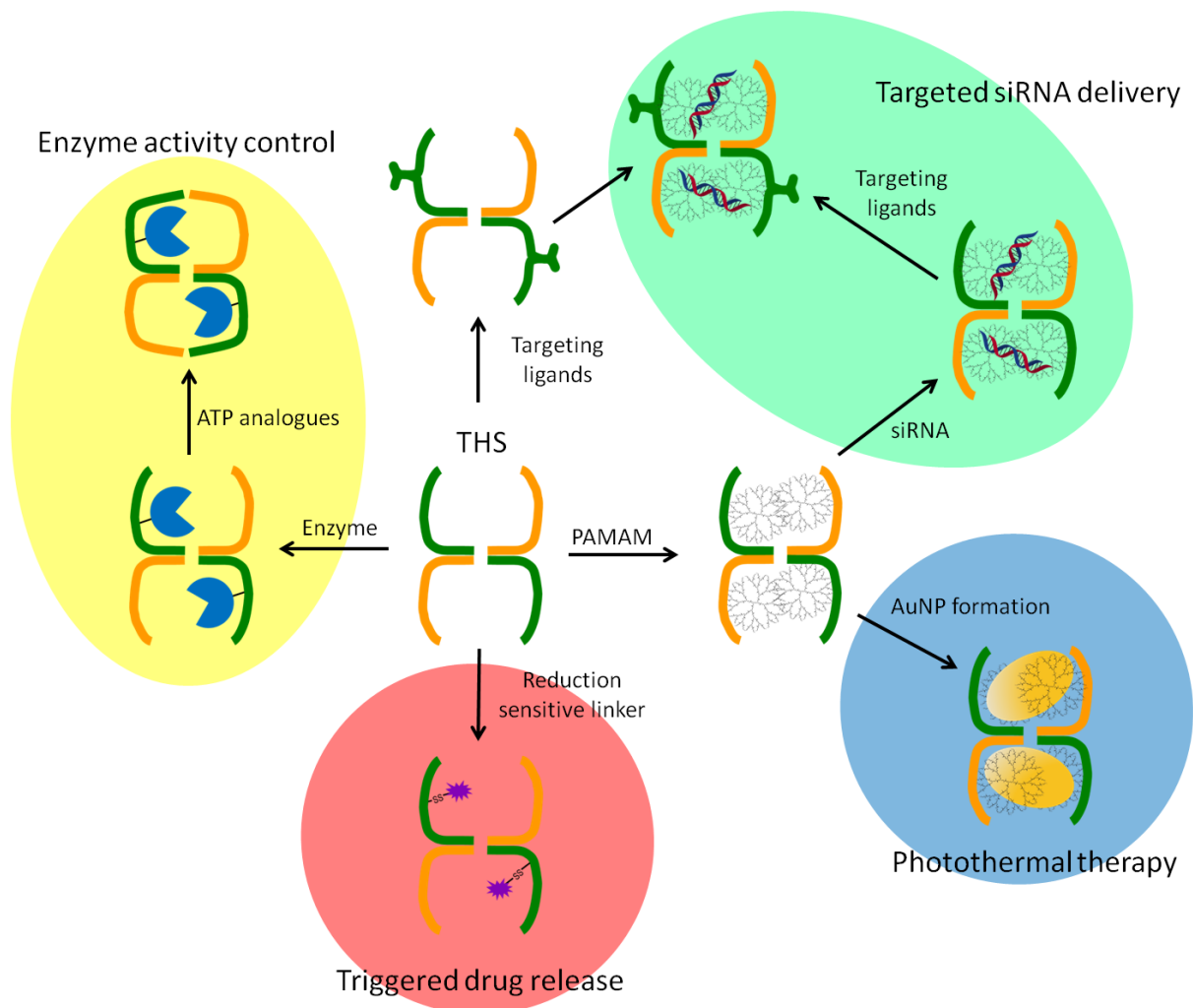


Fig. 4.1: Schematic overview of the different fields of application for THS in my thesis.

5. THS expression and purification

M.G. Nussbaumer

5.1 Introduction

In the following chapter, the THS expression will be described. The expression of THS turned out to be not that stable as expected. The protocol for expression and purification base on the research of Bigotti et al.¹³³ and was further developed by Bruns et al.⁷⁸ The main difficulty for the expression of THS is the equal expression of the two subunits for a high overall yield of THS. Bigotti et al.¹³³ constructed a pET-27b plasmid (pETTherm α/β), which has the two subunits in tandem, where the α -subunit is upstream and the β -subunit downstream and they are separated by a 220 base pair non-coding sequence. Each subunit sequence has a T7 promoter. It emerged, that the α/β subunit ratio was heavily imbalanced; therefore the α -subunit expression was controlled by the *lac* operator, to reduce the α -subunit expression. The expression of THS was conducted without induction with IPTG. Thus, the production of THS bases on a leaky expression. Bruns et al.⁷⁸ performed three point mutations on the pETTherm α/β plasmid in order to create a unique attachment point within the thermosome's cavity. The accessible cysteines of the subunits were exchanged to alanines (α : C363A; β : C364A) and a new cysteine was introduced at the position 316 of the β -subunit (K316C). The mutated plasmid was termed pETTherm α/β -mut.

5.2 THS expression

The pETTherm α/β -mut plasmid was expressed in BL21 (DE3) codon Plus RIL *E. coli* cells under kanamycin resistance. The DE3 genotype is needed to produce the T7-polymerase and the codon Plus RIL is due to special codons, because the gene of THS originates from an archaea. The transformation consistently yielded numerous *E. coli* expressing the plasmid, even when only 10 μ l of transformed cells were streaked out on the plate. Even though the plate can be stored in the fridge for 2-3 month, a new transformation was performed each time to yield the best results. Because of the leaky expression of THS, the cell growth of the expressing *E. coli* needed to be controlled. Therefore, the cell culture for the THS expression was done overnight and the temperature was kept at 30 °C.

5.3 THS purification

The purification difficulty lies in the number of steps and the low yield. To overcome low yields and difficult purification steps, affinity tags are often used.¹⁷⁶ Unfortunately, the N- and C-termini are hidden in the interior of the quaternary structure of the THS¹²³ and therefore, not suitable for tag-purification. Thus, different purification steps had to be applied. In general, three chromatographic purification steps were performed. First, an anion exchange chromatography followed by size exclusion and an additional anion exchange chromatography. This last step is especially important to purify only the fraction of THS with a balanced α/β subunit ratio.

The first purification step of the cell lysate was done with an anion exchange column. This step separates most of the other proteins and cell debris from THS. Two hardly separated peaks elute starting at around 260 ml (8 % gradient) and ending at 340 ml (34 % gradient), where the first peak is associated with THS (Fig. 5.1 A). Both peaks were pooled (266 ml – 326 ml). SDS-PAGE analyses show two bands around 60 kDa in these fractions (Fig. 5.1 B) representing the two THS subunits. Bands

around 60 kDa were also found in the first two flow-through fractions (0 – 100 ml). Hence, the flow-through fractions were applied a second time on the anion exchange column. The peak at around 300 ml was also present, indicating that the column was overloaded and some THS did not bind (data not shown).

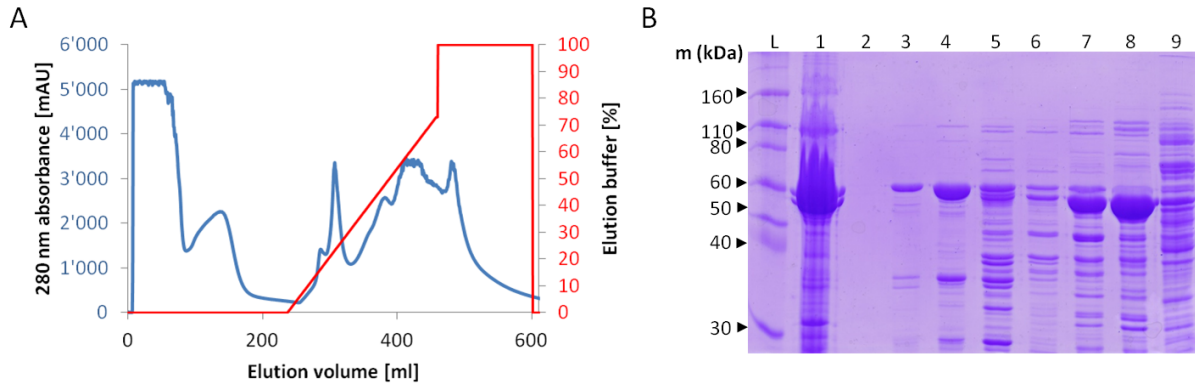


Fig. 5.1: **(A)** First anion exchange chromatogram: absorbance at 280 nm (blue), concentration of Elution Buffer (red). **(B)** SDS-PAGE analysis of different anion exchange chromatography fractions (1: 0 ml; 2: 100 ml; 3: 276 ml; 4: 286 ml; 5: 306 ml; 6: 326 ml; 7: 356 ml; 8: 426 ml). The fractions between 266 ml and 326 ml were pooled.

To separate fully assembled THS from free subunits size exclusion chromatography was performed as a second THS purification step. Two peaks were eluted during the size exclusion chromatography: a first, smaller peak (85 – 106 ml) and a second, bigger peak (106 – 165 ml) (Fig. 5.2 A). Both peaks show two bands in the SDS-PAGE around 60 kDa, which corresponds to THS subunits (Fig. 5.2 B). But only the first peak showed a fully assembled THS in native PAGE (Fig. 5.2 C). Hence the fractions of the first peak (74 – 106 ml) were pooled and further purified.

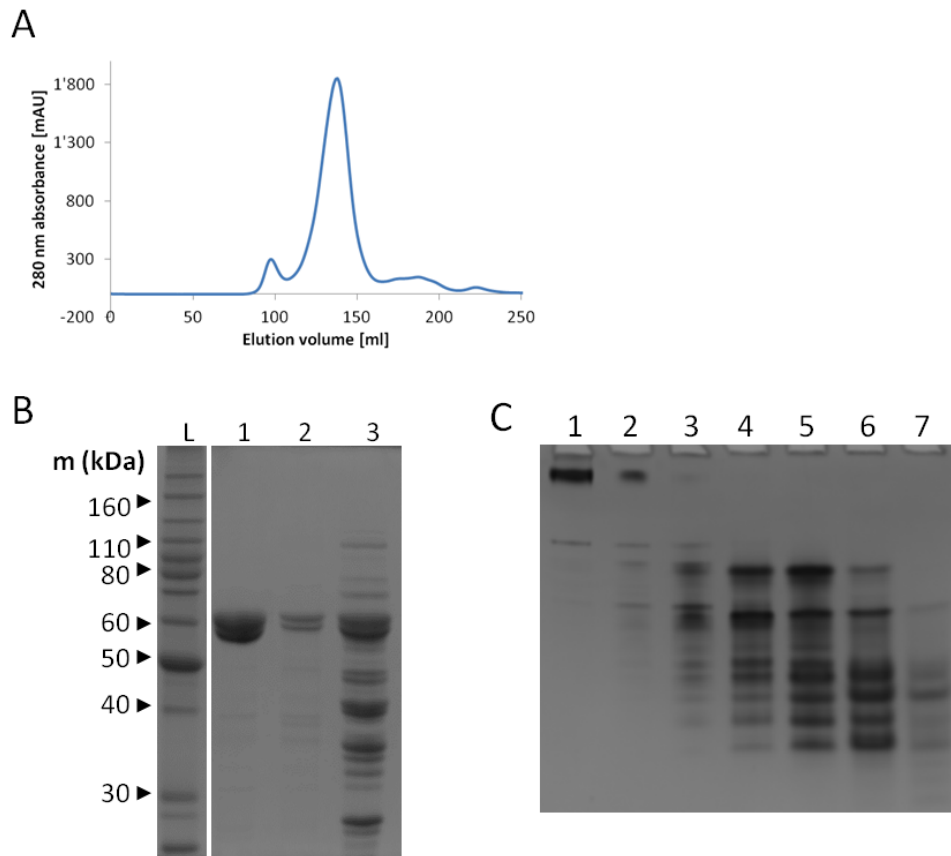


Fig. 5.2: **(A)** Size exclusion chromatogram (SEC) detected at 280 nm. **(B)** SDS-PAGE of SEC fractions; 1: 92 ml; 2: 106 ml; 3: 133 ml. **(C)** Native PAGE of SEC fractions: 1: 87 ml; 2: 97 ml; 3: 106 ml; 4: 115 ml; 5: 124 ml; 6: 133 ml; 7: 142 ml. The fractions between 74 ml and 106 ml were pooled and further purified.

THS with balanced α/β -subunit ratio was separated from mismatched α and β subunits with an additional anion exchange column purification (different anion exchange column as the first one). The chromatogram shows an intense, sharp peak at 81 ml (15% gradient), a broad peak starting from the sharp peak to around 170 ml (38% gradient) and a small peak around 172 ml (38% gradient) (Fig. 5.3 A). SDS-PAGE analysis suggests the first peak contains primarily α -subunit THS. The broad peak exhibits a shift in the α/β -subunit ratio from high α -subunit to higher β -subunit content by increasing the salt gradient (Fig. 5.3 A). However, it is more a decrease of α -subunit by constant β -subunit amount. The small peak at 174 ml appears to be THS formed from mostly β -subunits. The fractions between 105 ml (21% gradient) and 157 ml (34% gradient) were pooled and concentrated.

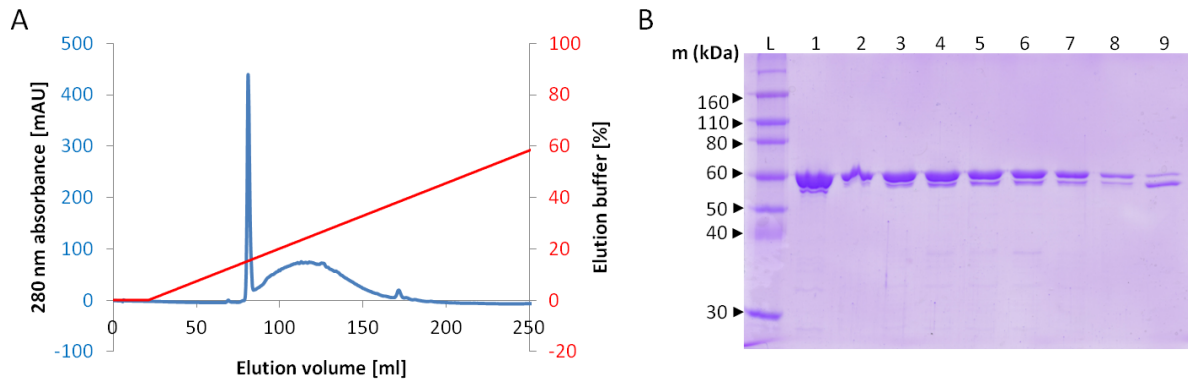


Fig. 5.3: (A) Chromatogram of the second anion exchange chromatography: absorbance at 280 nm (blue), concentration of Elution Buffer (red). (B) SDS-PAGE of the anion exchange chromatography fractions: 1: 81 ml; 2: 93 ml; 3: 105 ml; 4: 117 ml; 5: 129 ml; 6: 133 ml; 7: 141 ml; 8: 153 ml; 9: 169 ml. The fractions between 105 ml and 157 ml were pooled and concentrated to obtain pure THS.

The yield of THS production was measured with UV/Vis absorbance and was very inconsistent. Yields from 0.5 mg THS per l fermentation to about 5 mg THS per l fermentation were achieved. SDS-PAGE analysis showed the two THS subunit bands around 58 kDa (Fig. 5.4 A & B). However, an α/β -subunit ratio of 1:1 could not be achieved as reported by Bigotti and Bruns.^{78, 133} In further experiments (see 7.1 THS-Atto647 modification and 8.2 THS-PAMAM conjugation) we measured the ratio to be about $\alpha/\beta = 12.6/3.4$, which also corresponds to the intensity of the subunit bands on a SDS-PAGE gel (Fig. 5.4 B). We proceeded with this unbalanced THS, since we are not depending on a perfectly balanced α/β -ratio. However, it is crucial that THS is built with some β -subunits, which possess the introduced cysteines. These cysteines represent specific anchoring points for further modification of the THS. The results of profound analysis of THS are found in the next chapter 6. THS characterization.

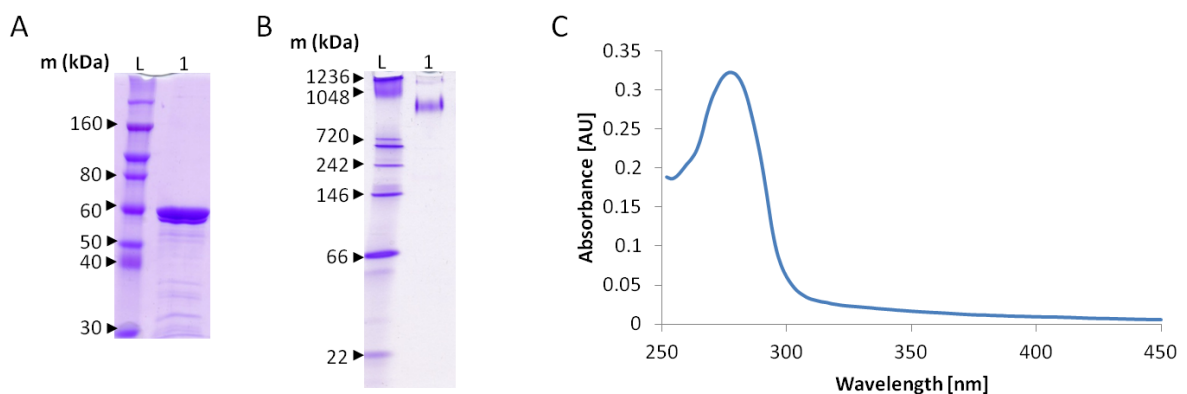


Fig. 5.4: (A) SDS-PAGE of THS. (B) Native PAGE of THS. (C) UV/Vis absorbance measurement to determine the concentration of THS.

6. THS characterization

M.G. Nussbaumer

THS was characterized with different techniques to verify its structure and its integrity, i.e. SDS-PAGE, ESI-MS (LC-MS, UPLC-MS), MALDI-MS, native PAGE, TEM and cryo-TEM.

6.1 Gel electrophoresis

Analysis with SDS-PAGE revealed the purity and the ratio between α - and β -subunit (*Fig. 6.1*). The two subunits don't have exactly the same molecular weight. They migrate slightly different and therefore form two distinguishable bands. The first band (alpha) is found slightly under the 60 kDa band of the protein standard with the second band being found directly underneath it. The second band often has a weaker intensity than the upper band, indicating an imbalance of α - to β - subunits. Furthermore, some minor impurities with molecular weight lower than 60 kDa are found in the SDS-PAGE analysis. However, it is not clear whether these impurities originate from degradation of THS, insufficient purification, or if these are proteins bound to the inside of THS. In the literature, it is stated, that the upper band is the α -subunit and lower band represents the β -subunit.⁷⁸ In order to confirm this, the accessible Cys at the β -subunit was labeled with Atto647-mal and a SDS-PAGE of THS-Atto647 was run. Therefore a fluorescent image and a coomassie stain were recorded (*Fig. 6.1*). From the fluorescent image primarily the lower band is visible. This finding supports the literature stating the lower band belongs to the β -subunit and the higher band represents the α -subunit.

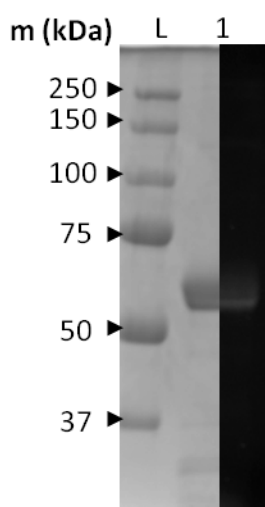


Fig. 6.1: SDS-PAGE of THS-Atto647 Coomassie stained (left) and unstained fluorescence image (right).

6.2 Electron microscopy

For this project it is crucial to have correctly assembled THS, i.e. the sixteen subunits are assembled in a barrel-like manner with a cavity in each hemisphere, where guest molecules can be hosted. For this purpose native PAGE analysis, TEM, and cryo-TEM images were performed and recorded.

THS shows a single band at around 1 MDa in native PAGE (*Fig. 5.4 B*). This mass coincides with the mass of a fully assembled hexadecameric THS. Interestingly, no impurity can be detected from native PAGE, supporting the idea that the impurities in the SDS-PAGE gel are coming from proteins bound to THS (*Fig. 6.1*).

The results from native PAGE confirm the mass of fully assembled THS, but do not report about its structure. TEM and cryo-TEM were able to reveal the structure of THS. TEM images show, on one hand, the top view of THS (standing), where the eight-fold symmetry of a hemisphere is seen, and on the other hand side view of THS (laying), where the two hemispheres and their cavities is seen (*Fig. 6.2 A*). In cryo-TEM images the resolution is slightly higher and the eight-fold symmetry in standing THS can be seen much better (*Fig. 6.2 B*). In contrast TEM images allow for a better examination of laying THS. From the cryo-TEM images, one hundred top view THSs were averaged and classified resulting in an electron density maps (*Fig. 6.2 C*). This map clearly shows eight black dots, which origins from the apical and intermediate part of the eight subunits.¹²³ In the middle there is a slightly darker area, which arises from the equatorial domains.

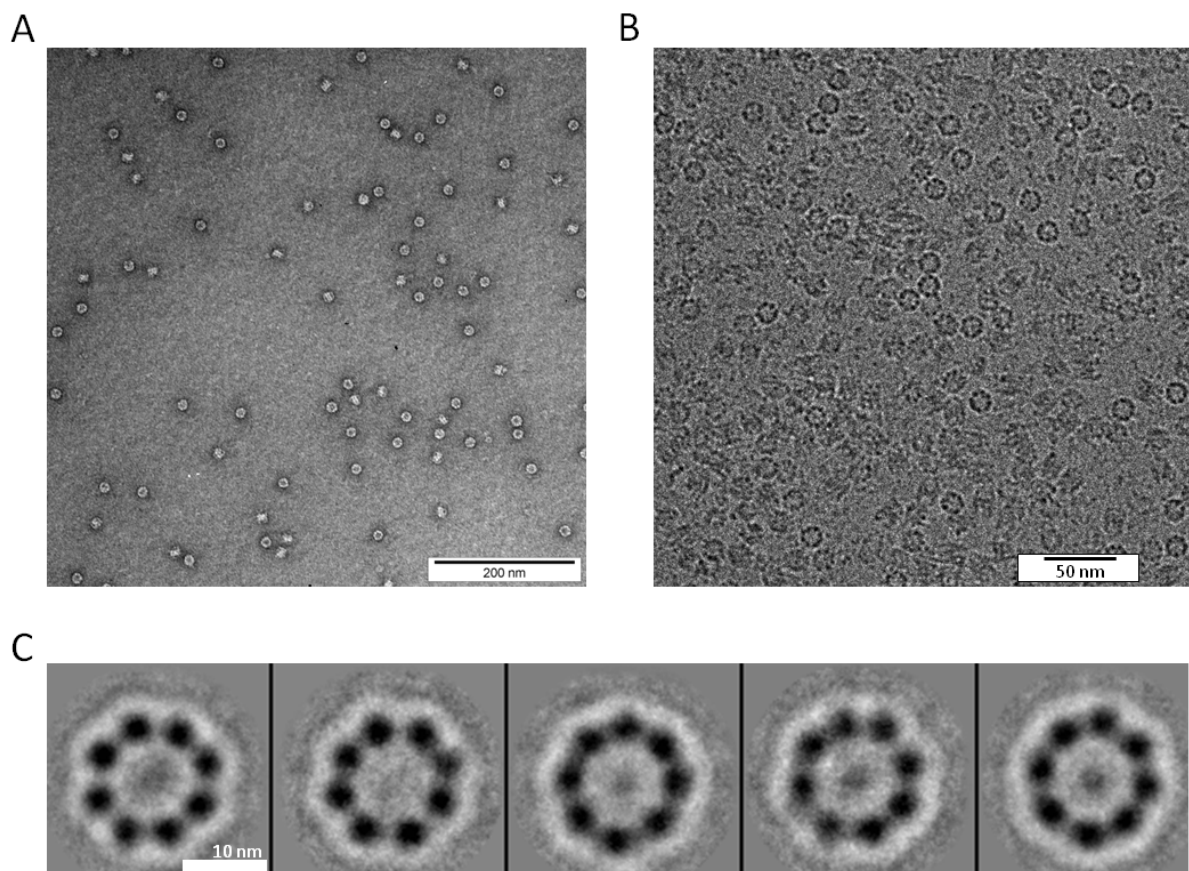


Fig. 6.2: Micrographs of THS recorded with TEM (**A**) and cryo-TEM (**B**). (**C**) Class average electron density map of THS.

From SDS-PAGE, native PAGE and TEM studies, it has been confirmed, that THS consists of two different subunits and THS is fully assembled in its natural hexadecimal quaternary structure. The next question that arises is if the introduced Cys are accessible and can act as anchor points for macromolecules. Additionally, the positions of the anchor points are of great interest, especially if they are in the cavity. To this end THS was labeled with 1.4 nm gold nanoparticles (nanogold) through a maleimide moiety, which bind to Cys of THS. This THS-nanogold complex was imaged with cryo-TEM. The image reveals up to two black dots per cavity of THS, proving the position of Cys in the inside of the THS' cavity (*Fig. 6.3*).

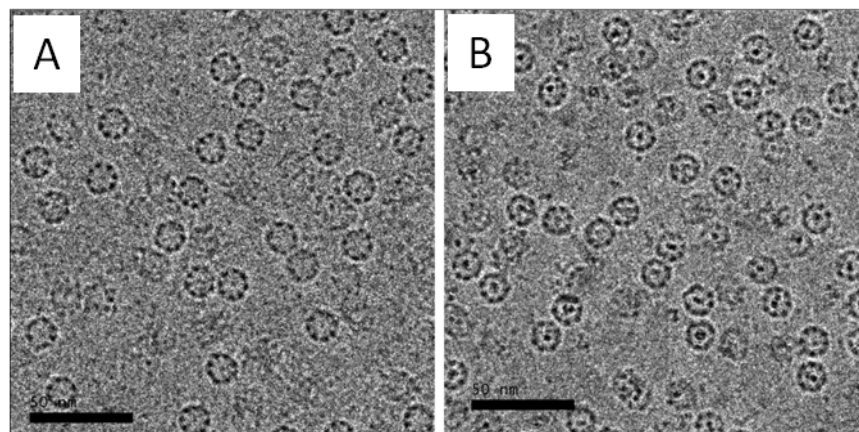


Fig. 6.3: Cryo-TEM image of THS (A) and THS-nanogold (B). Nanogold particles can be seen as intensive black dots. Scale bar: 50 nm.

6.3 Mass spectrometry

The molecular mass of native THS and its mutated variant is stated to be 960 kDa.^{78, 106} From sequencing the gene of the native THS, the mass of the α - and β -subunit was calculated to be 58'245 g mol⁻¹ and 58'480 g mol⁻¹, respectively, resulting in an overall mass of 933'800 g mol⁻¹ (internal data of Prof. N. Bruns). From the mutated version, there is only an incomplete gene sequence available. Therefore, various mass spectral approaches were performed to determine the molecular weight of the THS subunits.

For all the mass spectroscopical analysis THS was acidified. This has two reasons. First, THS has to be charged so that it can be measured by the detectors. Second, THS is too big for the detectors in its assembled state. Thus, THS has to fall apart to the subunits, which is the case if the pH is lower than pH 3¹¹⁴ (see chapter 6.4 *Stability test*). Therefore it should be possible to measure the mass of the subunits.

One method for mass spectroscopical analysis, which was applied is matrix-assisted laser desorption/ionization (MALDI) with a time-of-flight (TOF) detector. The ionization during this procedure is mild and low fragmentation occurs. Additionally, it produces only few multiply charged ions. Therefore, no deconvolution is needed. Due to this, the results are given as mass per charge (m/z). For THS, six main peaks were found: 29'145.4 m/z , 37'918.7 m/z , 38'945.4 m/z , 58'407.6 m/z , 881'44.1 m/z and 117'307.6 m/z (Fig. 6.4). The biggest peak arises at 58'407.6 m/z and corresponds to a subunit $(M+H)^+$. Accordingly, the peak at 29'145.4 m/z is supposed to be double charged subunits $(M+2H)^{2+}$. Dimers can be found at 117'307.6 m/z $(2M+H)^+$, triple charged dimers at 38'945.4 m/z $(2M+3H)^{3+}$ and double charged trimers at 88'144.1 m/z $(3M+2H)^{2+}$. All these peaks give a calculated mass around 58'400 g mol⁻¹ for a subunit. The small peak at 37'918.7 m/z does not belong into this row of multiple charged subunits and has to be considered as an impurity. This can be seen more clearly in the UPLC-MS (see below).

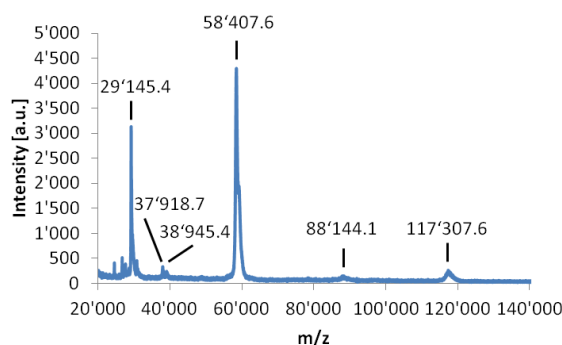


Fig. 6.4: MALDI-TOF-MS of THS.

Looking closer at the main peak, there is a shoulder appearing in the higher mass range. To investigate this shoulder, a mass spectrum was recorded in a smaller mass range focused on the area around the subunit peak. Multi-peak fitting of this zoomed spectrum results in peak maxima at 58'400 m/z and 59'000 m/z (*Fit. 6.5*).

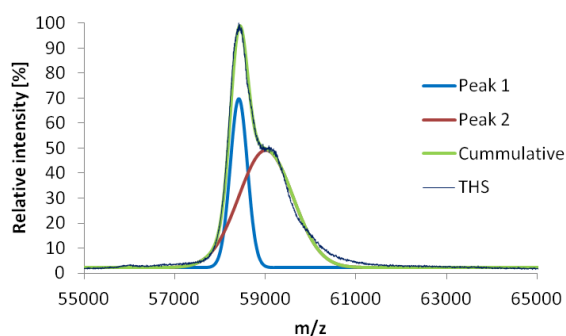


Fig. 6.5: Multi-peak fitting of the peaks around 58'500 m/z.

The masses of THS subunits were additionally examined with another method, the so-called ultra performance liquid chromatography electrospray ionization mass spectroscopy (UPLC/ESI-MS). In this method, the sample is first separated by liquid chromatography and subsequently the mass is directly measured with ESI-MS. This allows high sensitive and selective mass analysis. ESI is also a soft ionization method, which is not supposed to fragment bio-molecules. In contrast to MALDI, ESI results in multiply charged ions. Therefore, the result had to be deconvoluted to determine the real mass.

The diode array chromatogram of THS reveals a main peak eluting around 10.37 min with a small shoulder upstream of the main peak. At 10.74 min and 10.81 min two small peaks appear (*Fig. 6.6 A*). The mass spectra of the earlier eluting peak (1: 10.32 min), comprising the shoulder, and the later section of the main peak (2: 10.42) do not show any difference. Both of them reveal a main peak at 58'385 m/z (M_1+H)⁺ and its multiple charged species (*Fig. 6.6, Table 6.1*). As in the MALDI mass spectrum, there is also a minor peak, which is located slightly above the main peak, having the mass of 58'498 m/z (M_2+H)⁺. The ion peaks for the multiple charged species could also be found (*Fig. 6.6, Table 6.1*). The repetitive small peaks around the main peaks are artifacts of the deconvolution.

The third peak (3: 10.74 min) from the LC consists mainly of one species with a mass of 58'521 m/z. This could correspond to minor peak species, which have sodium bound (M_2+Na)⁺. In contrast, the

fourth peak of the LC (4: 10.81 min) shows a main mass peak at 37'979 m/z (M_3+H)⁺ and its multiple charged species (Fig. 6.6, Table 6.1).

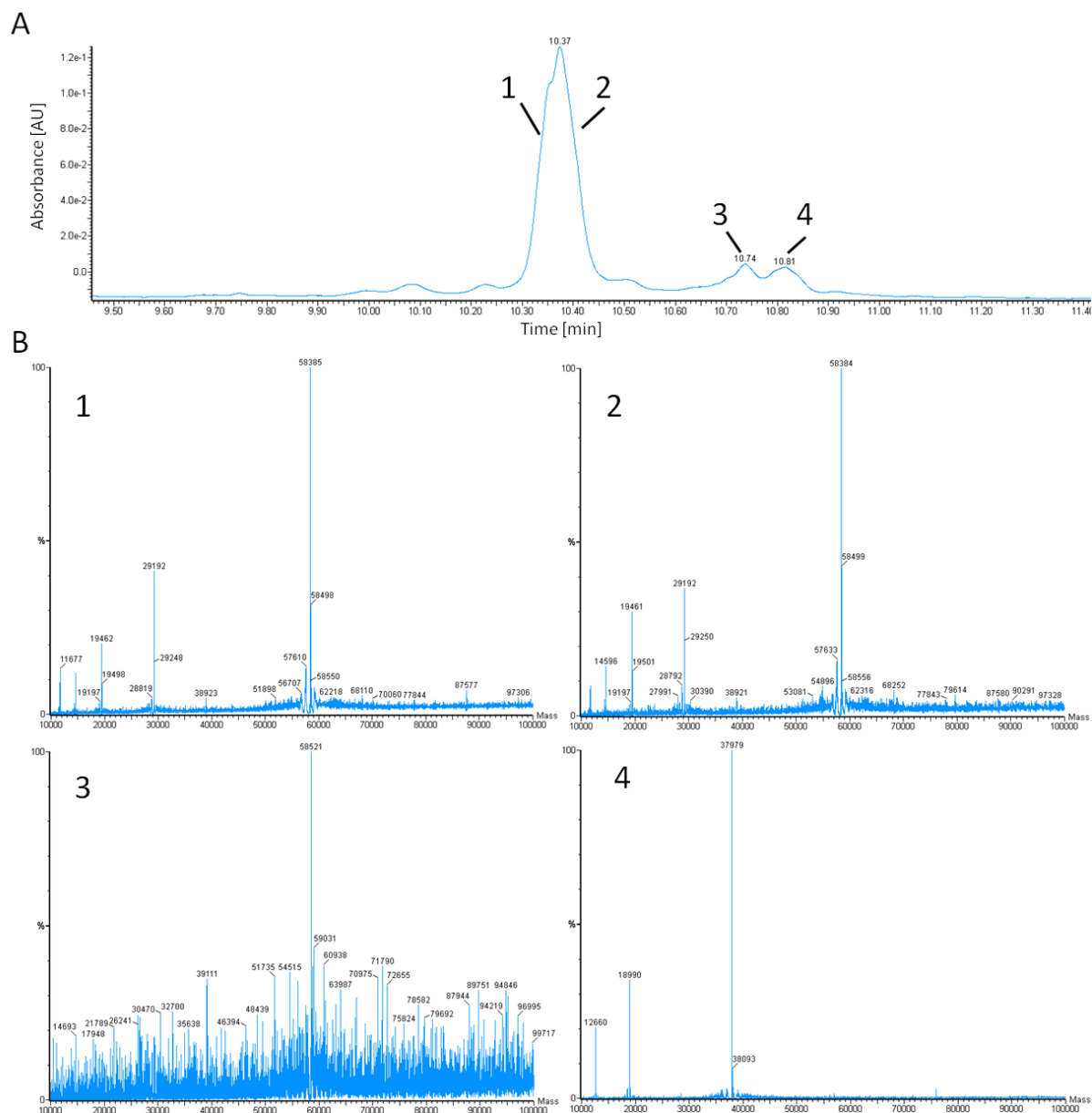


Fig. 6.6: Mass spectrum of THS analyzed with UPLC-ESI-MS. Chromatogram from UPLC (A) and the corresponding mass spectra (B).

Elution time [min]	Mass [m/z]	Ion
10.32	58'385	(M ₁ +H) ⁺
	29'192	(M ₁ +2H) ²⁺
	19'462	(M ₁ +3H) ³⁺
	14'596	(M ₁ +4H) ⁴⁺
	11'677	(M ₁ +5H) ⁵⁺
	58'498	(M ₂ +H) ⁺
	29'248	(M ₂ +2H) ²⁺
	19'498	(M ₂ +3H) ³⁺
10.74	58'521	(M ₂ +Na) ⁺
10.81	37'979	(M ₃ +H) ⁺
	18'990	(M ₃ +2H) ²⁺
	12'660	(M ₃ +3H) ³⁺

Table 6.1: Table of the mass peaks from UPLC-ESI-MS of THS (Fig. 6.6).

MALDI-MS as well as UPLC-ESI-MS show a main mass around 58'400 m/z. Also, in both of the methods, a less intense mass slightly higher than the main peak was present. MALDI-MS gave a mass of around 59'000 g mol⁻¹ for this peak, whereas UPLC-ESI-MS gives a mass of about 58'500 m/z.

Both, the major peak and the minor peak of mass spectroscopy around 58'500 m/z are supposed to be the α - and β -subunits of THS, which have a slightly different molecular weight. However, comparing SDS-PAGE analysis with results of MS, the results are confusing, because the more intensive band from SDS-PAGE shows a higher mass than the weaker band. On the other side, the more intensive peak from MS has a smaller mass compared to the minor peak. Therefore, it is not clear, which mass corresponds to which subunit.

The mass around 37'950 m/z occurring in MALDI-MS as well as UPLC-ESI-MS cannot be explained from any THS subunit or their multi charged species. It is supposed to be an impurity. This unknown protein is the main impurity, which can be found. It is also found on SDS-PAGE analysis (Fig. 6.1), but not on native PAGE (Fig. 5.4 B).

6.4 Stability test

It was often observed in the lab that THS is a very stable protein and can be stored for over a month in the fridge without any degradation. However, the stability of THS in different pH values and against organic solvents was tested.

In the literature, it is stated that THS is stable in a pH range between pH 4 - 12.¹¹⁴ This was reviewed by testing the stability of THS in a range of pH 3 - 9.5 by incubating it in solutions with different pH values for two hours and subsequent analysis on their structure by SDS-PAGE, native PAGE, and TEM.

The primary structure of THS was not affected by varying the pH, which can be derived from SDS-PAGE. However, native PAGE analysis showed the disintegration of THS' quaternary structure at pH 3, whereas the quaternary structure of THS was intact at pH 5.25, 7.5, and 9.5. These findings were confirmed by TEM whereat a pH above 3, fully assembled THSs were visible while no defined structure was found for the sample incubated at pH 3 (Fig. 6.7).

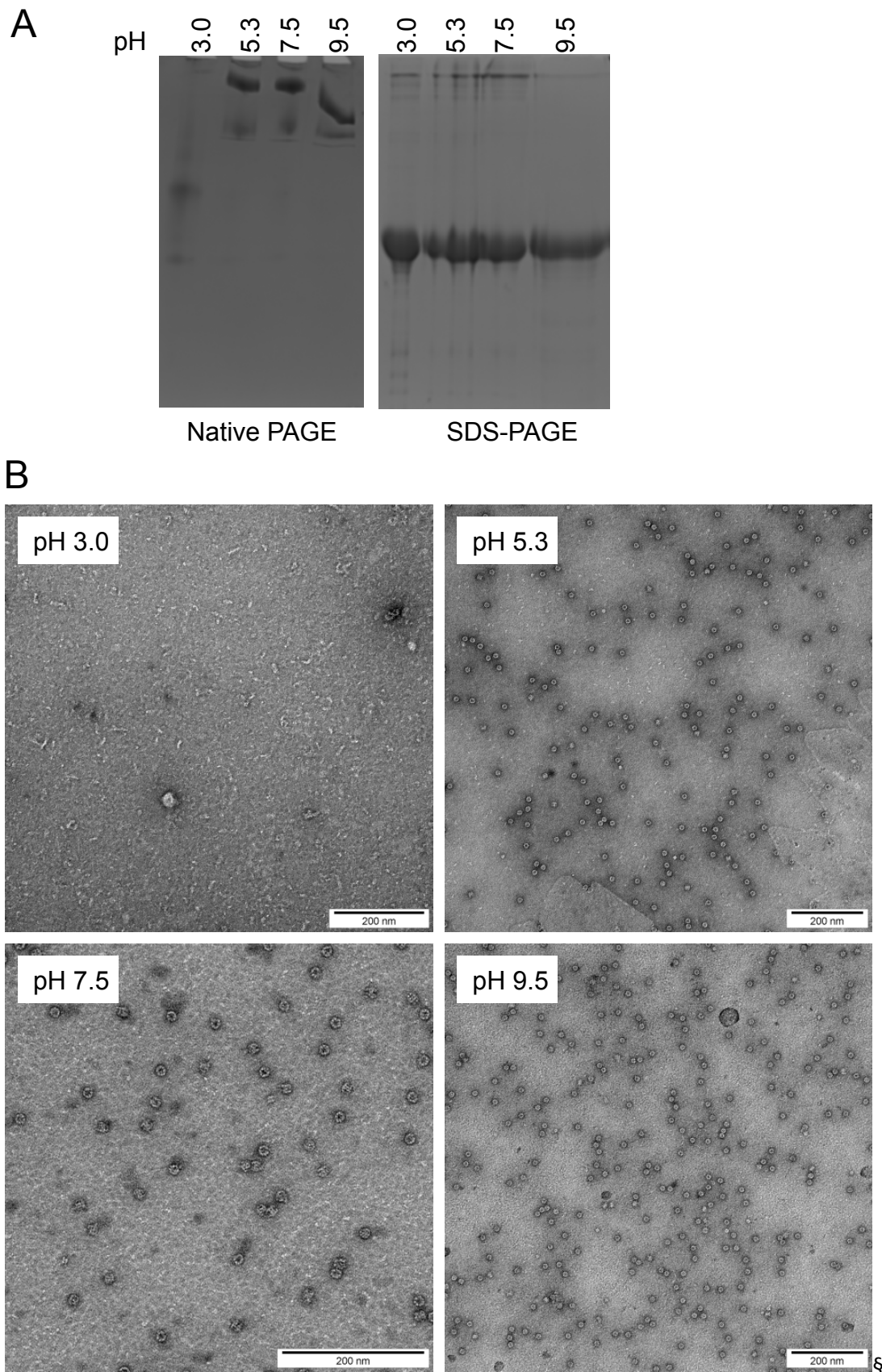


Fig. 6.7: (A) Native and SDS-PAGE of THS at different pH values. The band at pH 9.5 in the native PAGE was pulled down by its neighboring band (not shown). (B) TEM micrographs of THS at different pH values.

The stability of THS in organic solvents can be of particular interest for reactions with THS. Previously it was shown that THS was stable in 30 vol% of tetrahydrofuran (THF) in water.¹⁷⁷ Here, the stability was tested against dimethylformamide (DMF) and acetonitrile (AcN). To this end, THS was incubated overnight in different ratios of DMF or AcN to Buffer B and subsequently analyzed with native PAGE. While no change of the THS bands up to a DMF concentration of 20 vol% can be observed, an agglomeration of THS occurred at 30 vol% DMF. In contrast, THS in a 20 vol% AcN mixture starts to disassemble. This effect increased at higher AcN concentration (30 vol%).

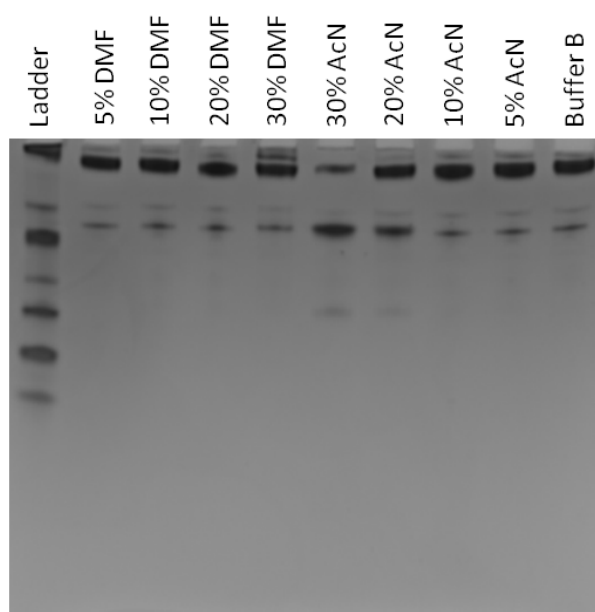


Fig. 6.8: Native PAGE of THS in different mixtures of either DMF/Buffer B or AcN/Buffer B.

In conclusion, we observe a disintegration of THS at pH 3 as it is described in literature.¹¹⁴ Additionally, we see that THS is less stable in DMF than in THF and even less stable in AcN.

7. Modification of THS with cell targeting ligands

Parts of this chapter are submitted:

M.G. Nussbaumer, M. Rother, K. Renggli, M. Chami and N. Bruns
Chaperonin-dendrimer conjugates for siRNA delivery

Other parts of this chapter are in preparation for publication:

M.G. Nussbaumer and N. Bruns

7.1 THS-Atto647 modification

To achieve effective NDDS, cell targeting or cell penetrating moieties can be incorporated to improve delivery. (See chapter 1. *Introduction nanomedicine*) Therefore, we modified THS with different cell targeting and penetrating moieties and analyzed their binding and uptake ability to different cell lines by flow cytometry (FC) and confocal laser scanning microscopy (CLSM). Both techniques need a fluorescent label to analyze the interaction of THS with the cells, so we conjugated the fluorescent dye Atto647-maleimide (Atto647-mal) to the cysteines of THS (*Fig. 7.1*). It has been shown that fluorophores, which are not shielded properly and come into contact with cells, often promote cellular internalization. This is due to their cationic or hydrophobic properties, resulting in an alleged uptake signal.^{178, 179} However, because the cysteines are located inside of the THS cavities, the Atto647 is shielded from its surrounding and does not come into direct contact with cells.

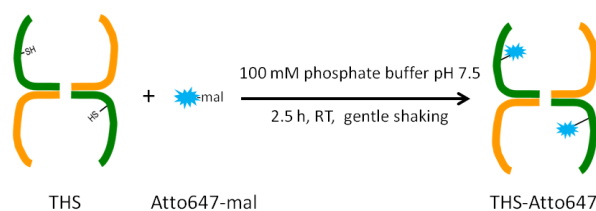


Fig. 7.1: Scheme of the conjugation of Atto647-mal to THS.

After conjugating Atto647-mal to THS, free dye was separated by size exclusion chromatography. The molecular substitution ratio (MSR), which is the number of Atto647 conjugated to each THS, was determined from UV/Vis spectra. From the specific absorbance at 645 nm of Atto647 and the absorbance of THS at 280 nm, corrected with the absorbance of the dye at this wavelength, a MSR of 3.4 was calculated. Thus, 3.4 cysteines per THS were labeled with Atto647 (*Fig. 7.2*). This result is in accordance with the MSR of THS-PAMAM (see chapter 8.2 *THS-PAMAM conjugation*).

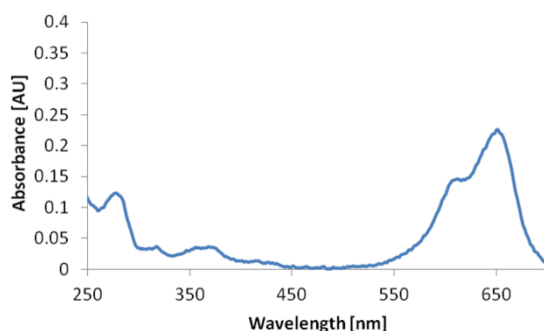


Fig. 7.2: UV/Vis spectrum of THS-Atto647.

THS-Atto647 was analyzed with fluorescence correlation spectroscopy (FCS) to determine if Atto647 was bound to THS or if incomplete purification by size exclusion chromatography led to the

presence of free dye. For Atto647-mal a diffusion time of 84.8 μs was measured and hence a hydrodynamic radius (R_H) of 0.58 nm was calculated. After conjugation of Atto647-mal to THS, the diffusion time increased to 1180 μs , which corresponds to a R_H of 8.1 nm (Fig. 7.3 A). This result corresponds well to the 8 nm radius of THS reported in literature¹⁰⁵ suggesting the successful binding of Atto647-mal to THS.

The THS-Atto647 conjugate was further analyzed with SDS-PAGE to confirm the binding of the dye to the cysteines at the β -subunit of THS. An SDS gel of THS-Atto647, first in the fluorescence mode and after Coomassie staining in visible mode, enabled the dye and the protein bands to be detected. The two subunits of THS were found at around 60 kDa, and the dye was located at the lower subunit band, corresponding to the β -subunit (Fig. 7.3 B). These results indicated that the binding of Atto647-mal to the cysteine located in the interior of the THS cavity was successful.

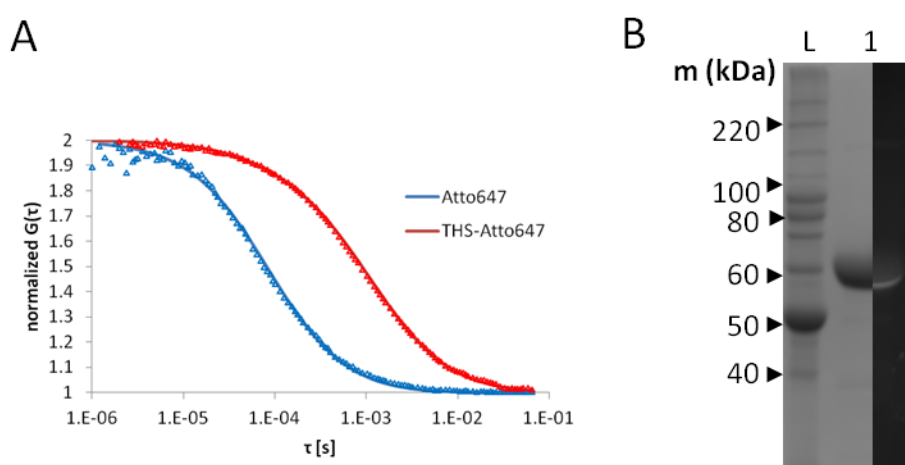


Fig. 7.3: (A) FCS curves of Atto647 (blue) and THS-Atto647 (red). (B) SDS-PAGE of THS-Atto647 Coomassie stained (left) and unstained fluorescence image.

7.2 Modification of THS with cell targeting ligands

In the following sections the conjugation of different cell targeting and cell penetrating moieties to THS is discussed, namely bombesin, biotin, somatostatin, cRGD, TAT, and VEGF. After conjugation of the moieties to THS, the conjugates were analyzed and tested for their ability to translocate THS into cells.

7.2.1 BBN-8/12EG-THS-Atto647

Bombesin (BBN, in literature also BBS) is a gastrin-releasing peptide (GRP) homologue from the amphibian *Bombina orientalis*. It can bind to the GRP receptor, which is a G protein-coupled receptor, that is often upregulated in breast and prostate cancer cells making BBN an interesting candidate for targeting different cancer cells.¹⁸⁰⁻¹⁸² BBN and its analogues have been used to transport different attached molecules to or into cells, for instance chelated radioactive elements (^{99m}Tc, ¹¹¹In or ¹⁷⁷Lu),^{181, 183} gold nanoparticles (AuNP),¹⁸⁰ iron oxide nanoparticles (SPION),¹⁸⁴ peptides¹⁸² and also large cargo, namely viral capsid from cowpea mosaic virus.¹⁸⁵ BBN is a tetradecapeptide (Glu-Gln-Arg-Leu-Gly-Asn-Gln-Trp-Ala-Val-Gly-His-Leu-Met-NH₂), where the peptides 7-13 seem to be crucial for the binding to the GRP receptors.^{181, 183} Therefore, a bombesin analogue with a sequence of Gln-Trp-Ala-Val-Gly-His-Nle-NH₂ was used. The leucine was exchanged to norleucine (Nle) to enhance the metabolic stability.¹⁸¹ At the C-terminus eight ethylene glycol units

(BBN-8EG), respective twelve ethylene glycol units (BBN-12EG), were inserted, which served as spacer between the peptide and phenyl isothiocyanate (PITC). PITC reacts with primary amines of lysines, forming an isothio urea bond.¹⁸⁶ Earlier experiments with a shorter 4EG spacer did not show any binding or uptake (Data not shown). Therefore, longer spacers were introduced between THS and BBN. The conjugation was done with a 300-fold excess of BBN over THS to allow for a sufficient modification of THS with BBN (*Fig. 7.4*).

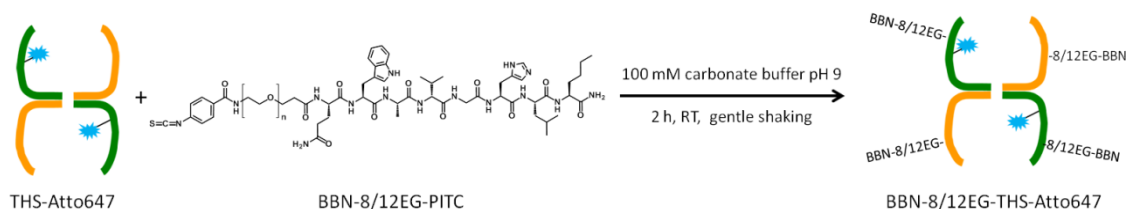


Fig. 7.4: Scheme of the conjugation of BBN-8/12EG-PITC to THS-Atto647.

After conjugating BBN, with two different lengths of spacer to THS, the conjugates were analyzed with UPLC-MS to confirm the conjugation (*Fig. 7.5*). A main mass of 58'385 m/z (M_1+H)⁺ eluting at 10.28 min was found. This corresponds to THS subunit, as seen from the mass analysis from unmodified THS (see chapter 6. *THS characterization*). Compared to the mass spectrum of unmodified THS, two additional peaks at elution times of 10.37 min and 10.42 min were found and determined to be 59'962 m/z and 59'965 m/z, respectively. These two masses correspond to THS subunits (M_2+H)⁺ modified with BBN-8EG (BBN-8EG-PITC: 1578 g mol⁻¹). Also the multi charged species are present in the mass spectrum (29'981 m/z (M_2+2H)²⁺, 19'988 m/z (M_2+3H)³⁺).

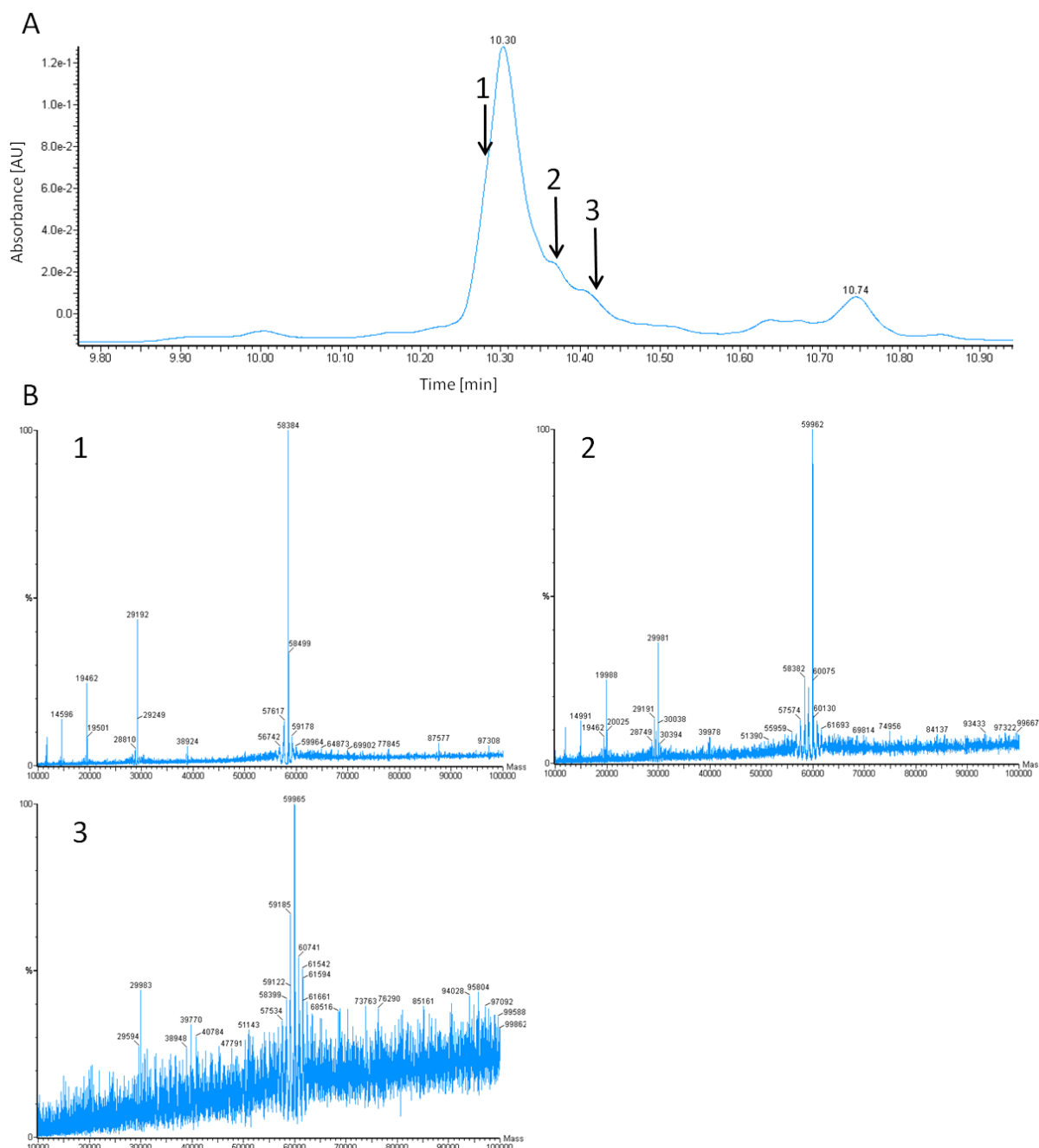


Fig. 7.5: Deconvoluted mass spectrum of BBN-8EG-THS analyzed with UPLC-ESI-MS. Chromatogram from UPLC (A) and the corresponding mass spectra (B). The arrows point at the elution time, when the mass spectra were recorded.

In the mass spectrum of BBN-12EG-THS, the unmodified subunits represent the main peak at an elution time of around 10.30 min. After 10.38 min of elution, a mass of 60'210 m/z was detected (Fig. 7.6). This corresponds to single-modified BBN-12EG-THS (BBN-12EG-PITC: 1825 g mol⁻¹). In contrast to BBN-8EG-THS, also the double modified specie was detected. At an elution time of 10.41 min a mass of 62'033 m/z was measured. At 8.01 min the unbound BBN-12EG was eluted (913 m/z M₃+2H)²⁺). Additionally, at 8.56 min a mass of 3606 m/z (1203 m/z (M₄+3H)³⁺) was detected. This mass could originate from a dimerization of BBN-12EG, but this is unclear. The mass at 8.95 min could not be deconvoluted. From these results we can conclude a successful conjugation of BBN-8EG and BBN-12EG to THS. Unfortunately, it was not possible to quantify the BBN per THS ratio.

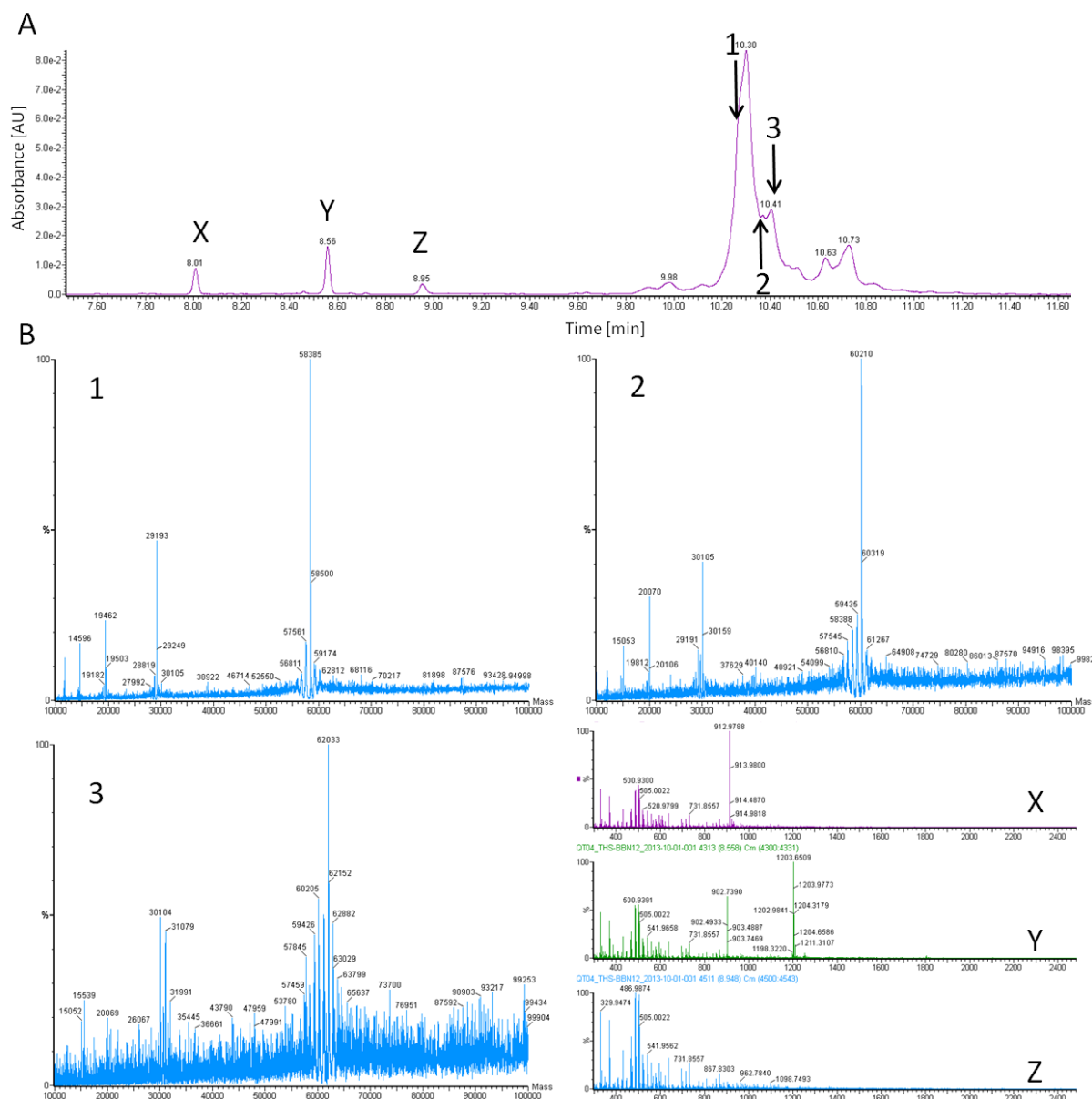


Fig. 7.6: Deconvoluted mass spectrum of BBN-12EG-THS analyzed with UPLC-ESI-MS. Chromatogram from UPLC (A) and the corresponding mass spectra (B). The arrows point at the elution time, when the mass spectra were recorded.

As aforementioned, GRP receptors are up-regulated in prostate cancer cells, such as PC-3 cells.¹⁸¹ Hence, the ability of BBN-8EG-THS-Atto647 and BBN-12EG-THS-Atto647 to interact with PC-3 prostate cancer cells was tested by flow cytometry. Cells treated for 2 h with Atto647, THS-Atto647, BBN-8EG-THS-Atto647 and BBN-12EG-THS-Atto647 exhibited about the same fluorescence intensity, which was roughly two-times higher than untreated PC-3 cells (Fig. 7.7). Thus, bombesin-carrying THS did not result in higher fluorescence compared to THS-Atto647.

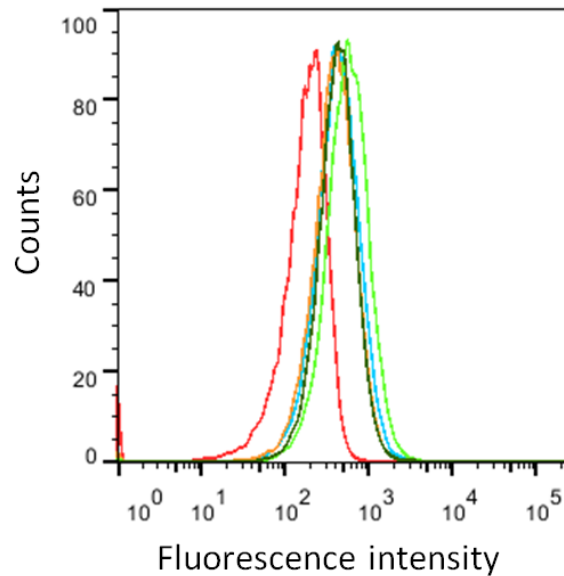


Fig. 7.7: Flow cytometry of PC-3 cells (red) and PC-3 cells incubated with Atto647 (dark green), THS-Atto647 (light green), BBN-12EG-THS (orange) and BBN-8EG-THS (blue).

Also from CLSM images of PC-3 cells treated 1 h with THS-Atto647, BBN-8EG-THS-Atto647 and BBN-12EG-THS-Atto647, respectively, no specific or unspecific binding or uptake of the THS-Atto647 conjugates by PC-3 cells could be observed (Fig. 7.8). Thus, this system is not suitable for targeting cells with THS. It is not clear, whether the PC-3 cells do not present GRP receptors or if the binding of this BBN peptide does not promote any interactions with PC-3 cells.

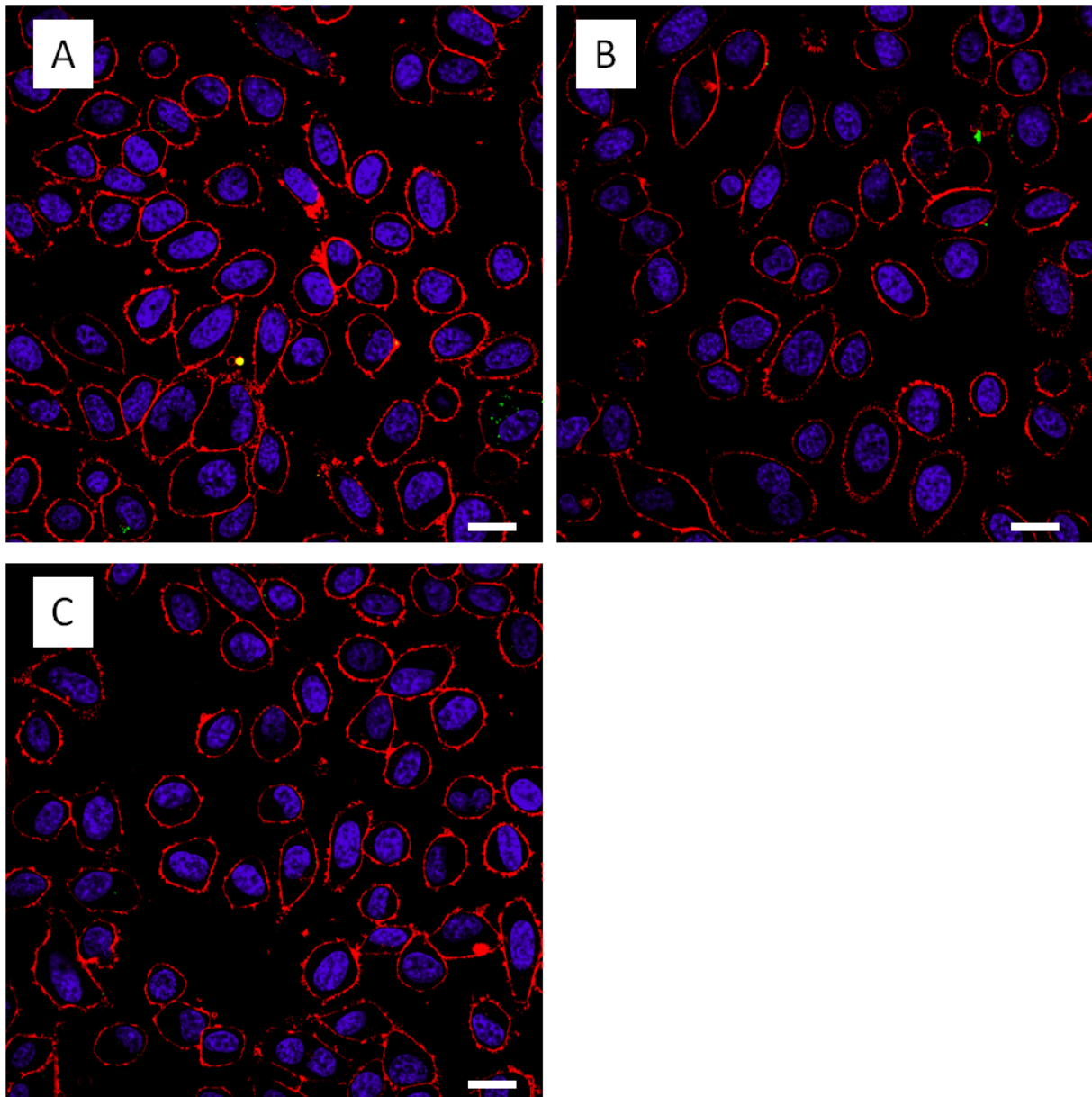


Fig. 7.8: CLSM images of PC-3 cells incubated with BBN-8EG-THS-Atto647 (**A**), BBN-12EG-THS-Atto647 (**B**) and THS-Atto647 (**C**). THS-Atto647 (green), nucleus (blue) and cell membrane (red). Scale bars: 20 μm .

7.2.2 Biotin-THS-Atto647

Biotin is an important nutrient for cells and is crucial for normal cell function, growth, and development of cells. Biotin and other vitamins are especially crucial for fast dividing cells. These cells up-regulate the expression of receptors for biotin uptake.¹⁸⁷ Therefore, in some studies biotin was attached to NDDS to target cancer cells such as OVCAR-3, HEK 293T, and HeLa cells.¹⁸⁸⁻¹⁹¹

For the conjugation of biotin to THS, we used biotinamidohehexanoic acid N-hydroxysuccinimide ester (biotin-LC-NHS); a biotin with an activated ester group (*Fig. 7.9*). This activated ester reacts primarily with the nucleophilic primary amine of lysine with release of the leaving group (NHS).¹⁸⁶ We used a 100-fold excess of biotin-LC-NHS over THS for the modification.

7. Modification of THS with cell targeting ligands

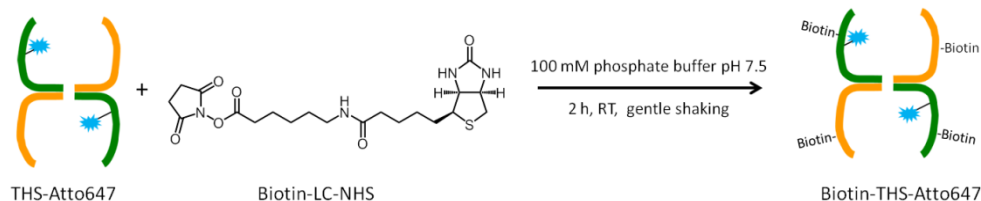


Fig. 7.9: Scheme of the conjugation of Biotin-LC-NHS to THS-Atto647.

We analyzed the biotin-THS-Atto647 conjugate with SDS-PAGE. Only a minor band shift of the biotin-THS-Atto647 was detectable, upon modification with biotin-LC (326.2 g mol^{-1}) (Fig. 7.10 A). The interaction of biotin-THS-Atto647 with the HeLa cancer cell line and the non-cancer cell line CHO-K1 as a control was studied with FC. For both cell lines, similar results were found. Only a slight fluorescence increase was measured, when incubated with biotin-THS-Atto647 or THS-Atto647. Even higher fluorescence was measured when the cells were incubated with free dye (Fig. 7.10 B). Like BBN-8/12EG-THS-Atto647, the biotin conjugate did not show any specific interaction with either HeLa or CHO-K1 cells. Therefore, we did not perform microscopy studies.

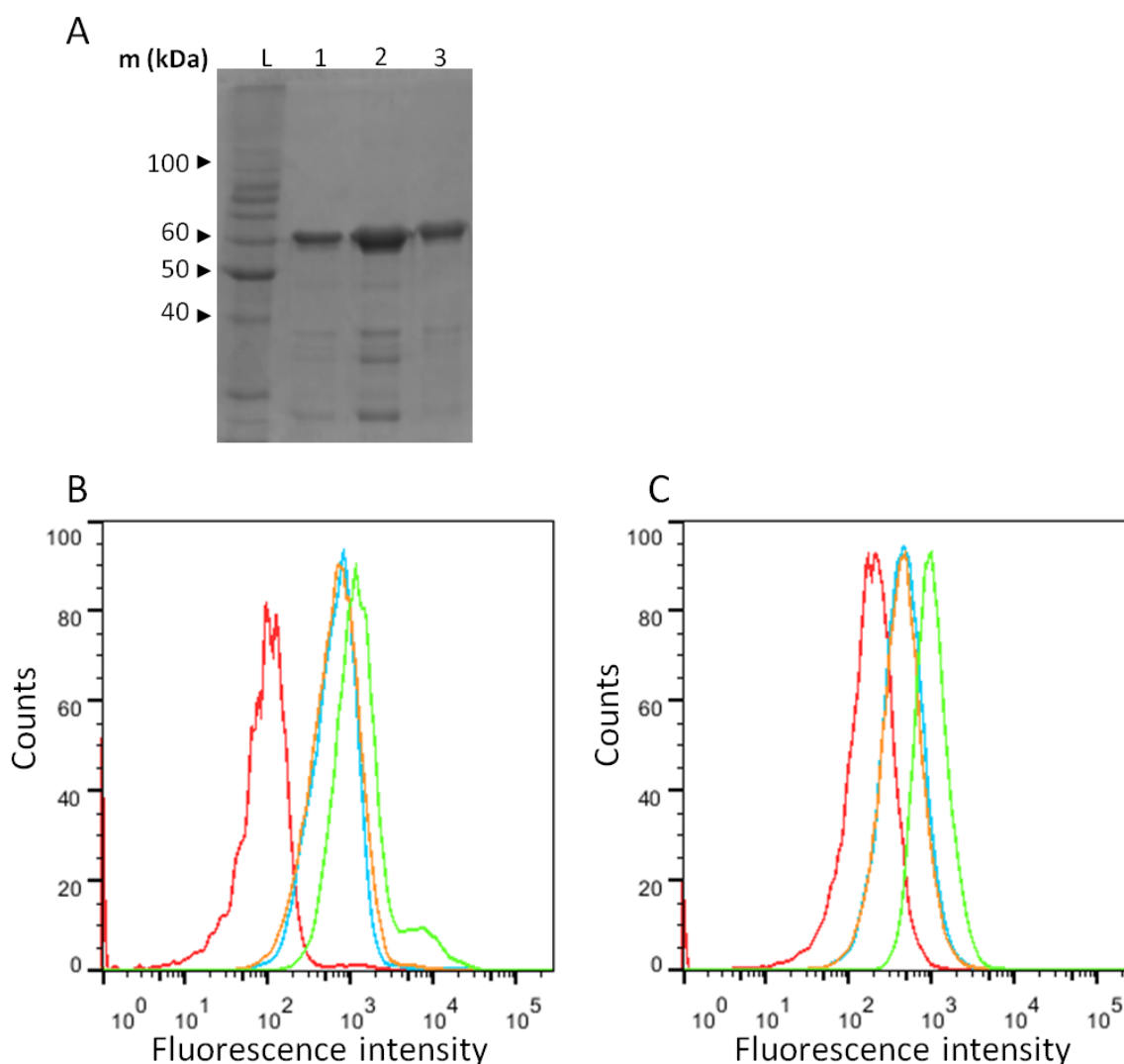


Fig. 7.10: (A) SDS-PAGE of THS (1), THS-Atto647 (2) and biotin-THS-Atto647 (3). Flow cytometry of HeLa cells (B) and CHO-K1 (C) incubated with Atto647 (light green), THS-Atto647 (orange), biotin-THS-Atto647 (blue) and cells alone (red).

7.2.3 FA-THS-Atto647

Like biotin the vitamin folic acid (FA) is essential in rapidly dividing cells. It acts as a co-factor in the nucleotide and DNA synthesis pathway. Fast dividing cells, such as cancer cells, express far more folic acid receptors than normal cells, making folic acid an interesting candidate for targeting cancer tissue.^{187, 192} FA was attached to different cargo to enhance their uptake in cells. Among others, the uptake of PAMAM,¹⁹³ VLP,¹⁹⁴ SPION¹⁹⁵ or chitosan nanoparticles (~ 100 nm)¹⁹⁶ could be boosted by conjugation to FA. HeLa, Caco-2, KB, and HT29 are cancer cell lines which showed an enhanced uptake of FA modified cargo.¹⁹⁴⁻¹⁹⁷

To modify THS-Atto647 with FA, we used a FA, which had a PEG₂₀₀₀ spacer and a succinimidyl activated ester and an approximate mass of about 2000 g mol⁻¹ (Fig. 7.11). A 50-fold excess of FA-PEG₂₀₀₀-NHS over THS was deployed for the modification.

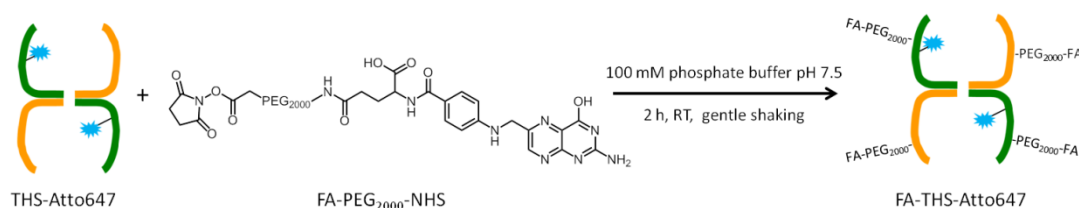


Fig. 7.11: Scheme of the conjugation of FA-PEG₂₀₀₀-NHS to THS-Atto647.

The mass change of FA modified THS was determined with MALDI-MS and SDS-PAGE. MALDI-MS results revealed additional shoulders after the modification of THS with FA-PEG₂₀₀₀-NHS (Fig. 7.12 A). Multi-peak fitting was done to determine the mass of these shoulders (Fig. 7.12 B). In Addition to the peaks at 58'490.9 \pm 284.4 m/z (maximum \pm HWHF) and 59'148.2 \pm 477.0 m/z, which were also observed in the unmodified THS spectrum, an additional prominent shoulder at 60'412.6 \pm 1637.7 m/z appeared. Two further small shoulders at 63'328.9 \pm 782.4 m/z and 64'708.3 \pm 1304.4 m/z were found. These three additional shoulders correspond to mono-, di-, and tri-FA-modified THS subunits. An averaged additional mass of 2137.7 \pm 255.0 m/z was calculated. This mass corresponds to that of FA-PEG₂₀₀₀. From SDS-PAGE an additional band just above the THS bands was observed, which corresponds to the FA-PEG₂₀₀₀-THS conjugate (Fig. 7.12 C). It is not clear what the band at around 120 kDa is. The band at the boundary of the stacking and the running gel is probably poorly soluble FA conjugates.

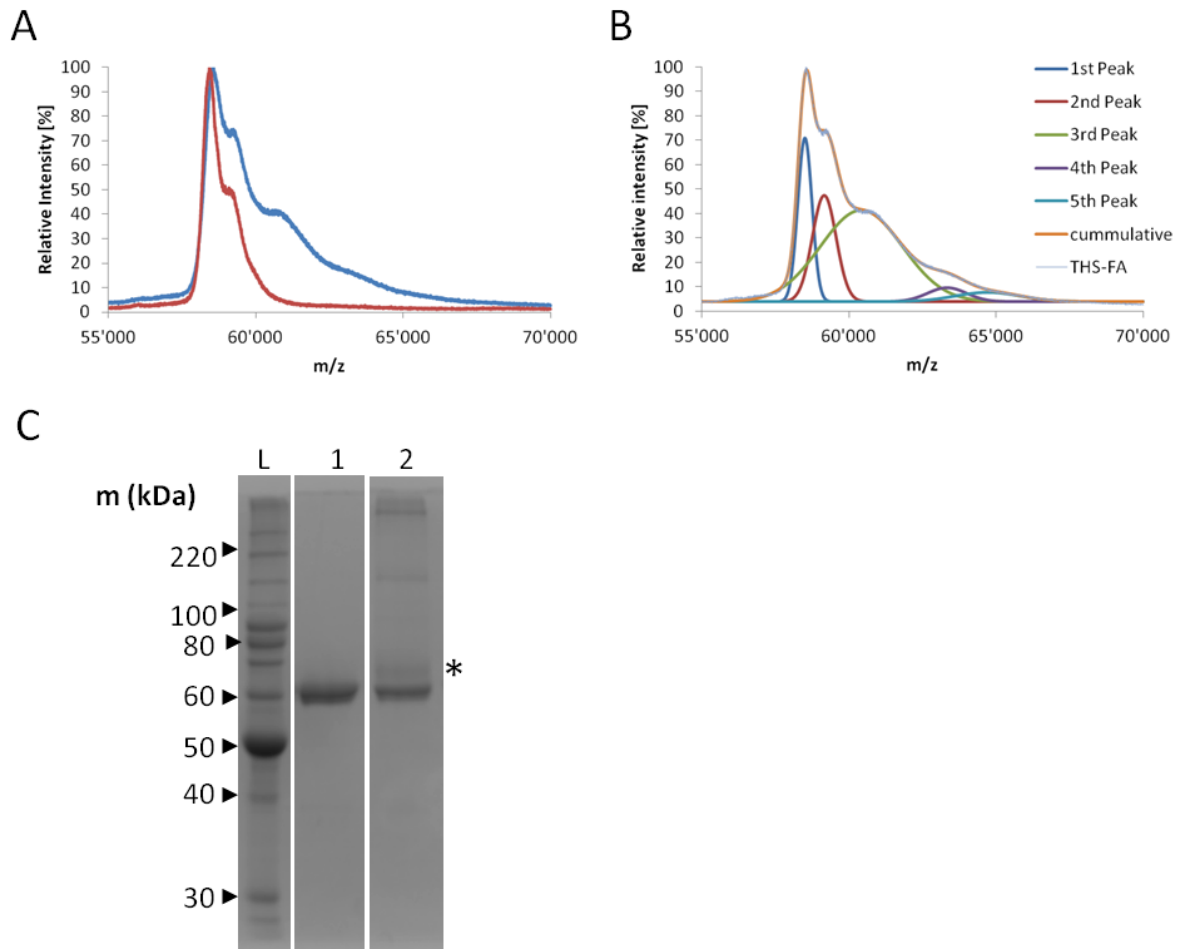


Fig. 7.12: (A) MALDI-MS of THS (red) and FA-THS (blue). (B) Multi-peak fitting of the mass spectrum of FA-THS. (C) SDS-PAGE of THS (1) and FA-THS (2), the asterisk indicates the FA-THS band.

The interaction of HeLa cells incubated for 2 h with FA-PEG₂₀₀₀-THS-Atto647 were investigated with FC and CLSM. As with the biotin-THS-Atto647 conjugate, no specific interaction of the FA conjugate with HeLa cells was measured. The FA conjugate increased the fluorescence even less than just the THS-Atto647 (1.9-fold vs. 4.7-fold) (Fig. 7.13 A). Also CLSM showed only little interactions of FA-PEG₂₀₀₀-THS-Atto647 with HeLa cells (Fig. 7.13 B & C). These results also disqualified this method to target cells.

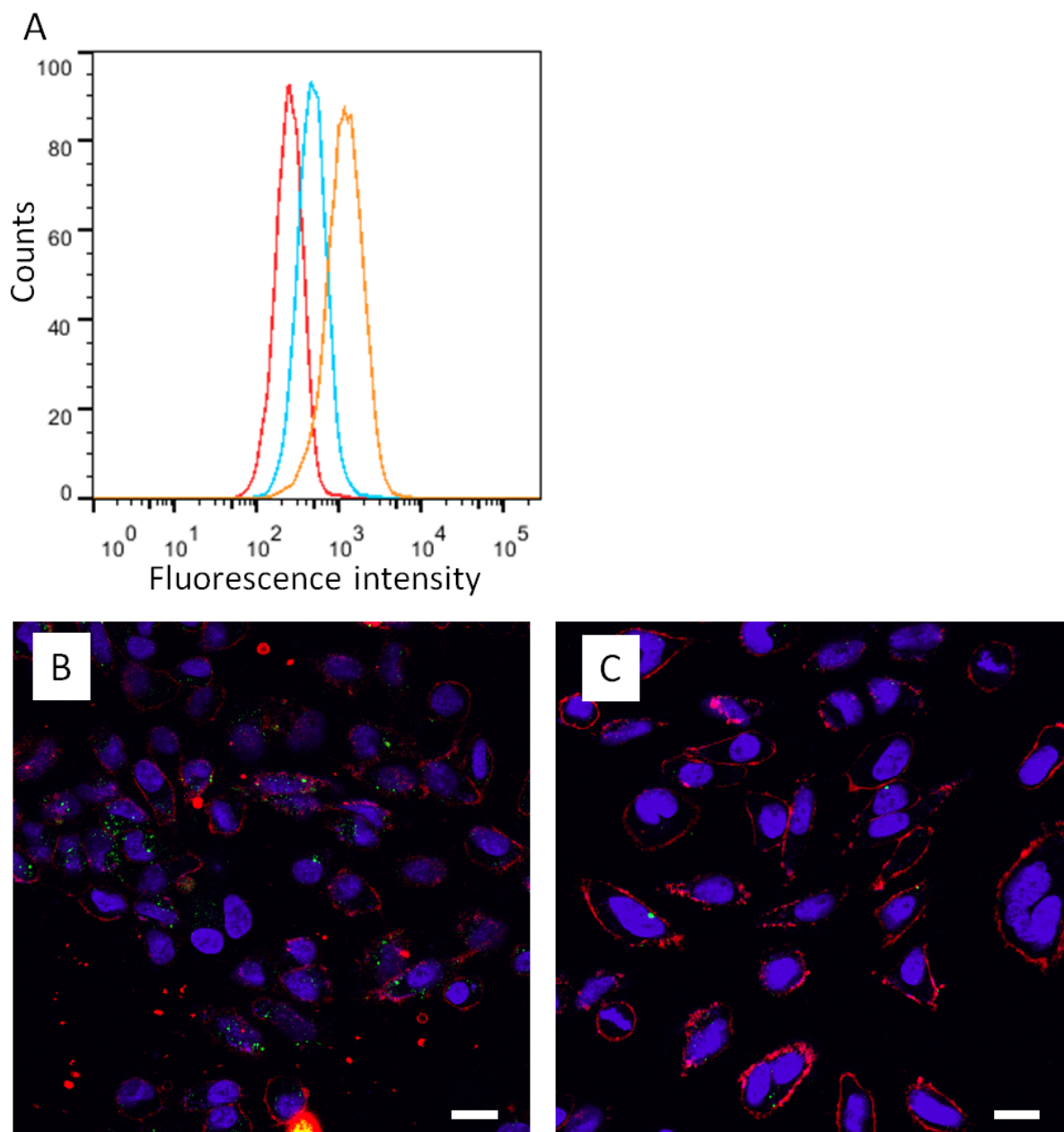


Fig. 7.13: (A) Flow cytometry of HeLa cells incubated with THS-Atto647 (orange), FA-THS-Atto647 (blue) and cells alone (red). CLSM images of HeLa cells incubated with THS-Atto647 (B) and FA-THS-Atto647 (C). THS-Atto647 (green), nucleus (blue) and cell membrane (red). Scale bars: 20 μm .

7.2.4 SST-THS-Atto647

Somatostatin (SST) is a neuropeptide, which inhibits the endocrine system and is involved in cell division, cell proliferation, and apoptosis. Five different SST receptors (SSTR 1-5) are identified, which belong to the GTP-binding-protein-coupled receptor family. An up-regulation of SSTR is found in several cancer cells, such as MCF-7 breast cancer cells.^{198, 199} Different NDSS were developed with SST or its analogues octreotide and lanreotide to bring lipid micelles,¹⁹⁸ PAMAM²⁰⁰ or the cancer drug paclitaxel¹⁹⁹ to cancer cells. CHO-K1 cells often served as a control cell line, because they are expressing SSTR only in low levels.¹⁹⁹

We conjugated S-HyNic (290.3 g mol^{-1}) to the primary amines of SST (1640 g mol^{-1}) using a five-fold excess of S-HyNic over SST. After separation of free S-HyNic from SST-HyNic, PEG₄-PFB modified THS

(100-fold excess of PEG₄-PFB over THS) was conjugated to SST-HyNic (Fig. 7.14 A). The number of formed bis-arylhydrazone bond between SST and THS was quantified with UV/Vis spectroscopy ($\lambda = 354$ nm), resulting in a 39.2 SST/THS modification (Fig. 7.14 B).

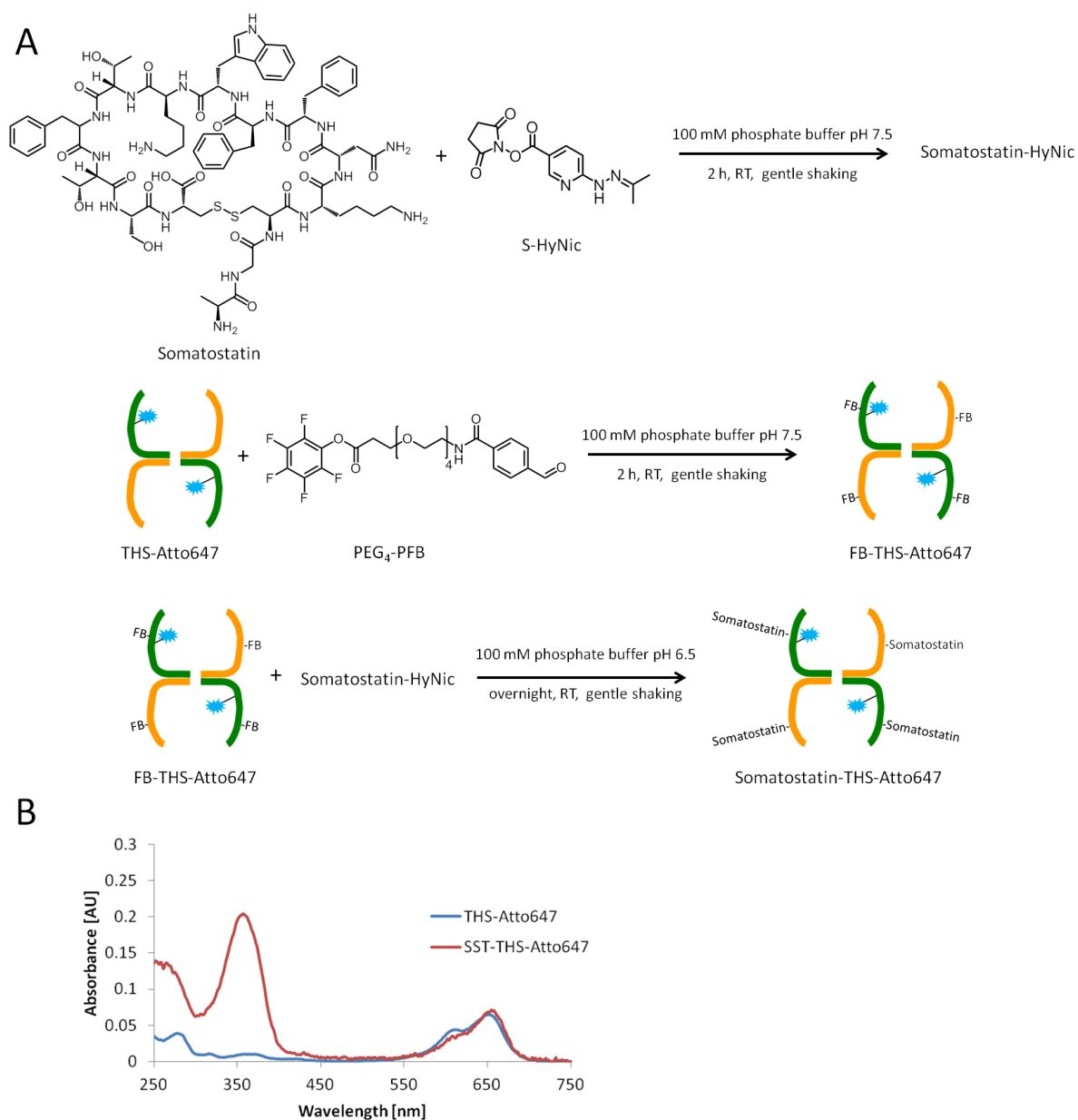


Fig. 7.14: (A) Scheme of the conjugation of Somatostatin to THS-Atto647. (B) UV/Vis spectra of THS-Atto647 (blue) and SST-THS-Atto647 (red).

Flow cytometry studies of SSTR up-regulated MCF-7 cells and SSTR low level expressing CHO-K1 cells incubated with THS-Atto647, SST-Atto647, and Atto647 revealed only an enhanced uptake of the dye, but no interaction of the SST-THS conjugate neither with CHO-K1 nor MCF-7 (Fig. 7.15). A reason for this could be that SST modified with S-HyNic may have interrupted the interaction between SST and its receptor. The crucial parts of SST for the binding are the cyclisation by the disulfide bond and the pharmacophore amino acid sequence Phe⁷-Trp⁸-Lys⁹-Thr¹⁰, which may have been altered upon modification with S-HyNic.²⁰¹ A different modification approach is needed to avoid modification of the crucial sequence.

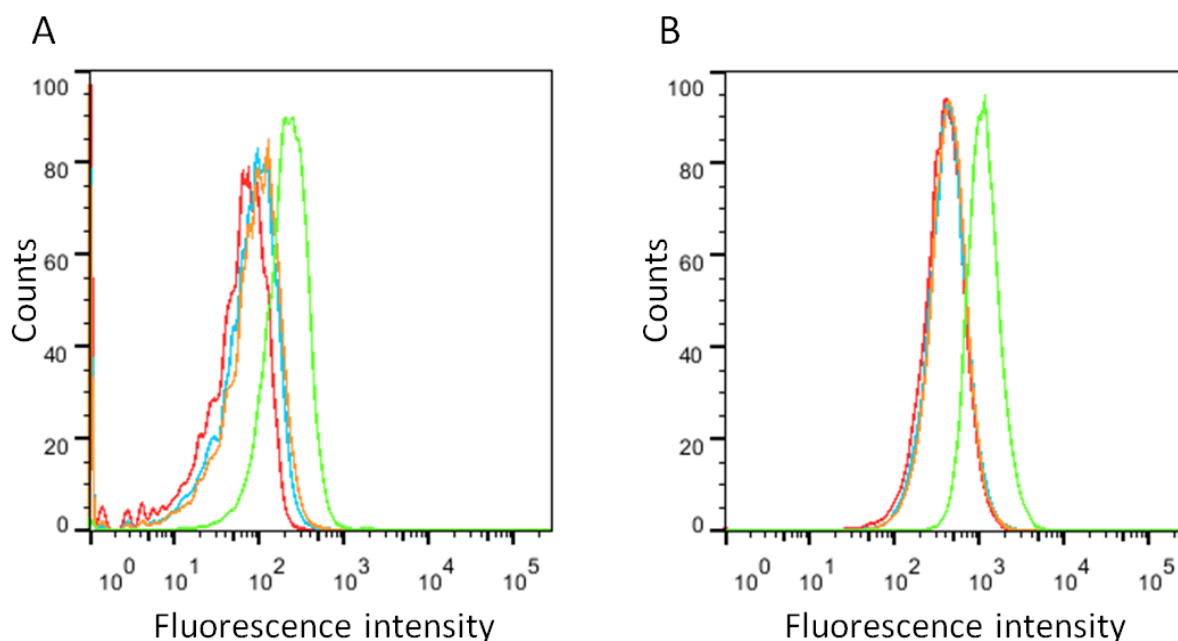


Fig 7.15: Flow cytometry of MCF-7 cells (**A**) and CHO-K1 (**B**) cells incubated with Atto647 (green), THS-Atto647 (orange), SST-THS-Atto647 (blue) and cells alone (red).

7.2.5 cRGDfC-THS-Atto647

As a further targeting ligand, we used a cyclic homologue of the tri-peptide Arg-Gly-Asp (RGD), namely cyclo(-Arg-Gly-Asp-D-Phe-Cys) (cRGDfC). RGD is a known amino acid sequence that binds integrin $\alpha_v\beta_3$ and enhances the cellular uptake of a variety of its cargo molecules.²⁰² $\alpha_v\beta_3$ integrins are up-regulated in fast dividing cells.⁸⁸ Cargos such as quantum dots,²⁰³ PAMAM-siRNA,²⁰⁴ SPION-PEG-Dox²⁰⁵ or apoferritin^{87, 88} was uptaken in cells by interacting with RGD. Also, some viruses use this strategy to enter cells.²⁰⁶ We chose the RGD homologue cRGDfC because of its Cys, which could serve as an attaching point to THS. THS-Atto647 was modified with the bifunctional linker SM(PEG)₂, which has a succinimidyl activated ester on one side, two ethylene glycol units as a spacer and a maleimide functionality for the conjugation to the thiol of cRGDfC (Fig. 7.16). A hundred fold excess of SM(PEG)₂ over THS and a 200-fold excess of cRGDfC over THS-SM(PEG)₂ was used. We did not have the possibility to quantify the cRGDfC modification of THS.

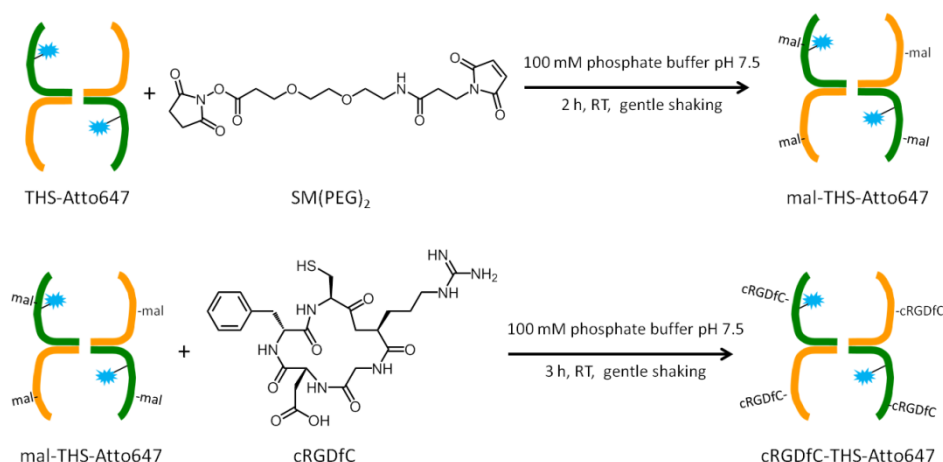


Fig. 7.16: Scheme of the conjugation of cRGDfC to THS-Atto647.

The modified cRGDfC-THS-Atto647 was tested on its interaction with human glioblastoma cell U-87 MG, which have an up-regulated expression of $\alpha_v\beta_3$ integrin, and MCF-7 breast cancer cells, not expressing this integrin.²⁰³ After 2 h of incubation, Atto647 increased the median fluorescence of MCF-7 cells 12.3-fold, whereas the fluorescence of MCF-7 cells incubate with THS-Atto647 increased only 1.7-fold, measured with FC (Fig. 7.17 A). cRGDfC-THS-Atto647 had only a small effect and increased the fluorescence 2.8-fold. These results show, that cRGD have only a very small influence on the interaction of THS with MCF-7 cells. What was remarkable was the difference in interaction of Atto647 and Atto647 bound to THS. The 7.1-fold lower interaction of THS-Atto647 with MCF-7 cells compared to Atto647, shows that Atto647 is shielded by the cavity of THS and does not interact with the cells. Many dye labeled systems suffer the problem of alleged interaction with cells due to the attached dye.^{178, 179} We overcome this problem by conjugating the dye into the cavity of THS, shielding the dye from interaction with the environment.

Examination of the interaction of cRGD modified THS with U-87 MG cells provide interesting results (Fig. 7.17 B). Incubation of cRGDfC-THS-Atto647 resulted in a 20.4-fold enhanced fluorescence intensity. However, THS-Atto647 without cRGD revealed a fluorescence increase of 49.4 times. This is a higher increase as observed with the free Atto647 dye (30.6-fold). Already after 10 min of incubation of U-87 MG cells with THS-Atto647 a 4.7-fold increased fluorescence was measured. The result that THS interacts more with U-87 MG cells than the cRGD modified THS implicate that cRGD is not crucial for the uptake of THS, rather THS alone is capable to interact with U-87 MG cells (see chapter 8. *Chaperonin-dendrimer conjugates for siRNA delivery*). This is supported by the fact that THS is taken up to an even higher extent than Atto647, which was not observed in any other cell line.

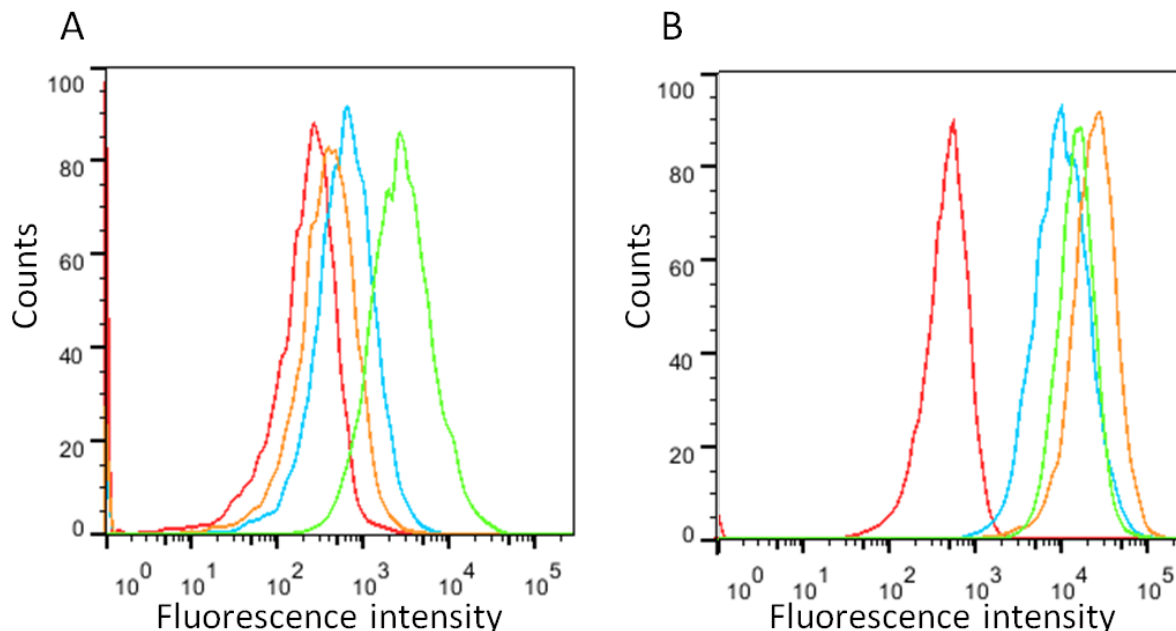


Fig. 7.17: Flow cytometry of MCF-7 cells (A) and U-87 MG (B) cells incubated with Atto647 (green), THS-Atto647 (orange), cRGDfC-THS-Atto647 (blue) and cells alone (red).

Flow cytometric measurements do not differentiate between delivery systems that enter cells and those that merely adsorb to the cell membrane. Therefore, the interaction of THS-Atto647 conjugate with U-87 MG cells was analyzed with a confocal laser scanning microscope (CLSM) (Fig. 7.18 A). Additionally, the cells were treated with a dye that stains acidic cell compartments. This allows to

track whether THS-Atto647 accumulates in lysosomes. After incubating the cells for 30 min in a solution of THS-Atto647, the protein cage was taken up into the cells. It was not located at the cell membrane and it was not translocated to the nucleus. Most of THS-Atto647 was also not co-localized with acidic compartments. The intracellular location of THS-Atto647 did not change at longer incubation time of 2 h (Fig. 7.18 A). Control experiments in which U-87 MG cells were incubated with free Atto647 showed some uptake into the cells, but most of the dye was co-localized with the cell membrane. Moreover, dye agglomeration occurred (Fig. 7.18 B). Thus the uptake of THS-Atto647 by U-87 MG cells is induced by THS and not Atto647. In conclusion, THS-Atto647 was found within U-87 MG cells already after 30 min, while free dye attached to the cell membrane. However, the results do not clarify whether the uptake of THS occurs via non-acidic compartments or if THS escaped acidic compartments within a few minutes.

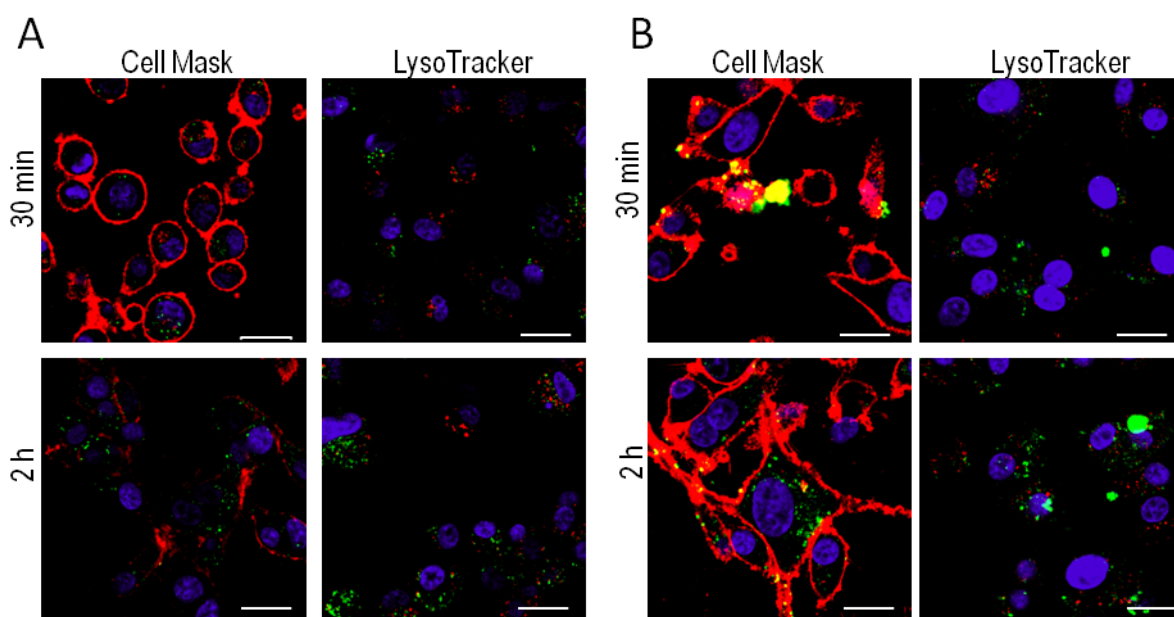


Fig. 7.18: CLSM images of U-87 MG cells incubated with THS-Atto647 (A) and Atto647 (B) for 30 min and 2h: Atto647 (green), nucleus (blue), Cell Mask: cell membrane (red), LysoTracker: acidic compartments (red); scale bars: 20 μm .

7.2.6 TAT-THS-Atto647

TAT is the most prominent representative of cell penetrating peptides (CPP). The nine amino acid sequence RKKRRQRRR (Tat 46-57) of transactivator-of-transcription-protein from HIV is the minimal sequence which induces protein transduction. A broad variety of cargo has been transported into different cells by TAT; ranging from small molecules (fluorophores and cancer drugs) to bigger cargo, such as peptides, nucleic acids, quantum dots, inorganic nanoparticles or proteins, and further to lipid and polymeric nanostructures with a diameter of around 200 nm.^{15, 207-209} However, the uptake mechanism is still under scientific discussion. The cationic character plays a crucial role by binding to the negatively charged cell membrane, but this is not a complete explanation. Different uptake mechanisms have been observed, with endocytic uptake and macropinocytosis appearing to be the main uptake mechanisms.^{15, 209} However, it is important to note that TAT is promiscuous and not a targeting ligand, but can help to bring the cargo into the cells.

For the conjugation of TAT to THS-Atto647, we chose a similar strategy as for the conjugation of SST to THS. A HyNic modified TAT (HyNic-GRKKRRQRRRPPQ-NH₂) was conjugated to PEG₄-PFB modified

THS-Atto647 (Fig. 7.19). A 100-fold excess of PEG₄-PFB to THS-Atto647 was used and after separation of unbound PEG₄-PFB, a 50-fold excess of TAT-HyNic to PFB-THS-Atto647 was used.

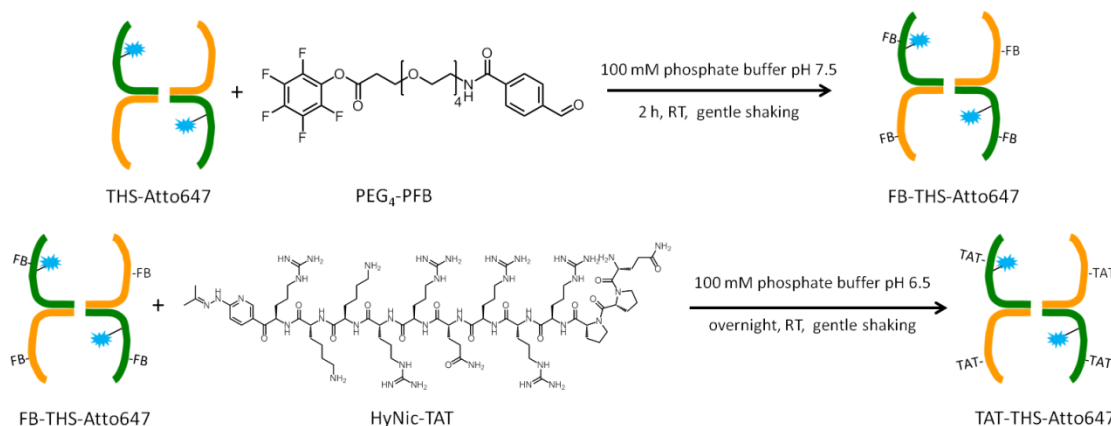


Fig. 7.19: Scheme of the conjugation of TAT to THS-Atto647.

From the absorption at 354 nm relative to the absorption of the dye at 645 nm, it was calculated that about 49 TAT peptides reacted per THS (Fig. 7.20 A). This result implies that almost every TAT-HyNic was conjugated to FB-THS-Atto647. A band shift of THS upon modification with TAT was observed by SDS-PAGE (Fig. 7.20 B). The band of TAT-THS-Atto647 subunits was around a mass of 65 kDa, which corresponds to about three TAT per THS subunit or about 50 TAT per THS, confirming the modification degree, which was measured with UV/Vis-spectroscopy (Fig. 7.20 A). In addition, the band of TAT modified THS subunits was much more blurred than unmodified THS subunits, indicating a heterogenous modification of the subunits. In contrast to unmodified THS, the fluorescence image of the TAT-THS-Atto647 band is not only located at a specific THS band (compare to Fig. 7.3 B), but is distributed over the whole band, suggesting that TAT bound to α - and β -subunits.

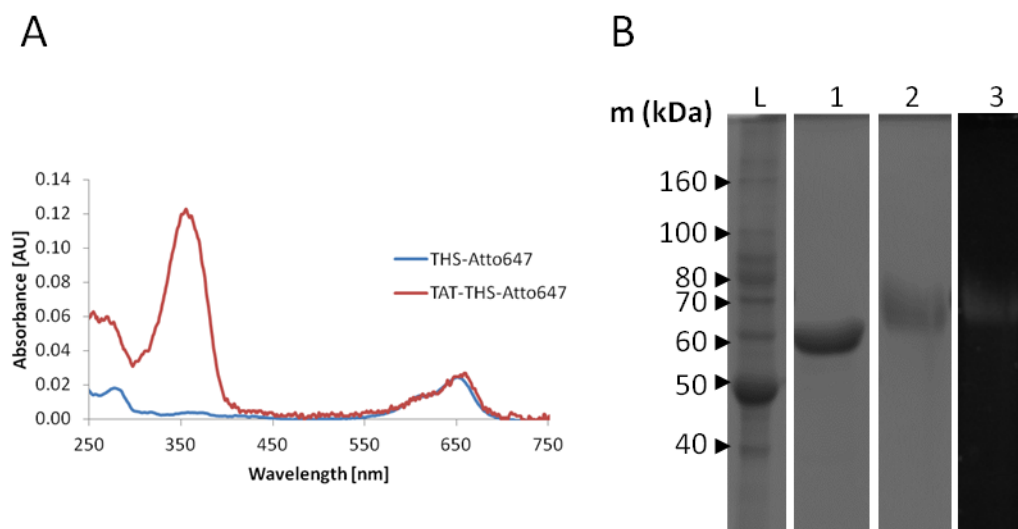


Fig. 7.20: (A) UV/Vis spectra of THS-Atto647 (blue) and TAT-THS-Atto647 (red). (B) SDS-PAGE of THS-Atto647 (1), TAT-THS-Atto647 Coomassie stained (2) and TAT-THS-Atto647 unstained UV-image (3).

TAT is known to facilitate uptake of cargo into PC-3 cells.²¹⁰ Therefore, these cells were incubated for 2h with TAT-decorated THS-Atto647, THS-Atto647, or free dye, and subsequently analyzed by flow cytometry (Fig. 7.21). The median fluorescence of the cells with TAT-THS-Atto647 increased

about 630 times compared to the background fluorescence of PC-3 cells. In comparison, unmodified THS-Atto647 showed only minor uptake by PC-3 cells, which manifested itself in a 2-fold increase in fluorescence. THS-Atto647 itself also induces a much higher fluorescent intensity (58.4-fold) than free dye. Additionally, cells were also incubated with TAT-THS-Atto647 for only 10 min to gain time-dependent uptake information. It is known, that TAT can translocate proteins within minutes into cells.²¹¹ In this time already 44 % of the interactions after 2 h occur. Hence, TAT-THS interacts with PC-3 cells in a fast manner.

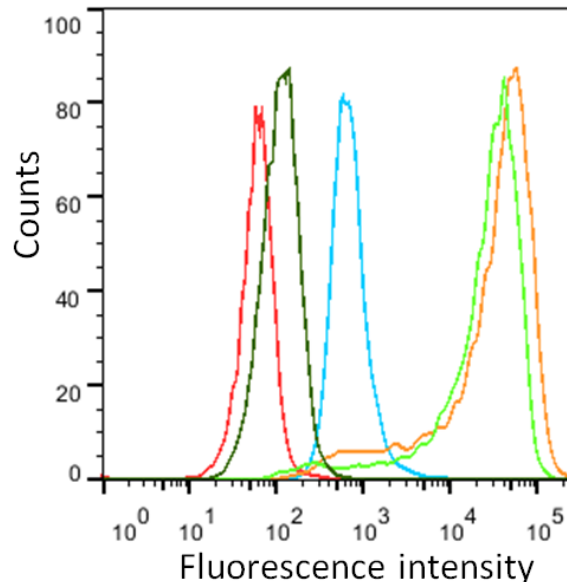


Fig. 7.21: Flow cytometry of PC-3 cells incubated with Atto647 (blue), THS-Atto647 (dark green), TAT-THS-Atto647 10 min (light green), TAT-THS-Atto647 2 h (orange) and cells alone (red).

The interaction of TAT-THS-Atto647 with PC-3 cells was additionally investigated by confocal microscopy (Fig. 7.22). After 30 min of incubation, TAT-THS-Atto647 was located at the cell membrane of PC-3 cells and had not yet entered the cells. After 2 h of incubation, TAT-THS-Atto647 was internalized into cells but not co-localized with acidic compartments or the nucleus. Concluding, the cell penetrating peptide is able to traffic the protein cage into these cells. After a phase where TAT-THS-Atto647 is located at the cell membrane, the protein cage is translocated to the cytosol. Taking into account that the general uptake mechanisms of TAT and its diverse cargo are still under scientific debate,²¹² it cannot be concluded whether TAT-THS enters the cells through the endosomal pathway and escapes the endosome, or if it reaches the cytosol by macropinocytosis.^{209, 213} However, we showed that TAT is capable to induce interaction between the chaperonin THS and PC-3 cells within 10 min and translocate THS into the cytoplasm in less than 2 hours.

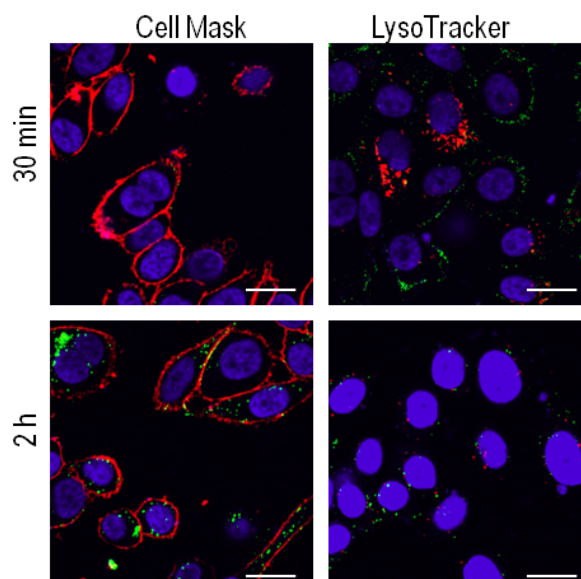


Fig. 7.22: CLSM images of PC-3 cells incubated with TAT-THS-Atto647 for 30 min and 2 h; TAT-THS-Atto647 (green), nucleus (blue), left: cell membrane (red), right: acidic compartments (red); scale bars: 20 μm .

7.2.7 VEGF-THS

Vascular endothelial growth factor (VEGF) is an important signaling protein for the process of new vessel forming (angiogenesis). As its name implies, VEGF stimulates the division and migration of endothelial cells. In tumors, VEGF is often up-regulated to ensure a sufficient supply of nutrients by newly formed blood vessels. Different drugs are on the market (e.g. Avastin) or in trials to either inhibit VEGF or to block its receptor (VEGFR).¹ We used VEGF as targeting moiety for VEGFR expressing human umbilical vein endothelial cells (HUVEC).

We modified VEGF with a ten-fold excess of S-HyNic, which then was conjugated in a three-fold excess to FB-THS-Atto647 (Fig. 7.23).

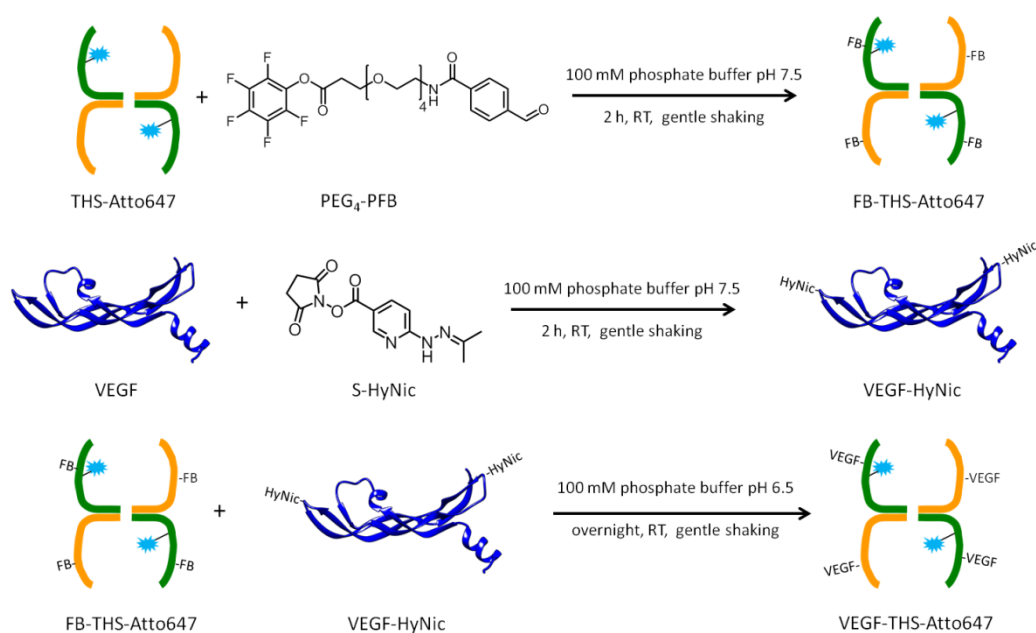


Fig. 7.23: Scheme of the conjugation of VEGF to THS-Atto647.

From UV/Vis measurement a modification of 0.5 VEGF per THS was calculated (Fig. 7.23 A). Flow cytometric studies revealed an enhanced interaction of VEGF-THS-Atto647 with HUVEC compared to THS-Atto647. HUVEC cells treated with VEGF-THS-Atto647 reveal two peaks; one at the same fluorescence at the main peak from THS-Atto647 and a peak at higher fluorescence intensity, indicating that some HUVEC cells have not up regulated VEGFR. In contrast, no enhanced uptake of the VEGF modified THS was seen with CHO-K1 cells, which do not express VEGFR (Fig. 7.23 B & C).

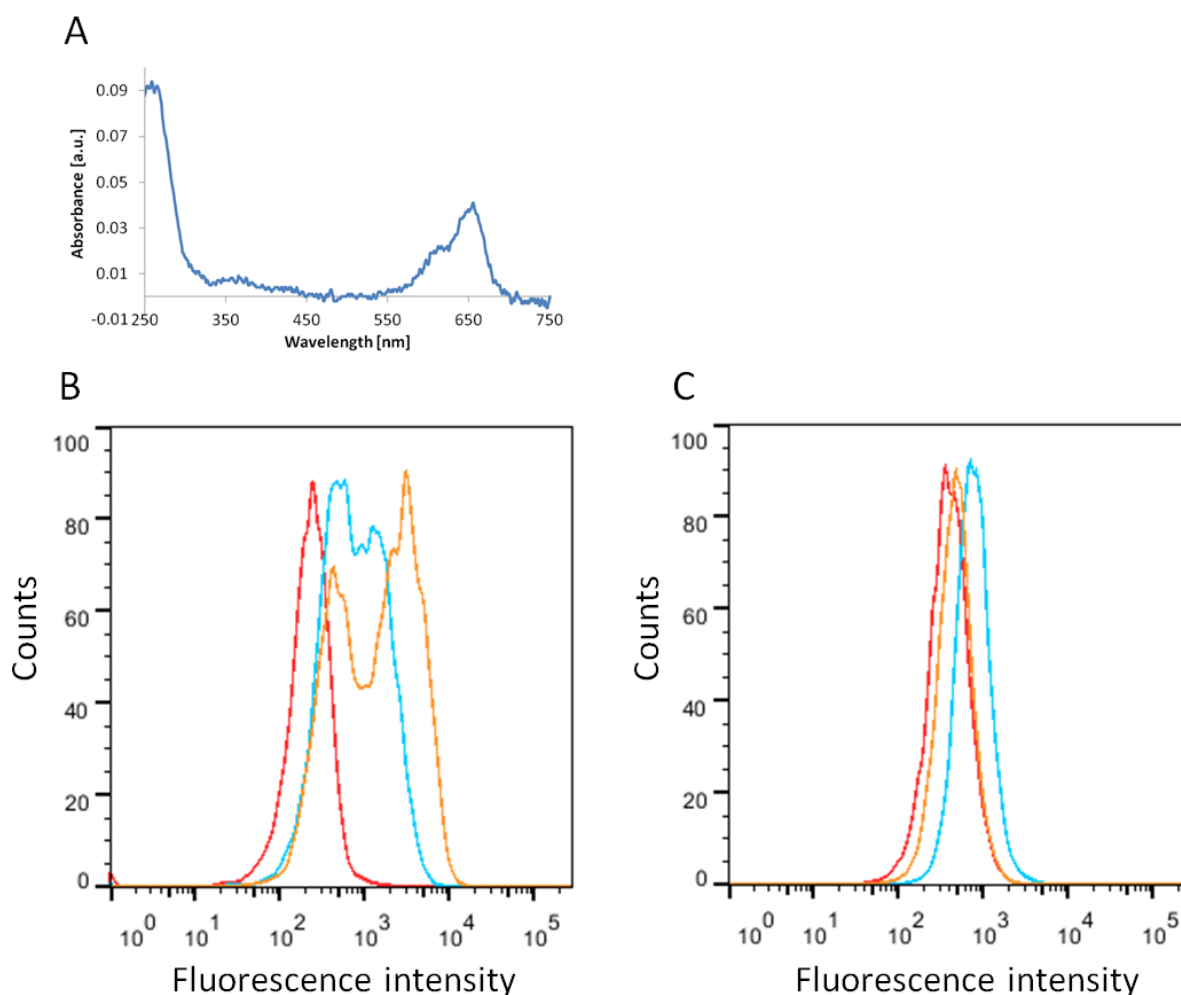


Fig. 7.24: (A) UV/Vis spectrum of VEGF-THS-Atto647. Flow cytometry of HUVEC (B) and CHO-K1 (C) cells incubated with THS-Atto647 (blue), VEGF-THS-Atto647 (orange) and cells alone (red).

From these results of the interaction of VEGF-THS with HUVEC and CHO-K1 cells, we suggest that VEGF-THS selectively interacts with the VEGFR presenting HUVEC, but not with CHO-K1 cells. However, due to high cost of VEGF and problems with the handling of HUVEC cells, this approach could not be further pursued. A cheaper alternative to VEGF protein would be small peptides, also binding to VEGFR.²¹⁴

7.3 Conclusions

To obtain an effective NDDS, the interaction between the NDDS and specific cells must be boosted. This can be achieved by attaching cell targeting or penetrating moieties to the NDDS. Hence we conjugated different moieties to THS and studied their interactions with different cells by flow cytometry and some also with fluorescence microscopy. To do so, we first conjugated the fluorescent

dye Atto647-mal to the cysteines in the cavity of THS. The conjugation was confirmed by UV-Vis spectroscopy, FCS and SDS-PAGE. From flow cytometrical interaction studies of THS-Atto647 with different cell lines (HeLa, MCF-7, CHO-K1 and PC-3) we could show, that THS-Atto647 interact less with cells as the free Atto647 dye does. This is supporting the concept that THS is shielding molecules, which are bound to the interior of THS' cavity, from the environment and prevent interaction with it.

We conjugated BBN with two different ethylene glycol spacers to THS and examined their interaction with PC-3 cells. The biotin-THS conjugate was tested on HeLa and CHO-K1 cells, SST-THS on MCF-7 and CHO-K1, FA-THS on HeLa cells, and cRGDfC-THS on MCF-7 and U-87 MG cells. None of these studies showed any enhanced interactions of the modified THS with the cells. However, it was found that THS lacking a targeting or penetrating ligand is translocated into the cytosol of U-87 MG to a high extent, making U-87 MG cells a target for THS based NDDS. The attachment of TAT peptides to THS drastically enhanced the interaction of THS with PC-3 cells. Within less than 10 min TAT-THS binds to the cells and moves into the cytosol within less than 2 hours. Thus, TAT can be used for fast translocation of THS into cells. By modifying THS with VEGF, it interacts specifically with HUVEC cells, but not with CHO-K1 cells. Thus, THS specifically targets U-87 MG cells. TAT enhances the uptake into cells, but in an unspecific manner and VEGF is for specific targeting of HUVEC cells.

8. Chaperonin-dendrimer conjugates for siRNA delivery

Parts of this chapter are submitted:

M.G. Nussbaumer, M. Rother, K. Renggli, M. Chami and N. Bruns
Chaperonin-dendrimer conjugates for siRNA delivery

8.1 Introduction

In this study THS was used as a nano-vehicle for siRNA delivery. THS features one of the largest pores within cage proteins (~ 8 nm) (see chapter 2.2 *Structure of the group II chaperonin from Thermoplasma acidophilum (Thermosome)*).^{105, 115, 116, 177} This property allows macromolecules to diffuse in and out of the cavities without affecting the structure of THS. Additionally, the cavities of THS are able to host guest molecules up to around 50 kDa.¹⁰⁵ In this system, the cationic dendrimer 4th generation PAMAM was chosen to complex and stabilize siRNA inside the THS cavities. Advantages of dendrimers over linear or branched polymers are their monodispersity, uniformity, and the high number of functional end groups (see chapter 3.4 *PAMAM as siRNA delivery reagent*).⁶¹ In a comparison of the different generations of PAMAM, the generation 4 showed an optimal charge density for siRNA-complexation¹⁷¹ and lower toxicity than for higher generations.¹⁷⁰ With a diameter of around 4 nm⁵⁷ PAMAM G4 fits well into the cavities of THS, which has an inner diameter of about 8.6 nm.¹⁰⁵ By conjugating PAMAM into THS, a well-defined system is created with advantages over naked PAMAM. Not only are the end groups of PAMAM, which are prone to interact with cells and initiate uncontrolled uptake of PAMAM into cells,^{215, 216} shielded, but also the size is defined by THS (16 nm). In contrast siRNA complexed with PAMAM forms much larger (> 100 nm)⁶⁴ and polydisperse aggregates.^{171, 217, 218}

Based on this background, a novel chaperonin based protein-polymer nano-vehicle for siRNA delivery was created (Fig. 8.1). To this end, PAMAM was conjugated to the cysteines of THS, which are located at the inner wall of the THS' cavity.⁷⁸ We examined the conjugation of PAMAM into THS and its capability to bind and stabilize siRNA. The uptake of THS into different cell lines was quantified and promoted by modifying THS with the cell penetrating peptide TAT.²¹⁹ Lastly The RNAi effect of siRNA bound to THS-PAMAM and its TAT modified equivalent were tested *in vitro*.

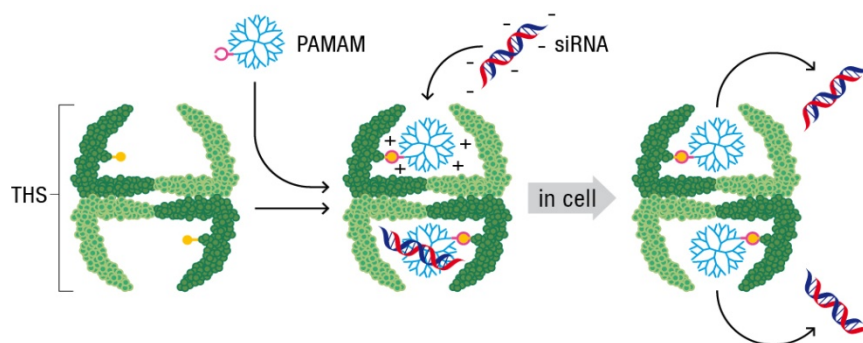


Fig. 8.1: Schematic diagram of conjugation of dendrimer into the protein cage

8.2 THS-PAMAM conjugation

For the conjugation of PAMAM into the cavity of THS, a linker was chosen that forms a resonance-stabilized hydrazone bond between THS and PAMAM (Fig. 8.2), which is stable in pH values ranging from pH 2 - 10. To this end, cysteines (Cys) in the THS cavities were first reacted with the

heterobifunctional linker maleimido trioxa-6-formylbenzamide (MTFB).⁷⁸ 3.8 ± 0.2 Cys per THS were modified with MTFB, as determined by UV-spectroscopy (Table 8.1).

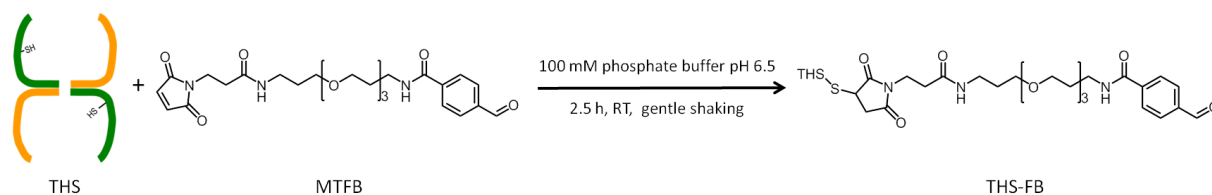


Fig. 8.2: Chemical pathway of the modification of THS with MTFB.

Wavelength [nm]	Absorbance	ϵ [$M^{-1} cm^{-1}$]	c [μM]	MSR
280	0.036	210880	1.7	3.8
350	0.012	18000	6.5	

Table 8.1: UV absorbance measurement of THS-MTFB reacted with 2-hydrzinyopyridine for molecular substitution ratio (MSR) calculation.

In parallel, PAMAM was modified with a heterobifunctional linker featuring an activated ester and a 6-hydrazino-nicotinamide group (HyNic) (Fig. 8.3). The degree of modification could be controlled by the concentration of HyNic in the reaction mixture (Fig. 8.4). For further experiments, reaction conditions were chosen that resulted in approximately four HyNic groups per PAMAM, which means that about 1/16 of the dendrimer's primary amine groups were modified.

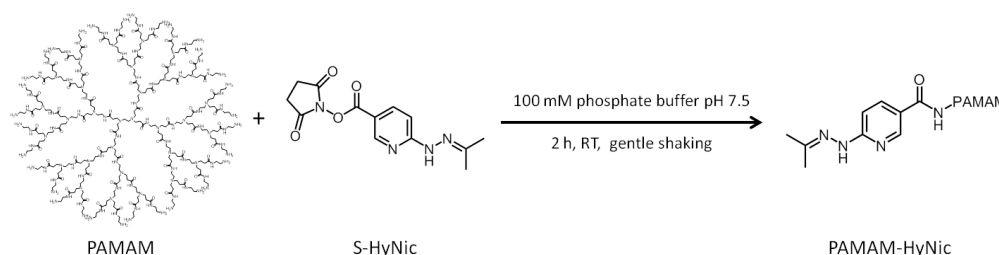


Fig. 8.3: Chemical pathway of the modification of PAMAM with HyNic.

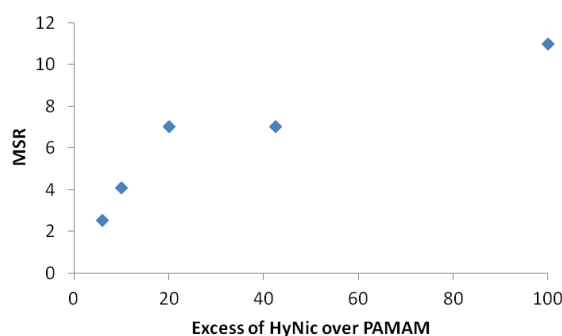


Fig. 8.4: Modification degree of PAMAM with HyNic depending on the excess of HyNic over PAMAM during the modification.

In a final step, THS-MTFB was incubated with an excess of PAMAM-HyNic overnight to conjugate PAMAM into the THS (Fig. 8.5). A kinetic study of the conjugation reaction showed that 80% of the THS-PAMAM bonds formed within 3 h (Fig. 8.6). The protein-polymer conjugate was purified by size

exclusion chromatography (Fig. 8.7 A). It eluted as a high molecular weight fraction at an elution volume of 35 ml and could be detected simultaneously at 280 nm (resulting from the absorbance of THS-PAMAM) and at 350 nm (resulting from the bisarylhydrazone linker). A second fraction, containing the excess of PAMAM that was not bound to THS eluted at a volume of 65 ml and absorbed only on the 280 nm channel. The baseline-separated elution peaks illustrate the successful separation of THS-PAMAM conjugate from free PAMAM. The UV/Vis spectrum of the conjugate shows the absorption of proteins and PAMAM at 280 nm and a peak at 354 nm that is characteristic for the bisarylhydrazone linker (Fig. 8.7 B). It was calculated from such spectra that 3.8 ± 0.2 hydrazone bonds per THS formed, suggesting that all of the modified cysteines in the THS were linked to PAMAM.

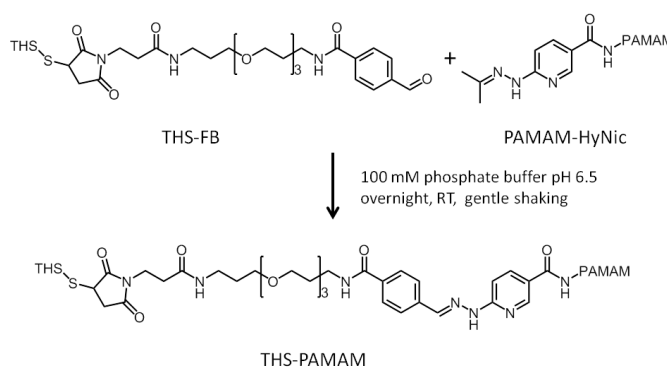


Fig. 8.5: Scheme of the linkage of PAMAM into THS.

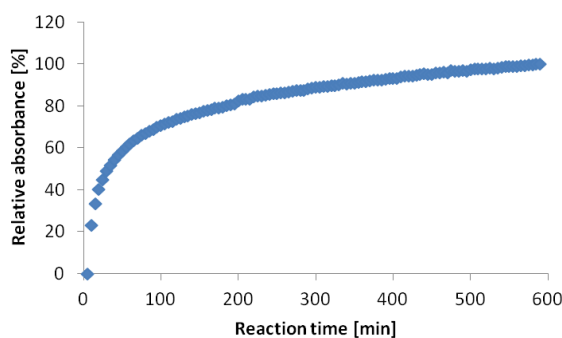


Fig. 8.6: Kinetics of THS-PAMAM formation tracked with UV/Vis absorbance at 350 nm during the reaction of THS-MTFB with PAMAM-HyNic.

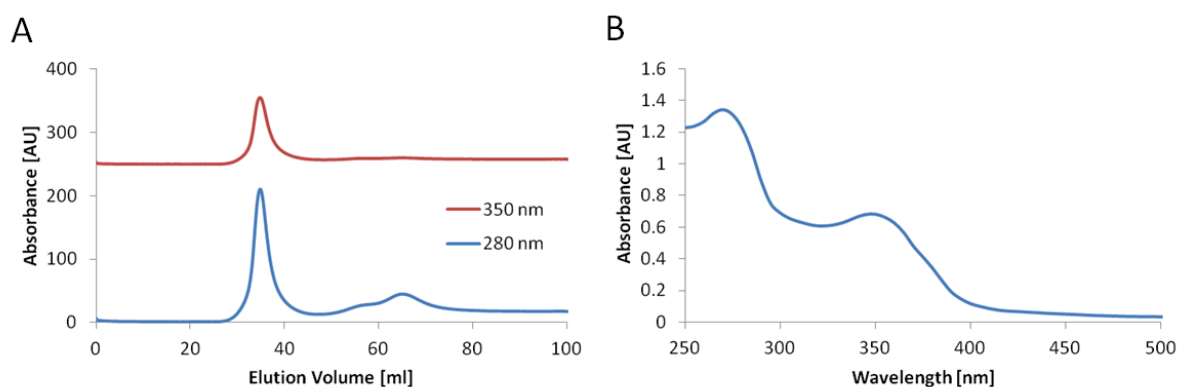


Fig. 8.7: (A) Size exclusion chromatogram of the purification of THS-PAMAM from excess of PAMAM at 280 nm (blue) and 350 nm (red). (B) UV/Vis spectrum of THS-PAMAM.

The change in molar mass of THS subunits due to PAMAM conjugation was analyzed with SDS-PAGE (Fig. 8.8 A). The THS subunits have a molecular weight of approx. 58 kDa. PAMAM exhibits a smeared band with a maximum slightly above 20 kDa. THS-PAMAM shows additional smeared lines at higher molecular weight than the THS subunits. In order to distinguish whether these new bands originate from PAMAM, the dendrimer was modified with an UV-active dye (Atto647) and conjugated into the THS. While the THS subunits are not visible in the UV image of the gel, most of the new bands in the conjugate are (Fig. 8.8 A). Therefore, it can be concluded that PAMAM is covalently bound to THS subunits. Moreover, the gel shows that there was no free PAMAM in the THS-PAMAM solutions. In order to assess the location of the dendrimer in the conjugates, gold nanoparticles were bound to PAMAM that was then conjugated to THS. Cryo-TEM revealed gold nanoparticles (AuNP) within the THS, confirming that the dendrimer was encapsulated into the protein cage (Fig. 8.9 C). Native polyacrylamide gel electrophoresis (PAGE) (Fig. 8.8 B), transmission electron microscopy (TEM) (Fig. 8.9 A) and cryo-TEM (Fig. 8.9 B) reveal that the integrity of the protein cage was not affected by the conjugation of PAMAM.

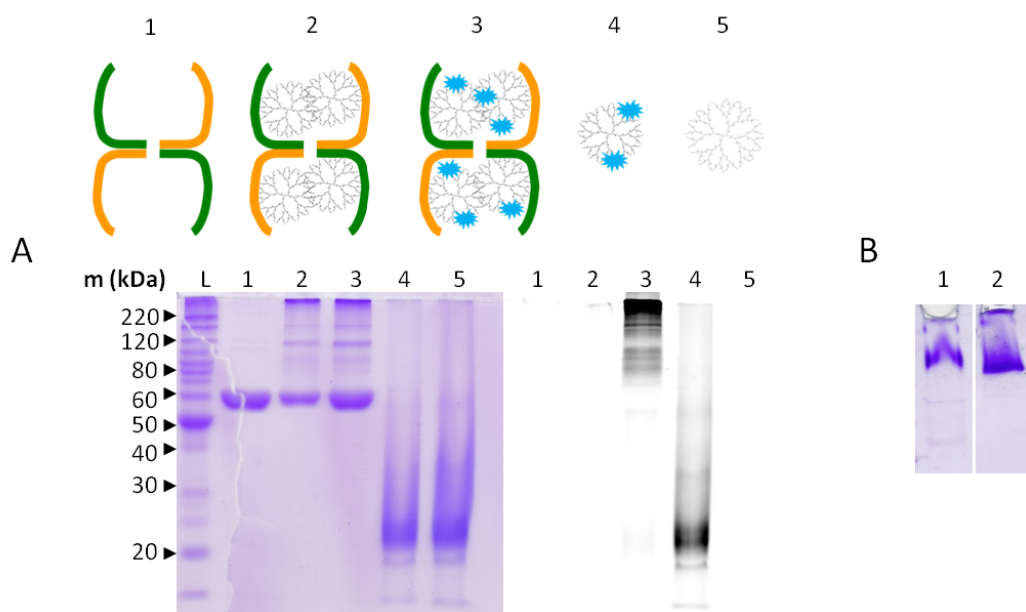


Fig. 8.8: (A) SDS-PAGE of THS (1), THS-PAMAM (2), THS-PAMAM-Atto647 (3), PAMAM-Atto647 (4) and PAMAM (5), stained with Coomassie Blue (left lanes) and inverted fluorescence image (right lanes). (B) Native PAGE of THS (1) and THS-PAMAM (2).

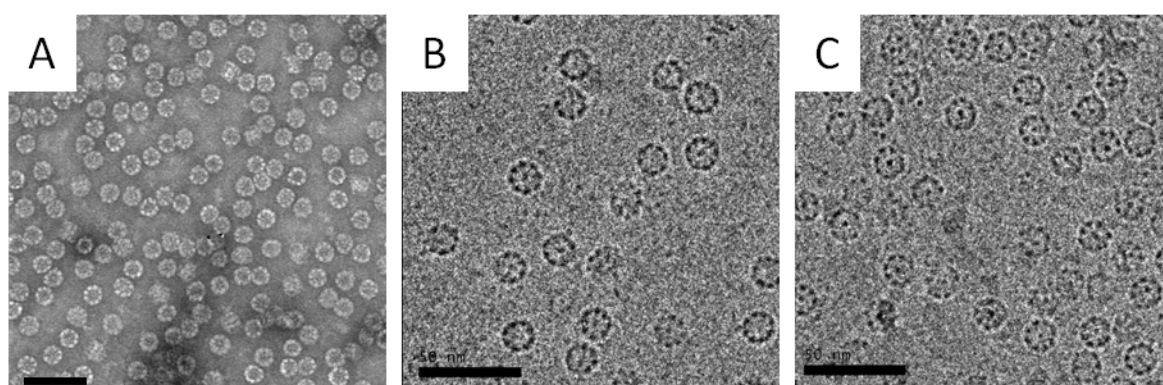


Fig. 8.9: (A) TEM image of THS-PAMAM. Cryo-TEM image of THS-PAMAM (B) and THS-PAMAM-AuNP (C). Scale bars: 50 nm.

As an additional technique to analyze the conjugation of PAMAM to THS, fluorescence correlation spectroscopy (FCS) was performed (Fig. 8.10). With FCS the diffusion time of a fluorescent particle through the confocal volume of the microscope is measured. The larger the labeled particle is, the bigger its diffusion time. From this, the size of the particle can be calculated. To measure the diffusion time, some free amine end groups of PAMAM were additionally modified with a fluorescent dye (Atto647-NHS) prior to its encapsulation into the THS, as it was done for SDS-PAGE analysis. The diffusion time of Atto647 was measured to be $\tau_D = 37 \mu\text{s}$ ($R_h = 0.58 \text{ nm}$), whereas Atto647 labeled PAMAM showed a diffusion time of $\tau_D = 190 \mu\text{s}$ ($R_h = 3.1 \text{ nm}$). A further increase of the diffusion time could be observed, after conjugation of the labeled PAMAM into the THS. A diffusion time of $\tau_D = 836 \mu\text{s}$ was measured for THS-PAMAM-Atto647, which corresponds to $R_h = 13.2 \text{ nm}$. The calculated hydrodynamic radii agree with similar previously reported results.²²⁰

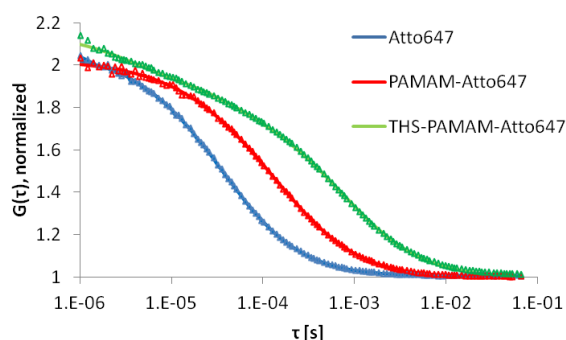


Fig. 8.10: Normalized FCS curve of Atto647 dye (blue), PAMAM-dye (red) and THS-PAMAM-dye (green) (raw data: triangles, fitted result: line).

We successfully conjugated PAMAM into the cavity of THS, without disrupting the quaternary structure of THS. During the conjugation the ratio of HyNic-modified PAMAM could be controlled, hence PAMAM featured about four HyNic, whereas the rest of the primary amine end-groups were not altered. From the size exclusion chromatogram during the purification and from SDS-PAGE studies we see a successful conjugation of PAMAM to THS. Additionally, we proved with TEM data that the cysteines, which are located at the inner wall of THS, act as anchoring points to place PAMAM in the interior of the THS cavity. From these and native PAGE data, we also show the integrity of THS after PAMAM conjugation. This allows us to go a step further and investigate the ability of the protein cage-polymer conjugate THS-PAMAM to bind and protect siRNA.

8.3 THS-PAMAM-siRNA

Since the conjugation of PAMAM into the cavity of THS was successful, the interactions of THS-PAMAM conjugates were of great interest for binding and delivering siRNA THS-PAMAM for siRNA delivery. We show binding of siRNA by the protein cage-polymer conjugate and furthermore we see a protective effect of THS-PAMAM for siRNA from RNase. Subsequently, the silencing effect of siRNA transfection in U87-MG cells by THS-PAMAM was quantified. To broaden the application range of THS-PAMAM as a siRNA delivery agent, we modified THS-PAMAM with TAT peptides, which translocate THS into PC-3 cells (see chapter 7.2.6 TAT-THS-Atto647). A significant silencing effect was measured with TAT-modified THS-PAMAM on PC-3 cells, whereas the unmodified protein-polymer conjugate did not show any silencing effects.

For siRNA delivery it is crucial to protect siRNA from degradation by RNases, as these enzymes are ubiquitously present in extracellular fluids.¹⁴⁵ Complexation of siRNA with PAMAM is a viable strategy to increase the stability of siRNA against RNases.²²¹ In order to test whether THS-PAMAM is also capable of protecting siRNA, we performed digestion experiments with RNase A. Since ethidium bromide only fluoresces when complexed to non-degraded siRNA, the degradation of siRNA could be determined with ethidium bromide-stained agarose gels (Fig. 8.12A). After 5 min of incubating free siRNA with RNase, the intensity of the siRNA band had already faded to below 50%. In contrast, the intensity of the band from THS-PAMAM-siRNA was still above 60% after an RNase incubation time of 40 min (Fig. 8.12 B). As a reference, siRNA was also complexed to unmodified PAMAM. Within the first 40 min of the experiment no markedly difference in siRNA degradation could be observed between siRNA complexed to THS-PAMAM or bound to PAMAM. These digestion experiments show that THS-PAMAM protects siRNA from degradation by RNase similar to free PAMAM.

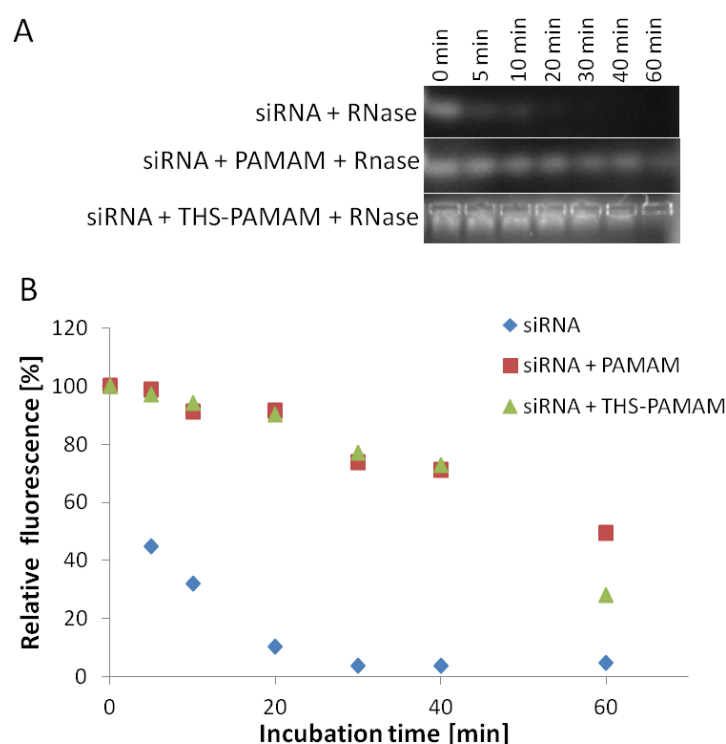


Fig. 8.13: (A) Digestion experiment with RNase A of siRNA, PAMAM-siRNA and THS-PAMAM-siRNA. (B) Fluorescence analysis of the digestion experiments: siRNA (□), PAMAM-siRNA (■) and THS-PAMAM-siRNA (▲).

8.3.2 siRNA transfection by THS-PAMAM

As THS is rapidly taken up by U-87 MG cells (see chapter 7.2.5 *cRGDfC-THS-Atto647*), it was tested if THS-PAMAM can deliver siRNA into the cytosol and trigger gene silencing. To this end, the protein-dendrimer conjugate was loaded with a siRNA that interferes with the messenger RNA of KIF11, a protein of the kinesin family. KIF11 regulates mitotic spindle formation during mitosis.²²² Depletion of KIF11 arrests the cell in the G2/M phase, so that a knockdown of KIF11 by siRNA will induce non-apoptotic, lysosomal cell death.²²³

KIF11 siRNA-loaded THS-PAMAM (100 nM siRNA) was added to U-87 MG cells and the cell viability was recorded after 72 h. As a negative control, THS-PAMAM was used to deliver scrambled siRNA to these cells. The final PAMAM concentration (from THS-PAMAM) was always under 1 μ M, where

PAMAM shows almost no toxicity for cells (see *SI Fig. 8.1* for 4th generation PAMAM toxicity).¹⁷⁰ THS-PAMAM/KIF11 siRNA reduced the viability of the cells to 79% ± 18% normalized to non-treated cells. THS-PAMAM with scrambled siRNA (*Fig. 4c*) did not affect the viability (106 % ± 28%). Thus, THS-PAMAM/KIF11 siRNA resulted in a reduction of U-87 MG cell viability by 25% (significance level $p = 0.029$) when compared to THS-PAMAM with scrambled siRNA (*Fig. 8.13*). These transfection results are comparable to other studies on KIF11 siRNA delivery, e.g. using lipid-coated poly(lactic-co-glycolic acid) nanoparticles as transfection agent.²²⁴ To set these findings into perspective, U-87 MG cells were transfected with KIF11 siRNA and scrambled siRNA using Lipofectamine 2000 (LF), a standard delivery agent for nucleic acids (*Fig. 8.13*).¹⁴⁹ The viability was reduced to 32% ± 4% when normalized to non-treated cells. However, LF with scrambled siRNA reduced cell viability significantly ($p = 0.0063$) to 48% ± 13%. Thus, the pronounced reduction in cell viability observed for siRNA-loaded LF is mainly due to the toxicity of the transfection agent, and only partially caused by KIF11 silencing. Gene silencing accounted for a reduction in cell viability by 34% ± 19%. In conclusion, the gene silencing efficiency of THS-PAMAM was slightly lower than the efficiency of LF. However, LF exhibited unspecific toxicity against the investigated cell line, while THS-PAMAM was not toxic (*Fig. 8.13*).

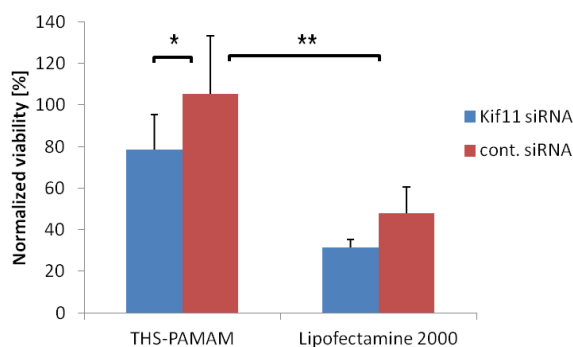


Fig. 8.14: Normalized viability of U-87 MG cells transfected with KIF11 siRNA (blue) or scrambled siRNA (red) with either THS-PAMAM or Lipofectamine 2000. (Two sided t-test; THS-PAMAM $n = 12$ each; Lipofectamine $n = 4$ each; *: $p < 0.05$; **: $p < 0.01$)

8.3.3 TAT-THS-PAMAM

To show the versatility of the protein cage as delivery platform and to perform siRNA-induced gene silencing in another cell type, THS-PAMAM was decorated with the cell penetrating peptide TAT. The peptide is known to facilitate the internalization of drugs, proteins, and nanoparticles.²⁰⁹ TAT was conjugated to the lysines of THS-PAMAM with a bisaryl hydrazone linker (*Fig. 8.14*). The newly formed bond between THS-PAMAM and TAT increased the UV-absorbance at 354 nm (*Fig. 8.15 A*), which made it possible to determine the amount of TAT bound to THS-PAMAM. On average, 6.7 ± 0.2 TAT peptides were conjugated to each THS-PAMAM. Addition of TAT to THS should increase the molar mass of a subunit by 2250 g mol^{-1} . This shift in molar mass can be observed in the SDS-PAGE analysis of the compound (*Fig. 8.15 B*).

8. Chaperonin-dendrimer conjugates for siRNA delivery

Innaugural dissertation
Martin G. Nussbaumer

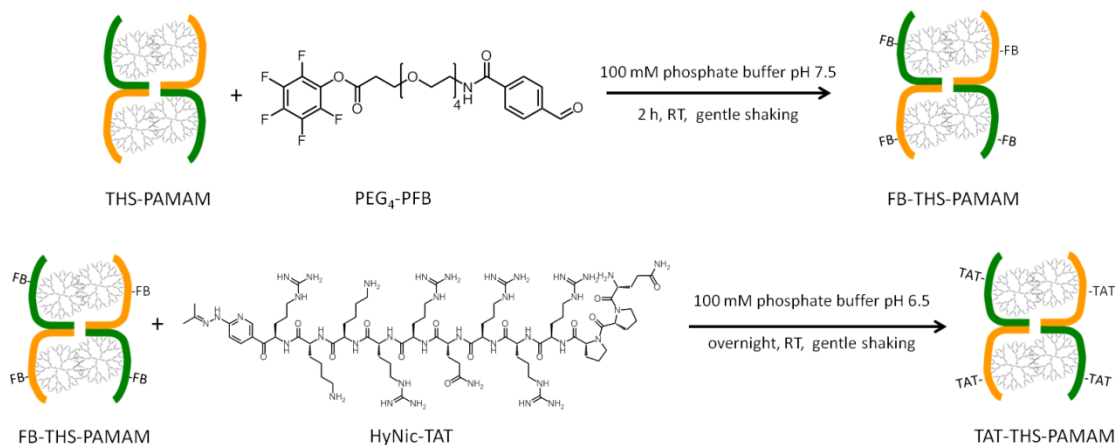


Fig. 8.15: Modification route of TAT-THS-PAMAM.

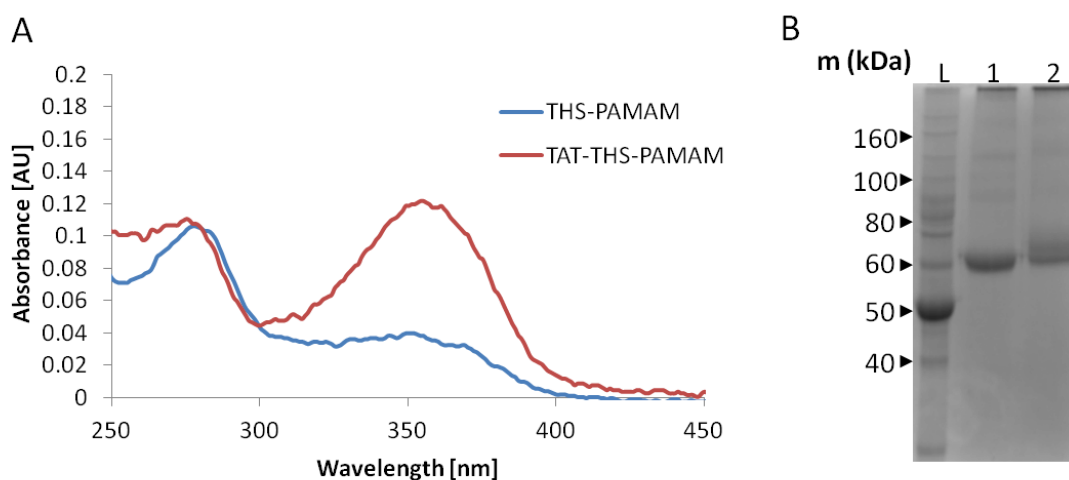


Fig. 8.16: (A) UV/Vis spectrum of THS-PAMAM (blue) and TAT-THS-PAMAM (red). (B) SDS-PAGE of THS-PAMAM (1) and TAT-THS-PAMAM (2).

8.3.4 siRNA transfection with TAT-THS-PAMAM to PC-3 cells

TAT-modified THS-PAMAM was used to deliver siRNA into PC-3 cells. To this end, TAT-THS-PAMAM was loaded with KIF11 siRNA and scrambled siRNA, respectively, and added to PC-3 cells. As control, the same experiments were performed with THS-PAMAM that lacked the cell penetrating peptide. The viability of cells incubated with KIF11 siRNA-loaded TAT-THS-PAMAM dropped to $69\% \pm 6\%$ compared to non-treated cells (Fig. 8.16). In contrast, the cell viability of THS-PAMAM without cell penetrating peptide enclosing KIF11 siRNA ($88\% \pm 5\%$) or scrambled siRNA ($90\% \pm 4\%$) varied only minimally. These results show that TAT-modified THS-PAMAM is able to transfect siRNA into PC-3 cells and that the presence of the cell penetrating peptide is crucial for this purpose. The performance of TAT-THS-PAMAM in delivering siRNA into PC-3 cells is roughly the same as THS-PAMAM delivering siRNA into U-87 MG cells.

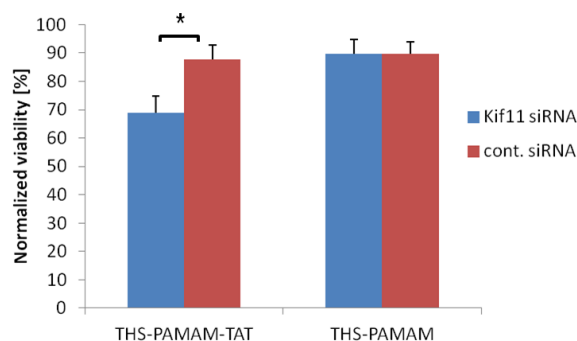


Fig. 8.17: Normalized viability of PC-3 cells transfected with KIF11 siRNA (blue) or scrambled siRNA (red) with either TAT-THS-PAMAM or THS-PAMAM. (Two sided t-test; TAT-THS-PAMAM $n = 4$ each; THS-PAMAM $n = 4$ each; *: $p < 0.05$)

8.4 Conclusions

siRNA is a promising drug because it can be used to silence the expression of diseases-related proteins. However, transfection agents have to be used to protect and traffic the therapeutic oligonucleotide into cells. We present a novel delivery platform for siRNA based on the protein cage THS. PAMAM was covalently bound into the THS in order to equip the protein with the ability to bind nucleic acids. THS-PAMAM stabilized siRNA against degradation by RNase. Significant siRNA-induced inhibition of proliferation in cancer cells was achieved with the THS-PAMAM transfection systems. In comparison to Lipofectamine 2000, the proliferation inhibition is slightly lower. However, LF is significantly more toxic to the cells than the protein-dendrimer conjugate.

THS-PAMAM conjugates offer several advantages over free PAMAM as transfection agent. The end groups of PAMAM are shielded, which can otherwise interact with cells and initiate uncontrolled uptake of PAMAM.⁶¹ Furthermore, the defined size of the THS-PAMAM nanoparticles fits well into the therapeutic size-window in which nano-carriers remain in the systemic circulation and are not affected by clearance through excretion in kidneys (≤ 10 nm) or by phagocytotic uptake and hepatic filtration (≥ 100 nm).¹⁷³ In contrast PAMAM-siRNA complexes form large (> 100 nm) and polydisperse aggregates.¹⁷¹ Decoration of THS with TAT is a first example for the versatility of the THS delivery platform. Protein cages can be easily modified by chemical or by genetic means with targeting ligands, such as RGD or folic acid.^{63, 194} This could enhance the specificity for certain cell types and would allow for a targeted drug-delivery with THS.

9. Reduction sensitive drug release

Parts of this chapter are in preparation for publication:

M.G. Nussbaumer and N. Bruns

9.1 Introduction

A key aspect for NDDS is a suitable drug release profile. To this end different strategies for a controlled drug release from protein cages were applied.⁶² One strategy is to conjugate the drug to the protein cage via thioether or amide bonds, which are then cleaved during biodegradation.^{68, 225} Other strategies use acidic conditions and high reductive potential as trigger for controlled release of drugs. During endocytosis the pH drops under pH 5. Under this condition hydrazone bonds are cleaved and the drug is released.^{75, 92, 226} Disulfide bonds are labile upon reduction. Inside cells mainly the tripeptide glutathione (GSH) maintains a reductive environment. Hence, drugs, which are bound to protein cages via a disulfide bond, are released in the cell.^{28, 68}

Previously we have shown that the cavity of THS is able to shield its cargo from interaction with the environment (see chapter 7. *Modification of THS with cell targeting ligands*). In this work, we coupled a dye as a model for a drug via a disulfide bond into the cavity of THS. Thereby the cysteines on the inner wall of the THS' cavity served as anchor point for the dye. As dye we chose Atto655. Electron donors like tryptophan or tyrosine efficiently quench the fluorescence of Atto655, which is a strong electron acceptor.²²⁷⁻²³⁰ Thus, Atto655 is only weakly fluorescent, when it is bound to THS, but is strongly fluorescent when the disulfide bond is reduced and Atto655 is released (*Fig. 9.1*). Hence, we could track the release of Atto655 from THS. We measured the release dynamics of Atto655 upon addition of GSH with FCS and compared the results with THS-Atto647. Atto647 is not quenched by THS and was conjugated to THS with a non-cleavable linker (see chapter 7.1 THS-Atto647 modification). Additionally, we tested the release dynamics of THS-SS-Atto655 and THS-647 in U87-MG cells (*Fig. 9.1*). This project is a pilot study to show triggered release of the THS' cargo and should show the versatility of THS as drug delivery system.

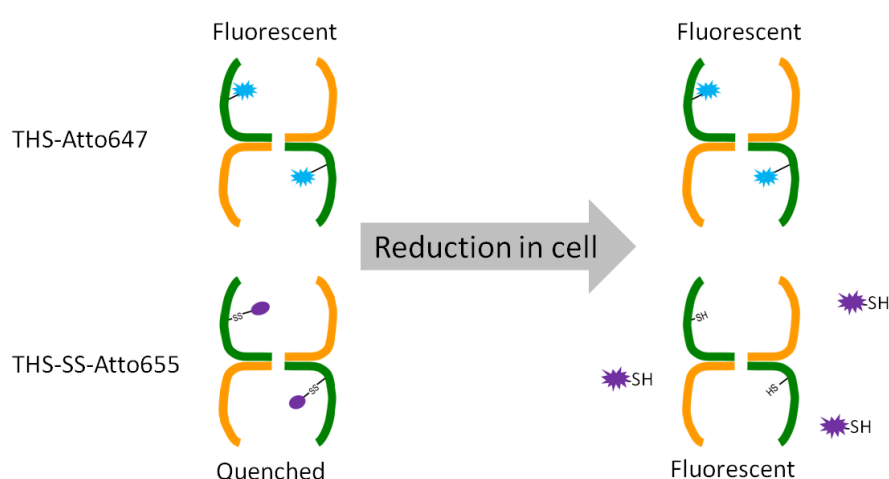


Fig. 9.1: Scheme of cargo release in the reductive environment of cells. We investigated the behavior of THS-Atto647 and THS-SS-Atto655 in the reductive environment of cells. While Atto655 is quenched, when bound to a protein, Atto647 is not quenched. This approach allows us to track the release of Atto655 from THS.

9.2 Results and discussions

To introduce a reduction sensitive linkage between THS and the dye (Atto655), we chose a similar chemistry as described in the modification of THS with PAMAM (see . 8.2 THS-PAMAM conjugation). We modified the cysteines of THS with a hetero-bifunctional maleimido-2-hydraziniumpyridine (MHP). On the other side, primary amino-Atto655 fluorescent dye (Atto655-NH₂) was modified with a hetero-bifunctional linker that features a succinimidyl activated ester (NHS) and a 4-formylbenzamide moiety, which are connected with a disulfide linkage (S-SS-4FB). This linker introduces a reduction sensitive disulfide bond, which is cleaved in the reductive environment inside cells. In the last step, Atto655-SS-FB was conjugated into THS-HP (Fig. 9.2).

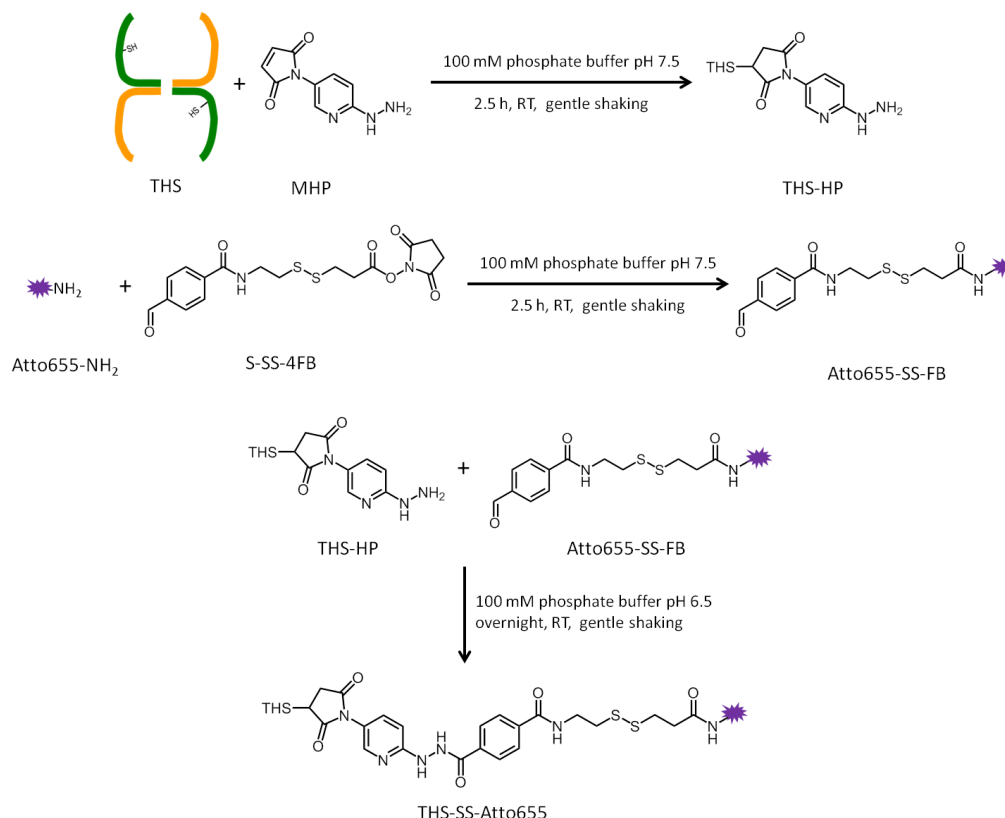


Fig. 9.2: Chemical pathway of the conjugation of Atto655-NH₂ into THS with inserting a reduction sensitive disulfide bond.

After modification of Atto655-NH₂ with S-SS-4FB, the product was purified by high-performance liquid chromatography (HPLC) (SI Fig. 9.1) and analyzed with liquid chromatography – electron spray ionization – mass spectroscopy (LC-ESI-MS). The educts S-SS-4FB and Atto655-NH₂ eluted in LC-ESI-MS around 7.3 min and 5.4 min, respectively (SI Fig. 9.2-3). The product had the main peak at around 7.0 min and the peaks of the educts were not present anymore. The peak around 7.0 min had a main mass of 865.4 m/z (M+H)⁺ in the positive mode measurement. This corresponds to the mass of Atto655-SS-FB (864.4 g mol⁻¹) (Fig. 9.3 A & B). The mass of 433.2 m/z (M+2H)²⁺ represents double charged species. Additionally, Atto655-SS-FB in combination with a sodium ion was found (887.4 m/z, M+Na)⁺. The additional masses of 352.4 g mol⁻¹, 279.1 g mol⁻¹ and 225.2 g mol⁻¹ are most likely fragmentation products, which can occur upon ion formation with ESI.²³¹ The mass of the modified Atto655 was also observed in negative mode (863.8 m/z, (M-H)⁻) (Fig. 9.3 A & C). It is not clear what the peak at 895.5 m/z represents.

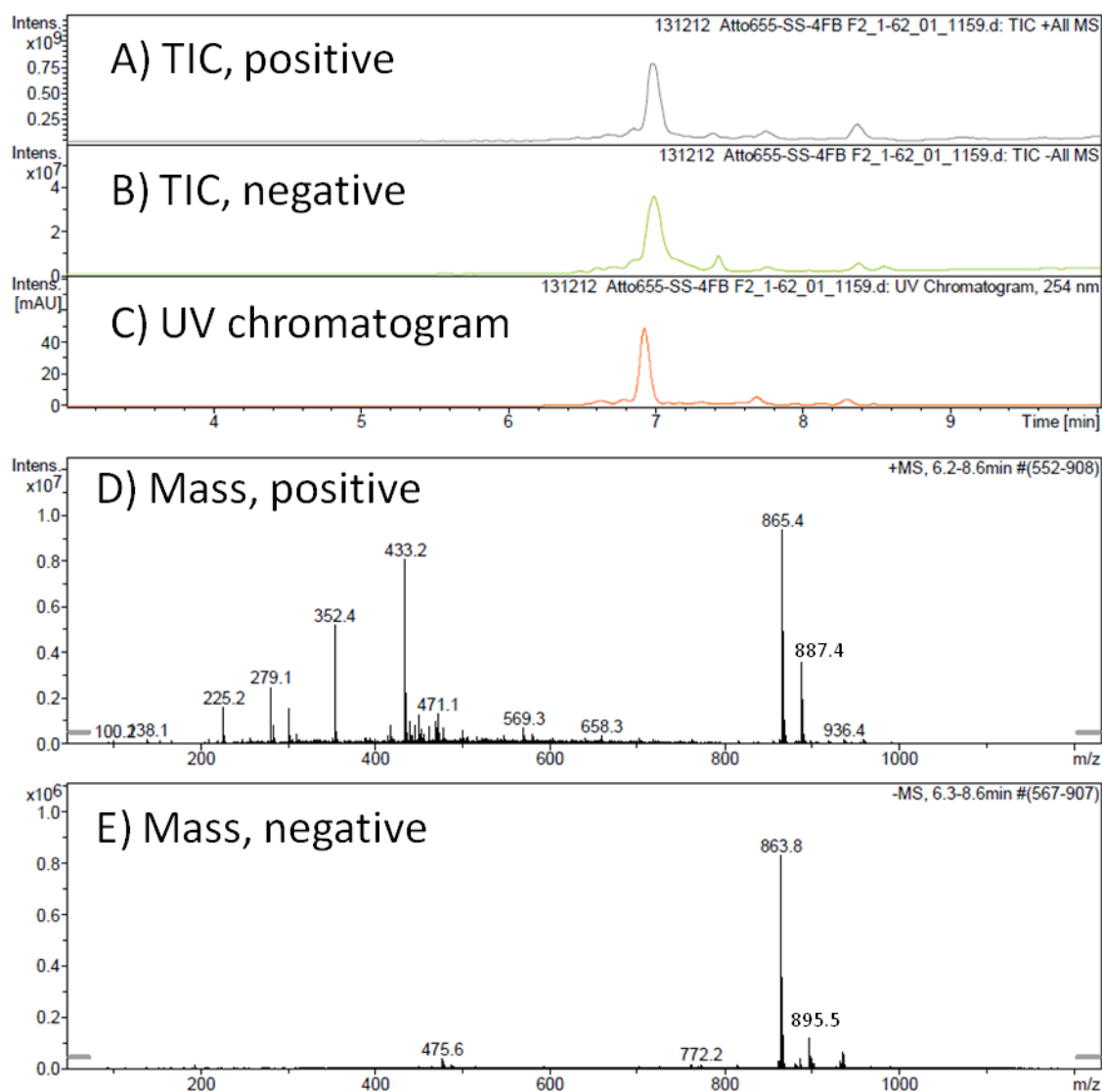


Fig. 9.3: Mass analysis with LC-MS of Atto655-SS-FB. Total ion current (TIC) in positive (A) and negative mode (B) and UV chromatogram at 254 nm (C); mass spectrogram of the elution peak from 6.2 – 8.6 min in positive mode (D) and negative mode (E).

Atto655 was conjugated into the THS by incubating a THS-HP with a 20-fold excess of S-SS-Atto655. The conjugate was then purified on a desalting column. From the absorbance at 280 nm and 663 nm, a ratio of 0.43 dye molecules per THS was calculated (Fig. 9.4). The formation of the bisarylhydrazone linker was confirmed by the presence of an absorbance band at 354 nm. However, its intensity is too low to allow for a reliable quantification of the number of linkers per THS. The conjugation of THS-Atto647 was done as reported in chapter 7. *Modification of THS with cell targeting ligands.*

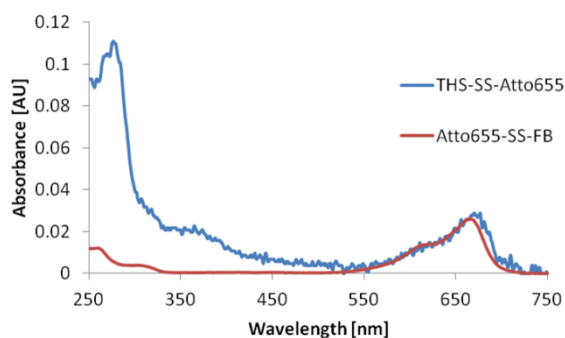


Fig. 9.4: UV/Vis spectrum of THS-SS-Atto655 and spectrum of Atto655-SS-4FB, normalized to the absorbance at 663 nm.

The quenching of Atto655 upon conjugation to a protein and the recovery of the fluorescence after cleavage from the protein was investigated with another model system BSA-SS-Atto655 (Fig. 9.5). To this end, the fluorescence of Atto655 and BSA-SS-Atto655 was measured in a reductive environment (10 mM glutathione) over time. Even though the dye concentration was the same for both samples, Atto655 bound to BSA exhibited a reduced fluorescence due to quenching. While the fluorescence of Atto655 slowly decreased over time, the fluorescence of BSA-SS-Atto655 increased. Indicating the release of Atto655 from BSA and recovery of the fluorescence of Atto655 (Fig. 9.5).

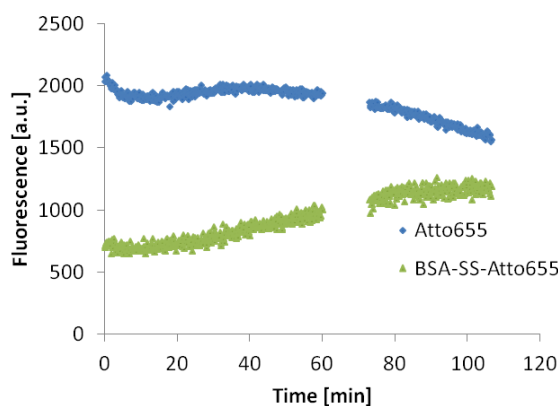


Fig. 9.5: Time dependent fluorescence emission of Atto655-NH₂ (blue) and BSA-SS-Atto655 (green) in a reductive environment. Excited at 663 nm and measured at 684 nm.

Even though the fluorescence of Atto655 was partly quenched when bound to proteins, it was possible to measure time-dependent fluorescence correlation spectroscopy (FCS) of THS-SS-Atto655 under reductive conditions to study the release behavior of the dye. In cancer cells the glutathione (GSH) concentration is up to 10 mM.²³² Therefore, we used 10 mM GSH for the reduction of the disulfide bond between THS and Atto655, which resulted in the release of the dye. A shift to lower diffusion times in the correlation curve of THS-SS-Atto655 was observed, starting after four hours (Fig. 9.6 A). Only a small shift was seen for THS-Atto647, where the bond between THS and the dye was not sensitive to reduction (Fig. 9.6 B). The percentage of free dye was determined from the FCS curves. About 45% of dye was released within 6 h in case of THS-SS-Atto655. This was not observed with the reductive stable linkage (Fig. 9.6 C). It has been shown that the release upon reduction of disulfide bonds with GSH is rather slow and takes several hours.²³³

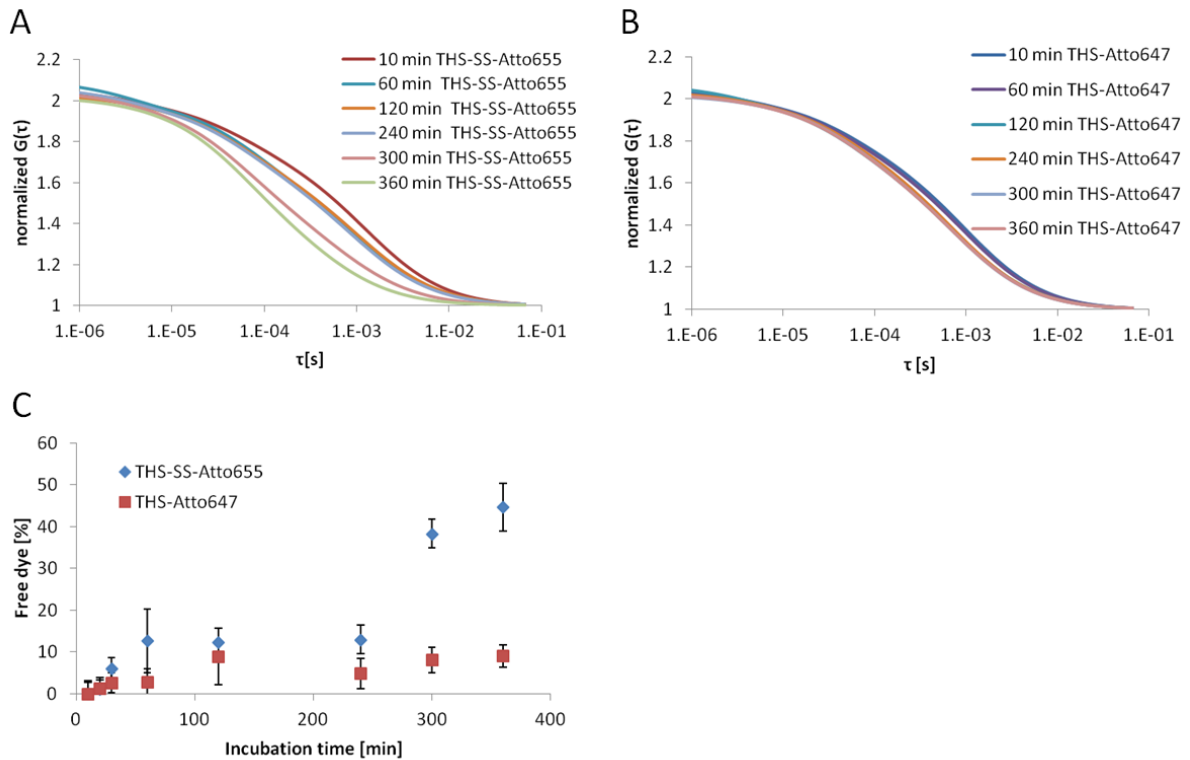


Fig. 9.6: Selected FCS curves of cargo release dynamics of THS-SS-Atto655 (A) and THS-Atto647 (B) in reductive environment (10 mM GSH); free dye fraction from fitted FCS-curves (C).

As aforementioned (see chapter 7. *Modification of THS with cell targeting ligands*), THS is taken up by U87-MG cells. These cells served as a model cell line to test the release of cargo that was bound to THS via a disulfide linker. We incubated U87-MG cells with the reduction-stable THS-Atto647 and the cleavable THS-SS-Atto655, respectively, for different times and subsequently measured the mean fluorescence intensity of the cells with flow cytometry (FC). Within an hour the fluorescence intensity of U87-MG cells incubated with THS-Atto647 increased to about 40% of the final value after four hours (Fig. 9.7 A & C), during this time the fluorescence of the cells incubated with THS-SS-Atto655 was still below 10% (Fig. 9.7 B & C). After two hours the fluorescence of cells with THS-Atto647 increased further to around 70%. The fluorescence intensity of cells with THS-SS-Atto655 showed a much higher intensity than an hour before (~50%). The fluorescence of THS-Atto647 is immediately detected by FC, whereas the fluorescence of THS-SS-Atto655 is seen with a delay, because Atto655 bound to THS is quenched and can only be seen, when Atto655 is released from THS. This could explain the delayed fluorescence of cells incubated with THS-SS-Atto655 as measured by FC.

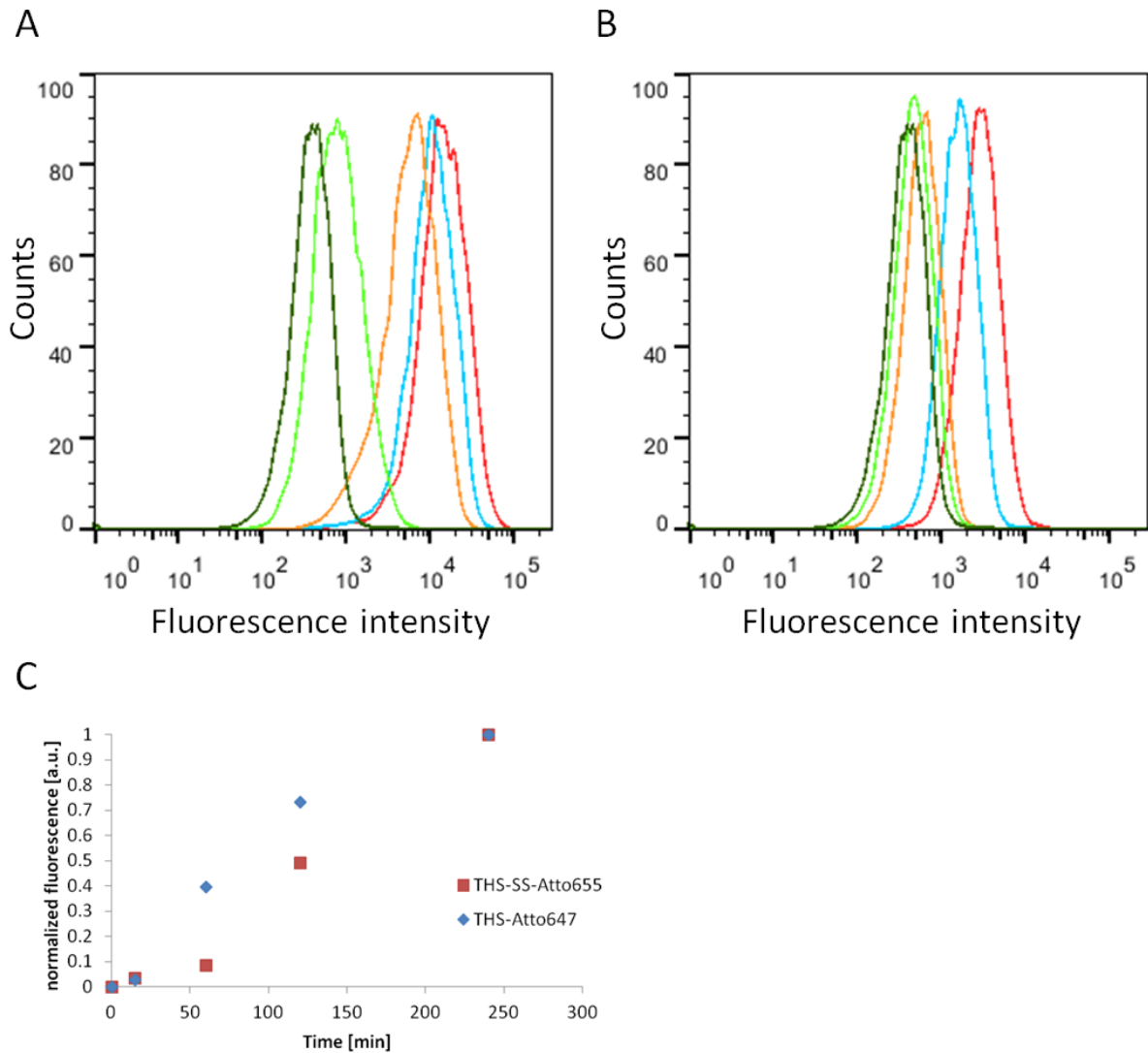


Fig. 9.7: Time dependent flow cytometric analysis of cell fluorescence upon incubation of U87-MG cells with THS-Atto647 (A) and THS-SS-Atto655 (B) for 15 min (light green), 1 h (orange), 2 h (blue), 4 h (red) and cells alone (dark green). (C) Plot of the normalized fluorescence from (A) and (B).

Further examination of the interaction between U87-MG cells and THS with the dye bound via reduction stable and cleavable linker was performed by confocal laser scanning microscopy (CLSM). THS-Atto647 can be seen in the cytosol already after 15 min. In contrast, Atto655 was only weakly detected after 15 min, indicating that the disulfide bond was not yet cleaved and therefore Atto655 was still quenched by THS. After two hours cells incubated with THS-Atto647 were crowded with dye. Incubated with THS-SS-Atto655, the cells exhibit also a high number of fluorescent spots, but less than with Atto647. The high protein concentration in the cell may also quench some of the Atto655 fluorescence. Therefore the fluorescence measured in FC and CLSM is lower for Atto655 than for Atto647. Cells incubated with free Atto655 reveal a different distribution pattern than Atto655 that was translocated by THS. After 15 min Atto655 was mainly located at the cell wall and after two hours also in the cytosol, but much less defined when compared to Atto655 that was bound to THS.

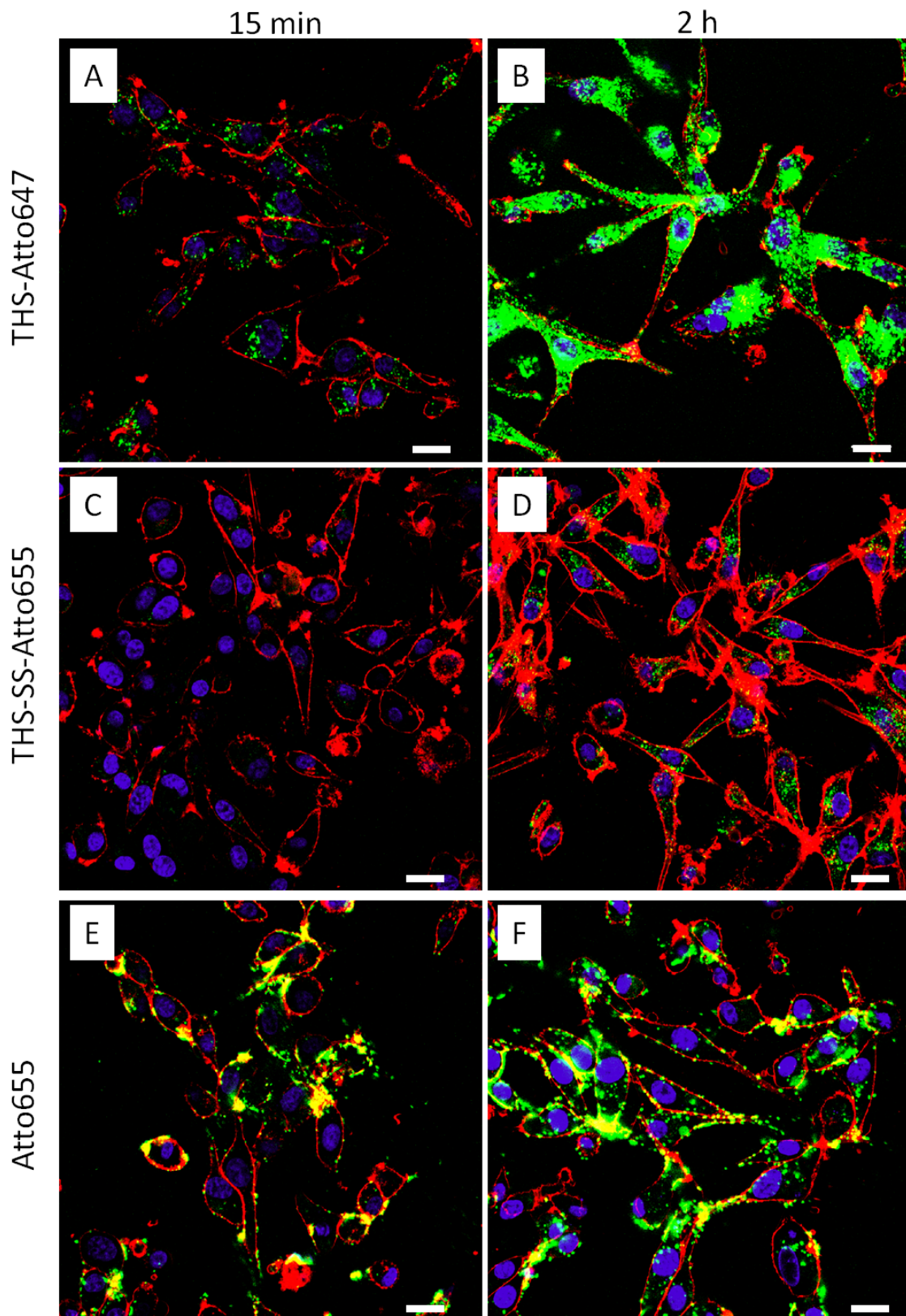


Fig. 9.8: CLSM images of U87-MG cells incubated with THS-Atto647 (A & B), THS-SS-Atto655 (C & D) or free Atto655 (E & F) for 15 minutes (A, C & E) and 2 hours (B, D & F). Atto647 and Atto655 (green), nucleus (blue) and cell membrane (red); scale bars: 20 μm .

9.3 Conclusions

In this pilot study we have successfully demonstrated a reduction-triggered release of Atto655, which was primarily bound to THS via a reduction sensitive disulfide bond. The release dynamics of Atto655 in an artificial reductive environment (with GSH) and in the natural reductive environment in cells was determined by FCS and FC. THS-Atto647 did not show any release of the dye, whereas the disulfide bond in THS-SS-Atto655 was cleaved by GSH. The reduction of the disulfide bond was observed after four hours in the artificial system. In cells the reduction of the disulfide bond was observed indirectly. Atto655 is mainly quenched when bound to THS but is fluorescent, when it is cleaved. Thus, the delayed observation of fluorescence for the cells treated with THS-SS-Atto655 indicated the release of Atto655 inside cells.

These results suggest that THS can serve as NDDS with triggered release of its cargo. For further studies, the cargo can be varied from small drug molecules (e.g. Dox) to big pharmaceutical peptides (e.g. Lys-Leu-Ala-Lys-Leu-Ala-Lys). Also, a combination of THS with PAMAM is possible, where the cargo is bound via disulfide bonds to PAMAM to increase the cargo density.

10. THS activity and conformation

Parts of this chapter are in preparation for publication:

M.G. Nussbaumer, K. Renggli, R. Urbani, N. Sauter, T. Pfohl and N. Bruns

10.1 Introduction

Bigotti et al.¹³³ measured the ATPase activity of the native THS and different other studies showed the conformational state of group II chaperonins depending on the stage of the ATPase cycle.^{116, 117, 134} To this end, different ATP analogues were used to mimic the hydrolytic states of ATP. For this reason, adenosine 5'-(gamma-thiotriphosphate) (ATP- γ -S) or Adenosine 5'-(β,γ -imido)triphosphate (AMP-PNP), which hydrolyze at a much lower rate than ATP, are used to represent the docking of ATP to the chaperonin. ADP-AIF_x and ADP-AIBe_x represent species, which underwent hydrolysis, but are not prone to leave the nucleotide binding pocket. The conformations of the chaperonins were investigated with different techniques like SAXS,¹²⁸ TEM,^{117, 234} native PAGE^{116, 235} and degradation assays with proteases followed by SDS-PAGE.^{116, 129, 236}

10.2 ATPase activity of THS

We investigated our mutated THS respective to its ATPase activity and conformational change depending on added ATP or its analogues. These investigations were especially done in regard to activity of enzymes conjugated into the cavity of THS and whether the activity of the enzyme is switchable depending on the added nucleotides (see chapter 11. *THS as controllable nanoreactor for biotransformations*).

The ATPase activity was measured with a dye based ATPase assay around the maximal activity of THS (55° C) and at 37° C. Additionally, the pH-dependence at pH 5.3 and 7.4 was investigated. The ATP hydrolysis rate of THS in pH 7.4 at 55° C was $6.8 \pm 0.5 \text{ ATP}_{\text{hyd}} \text{ THS}^{-1} \text{ min}^{-1}$. At lower temperature (37° C) the hydrolysis rate is reduced to $2.0 \pm 0.3 \text{ ATP}_{\text{hyd}} \text{ THS}^{-1} \text{ min}^{-1}$ (Fig. 10.1). Waldmann et al. determined the temperature dependence of ATPase activity at pH 7.5 of native THS. It was shown, that the activity has a maximum at the optimal growth temperature of its origin species *T. acidophilum*, which is 58° C.¹¹⁴ At this temperature native THS exhibit a hydrolysis rate of $3.6 \text{ ATP}_{\text{hyd}} \text{ THS}^{-1} \text{ min}^{-1}$. However, in a later study by Bigotti et al. about this issue, a hydrolysis rate of $3.1 \text{ ATP}_{\text{hyd}} \text{ ring}^{-1} \text{ min}^{-1}$ was measured at 55° C and pH 7.5, which corresponds to $6.2 \text{ ATP}_{\text{hyd}} \text{ THS}^{-1} \text{ min}^{-1}$.¹³³ Our results are comparable to this result. Especially, because we also measured the ATPase activity with a dye based assay as used in the Bigotti paper, whereas Waldmann et al. used a coupled enzyme assay. Interestingly, the ATPase activity results at 37° C corresponds quite well to the results of Waldmann et al., where they measured about $1.8 \text{ ATP}_{\text{hyd}} \text{ THS}^{-1} \text{ min}^{-1}$. The ATPase activity of THS at 37° C was not measured by Bigotti. The Bigotti paper did not refer to Waldmann's results.

At lower pH condition (pH 5.3) only at 55° C some ATPase activity was detected. However, the error was bigger than the actual value ($0.3 \pm 0.4 \text{ ATP}_{\text{hyd}} \text{ THS}^{-1} \text{ min}^{-1}$). At 37° C no ATP activity could be determined.

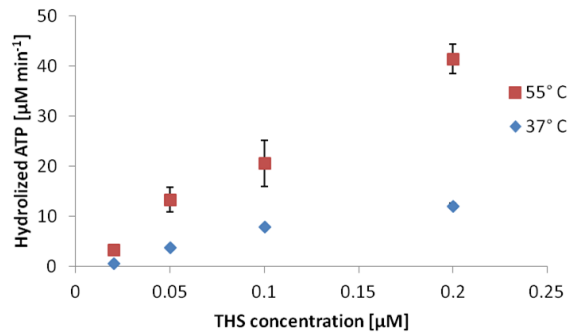


Fig. 10.1: ATPase activity of THS in Tris buffer pH 7.4 at 55°C (red) and 37°C (blue).

10.3 Conformational analysis of THS depending on ATP and its analogues

10.3.1 Native gel analysis

It has been shown that conformational changes upon addition of different nucleotides of some group II chaperonins can be detected with native PAGE. A closed conformation results in a further migration of the proteins in the gel. This was reported with the eukaryotic chaperonin TRiC²³⁷ and a chaperonin from the archaea *Methanococcus maripaludis* (Mm-Cpn).^{116, 238} ATP and ATP-AIFx induces a closed state of the chaperonin. However, only ATP-AIFx induces the characteristic faster electrophoretic migration on native PAGE gels.¹¹⁶

In our studies, we could not observe any of these effects. THS incubated with either EDTA (apo-state, open conformation), ATP (closed or bullet shape), ATP-AIFx (closed) or ATP-γ-S (partly closed) exhibited the same electrophoretic shifts on native gels (Fig. 10.2). Probably, THS has other properties as other chaperonins and this method is not suitable to detect the conformational changes of THS.

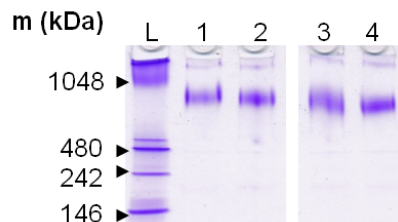


Fig. 10.2: Native PAGE of THS incubated with EDTA (1), ATP (2), ATP-γ-S (3) and ATP-AIFx (4).

10.3.2 Degradation assay

Another method for the determination of the conformational state is based on proteolysis. For this purpose, the chaperonins with different nucleases are incubated with proteases, e.g. proteinase K or thermolysin. The helical protrusions at the apical side of the THS subunits are vulnerable to digestion by proteases. In an open conformation the protrusions are accessible to the proteases, but in a closed state the protrusions form a lid and are therefore not accessible anymore for proteases. Thus chaperonins are partly protected from proteolytic degradation in their closed conformation.^{116, 129, 134, 236, 237} The most protective effect on TRiC had ATP-AIFx followed by ATP, suggesting that ATP-AIFx closes both rings of the chaperonin, whereas ATP closes only one ring at the time and opens up again after hydrolysis.¹¹⁶ Also the non-hydrolyzable AMP-PNP showed a protective effect on the chaperonin of *Thermococcus* strain KS-1.¹²⁹

We analysed the protective effect of ATP, ATP-AIFx and ATP- γ -S against degradation of THS by proteinase K.¹³¹ To this end, THS was incubated in ATP or its analogues for 30 min at pH 5.25 and subsequently proteinase K was added. After 10 min at room temperature, the reaction was stopped with PMSF and the samples were immediately analysed with SDS-PAGE. Upon degradation of THS with proteinase K (PK), the bands of THS' subunit faded. Especially, the α -subunit was impaired, whereas the β -subunit was much less degraded by PK (*Fig. 10.3*). Three main degradation products appeared, one at a mass around 27 kDa and two around 35 kDa. The PK was too low concentrated to be seen on the SDS-PAGE. THS with EDTA or ATP- γ -S was degraded the most. THS incubated with ATP-AIFx with low ATP concentration (1 mM) was degraded less, but still more than with ATP. Both THS-subunits were the most intact, when incubated with ATP-AIFx with high ATP concentration (6 mM) (*Fig. 10.3*).

Our experiments degrading THS with PK show similar results, as reporter for Mm-Cpn and TRiC.^{116, 131} THS in the open conformation is degraded the most, whereas ATP and ATP-AIFx is protecting the THS from degradation. As mentioned in the work of Reissmann et al.¹³¹, we also observed ATP concentration dependence, when mixed with AIFx. These findings are leading to the conclusion, that higher ATP concentration forces the THS to the closed conformation. THS is then fixed in the closed conformation with ADP-AIFx, which does not leave the nucleotide binding pocket. In contrast to the drastic protective effect of the non-cleavable AMP-PNP shown by Iizuke et al.,¹²⁹ ATP- γ -S does not have any influence on the degradation of THS. However, the protective effect on THS is lower than on Mm-Cpn or TRiC.^{116, 131}

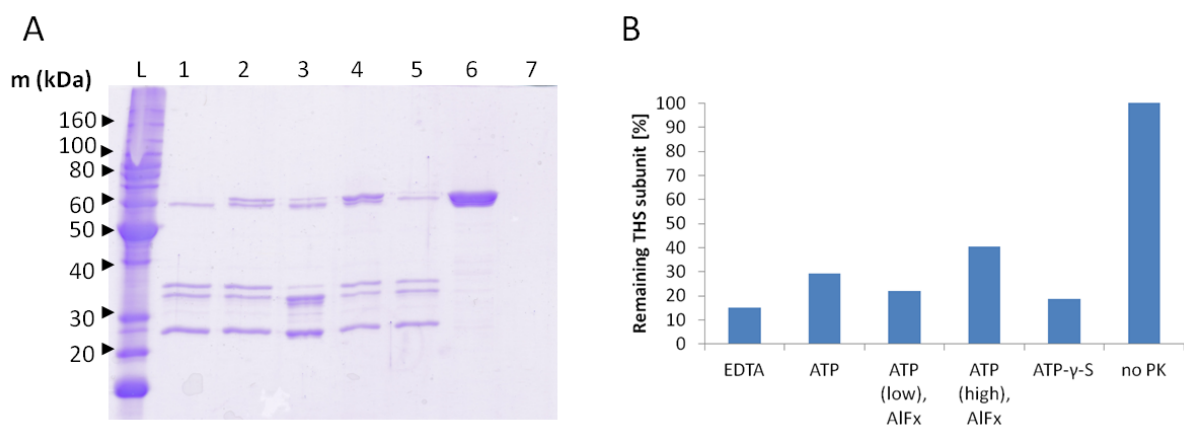


Fig. 10.3: (A) SDS-PAGE analysis of THS degraded with proteinase K incubated with EDTA (1), ATP (2), ATP-AIFx (1 mM ATP) (3), ATP-AIFx (6 mM ATP) (4), ATP- γ -S (5), no addition (6) and only proteinase K (PK) (7). (B) Intensity analysis of the intact THS' subunits from the SDS-PAGE gel.

10.3.3 SAXS analysis

Small-angle X-ray scattering (SAXS) represents a method for structural analysis of proteins. SAXS is based on elastic scattering of X-rays on electrons. Due to inhomogeneities of the electron density in a protein, the scattering of the beam at small angles provides structural information about the protein.²³⁹ In contrast to other X-ray scattering techniques, the sample can be in solution. The pair distance distribution function, which is calculated from a Fourier transform of the scattering curve, gives the distance between electrons in the sample and out of it the radius of gyration (R_g) can be calculated.^{239, 240} A set of different geometries with their respective scattering curves and pair distance distribution function is presented in *Fig. 10.4*.

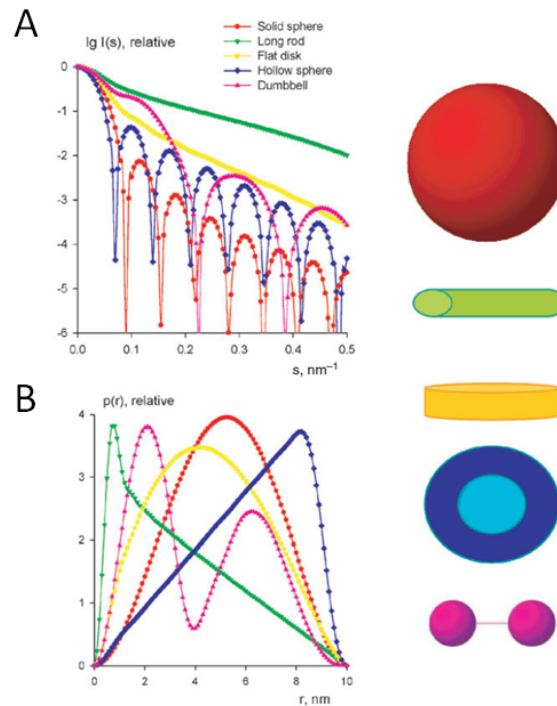


Fig. 10.4: Theoretical scattering curves **(A)** and their pair distance distribution functions **(B)** for different shapes of macromolecules. By courtesy of Svergun et al.²³⁹

It has been shown that wtTHS exhibits a displacement of the pair distance distribution function to higher radius upon adding ATP or ATP-AIFx, which indicates an opening of the wtTHS.¹²⁸ This actually disagrees newer findings, which show a closing upon ATP and ATP-AIFx binding.¹¹⁶ Later SAXS studies on other group II chaperonins exhibit a more compact structural conformation when ATP or ATP-AIFx is bound, indicating a closing of the chaperonins.^{134, 237}

We examined our mutant THS with SAXS on its structural conformation in absence of nucleotides and magnesium or in presence of magnesium and ATP or its analogue ATP-AIFx at room temperature and pH 5.25. SAXS data show a contraction of THS upon addition of either ATP or ATP-AIFx compared to absence of nucleotides and of magnesium (EDTA was added to bind magnesium traces) (Fig. 10.5). Analysis of the scattering profile resulted in a R_g of $88.0 \pm 0.2 \text{ \AA}$ for THS without nucleotides. With ATP and ATP-AIFx the R_g was calculated to $85.2 \pm 0.2 \text{ \AA}$ and $82.5 \pm 0.3 \text{ \AA}$, respectively. These values show a partly closing of the THS with ATP and an even further closing with ATP-AIFx. SAXS is a representation of the mean distribution of the electron density throughout a high number of particles. Therefore, it cannot be concluded, whether the particles with ATP have one fully closed ring or both rings are only partly closed. However, it seems that ATP-AIFx is closing the THS to a higher extend. This is in agreement to the findings of Frydman and co-workers.¹¹⁶ They reported a partly closing of one ring upon ATP binding, a complete closing when ATP is hydrolyzed and a reopening when ADP and Pi is released. Additionally, the two rings have a negative cooperation, thus chaperonins have a two-stroke ATPase cycle. Hence, in average THS is partly closed during the ATPase cycle. ATP-AIFx in high concentration (6 mM ATP) arrests both rings of THS in the closed conformation, resulting in a smaller R_g as THS with ATP. This behavior was also shown with another archaeal group II chaperonin, but with BeFx instead of AIFx.¹³⁴ However, the measured R_g values are about 10 \AA and 20 \AA bigger compared to the ones of the archaeal chaperonin from *Thermococcus* strain KS-1 and the eukaryotic TRiC, respectively.^{134, 237}

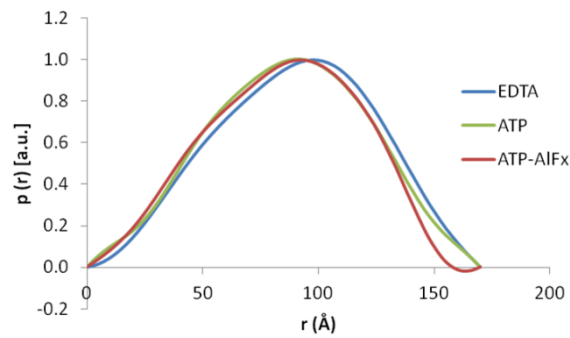


Fig. 10.5: Pair distribution functions of THS incubated with EDTA (blue), ATP (green) or ATP-AIFx (red).

10.3.4 TEM analysis of the conformational state of THS

Cryo-TEM was used to elucidate the conformational states of group II chaperonins by the groups of Saibil^{117, 241} and Baumeister²⁴². The analysis of the conformational state of the group II chaperonin Mm-cpn upon addition of ATP-AIFx showed that 35% were in the open conformation (open-open), 50% in the bullet conformation (open-close) and 15% in the closed (close-close) conformation.

To investigate the conformation of THS upon addition of EDTA or ATP-AIFx and $MgCl_2$, we incubated THS with the corresponding substrate at pH 7.4 and imaged the samples with TEM (Fig. 10.6 A & B). We picked 828 and 622 particles by hand for ATP-AIFx and EDTA, respectively, and classified them manually into the three categories open, bullet and closed conformation as it was done in the Saibil paper.¹¹⁷ We had to include two other categories: one for the non-determinable (n/a) and a category for the THS, which had their intermediate plane perpendicular to the grid (upright). In this position, it was not possible to classify them. The proportion of THS with non-determinable conformation was about the same for ATP-AIFx and EDTA (32% and 36%) (Fig. 10.6 C). The proportion of the upright position was lower with ATP-AIFx (20%) than with EDTA (35%). ATP-AIFx had only a small influence on the proportion of THS in the bullet conformation (6% vs. 4% for EDTA). The biggest difference was found in the proportion of open and closed states. With ATP-AIFx only 3% were in the open state, whereas 16% of THS were in the open state with EDTA. The proportion of the closed state behaved opposing. 39% were in the closed conformation with ATP-AIFx and 9% with EDTA (Fig. 10.6 C).

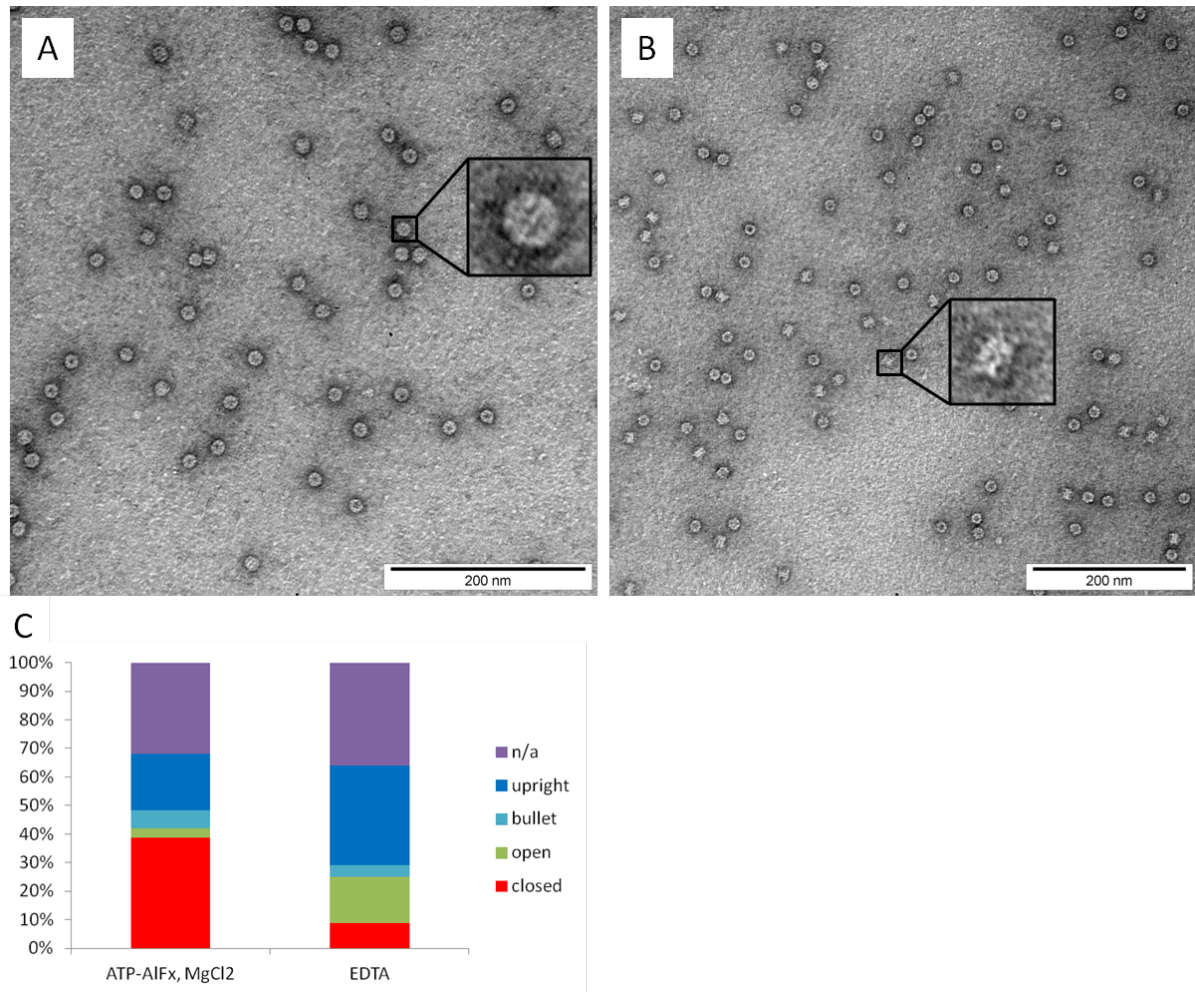


Fig. 10.6: TEM micrographs of THS incubated with ATP-AIFx (A) or EDTA (B), inlets are 4 times zoomed. (C) Manual classification of the conformation of THS upon addition of ATP-AIFx, MgCl₂ or EDTA: non-determinable (violet; n/a), upright position (dark blue), bullet conformation (light blue), open conformation (green) and closed conformation (red).

From these results, a shift of the proportion of open to closed conformation upon addition of ATP-AIFx was observed. However, it is difficult to manually classify THS in the different conformation from TEM micrographs. Unfortunately, we had too less TEM micrographs, which fitted the requirements for computational analysis of the particles. Hence, these results have to be treated with caution.

10.3.5 Conclusions on the THS' conformations

We investigated the conformation of THS with EDTA or with ATP and its analogues ATP-AIFx and ATP- γ -S. The biggest effect on THS was observed with ATP-AIFx. THS incubated with ATP-AIFx was least degraded by PK (6 mM ATP), exhibited the smallest structure in SAXS and seemed to shift the conformation proportion of THS to the closed state. Indicating, ATP-AIFx fixes THS in the closed conformation. ATP has a lower protective effect on the degradation of THS and revealed a slightly bigger structure as with ATP-AIFx in SAXS measurements. This behaviour suggests a bullet conformation or rather a closing and reopening activity of THS with ATP. THS with EDTA is mainly in the open conformation, which is confirmed by the results, that THS is degraded the most by PK and exhibited the biggest R_g . In addition, the open conformation was also found more often in TEM analysis than with ATP-AIFx. We have too less data to conclusively give a statement about the influence of ATP- γ -S on the conformation of THS. To gain more insight in the conformational changes

of the mutated THS, SAXS measurements with ATP- γ -S would be interesting. Additionally, cryo-TEM with computational analysis of THS with all the additions would be from interest. For further information, the experiments should also be done with AMP-PNP, a further ATP analogue, similar to ATP- γ -S.

11. THS as controllable nanoreactor for biotransformations

Parts of this chapter are in preparation for publication:

M.G. Nussbaumer, K. Renggli and N. Bruns

11.1 Introduction

Enzymes in nano-reactors have attracted much attention recently. Incorporating enzymes into nano-compartments has a drastic influence on the reaction kinetics and can lead to unique characteristics of the products.^{80, 243, 244} Besides liposomes and polymerosomes, protein cages represent an alternative approach to construct nano-reactors. The pores of protein cages are often stimuli responsive and can be switched between an open and a closed state.^{102, 103, 120, 245} This can be capitalized for switching between a higher and a lower state of permeability for substrates and therefore the enzymatic activity can be controlled.²⁴⁶ Most of the protein cages, which were used to create nano-reactors for enzymes, are based on virus like particles (VLP).^{70, 96, 97, 247} However, VLP have the drawback that they have to be chemically disassembled for loading with enzymes or the enzymes are genetically fused to the capsid proteins,²⁴⁸ the later can lead to a loss in modularity. Additionally, only some VLPs can be switched between two different states for the control of enzyme activity.

The cavities of THS represent nano-reactors that can host macromolecules and proteins up to 50 kDa in molecular weight.¹⁰⁵ In the apo-state (without nucleotides), the THS is in an open conformation, exhibiting a pore with about 8 nm in diameter. The pores of THS represent one of the largest switchable pores in protein cages and enable the diffusion of macromolecules and proteins in and out of the cavity without affecting the integrity of THS.⁷⁸ Upon addition of ATP, the natural ATPase function of THS is induced, resulting in an opening and closing of the cavity by the build in lid. Whereas the binding of ATP results in a partly closed conformation and the hydrolysis closes the THS entirely.¹¹⁶ The cavity opens again, when ADP and Pi is released from the nucleotide binding pocket.¹⁰⁶ This closing mechanism has a negative inter-ring cooperativity, resulting in a two stroke motion.¹³⁴ THS can be hold in the different states of the ATPase cycle by adding different ATP-analogues. The non-hydrolysable ATP- γ -S and AMP-PNP arrest the THS in a partly-closed conformation.¹¹⁶ To fix THS in the closed conformation, ATP-AIFx has to be added. ATP-AIFx rest much longer in the nucleotide binding pocket compared to ADP-Pi.¹⁰⁵ However, a fully closing of THS can only be achieved at high ATP-AIFx concentration, due to the negative inter-ring cooperativity.¹¹⁶ While THS has a big pore in the open conformation, there are only sixteen small side windows present in the wall of the cavity, allowing only small molecules to diffuse into the cavities.¹⁰⁵

The ability to host proteins in a cavity that can be opened and closed in a controlled fashion makes THS an interesting candidate as a controllable nano-reactor. By conjugating the enzyme horse radish peroxidase (HRP) into THS, we investigated, whether it is possible to control the HRP activity depending on the conformation of THS. The cavity of THS is large enough to host HRP with its size of 44 kDa (*Fig. 11.1*). HRP is a heme protein from the root of the horseradish plant and uses hydrogen peroxide to oxidize substrates including aromatic phenols, indoles or amines.^{249, 250} By wisely choosing the substrate, the oxidized products can be detected by spectrophoto- or fluorometric methods. This catalytic property has made HRP to an excellent marker protein, for instance in ELISA or western blot.

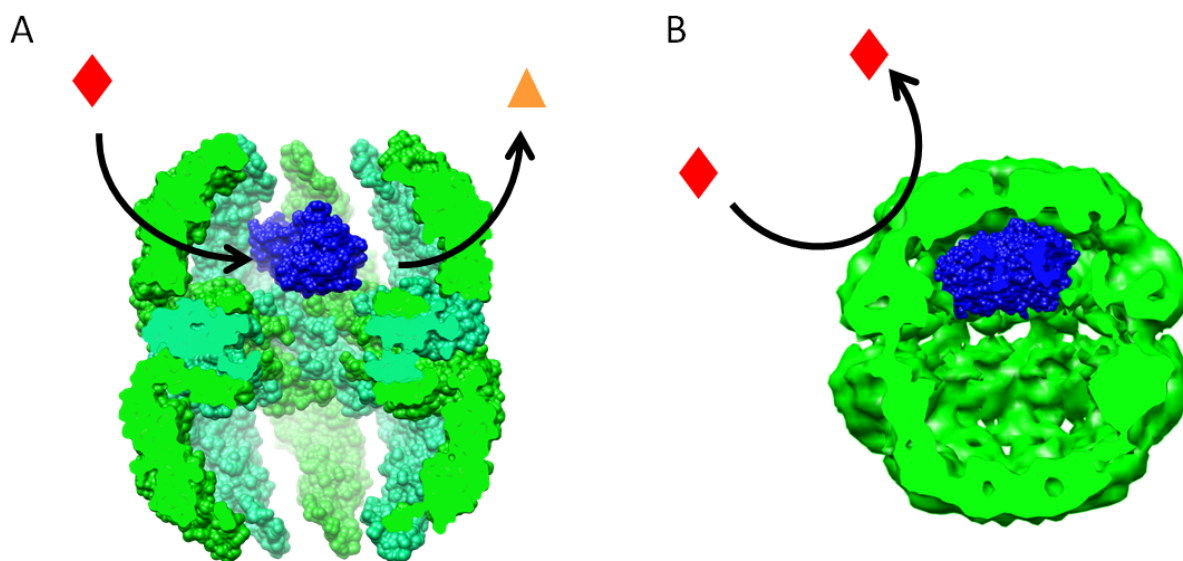


Fig. 11.1: Conceptual figure of a controllable THS-HRP nano-reactor. **(A)** Profile of a group II chaperonin (*Mm-cpn*) in the ATP bound state with HRP in its cavity. **(B)** Profile of HRP in a closed *Mm-cpn*. (protein structure source: *Mm-cpn* open: PDB 3izh; *Mm-cpn* closed: EMD 1398; HRP: PDB 1gwu)

11.2 Results

11.2.1 THS-HRP conjugation

In a previous study Bruns et al. demonstrated that it is possible to conjugate proteins in the cavities of THS.⁷⁸ They conjugated cyan fluorescent protein (eCFP) and yellow fluorescent protein (eYFP) each into one of the cavities of THS, creating a FRET pair, which was able to report damages in polymeric materials. The two fluorescent proteins were conjugated via a stabilized hydrazone bond to the cysteines in the THS' cavity. We used the same approach for linking HRP into THS. The activity of the THS-HRP complex was investigated depending on the structural conformation of THS.

The conjugation of HRP into the cavity of THS was achieved by modified HRP with a heterobifunctional linker featuring an activated ester and a 6-hydrazino-nicotinamide group (HyNic). In parallel the cysteins in the cavity of THS were modified with the heterobifunctional linker maleimido trioxa-6-formylbenzamide (MTFB). The modified THS-MTFB and HRP-HyNic were conjugated in a final step and unbound HRP was separated from THS-HRP with a size exclusion column. From its chromatogram, a first peak around 35 ml is present in the 280 nm channel, as well as a small peak in the 403 nm channel, corresponding to the THS-HRP conjugate (*Fig. 11.2*). A later fraction around 60 ml was found in the 280 nm and in the 403 nm channel, which corresponds to free HRP. HRP has beside the proteinaceous specific absorption at 280 nm an additional and much stronger absorption at 403 nm, which is specific for its heme group. The big size of this peak is a result of the used excess of HRP over THS to achieve maximum loading of THS. The baseline separation of the two fractions shows the successful separation of THS-HRP from free HRP.

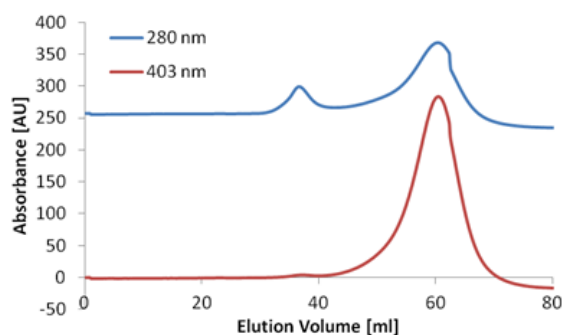


Fig. 11.2: Size exclusion chromatogram of the separation of THS-HRP and unbound HRP detected at 280 nm (blue) and 403 nm (red).

The ratio of HRP in THS in the purified THS-HRP was measured with a UV/Vis spectrometer. The absorbance at 280 nm in the UV/Vis spectrum arises mainly from THS and only to a minor extent from HRP. Due to the weak absorbance and the proximity to the heme peak, the absorbance of the hydrazone bond between THS and HRP cannot be determined properly. However, from the peak ratio of 403 nm to 280, the amount of HRP in THS was calculated to be 0.3 (Fig. 11.3).

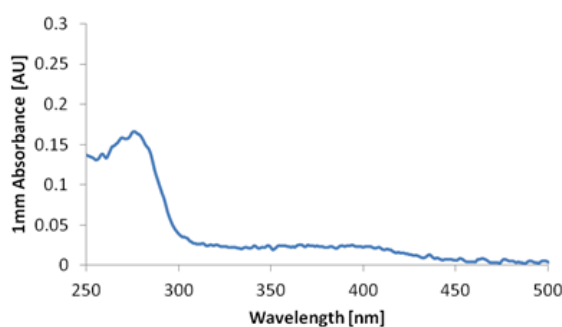


Fig. 11.3: UV/Vis spectrum of THS-HRP.

A change in molecular mass of some subunits could be observed on SDS-PAGE gel upon modification of THS with HRP. An additional band at around 100 kDa was found (Fig. 11.4). This corresponds to the mass of a THS subunit-HRP (58 kDa + 44 kDa). Another band above could correspond to conjugate of two THS subunits with a HRP (~ 150 kDa).

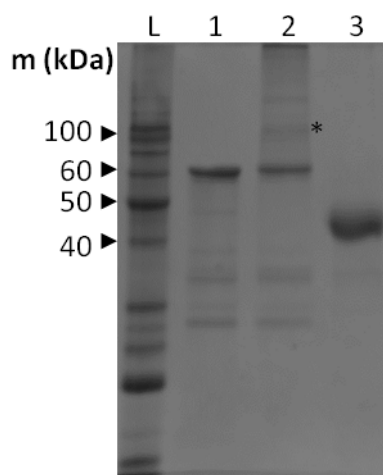


Fig. 11.4: SDS-PAGE of THS (1), THS-HRP (2, THS-HRP is asterisked) and HRP (3).

11.2.2 ATPase activity of THS-HRP

In a first step, we investigated, whether modification of THS with HRP is impairing the ATPase cycle of THS. The modification of the inner wall of THS with protein could disturb the movement of the subunits upon binding and hydrolysis of ATP. This can influence its ATPase activity. Thus, the ATPase activity of the THS-HRP conjugate was measured. Results show that the HRP conjugated into THS decreased the ATPase activity seriously. The ATPase activity decreases from $2.0 \pm 0.3 \text{ ATP}_{\text{hyd}} \text{ THS}^{-1} \text{ min}^{-1}$ for THS to $0.3 \pm 0.1 \text{ ATP}_{\text{hyd}} \text{ THS}^{-1} \text{ min}^{-1}$ for THS-HRP at 37°C and pH 7.4 (Fig. 11.5). Thus, the conjugation of HRP into THS impairs the ATPase activity. This decrease in ATPase activity can be caused by the tight binding of HRP to THS' subunits. The tight binding of HRP, which is about two thirds of the subunits mass, in proximity to a subunit hinders the movement of this subunit. Also the movement of other subunits could be hindered, resulting in the reduction of ATPase activity. However, the six-fold decrease of the ATPase activity compared to unconjugated THS is quite surprising. If we suggest, that HRP in THS stops the ATP activity in both rings would mean that five out of six THS have at least one HRP conjugated to the cavities. But from fluorescent absorbance, we calculated a ratio of about one HRP per three THS. Thus there must be also another effect, which we cannot explain at this moment.

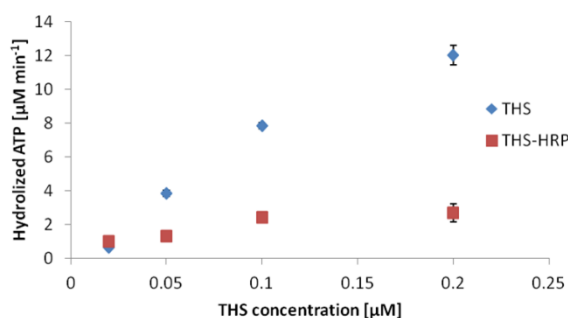


Fig. 11.5: ATPase activity of THS (blue) and THS-HRP (red).

11.2.3 HRP activity in THS

We investigated, whether the modification of HRP is impairing its oxidative capability. HRP activity measurements at pH 7.4 and 37°C with 2,2'-azino-bis(3-ethylbenzthiazoline-6-sulfonic acid) (ABTS) resulted in an activity of $1.87 \pm 0.14 \mu\text{M min}^{-1} \mu\text{M}^{-1}$ for HRP. The HyNic modified HRP showed a slightly lower activity ($1.55 \pm 0.03 \mu\text{M min}^{-1} \mu\text{M}^{-1}$). After conjugating HRP-HyNic into THS, the activity decreased to $1.11 \pm 0.05 \mu\text{M min}^{-1} \mu\text{M}^{-1}$ (Fig. 11.6). Thus, modification of HRP is reducing its activity, but it still keeps about 60% of its capability to oxidize ABTS, when incorporated in THS.

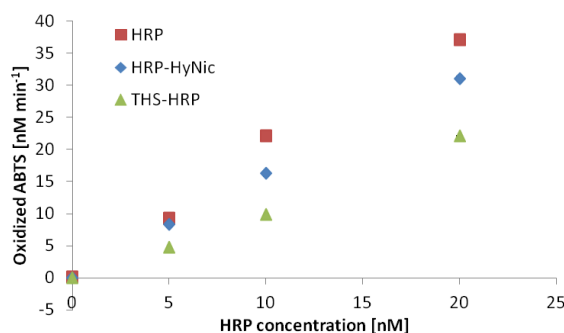


Fig. 11.6: Enzymatic activity of HRP (red square), HyNic modified HRP (blue diamond) and HRP conjugated into THS (green triangle).

11.2.4 Influence on the oxidative activity of THS-HRP upon addition of ATP or ATP analogues

We examined if conformational changes of THS upon addition of ATP or ATP analogues can alter the diffusion rate of reactant and product, consequently changing the oxidative activity of HRP incorporated in THS. To this end, the oxidative activity of THS-HRP was measured with two different substrates at 37° C and pH 7.4. On one hand, we measured the change in absorbance at 420 nm upon oxidation of ABTS and on the other hand, the change in fluorescence of dihydrogen rhodamine 6G (dhRh6G) excited at 520 nm and emitted at 555 nm.^{246, 251} These two substrates exhibit different characteristics. ABTS is smaller and more polar compared to the larger and more hydrophobic dhRh6G (Fig. 11.7).²⁵² It was examined if these differences can influence the activity of THS-HRP.

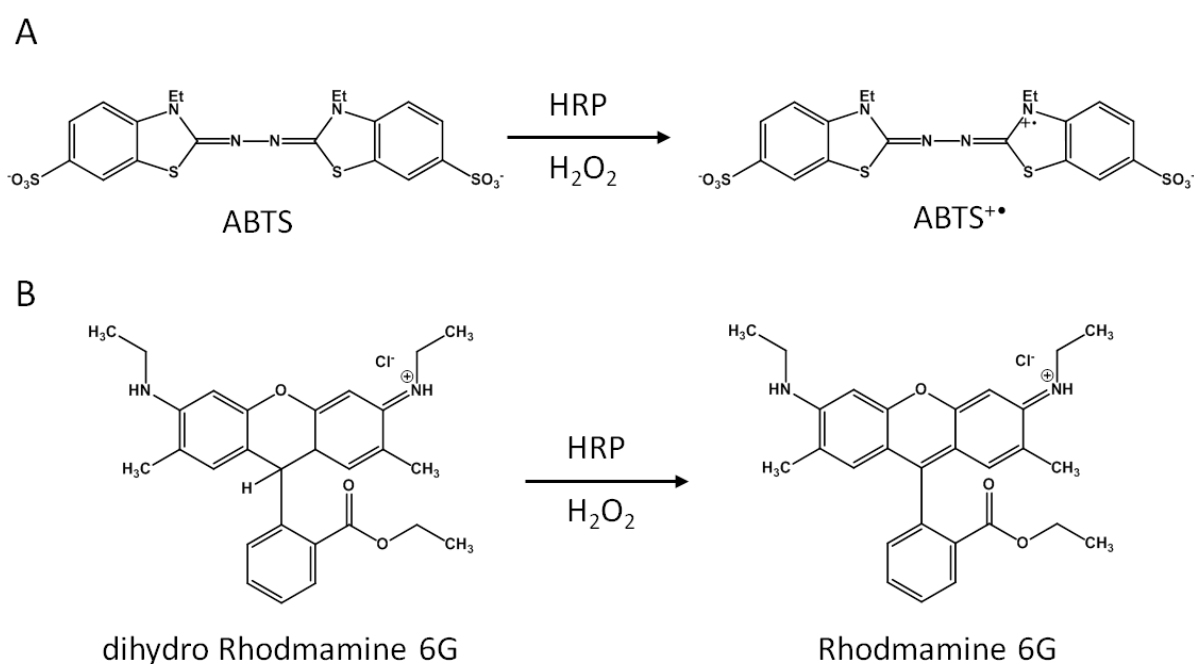


Fig. 11.7: Chemical structure of ABTS (**A**) and dhRh6G (**B**) before and after the reaction with HRP and H_2O_2 .

11.2.4.1 ABTS assay

First we tested the influence of ATP, ATP- γ -S and ATP-AIFx on the activity of HRP itself with ABTS as substrate. While ATP and its analogue ATP-AIFx did not have a big influence on the activity, no activity could be detected with the ABTS assay when the non-hydrolysable ATP- γ -S was present (Fig. 11.8 A). Similar results were obtained with THS-HRP. ATP and ATP-AIFx altered the HRP activity only slightly, whereas no activity was measured with ATP- γ -S (Fig. 11.8 B & C). The loss of activity with ATP- γ -S could be caused by the radical scavenging ability of the thiol in ATP- γ -S. In the body, the thiols of glutathione (GSH) and proteins act as natural free radical scavenger, protecting the body from damage.²⁵³ In this system, ATP- γ -S could react with the radical form of ABTS, returning it to the non-radical form. Because only the radical form of ABTS is absorbing at 420 nm, no activity is detected.

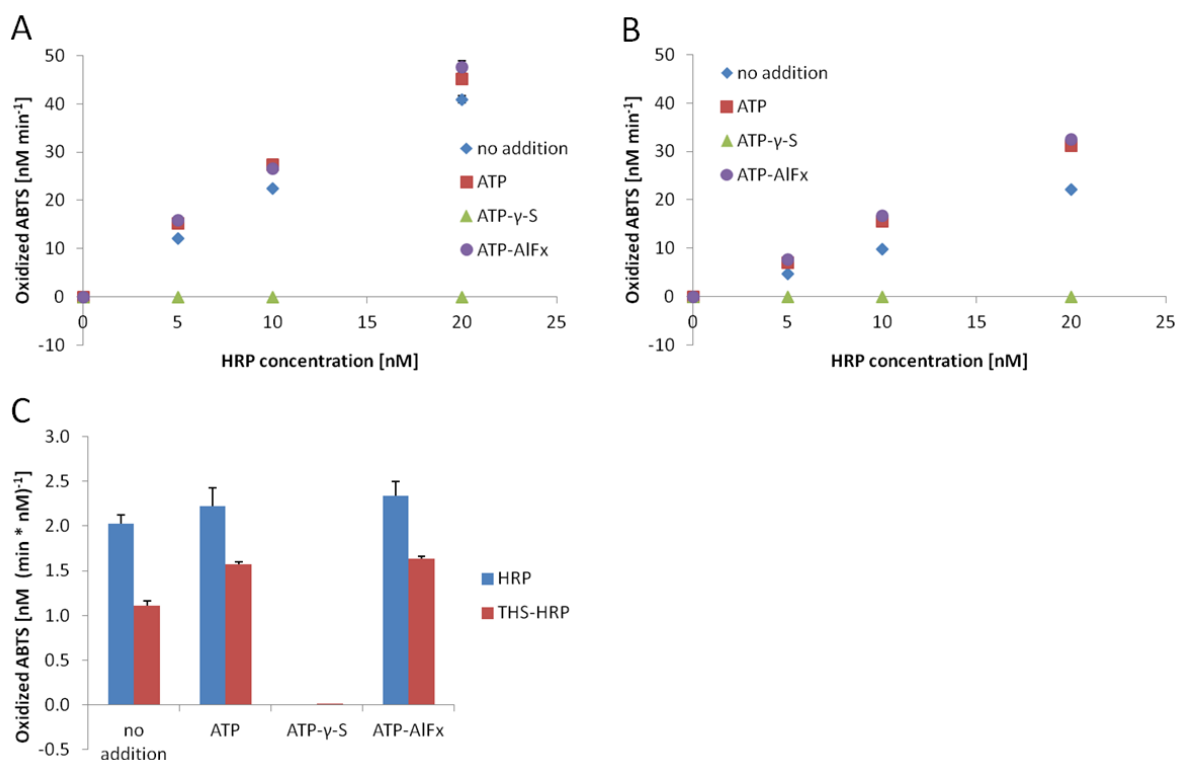


Fig. 11.8: Enzymatic activity of HRP (**A**) and THS-HRP (**B**) measured with an ABTS assay. The activity was measured without any addition (blue diamond), ATP (red square), ATP- γ -S (green triangle) and ATP-AIFx (violet circle). (**C**) Comparison of the activity of HRP and THS-HRP with the different substrates.

11.2.4.2 DhRh6G assay

We could not observe a difference in activity between free HRP and HRP bound to THS depending on different ATP analogues with the ABTS-assay. Therefore, we tested the activity with dihydro rhodamine 6G (dhRh6G) as substrate. DhRh6G is not fluorescent itself, but HRP oxidize dhRh6G with hydrogen peroxide to the fluorescent Rhodamine 6G (Rh6G). In contrast to the assay with ABTS, this assay does not depend on a radical form of the substrate.

It was found that ATP, ATP- γ -S and ATP-AIFx enhanced the activity compared to HRP without any addition of substrate (Fig. 11.9 A). The activity of HRP bound to THS was also increased with ATP and ATP-AIFx (Fig. 11.9 B). The only big difference between HRP and THS-HRP could be observed with ATP- γ -S. The activity of THS-HRP with ATP- γ -S dropped to under 10% of the activity of free HRP (Fig. 11.9 C).

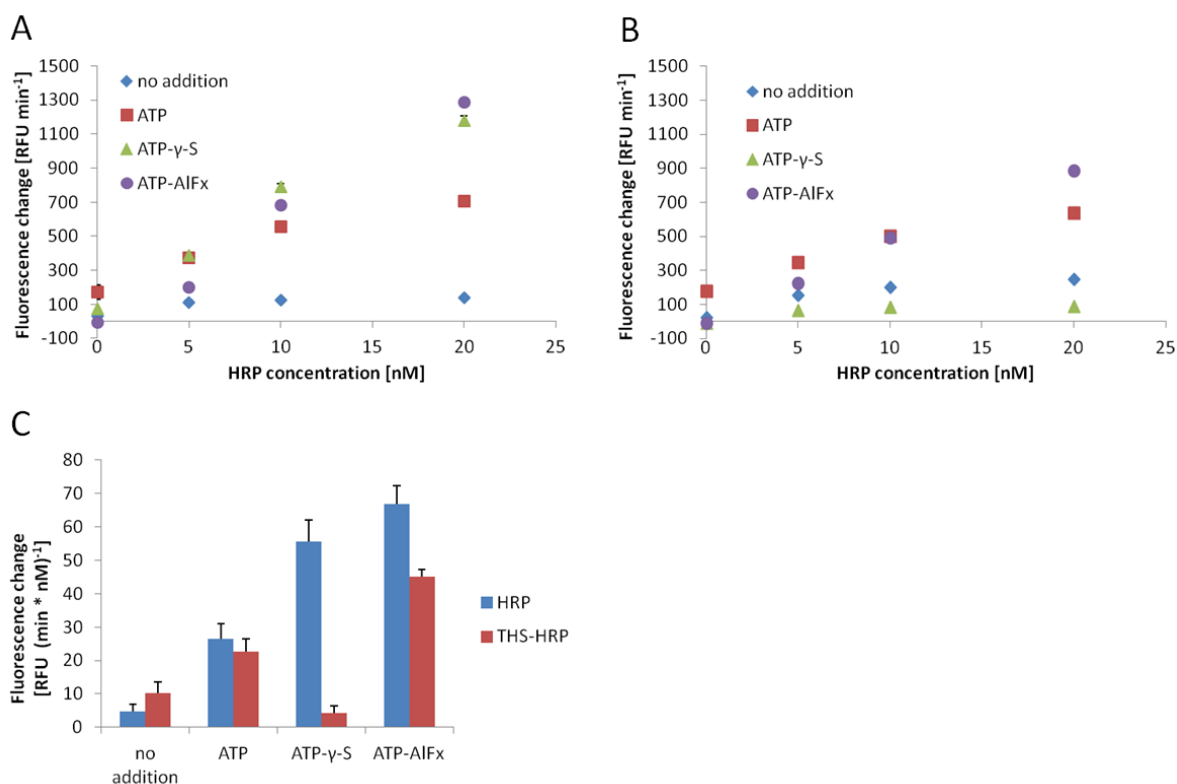


Fig. 11.9: Enzymatic activity of HRP (A) and THS-HRP (B) measured with a dhRh6G assay. The activity was measured without any addition (blue diamond), ATP (red square), ATP-γ-S (green triangle) and ATP-AIFx (violet circle). (C) Comparison of the activity of HRP and THS-HRP with the different substrates.

11.2.5 Conclusions

The two substrates, ABTS and dhRh6G, for activity measurement of HRP showed quite different results. ATP and ATP-AIFx did not change the oxidative activity of HRP. In contrast, with ATP-γ-S no HRP activity was measured with the ABTS assay. The thiol of this non-hydrolyzable ATP analogue could act as a radical scavenger on the UV absorbing ABTS radical, which is produced by HRP. This may be an explanation why no HRP activity was measured when ATP-γ-S was added.

Using dhRh6G for activity measurement showed another image. At these series of measurements, the activity of free HRP was enhanced by addition of nucleotides, with a succession of ATP-AIFx > ATP-γ-S > ATP. An activity boosting effect of nucleotides on peroxide-mimics was previously reported.²⁵⁴⁻²⁵⁶ It was shown that nucleotides can boost the enzymatic activity of a DNAzyme based on a G-quadruplex/hemin system. ATP showed the strongest effect over other nucleoside triphosphates and over ADP and AMP.²⁵⁴ It was suggested, that the hydrolysis of ATP enhanced the electron-transfer during the catalytic step. This was supported by the finding, that ADP and the non-hydrolyzable ADPNP showed lower activation. Additionally, nucleotides could figure as H₂O₂-activator.²⁵⁵ However, this boosting effect by nucleotides is not reported on the activity of peroxidases and it is not clear if these findings can be also adapted for our system. Additionally, the mentioned studies used an ABTS assay. With this assay we could not observe this trend; only with the dhRh6G assay the boosting effect was observed. Thus, it is not clear whether the higher activity of HRP observed with dhRh6G origin from this effect or a total different effect is the reason.

A drop in activity of HRP conjugate to THS compared to free HRP was observed with ATP- γ -S. This decrease of THS-HRP activity upon ATP- γ -S could be explained that ATP- γ -S closes THS partly, whereas ATP and ATP-AlFx does not have such an effect. Probably, the ATPase cycle of THS is interrupted by HRP after ATP binding and stabilized by ATP- γ -S. However, this explanation is contradictory to the findings from the chapter 10. *THS activity and conformation* where ATP-AlFx seems to close THS.

In general, only ATP- γ -S influences the activity of HRP in a way that THS-HRP could be used as a controllable nano-reactor. But the reason for this behaviour is not understand yet. More studies could be performed to further reveal the interplay of THS-HRP with different nucleotides and substrate. It would be interesting, how the activity would be with the non-hydrolyzable AMPNP analyzed with ABTS to circumvent the problems with ATP- γ -S and if the same results would be found for this nucleotide with the dhRh6G assay.

12. Gold nanoparticle formation in THS-PAMAM

Parts of this chapter are in preparation for publication:

M.G. Nussbaumer, C. Bisig and N. Bruns

12.1 Introduction gold nanoparticles

Gold nanoparticles (AuNP) are used in a broad field of applications in biology and medicine. Traditionally, AuNP were used as labeling agents to increase the contrast for microscopy, such as optical microscopy and transmission electron microscopy (TEM), but also photothermal and photoacoustic imaging.¹⁷⁴ For medicinal issues, AuNP have been widely investigated for photothermal therapy in cancer treatments.^{257, 258} Light at the plasmon resonance frequency excites the free electrons on the surface of the AuNP. This energy is then transferred to the crystal lattice resulting in a heating of the AuNP and subsequently its environment. Thus, AuNP in cancer tissue heat up the tumor upon light irradiation, causing tumor cell death.²⁵⁹

In this project, we investigate the formation of gold nanoparticles in the protein-polymer conjugate THS-PAMAM (see chapter 8.2 *THS-PAMAM conjugation*) (Fig. 12.1). Several studies showed controlled formation of AuNP in presence of PAMAM.^{260, 261} During this process chlorauric acid (HAuCl_4) bind to the amines of PAMAM and upon reduction (e.g. with NaBH_4) forms AuNP.¹⁷⁵ However, often aggregation occurs.²⁶⁰ In our system the formation of AuNP take place in the cavity of THS. This should avoid aggregation and control the size of AuNP. In previous studies the formation of different metal nanoparticles in protein cages has been shown. First, iron sulfide nanoparticles were synthesized in ferritin.²⁶² Following, different inorganic nanoparticles were formed or incorporated in various protein cages.²⁴³ However, there are only few studies where AuNP are synthesized in the cavity of protein cages.^{263, 264} We want to expand this field and take advantage of the ability that PAMAM assists the formation of AuNP and the advantage of protein cages to serve as defined nanostructure during the AuNP formation.

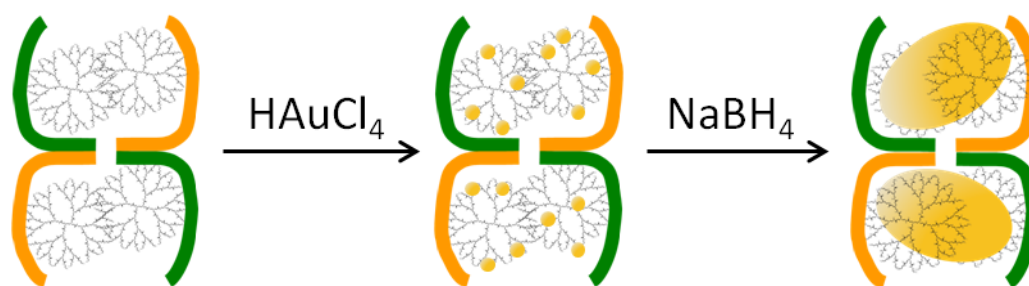


Fig. 12.1: Schematic representation of the formation of AuNP in THS-PAMAM upon loading THS-PAMAM with HAuCl_4 and subsequently reduction with NaBH_4 .

12.2 Results and discussions

To form AuNP, gold ions ($110 \mu\text{M HAuCl}_4$) associate with the positive charged PAMAM. Subsequently, gold is reduced with the reduction agent NaBH_4 .^{260, 265} When HAuCl_4 is reduced without PAMAM, gold nanoparticles forming a network are observed in TEM (Fig. 12.2 A). Formation of AuNP in the presence of PAMAM results in AuNP-“islands” with a broad size distribution (Fig. 12.2 B). These islands are suggested to be aggregates of gold and PAMAM.^{257, 266}

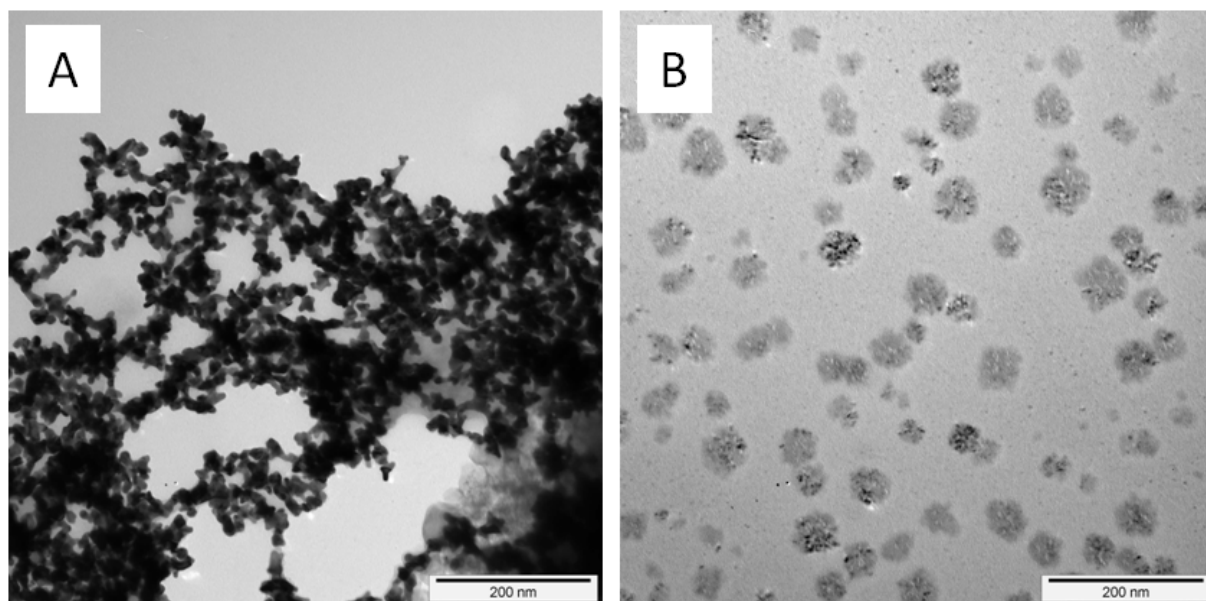


Fig. 12.2: TEM images of AuNP formed upon reduction with NaBH_4 without (A) and with PAMAM (B). All TEM images were negatively stained with 1% uranyl acetate.

We used the same method to form AuNP in presence of THS-PAMAM. THS-PAMAM was produced as described in chapter 8.2 *THS-PAMAM conjugation*. During the formation of AuNP with THS-PAMAM, also AuNP aggregates were formed, which are not associated with THS-PAMAM. Therefore, the sample were filtered (cut off: $0.22 \mu\text{m}$) to remove bigger gold aggregates. The UV/Vis spectrum of AuNP formation in presence of THS-PAMAM shows the absorption of THS at 280 nm and of the bond between THS and PAMAM at 354 nm. Moreover, it also shows a broad peak around 520 nm, which is characteristic for AuNPs (Fig. 12.3).²⁶⁷ In contrast, AuNP formation in presence of THS and subsequent filtration, showed only a peak at 280 nm from THS. Thus, AuNP are not associated with THS but with THS-PAMAM.

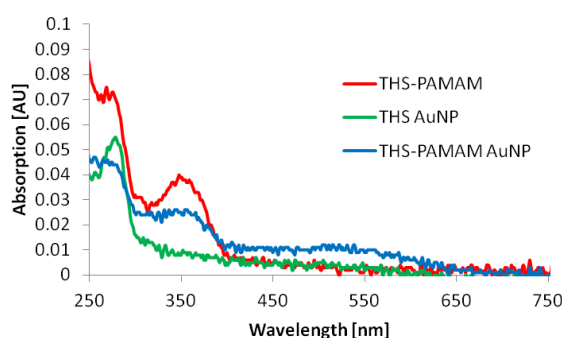


Fig. 12.3: UV/Vis spectrum of THS-PAMAM (red); AuNP formed in the presence of THS (green) and THS-PAMAM (violet) and subsequently filtered.

AuNP formed with THS-PAMAM were investigated with TEM. These images show that the highly reductive conditions during the AuNP synthesis did not harm the THS' quaternary structure. Thus, THS is suitable for AuNP formation. We applied three different methods to form AuNP with THS-PAMAM. We incubated THS-PAMAM with low concentration of HAuCl_4 ($110 \mu\text{M}$) for 45 min, added afterwards NaBH_4 and incubated it for another 45 min (Fig. 12.5 B). We did the same procedure but with ten times higher HAuCl_4 (1.1 mM) concentration (Fig. 12.5 C). In the third variant we repeated the low HAuCl_4 ($110 \mu\text{M}$) concentration method five times, but with HAuCl_4 incubation time of just 15

min (*Fig. 12.5 D*). The analysis of the TEM images showed that higher gold concentration formed more AuNP per THS-PAMAM (15.6%) than with low gold concentration (2.3%), whereas the size of the AuNP was about the same (low gold: 4.0 ± 1.5 nm, high gold: 3.9 ± 1.4 nm) (*Fig. 12.5 F*). In contrast, the repetitive method created much more AuNP per THS-PAMAM (75.7%) than the other methods. Additionally, smaller AuNP were produced (2.4 ± 1.0 nm) (*Fig. 12.5 E*). The smaller size of the AuNP could be caused by the shorter incubation time with HAuCl_4 . As UV/Vis spectrum supposed, no AuNP were formed in THS without PAMAM (*Fig. 12.5 A*).

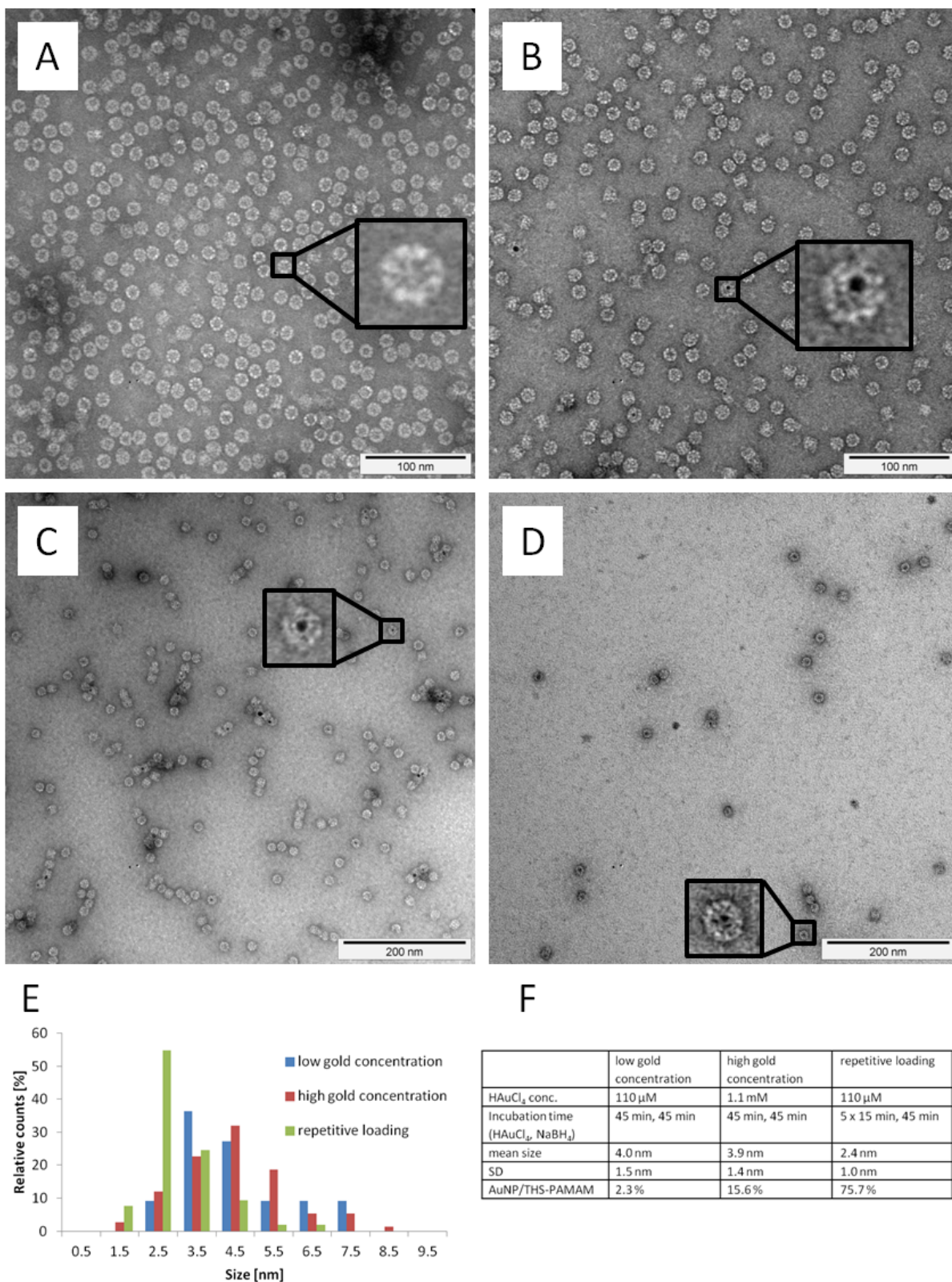


Fig. 12.4: TEM image of AuNP formed in presence of THS (A), THS-PAMAM with low gold concentration (110 μM H_{AuCl₄}) (B), high gold concentration (1.1 mM H_{AuCl₄}) (C) and repetitive gold loading (5 x 110 μM H_{AuCl₄}) (D). Size distribution of the samples (E), table of preparation methods and statistical values (F). Insets are in 4.4 x zoom. All TEM images were negatively stained with 1% uranyl acetate.

12.3 Conclusions

In conclusion, we show the feasibility of AuNP formation within THS-PAMAM, whereby the presence of PAMAM is crucial for the AuNP formation in the cavity of THS. By varying the gold concentration, we could mainly enlarge the number of AuNP in THS-PAMAM. Even higher numbers were found with repetitive loading. Shortening the incubation time with chlorauric acid resulted in smaller AuNP. In general, AuNP formation in THS-PAMAM results in a small size distribution. In contrast to our results from AuNP formation with PAMAM and a study from Hoffman et al.,²⁶⁰ THS-PAMAM formed much less aggregates. From other studies (see chapter 7. *Modification of THS with cell targeting ligands*) THS can be modified and used for active targeting to desired tissue. In a longer term, this would open the possibility to use THS in photothermal therapies. Additionally, AuNP in combination with palladium could serve as catalytically active nanoparticles.²⁶³

13. Conclusions and Outlook

13.1 Conclusions

The aim of this work was to show the versatility of THS, focusing on siRNA delivery to cells, but also on THS as a delivery agent for anti-cancer drug, for enzyme activity control, and for controlled AuNP formation.

First of all, THS was expressed and purified with yields between ~2-20 mg per 4 l fermentation batch. We characterized THS with different techniques (SDS-PAGE, native PAGE, MALDI-MS, LC-MS, TEM and cryo TEM) to get a well defined image of THS. A mass of the both subunits around $58'500 \text{ g mol}^{-1}$ were measured and the eight-fold pseudo-symmetry of the THS' quaternary structure was visualized. Tests showed high stability of THS against pH (at least stable at pH 5.25 - pH 9.5) and against solutions containing up to 20% DMF and 10% AcN. Additionally, we measured the ATPase activity of THS to be $6.8 \pm 0.5 \text{ ATP}_{\text{hyd}} \text{ THS}^{-1} \text{ min}^{-1}$ in pH 7.4 at 55° C and $2.0 \pm 0.3 \text{ ATP}_{\text{hyd}} \text{ THS}^{-1} \text{ min}^{-1}$ in pH 7.4 at 37° C . All of these results match previous literature precedence.^{114, 133}

Cell targeting of NDDS is crucial to achieve effective cell uptake of NDDS. Therefore, different cell targeting or penetrating ligands were attached to THS, and their interaction with cells was investigated by flow cytometry and fluorescent microscopy. We conjugated a fluorescent dye to the cysteines in the THS cavity allowing the investigation of the interaction between THS-ligand and cells, without the influence of the dye on the cell-interaction. With the ligands BBN-8/12EG, biotin, folic acid, somatostatin, and cyclic RGD, no interaction with corresponding cells was observed. However, during these experiments U87-MG cells exhibited uptake of THS, making them a suitable target for THS-based therapies. Conjugation of TAT, a cell penetrating peptide, to THS resulted in a high uptake of THS-TAT in PC-3 cells. With VEGF, we found a selective ligand that enhances the uptake of THS in HUVEC but not CHO-K1 cells. Thus, we found a cell line, U87-MG, which can be target by THS without modification. By conjugating TAT to THS we can trigger unspecific cell-uptake and VEGF act as specific ligand.

For the purpose of siRNA delivery, we conjugated the dendritic polymer PAMAM into THS via a stabilized hydrazone linker, resulting in about 3.8 ± 0.2 formed bonds. We proved that PAMAM was conjugated into the cavity of THS and that it did not affect the integrity of THS. The THS-PAMAM protein-polymer conjugate showed the ability to bind siRNA and protect siRNA from the degradation by RNase. We measured a loading capacity of one siRNA per THS-PAMAM. This is quite low and achieving a higher loading capacity will be further studied. Nevertheless, a silencing effect was observed when siRNA was transfected with THS-PAMAM to U87-MG. Compared to Lipofectamine 2000, THS-PAMAM showed a slightly lower efficiency, but was not toxic for the cells. The TAT modified THS-PAMAM-siRNA was additionally able to induce RNAi in PC-3 cells, which was not the case with non-modified THS-PAMAM-siRNA. Despite the rather low siRNA loading, THS-PAMAM showed the ability to be used as a non-toxic siRNA delivery agent for different cell types.

In addition to siRNA delivery, we explored the possibility to transport cargo into cells, where it could be released upon interaction with the reductive environment in the cells. To this end, we conjugated a dye with a disulfide containing linker to the cysteine of THS. The dye was quenched when it is bound to a protein, which enabled us to track the release of the dye. The release was

measured in artificial reductive environment and in cells. These results are a proof of principle for the reductive release of cargo that was translocated into cells with THS.

The conformational state of THS upon exposure to ATP or ATP analogues was explored. Although other studies showed a clear image of how ATP and different ATP analogues influence the conformation of chaperonins that are related to THS, such as TRIC/CCT, detailed information for THS was unknown. Our experiments suggest that ATP-AIFx is able to close THS and that THS rests in a predominantly open conformation in the absence of nucleotides. The effect of other THS analogues on THS' conformation could not be unequivocally proven. We exploited the ATP-dependent opening and closing mechanism of the lid to create a controllable nano-reactor. To this end, we conjugated the enzyme HRP into THS and examined the HRP activity depending on different substrates, which mimicked the different stages of ATP hydrolysis. The conjugation of HRP into THS was successfully done via a resonance stabilized hydrazone linker. The ratio of HRP per THS was about 0.3. The conjugation of HRP into THS impaired the ATPase activity of THS unduly (decreased to 15% activity), whereas the activity of HRP was decreased moderately (decrease to 60% activity). The dependence of the HRP in THS activity on the different nucleotides was measured with two different substrates, namely ABTS and dhRh6G. No difference in HRP activity of THS-HRP compared to free HRP could be measured with ABTS as the substrate upon addition of the different nucleotides (except the decrease of activity upon binding to THS). Most intriguing was that ATP- γ -S impaired the ABTS assay, suggesting that ATP- γ -S quenches the colored ABTS⁺-radical. With dhRh6G as the substrate, a boosting of the HRP activity upon addition of the different nucleotides was observed. This effect could not be explained. As with ABTS, ATP and ATP-AIFx did not show any change in THS-HRP activity, but ATP- γ -S decreased the THS-HRP activity to 10% of free HRP, possibly because the THS conformation controls the activity of HRP. However, more pronounced ATP-dependent activity effects would be desirable and should be investigated in future work.

In a short chapter, we describe the formation of gold nano-particles in THS-PAMAM. By a repetitive gold ion reduction protocol, a loading of 76% of gold nanoparticle per THS-PAMAM was achieved. By varying the protocol, the size of the nanoparticles could be tuned from 2.4 ± 1.0 nm to 4.0 ± 1.5 nm.

The versatility of THS has already been shown in previous work by Prof. N. Bruns et al.. Two different fluorescent proteins were conjugated to the cavity of THS to act as a mechanical sensor based on FRET.⁷⁸ In a later work, they used the THS' cavity as a nano-reactor for polymerization.¹⁷⁷ This broadened the application field of THS and paved the way for THS based NDDS. Besides further characterization of the mutated thermosome, we created a protein-polymer conjugate for siRNA delivery purposes, which encapsulates, hosts, protects, and releases guest molecules. In doing this, THS revealed high stability and the ability to be easily modified. An advantage over other protein cages is the ability of THS to encapsulate and release macromolecules through its big pore without harming the integrity of THS. The application of THS as a nanoreactor for enzymes, and preliminary investigations on THS as host for reduction cleavable drugs, emphasize the versatility of THS. The well defined size, non-toxicity and ability to modify THS in a customized way make THS to a promising and versatile nano drug delivery system.

13.2 Outlook

We see the biggest potential for THS as nano drug delivery system. But for this purpose, the expression and purification has to be simplified and shortened. One way to achieve this aim is to attach an affinity-tag at a terminus of a THS subunit for affinity-tag purification. But for this purpose,

the termini have to be moved to the outer surface of the THS, which can be done by a so-called circular permutation. Such a circular permutation was already showed for chaperonins, among others, for the thermosome of *T. acidophilum*.^{268, 269} Besides affinity tags for purification purposes, other sequences could be fused to the termini of THS such as cell targeting and/or penetrating peptide sequences or peptide tags (e.g. SpyTag²⁷⁰ or SYNZIP²⁷¹) for specific attachments of targeting moieties. Additionally, unnatural amino acids could be genetically introduced to the termini to have further specific anchor sites. With bioorthogonal chemistry, ligands can be attached on these non-proteinogenic amino acids.^{272, 273}

PAMAM, with its 64 primary amine groups, can be modified to a high degree with different molecules like drugs or contrast agents. We showed that it is possible to modify PAMAM with AuNPs and conjugate it into THS. Different small-molecular drugs could be conjugated via cleavable linkers (e.g. redox-, esterase- or pH-labile-linkers) to the primary amines of PAMAM and subsequently linking to THS. By conjugating contrast agents to PAMAM in THS, it could be possible to create a targetable nano system with a high density of contrast agents, such as superparamagnetic iron-oxide nanoparticles (SPIONS)^{1, 195, 274, 275} or gadolinium²⁷⁶ for MRI applications.

In addition, macromolecules could be directly conjugated to the cysteines of THS via cleavable linkers. One example is the pharmaceutically active peptide KLAK, which is much less toxic to eukaryotic cells when it is outside of the cell than when it is inside the cell where it exhibits its mitochondrial toxicity.^{277, 278} Another possibility would be to use THS as transporter for enzyme replacement therapy,^{279, 280} like the tumor suppressor p53.²⁸¹⁻²⁸³

One drawback of THS-based NDDS is possible immunogenicity, which is a general issue for protein based systems.²⁸⁴ However, a common approach to overcome this problem is modifying THS with polymer stealthing moieties to shield it from the immune system.^{62, 285} In future studies one should focus the attention on this purpose and conduct careful immunogenicity studies.

Overall, a lot of different modifications of THS are waiting to be done to promote practical applications of THS. There is plenty room at the THS.

14 Experimental sections

14.1 Materials

All chemicals were purchased from Sigma-Aldrich, unless stated otherwise. Maleimido trioxa-6-formylbenzamide (MTFB), succinimidyl-6-hydrazinonicotinamide acetone hydrazone (HyNic), tetra ethylene glycol pentafluorophenyl ester 4-formylbenzamide (PEG₄-PFB), maleimido-2-hydraziniumpyridine (MHP), succinimidyl-disulfide-4-formylbenzamide (S-SS-4FB) and 6-hydrazinonicotinamide acetone hydrazone-GRKKRRQRRRPPQ-NH₂ (TAT-HyNic) were purchased from Solulink (USA). Following cell lines were purchased from ATCC (USA): breast adenocarcinoma cells MCF-7 (ATCC HTB-22), Chinese hamster ovary cells CHO-K1 (ATCC CCL-61), vascular endothelium cells HUVEC (ATCC CRL-1730), glioblastoma cells U-87 MG (ATCC HTB-14) and cervical cancer cells HeLa (ATCC CCL-2). Prostate cancer cells PC-3 (ATCC CRL-1435) were a kind gift of Prof. T. Mindt's group (University Hospital Basel) and purchased from HPA Culture Collections (UK). *E. coli* strain BL21(DE3) CodonPlus-RIL from Agilent (USA), Membrane and centrifugal filters were purchased from Merck Millipore (USA), RNase A from Roche (Switzerland), Atto dyes from ATTO-TEC (Germany), 4%-20% precast gel (10 well, mini-protean) from Bio-Rad (USA), GelRed from Biotium (USA), cell culture flasks and 24- & 96-well plates from BD Bioscience (USA), 8-well microscope chamber slides from Nunc (USA) and scrambled siRNA from Microsynth (Switzerland). 6X MassRuler DNA Loading Dye, Hoechst 33342, CellMask orange, LysoTracker Red DND-99, penicillin-streptomycin-mix, 100x non-essential amino acids solution, silencer KIF11 (Eg5) siRNA and Lipofectamine[®] 2000 (LF) were purchased from Thermo Fisher Scientific (USA). 1.4 nm monomaleimido nanogold (AuNP-mal) and 1.4 nm mono-sulfo-NHS-nanogold (AuNP-NHS) were obtained from Nanoprobes (USA).

14.2 Buffers and broths

Compositions of used buffers and broths (in alphabetical order):

5x Loading Buffer: 150 mM Tris/HCl pH 6.8, 70% glycerol, 0.01% w/v bromophenol blue

AXC Buffer: 20 mM Tris/HCl pH 7.5, 1 mM ethylenediaminetetraacetic acid (EDTA), 0.02% w/v NaN₃

Buffer A: 100 mM sodium phosphate pH 7.5, 150 mM NaCl

Buffer B: 100 mM sodium phosphate pH 6.5, 150 mM NaCl

Elution Buffer: 20 mM Tris/HCl pH 7.5, 500 mM NaCl, 1 mM EDTA, 0.02% w/v NaN₃

Lysis Buffer: 20 mM Tris/HCl pH 7.5, 1 mM EDTA, 0.02% w/v NaN₃, 1 mM dithiothreitol (DTT), 1 mM benzamide, 1 mM phenylmethanesulfonyl fluoride (PMSF), 30 µg ml⁻¹ DNase I, 10 µg/ml RNase A

Lysogeny Broth: 10.0 g l⁻¹ tryptone, 5.0 g l⁻¹ yeast extract, 10.0 g l⁻¹ NaCl, adjusted to pH 7.5 with NaOH

SEC Buffer: 20 mM Tris/HCl pH 7.5, 100 mM NaCl, 1 mM EDTA, 0.02% w/v NaN₃

PBS: 1.15 g l⁻¹ Na₂HPO₄ (anhydrous) pH 7.4, 8.0 g l⁻¹ NaCl, 0.2 g l⁻¹ KH₂PO₄, 0.2 g l⁻¹ KCl

Terrific Broth: 12.0 g/l enzymatic casein digest, 24.0 g/l yeast extract, 12.3 g/l potassium phosphate (dibasic, trihydrous), 2.2 g/l potassium phosphate (monobasic, anhydrous), 8 ml/l glycerol, 100 µl/l Antifoam 204

Tris-glycine Buffer: 25 mM Tris pH 8.25, 192 mM glycine

14.3 Methods

All concentrations are given as end concentrations in the reaction mixture, if not stated otherwise. Concentration measurements were performed with NanoDrop 2000c (Thermo Scientific, USA), if not

stated otherwise, and calculated with following extinction coefficients: THS $\epsilon_{280\text{nm}} = 210'880 \text{ M}^{-1} \text{ cm}^{-1}$,^{1, 78} hydrazone bond $\epsilon_{354\text{nm}} = 29'000 \text{ M}^{-1} \text{ cm}^{-1}$ (according to the manufacturers protocol; Solulink, USA),¹⁸⁶ siRNA $\epsilon_{260\text{nm}} = 300'000 \text{ M}^{-1} \text{ cm}^{-1}$ (determined by absorption measurements at different concentrations). All conjugation products were extensively purified with Amicon centrifugal filters (Merck Millipore, USA) (THS: MWCO: 100 kDa; PAMAM: MWCO: 3 kDa), if not stated otherwise. Buffer exchange and concentration steps were carried out by centrifugal filtration in the same way, if not stated otherwise. All chromatography steps were conducted on the fast protein liquid chromatography (FPLC) system ÄKTA FPLC (GE Healthcare, UK) with a P-900 pump, UV-900 UV/Vis detector, pH/C-900 pH and conductivity meter, Inv-907 motor valve, M-925 mixer and a CU-950 control unit at room temperature, if not stated otherwise. All graphs were plotted with Excel 2007 (Microsoft, USA) and all graphics were arranged in PowerPoint 2007 (Microsoft, USA). Chemical structures were drawn in ChemBioDraw 14 (CambridgeSoft Corp., USA). Protein models were made with Chimera 1.9 (UCSF, USA).

THS expression:

THS was expressed similar as earlier reported by Bruns *et al.*⁷⁸ Briefly, a pET plasmid with the mutated THS gene was transfected into the *E. coli* strain BL21(DE3) CodonPlus-RIL according to the manufacturer's protocol. A preculture was grown in 5 ml Lysogeny Broth at 37° C under shaking for 6h. Cell culture was grown in eight 2 l fermentation flasks (0.5 l each) under shaking for 20 h at 30° C in Terrific Broth under kanamycin resistance without induction of IPTG. Cells were harvested by centrifugation at 6'700 g for 20 min at 4° C. Cells were resuspended in Lysis Buffer and first lysed by sonication at 4° C for 5 min and second three times with a French press (EmulsiFlex-C3, Avestin, Canada). The lysed cells were centrifuged for 25 min at 20'000 g and subsequently the supernatant was set to pH 7.5 with 500mM Tris/HCl pH 8 and incubated for 30 min at 37° C to activate DNase and RNase. The supernatant was centrifuged again at 6'700 g for 20 min at 4° C and sterile-filtered with membrane filters (0.45 μm). The supernatant was loaded on a 50 ml Superloop (GE Healthcare, UK) and separated with anion exchange chromatography (Hi Prep 16/10 Q FF column; GE Healthcare, UK) with a gradient of NaCl (0 mM – 500 mM). The fractions were analyzed with SDS-PAGE and the corresponding fractions were pooled, sterile filtered (0.45 μm) and subsequently concentrated. The buffer was exchanged to SEC Buffer with centrifugal filters (MWCO: 100 kDa). The sample was further separated with a size exclusion chromatography (SEC) having two SEC column in series (Suprose 6 prep grade and HiPrep Sephacryl S-200 HR; GE Healthcare, UK). After analyzing the fractions with native PAGE, corresponding fractions were pooled, filtered, concentrated and the buffer was exchanged to AXC buffer. The last purification step was performed with a MonoQ 10/100 GL (GE, USA) anion exchange column with a gradient of NaCl (0 mM – 500 mM). Fractions were analyzed with SDS-PAGE and those fractions with a balanced α/β -ratio were pooled, filtered, concentrated and the buffer was exchanged to Buffer B with 0.02% w/v NaN_3 . THS was stored in the fridge.

SDS-PAGE:

SDS-PAGE gels were prepared according to Laemmli's protocol and adapted from "Commonly Used Techniques in Molecular Cloning," Appendix 8, in *Molecular Cloning, Volume 3, 3rd edition*, by Joseph Sambrook.^{286, 287} The samples were denaturated at 95°C for 3 min and subsequently loaded on 12% SDS-PAGE gel and run for 70 min at constant voltage of 200 V. For specific gels, a fluorescence image (Bio-Rad Gel doc EZ imager) was recorded before staining with Coomassie blue.

Native-PAGE:

The samples were mixed with 5x Loading Buffer, loaded on a 4%-20% precast gel (10 well, mini-protean, Bio-Rad, USA) and run in Tris-glycine Buffer for 3.5 h at constant 100 V. Gels were stained for 30 min with GelRed and a fluorescence image was recorded (Bio-Rad Gel doc EZ imager).

THS-Atto647 labeling:

Cysteines of THS were labeled with Atto647-maleimide (Atto647-mal) by reacting THS with a 40-fold excess of Atto647-mal. To this end, 7 μM THS was reacted with 280 μM Atto647-mal in Buffer B for 2.5 h at RT under shaking. THS-Atto647 was purified from free dye with HiTrap desalting columns (Sephadex G25 Superfine; GE Healthcare, UK). Concentration and buffer exchange was performed with centrifugal filters (MWCO: 100 kDa).

Transmission electron microscopy (TEM):

5 μl of 20 nM protein solutions were deposited for 60 s on a glow-discharged grid, washed twice with ddH₂O and negatively stained twice with 1% uranyl acetate solution. The samples were imaged with a Fei Morgagni 268 D TEM at an accelerating voltage of 80 kV.

Cryo-transmission electron microscopy (Cryo-TEM):

A 4 μl aliquot of sample was adsorbed onto glow-discharged holey carbon-coated grid (Quantifoil, Germany), blotted with Whatman filter paper and vitrified into liquid ethane at -178 °C using a vitrobot (FEI company, Netherlands). Frozen grids were transferred onto a Philips CM200-FEG electron microscope using a Gatan 626 cryo-holder (GATAN, USA). Electron micrographs were recorded at an accelerating voltage of 200 kV and a nominal magnification of 50000 x, using a low-dose system ($10 \text{ e}^-/\text{\AA}^2$) and keeping the sample at -175 °C. Defocus values were -4 μm . Micrographs were recorded at 4K x 4K CMOS camera (TVIPS, Germany). Cryo-TEM density maps were processed with EMAN2 from 100 particles.

MALDI-MS:

To measure MALDI-MS 1 μl of about 10 μM sample was mixed with 3 μl 10 mg/ml sinapinic acid in 40% acetonitrile and 60% trifluoroacetic acid (0.1% v/v) and incubated for 1 h. 2 μl of the mix was applied on a MSP 96 target ground steel plate (Bruker, USA) and let dry for another hour. MALDI-MS was measured on a microflex FLEX-PC (Bruker, USA) in linear mode with positive voltage. 1000 shots were recorded. Multi-peak fitting was performed with OriginPro 8 (OriginLab, USA).

UPLC-MS:

UPLC-MS was measured at an open access instrument at Novartis (Basel Campus). Unfortunately, neither the instrument data nor the procedure was communicated.

THS stability tests:

Following buffers were used for the different pH values: 100 mM Citrate buffer pH 3, 150 mM NaCl; 100 mM MES pH 5.3, 150 mM NaCl; PBS pH 7.5; 500mM carbonate pH 9.5, 150mM NaCl. 1.1 μl 18.2 μM THS was filled up to 20 μl with corresponding buffer to a final THS concentration of 1 μM . The

THS samples were incubated for 2 h at RT and subsequently native PAGE and TEM analysis were done.

For the stability tests in organic solvents 2 μ l 5 μ M THS was mixed with 10 μ l of different ratios of DMF or AcN with 0.1x Buffer B. The samples were incubated overnight at RT and subsequently analysed with native PAGE.

FCS:

A Zeiss 510-META/Confocor2 laser-scanning microscope equipped with an argon and He/Ne laser and a 40_{water}-immersion objective (Zeiss C/Apochromat 40X, NA 1.2) was used in FCS mode. Fluctuation traces were recorded ten times at 15 seconds each. The samples were excited at 633 nm and the emission was collected with a LP-filter at 650 nm. Fluorescence intensity fluctuations were analyzed in terms of an autocorrelation function with the LSM 510/Confocor software package (Carl Zeiss AG, Switzerland). The triplet fraction was set to a correlation time of 3 μ s.

Conjugation of BBN-8/12EG-PITC to THS and THS-Atto647:

For the modification of THS and THS-Atto647 with BBN-8/12EG-PITC a 300-fold excess of BBN over THS was used. 20 μ l 5.0 μ M THS was reacted with freshly prepared 30 μ l 1 mM BBN-8EG-PITC in 100 mM carbonate buffer pH 9 for 2h at RT under gentle shaking. For the modification of THS-Atto647 with BBN 20 μ l 6.5 μ M THS-Atto647 was reacted with 39 μ l 1 mM BBN-8EG-PITC in 100 mM carbonate buffer pH 9 for 2h at RT under gentle shaking. Same procedures were applied for the conjugation of THS and THS-Atto647 with BBN-12EG-PITC. Free BBN-8/12EG-PITC was separated from BBN-8/12EG-THS and BBN-8/12EG-THS-Atto647 by filter centrifugation (MWCO: 100 kDa). The buffer of BBN-8/12EG-THS was exchanged to water and the buffer of BBN-8/12EG-THS-Atto647 to PBS. Uptake of BBN-8/12EG-THS-Atto647 by PC-3 cells was studied with FACS and CLSM.

Conjugation of Biotin-LC-NHS to THS-Atto647:

For the modification of THS-Atto647 with Biotin-LC-NHS a 100-fold excess of Biotin over THS was used. 15 μ l 12.8 μ M THS was reacted with 85 μ l 190 μ M Biotin-LC-NHS in Buffer A for 2h at RT under gentle shaking. Free Biotin was separated from Biotin-THS-Atto647 by filter centrifugation (MWCO: 100 kDa). The buffer was exchanged to PBS. Cell-uptake of Biotin-THS-Atto647 was studied with FACS on HeLa and CHO-K1 cells.

Conjugation of FA-PEG₂₀₀₀-NHS to THS-Atto647:

For the modification of THS-Atto647 with FA-PEG₂₀₀₀-NHS a 50-fold excess of Biotin over THS was used. 30 μ l 8.5 μ M THS was reacted with 70 μ l 128 μ M FA-PEG₂₀₀₀-NHS in Buffer A for 3h at RT under gentle shaking. Free folic acid was separated from FA-THS-Atto647 by filter centrifugation (MWCO: 100 kDa). The buffer was exchanged to PBS. Uptake of FA-THS-Atto647 by HeLa cells was studied with FACS and CLSM.

Conjugation of Somatostatin to THS-Atto647:

For the modification of THS-Atto647 with SST, THS-Atto647 was first modified with a 100-fold excess of PEG₄-PFB and SST with a 5-fold excess of HyNic. To this end, 15 μ l 12.8 μ M THS was reacted with 85 μ l 225 μ M PEG₄-PFB in Buffer A and 50 μ l 1 mM SST was reacted with 150 μ l 1.67 μ M HyNic

in Buffer A for 2 h at RT under gentle shaking. Free educts were separated from FB-THS-Atto647 by filter centrifugation (MWCO: 100 kDa) and from Somatostatin-HyNic by dialysis (MWCO: 500-1000Da) against Buffer B (buffer change after 1 h, 3 h, 7 h and 15 h). A 200-fold excess of SST-HyNic over FB-THS-Atto647 was used for the SST-THS-Atto647 conjugation. 15 μ l 12.8 μ M THS-FB was reacted with 38.4 μ l 1 mM SST-HyNic in Buffer B for 2 h at RT under gentle shaking. Free Somatostatin was separated from SST-THS-Atto647 by filter centrifugation (MWCO: 100 kDa). The buffer was exchanged to PBS. Cell-uptake of SST-THS-Atto647 was studied with FACS on MCF-7 and CHO-K1 cells.

Conjugation of cRGDFc to THS-Atto647:

THS-Atto647 was first modified with SM(PEG)₂. Therefore, a 100-fold excess of SM(PEG)₂ over THS was used. First, 20 μ l 6.5 μ M THS-Atto647 was reacted with 30 μ l 433 μ M SM(PEG)₂ in Buffer A for 2 h at RT under gentle shaking. Free SM(PEG)₂ was separated from mal-THS-Atto647 by filter centrifugation (MWCO: 100 kDa). In a second step, 100 μ l 1.3 μ M mal-THS-Atto647 was reacted with a 200 fold excess of cRGDFc (2.6 μ l 10 mM) in Buffer A. Free cRGDFc was separated from cRGDFc-THS-Atto647 by filter centrifugation (MWCO: 100 kDa). The buffer was exchanged to PBS. Cell-uptake of cRGDFc-THS-Atto647 was studied with FACS and CLSM on MCF-7 and U-87 MG cells.

Conjugation of HyNic-TAT to THS-Atto647:

THS-Atto647 was first modified with PEG₄-PFB. Therefore, a 100-fold excess of PEG₄-PFB over THS was used. First, 42 μ l 6.1 μ M THS-Atto647 was reacted with 58 μ l 440 μ M SM(PEG)₂ in Buffer A for 2 h at RT under gentle shaking. Unbound PEG₄-PFB was separated from FB-THS-Atto647 by filter centrifugation (MWCO: 100 kDa). In a second step, 100 μ l 2.55 μ M FB-THS-Atto647 was reacted with a 50 fold excess of HyNic-TAT (50 μ l 255 μ M) in Buffer B. Free HyNic-TAT was separated from TAT-THS-Atto647 by filter centrifugation (MWCO: 100 kDa). The buffer was exchanged to PBS. Uptake of TAT-THS-Atto647 by PC-3 was studied with FACS and CLSM.

Conjugation of VEGF to THS-Atto647:

For the modification of THS-Atto647 with VEGF, THS-Atto647 was first modified with a 100-fold excess of PEG₄-PFB and VEGF with a 10-fold excess of HyNic. To this end, 15 μ l 12.8 μ M THS was reacted with 85 μ l 225 μ M PEG₄-PFB in Buffer A and 52 μ l 10 μ M VEGF was reacted with 48 μ l 108 μ M HyNic in Buffer A for 2 h at RT under gentle shaking. Free educts were separated from FB-THS-Atto647 by filter centrifugation (MWCO: 100 kDa) and from VEGF-HyNic also by filter centrifugation (MWCO: 3 kDa). A 3-fold excess of VEGF-HyNic over FB-THS-Atto647 was used. 50 μ l 3.8 μ M THS-FB was reacted with 50 μ l 10 μ M VEGF-HyNic in Buffer B for 2h at RT under gentle shaking. Free VEGF-HyNic was separated from VEGF-THS-Atto647 by filter centrifugation (MWCO: 100 kDa). The buffer was exchanged to PBS. Cell-uptake of VEGF-THS-Atto647 was studied with FACS on HUVEC and CHO-K1 cells.

Cells:

All cell lines were grown at 37°C under a 5% CO₂ atmosphere in specific cell culture media (further labelled as 'normal cell grow conditions'). Cell culture media were: HeLa and PC-3: Dulbecco's modified Eagle medium (DMEM); CHO-K1: Roswell Park Memorial Institute medium 1640 (RPMI); HUVEC: DMEM, 20 U ml⁻¹ Heparin, 30 μ l ml⁻¹ endothelial cell growth supplement (ECGS); MCF-7 and

U-87 MG: minimum essential medium Eagle (MEME) with non-essential amino acids (NEAA). All media were with 10% fetal calf serum (FCS), 200 U ml⁻¹ penicillin and 200 µg ml⁻¹ streptomycin. When cells reached a confluency of about 80%, they were split and subcultured by trypsinization.

Flow cytometry:

For FC measurements 100'000 cells were seeded into 24-well plates, filled up with 1.5 ml cell culturing medium and incubated under normal cell culture conditions. After 2 days the medium was aspirated, the samples were added and filled up to 100 µl with cell culturing medium so that the final dye (Atto647 or Atto655) concentration was: BBN-8/12EG-THS-Atto647: 200 nM, Biotin-THS-Atto647: 100 nM, FA-THS-Atto647: 100 nM, SST-THS-Atto647: 100 nM, cRGDFC-THS-Atto647: 200 nM, THS-Atto647: 200 nM, TAT-THS-Atto647: 150 nM and VEGF-THS-Atto647: 200 nM. After 2 h or 10 min of incubating under normal cell grow conditions, the cells were washed with PBS, trypsinized and put on ice. FACS measurements were performed with a FACSCanto II (BD, USA) with at least 10'000 cells. The cells were excited with a HeNe-laser at 633 nm and the emitted light passed through a Band Pass 660/20 filter before reaching the detector. Data were processed with FlowJo Vx (Tree Star, USA) and a histogram of fluorescence of single cells only was plotted. The median fluorescence values of cells treated with samples was compared to the median fluorescence of untreated cells.

Live cells images:

For live images 50'000 cells were seeded in 8-well microscope chamber slides for 24 h in normal cell culture conditions. Before adding the samples to the cells, old medium was removed; new medium was added to such an amount that in the end the total volume with sample resulted to be 100 µl. The final dye (Atto647) concentrations were following: BBN-8/12EG-THS-Atto647: 200 nM, FA-THS-Atto647: 200 nM, cRGDFC-THS-Atto647: 200 nM, THS-Atto647 200: nM, TAT-THS-Atto647: 40 nM and for the reductive release studies dye concentration were THS-SS-Atto655: 500 nM and THS-Atto647: 500 nM. After 10 min or 2 h incubation under normal cell growing conditions the cells were washed with PBS and 400 µl serum free medium was added. To stain nuclei, cell membrane and/or acidic compartments, the cells were incubated in 0.2 µg ml⁻¹ Hoechst 33342 for 25 min and 2.5 µg ml⁻¹ CellMask orange for 5 min or 20 nM LysoTracker Red for 10 min, respectively. Subsequently, cells were washed with PBS and wells were refilled with 400 µl PBS. Cell imaging was performed by confocal laser scanning microscopy (CLSM) with a Zeiss 510-META/Confocor2 microscope equipped with a laser diode (405 nm), argon laser (488 nm) and a helium/neon laser (633nm); and a 40x_water-immersion objective (Zeiss C-Apochromat 40x/1.2 W corr). The samples were excited at 405 nm, 514 nm (NFT mirror 545) or 633 nm (NFT mirror 545) and the emission was collected with a broad pass filter at 420-480 nm, a broad pass filter 560-615 nm or an long pass filter at 650 nm, respectively. The pinholes were set to 61 µm, 80 µm and 92 µm, respectively. The cells were imaged in multitrack mode with a resolution of 1024 x 1024 pixels (225 µm x 225 µm) with a pixel time of 25.6 µs. Some images were cropped to 512 x 512 pixels (112 µm x 112 µm) using LSM Image Browser (Zeiss).

THS-PAMAM conjugation:

THS (10 µM) was reacted with MTFB (2 mM; 200 equiv. to THS; 12.5 equiv. to subunits) in Buffer A for 2.5 h at RT under shaking. Subsequently, the buffer was exchanged to Buffer B. PAMAM (500 µM) was modified in Buffer B at RT for 2 h under shaking with a 10-fold excess of HyNic (5 mM). After

purification, modified THS- and modified PAMAM were mixed to a final concentration of 10 μM and 500 μM , respectively. The solution was incubated overnight in Buffer B at RT under gentle shaking. The conjugation kinetic was measured with a Specord 210 plus spectrometer (analyticjena, Germany). Separation of THS-PAMAM from excess of PAMAM was carried out by SEC (HiPrep 16/60 Sephacryl S-200 column) in SEC Buffer. Chromatograms at 280 nm and 350 nm were recorded and the peaks were pooled and concentrated. NaN_3 was removed and buffer was exchanged to the buffers needed for the various further experiments by centrifugal filtration.

Molecular substitution ratio (MSR) of THS-MTFB:

To determine the degree of modification of THS with MTFB, THS-MTFB was reacted with 2-hydrazinopyridine. 1.7 μM THS-MTFB was reacted with 450 μM 2-hydrazinopyridine in 100 mM sodium citrate buffer pH 5.0 for 30 min at 37°C. The absorbance was measured at 350 nm, whereby the absorbance of the negative control (450 μM 2-hydrazinopyridine) was subtracted.

MSR of PAMAM-HyNic:

PAMAM was modified with HyNic as described in “*THS-PAMAM conjugation*”, but the excess of HyNic over PAMAM was varied between 6 and 100. To measure the MSR, 10 μM PAMAM-HyNic was incubated with 450 μM 4-nitrobenzaldehyde in buffer A for 30 min at 37°C. The absorbance was measured at 390 nm ($\epsilon_{390\text{ nm}} = 24'000\text{ M}^{-1}\text{ cm}^{-1}$) using a SpectraMax M5^e (Molecular Device) spectrometer, and the absorbance of the negative control (450 μM 4-nitrobenzaldehyde) was subtracted. The degree of modification could be controlled by the concentration of HyNic in the reaction mixture.

THS-PAMAM conjugate analysis:

For SDS-PAGE and FCS analysis of the conjugate, PAMAM-HyNic was labelled with Atto647-hydroxysuccinimide (-NHS) by reacting PAMAM-HyNic (133 μM) with a 5-fold excess of Atto647-NHS (666 μM) in Buffer A for 1.5 h at RT in the dark. Unbound Atto647 was separated by rigorous dialysis (MWCO: 10 kDa) against 0.1 M NaCl. Then, the sample was concentrated and the buffer exchanged with centrifugal filters (MWCO: 3 kDa). Some of Atto647-PAMAM-HyNic was further linked to THS-FB.

THS-AuNP:

30 μl 10 μM THS was reacted with a 20-fold excess of 1.4 nm monomaleimido nanogold (AuNP-mal) (100 μl 60 μM) in Buffer B for 2 h at RT under gentle shaking. The sample was purified by size exclusion from unreacted AuNP by SEC as described in above (*THS-PAMAM conjugation*).

THS-PAMAM-AuNP:

4 μl 500 μM PAMAM was modified with 100 μl 60 μM 1.4 nm mono-sulfo-NHS-nanogold (AuNP-NHS) and 4 μl 5 mM HyNic in Buffer A for 1.5 h at RT under gentle shaking. Free HyNic was removed with centrifugal filters (MWCO: 3 kDa). THS-MTFB was modified with AuNP-PAMAM-HyNic as described above (*THS-PAMAM conjugation*).

siRNA binding to THS-PAMAM:

THS-PAMAM (3 μM) was incubated with a 5-fold excess of siRNA (15 μM) in RNase free Buffer A for 10 min at 37 °C. Unbound siRNA was removed by extensive centrifugal filtration (MWCO: 100 kDa). siRNA on the THS-PAMAM was quantified by UV/Vis spectroscopy. To this end, the absorbance spectrum of THS-PAMAM in the absence of siRNA was normalized to the absorbance of THS-PAMAM-siRNA at 354 nm. The concentration of siRNA was calculated from the difference in absorbance at 260 nm.

Electrophoretic mobility shift assays (EMSA):

Samples were run for 40 min at constant voltage of 100 V on a 1.2 % agarose gel in TRIS-acetate-EDTA (TAE) buffer. The gel was stained with GelRed stain and a UV-image was recorded (Bio-Rad Gel doc EZ imager). THS-PAMAM and THS concentration of 6 μM and siRNA concentration of 2 μM were used for the samples. The samples were incubated for 10 min at 37°C. To selected samples SDS was added to a final concentration of 0.4% and incubated for another 10 min at RT. 10 μl of each sample were mixed with 2 μl loading buffer (6X MassRuler DNA Loading Dye) and loaded on the gel.

Digestion assays:

siRNA (2 μM) was incubated with either PAMAM (6 μM), THS-PAMAM (6 μM , PAMAM-concentration) or on its own for 10 min at 37°C. Then, 50 U ml^{-1} RNase A was added and the solutions were incubated at 37°C for defined time intervals (0 min, 5 min, 10 min, 20 min, 30 min, 40 min and 60min). SDS was added to a final concentration of 0.4% to all the samples except the ones with THS-PAMAM. Immediately thereafter, the samples were analyzed by agarose gel electrophoresis and imaged with a fluorescence gel reader. Fluorescence intensity analysis was performed with ImageJ 1.48v (NIH, USA). The fluorescence was normalized to the fluorescence of the samples that were incubated for 0 min.

THS-PAMAM-TAT:

THS-PAMAM (5.4 μM) was modified with a 20-fold excess of PEG₄-PFB (108 μM) in Buffer A for 2 h at RT under shaking. The product was purified and the buffer was exchanged to Buffer B by filter centrifugation (MWCO: 100 kDa). The resulting THS-PAMAM-PFB (5.4 μM) was reacted with a 20-fold excess of TAT-HyNic (108 μM) in Buffer B overnight at RT under shaking. Free TAT-HyNic was separated from TAT-THS-PAMAM by filter centrifugation (MWCO: 100 kDa).

siRNA delivery:

Silencer KIF11 (Eg5) siRNA (sequence not provided by the supplier) was used as active siRNA and scrambled siRNA with following sequence was used as negative control: 5'-AGG UAG UGU AAU CGC CUU GTT-3'. KIF11 siRNA or scrambled RNA were bound to THS-PAMAM or TAT-THS-PAMAM as described above. siRNA transfection was performed according to the reversed siRNA transfection protocol from the manufacturer (Invitrogen, USA). For this purpose THS-PAMAM-siRNA, TAT-THS-PAMAM-siRNA or 0.5 μl LF and siRNA were pipetted into wells of a 96-well-plate and filled up to 10 μl with RNase free buffer, resulting in a siRNA concentration of 1 μM . After 10 min 5'000 cells were added to each well and filled up to 100 μl with medium without serum and antibiotics, resulting in a final siRNA concentration of 100 nM. All experiments were conducted with KIF11 siRNA and scrambled siRNA to calculate the viability decrease due to KIF11 siRNA. The medium was exchanged to normal growth medium after 5 h. The cells were incubated 72 h in total under normal growth

conditions. The cell viability was determined with the cell counting kit-8 (CCK-8). Absorbance of converted CCK-8 was measured at 450 nm with a SpectraMax M5^e (Molecular Device) plate reader. As background medium plus CCK-8 was measured which was subtracted from the data. The viabilities of cells treated with siRNA and scrambled RNA were normalized to the viability of untreated cells. All measurements were performed in multiple, whereas n indicates the number of experiments. All data were first tested with Prism (GraphPad, USA) to confirm that they are normally distributed and have the same variance. As this was the case, two-sided Student's t-test were applied, whereas significant level was set to $p < 0.05$ (*) and $p < 0.01$ (**). Data are presented as mean \pm SD.

Conjugation of Atto655-NH₂ to THS via linker containing a disulfide bond:

First, Atto655-NH₂ was modified with a 10-fold excess of S-SS-4FB. To this end 150 μ l 1 mM Atto655-NH₂ was reacted with 350 μ l 4.29 mM S-SS-4FB in Buffer A for 2.5 h in the dark at RT under gentle shaking. The product was purified with a Prominence UFLC Fast LC (Shimadzu, Japan) equipped with a reversed phase Chromolith column (Chromolith Performance RP-18e 100-4.6 mm). A linear gradient from 90% milli-Q water with 2% acetic acid to 40% AcN was run with a flow rate of 7.5 ml min⁻¹. A continuous spectrum from 300 – 800 nm was recorded (deuterium and tungsten lamp). The fractions which absorbed at 654 nm the most (around 2.2 ml, 52% AcN) were pooled, neutralized with ammonium and subsequently lyophilized. The lyophilized Atto655-SS-FB was dissolved in Buffer B and analysed with LC-ESI-MS. At this step the liquid chromatography was performed with a Prominence UFLC Fast LC (Shimadzu, Japan). A linear gradient from 90% milli-Q water with 0.01% formic acid to 95% AcN with 0.01% formic acid was run with a flow rate of 0.5 ml min⁻¹. The absorbance at 254 nm was recorded. The masses were measured with an amaZon X ESI-MS (Bruker, USA) in positive and negative mode with a scan area of 75 – 1200 m/z. The data were analyzed with Compass DataAnalysis (Bruker, USA).

THS was first modified with a 200-fold excess of MHP. 50 μ l of 14.1 μ M THS was reacted with 50 μ l 2.82 mM MHP in Buffer A for 2.5 h at 37° C under gentle shaking. Unbound MHP was separated from THS-HP by filter centrifugation (MWCO: 100 kDa) and the buffer was changed to Buffer B. A 20-fold excess of Atto655-SS-FB over THS-HP was used. 60 μ l 6 μ M THS-MHP was reacted with 140 μ l 70 μ M Atto655-SS-FB in Buffer B over night at RT under gentle shaking. THS-SS-Atto655 was purified from free dye with HiTrap desalting columns (Sephadex G25 Superfine; GE Healthcare, UK). Concentration and buffer exchange was performed with centrifugal filters (MWCO: 100 kDa).

BSA-SS-Atto655 conjugation:

The conjugation of BSA-SS-Atto655 was done similarly to the conjugation of THS-SS-Atto655. 100 μ l 40 μ M BSA was reacted with 2 μ l 50 mM HyNic (25-fold excess over BSA) for 2.5 h at 37° C under gentle shaking. Unbound HyNic was separated from BSA-HyNic by filter centrifugation (MWCO: 30 kDa) and the buffer was changed to Buffer B. A 20-fold excess of Atto655-SS-FB over BSA-HyNic was used. 20 μ l 40 μ M BSA-HyNic was reacted with 230 μ l 70 μ M Atto655-SS-FB in Buffer B over night at RT under gentle shaking. BSA-SS-Atto655 was purified from free dye with HiTrap desalting columns (Sephadex G25 Superfine; GE Healthcare, UK). Concentration and buffer exchange was performed with centrifugal filters (MWCO: 30 kDa).

Reduction kinetic of BSA-SS-Atto655 (fluorescence):

The change in fluorescence of 5 μM BSA-SS-Atto655 and 5 μM Atto655 in 10 mM GSH was measured with a SpectraMax M5^e (Molecular Device) plate reader. The samples were excited at 663 nm and the emission was recorded at 684 nm, with a cut-off at 665 nm. The reaction was done at 37° C.

Reduction kinetic of THS-SS-Atto655 (FCS):

FCS curves of THS-SS-Atto655 and THS-Atto647 were measured in 10 mM GSH after 10 min, 20 min, 30 min, 60 min, 120 min, 240 min, 300 min and 360 min incubation. Thereby, the samples had a dye concentration of 10 nM. The FCS curves were fitted with a two-component-fit, where one component (free dye) was fixed to 55 μs (measured diffusion time of the dyes) and one component (THS-dye) was set free. For the analysis of the curves the percentages of the free dye component after 10 min were used as background and therefore subtracted from all results.

Flow cytometry analysis of U87-MG cells with THS-SS-Atto655 and THS-Atto647:

FC studies were conducted as described above. THS-SS-Atto655 and THS-Atto647 were added to U87-MG cells to a final dye concentration of 150 nM and incubated for 15 min, 1 h, 2h and 4h. Subsequently, the cells were analysed by FC. For the analysis of the data the median fluorescence of the untreated cells were set to zero and the median fluorescence of cells treated 4 h with THS-SS-Atto655 and THS-Atto647 was set to one.

ATPase activity of THS:

The ATPase activity of THS was measured by incubating different concentrations of THS (0.02 μM , 0.05 μM , 0.1 μM and 0.2 μM) with 20 mM ATP in either 100 mM MES buffer pH 5.25, 150 mM NaCl, 5 mM MgCl_2 or 30 mM Tris-HCl buffer pH 7.4, 100 mM KCl, 5 mM MgCl_2 . These reactions were incubated for 30 min at either 37° C or 55° C. The released phosphate was subsequently measured with an improved malachite green assay (QuantiChrom ATPase/GTPase Assay Kit, DATG-200, BioAssay Systems, USA). The data were analysed according the manufacturer's protocol.

Analysis of THS' conformation with native PAGE:

0.5 μM THS was incubated with either (1) 5 mM EDTA; (2) 5 mM MgCl_2 and 1 mM ATP; (3) 5 mM MgCl_2 and 25 mM ATP- γ -S; or (4) 5 mM MgCl_2 , 1 mM ATP, 1 mM $\text{Al}(\text{NO}_3)_3$ and 6 mM NaF in 100 mM MES buffer pH 5.25 and 150 mM NaCl for 30 min at 37° C. Subsequently, the samples were analyzed with native PAGE.

Degradation assay with THS with different nucleotides:

0.25 μM THS was incubated with either (1) 5 mM EDTA; (2) 5 mM MgCl_2 and 1 mM ATP; (3) 5 mM MgCl_2 , 1 mM ATP, 4 mM $\text{Al}(\text{NO}_3)_3$ and 30 mM NaF; (4) 5 mM MgCl_2 , 6 mM ATP, 4 mM $\text{Al}(\text{NO}_3)_3$ and 30 mM NaF; (5) 5 mM MgCl_2 and 15 mM ATP- γ -S in 100 mM MES buffer pH 5.25, 150 mM NaCl for 30 min at 37° C. 5 μl of 8 $\mu\text{g}/\text{ml}$ proteinase K was added to 15 μl of the samples and incubated for 10 min at RT. The reaction was stopped with 0.5 μl 300 mM PMSF and the samples were set on ice. Subsequently, the samples were analyzed with SDS-PAGE.

Small angle X-ray scattering (SAXS):

50 μl of 2 μM ($\sim 2 \text{ mg ml}^{-1}$) THS with either (1) 5 mM EDTA; (2) 5 mM MgCl_2 and 1 mM ATP; or (3) 5 mM MgCl_2 , 6 mM ATP, 4 mM $\text{Al}(\text{NO}_3)_3$ and 24 mM NaF in 100 mM MES buffer pH 5.25, 150 mM NaCl was incubated at 37° C for 15 min. Subsequently, the samples were loaded into a glass capillary ($d = 1 \text{ mm}$, thickness of the wall = 0.01 mm) and sealed with wax. Small angle X-ray scattering (SAXS) measurement were conducted on a Bruker AXS Nanostar with an Incoatec Cu - μS Microfocus X-ray source ($\lambda = 0.154 \text{ nm}$) and a VANTEC 2000 2D detector. The measurements were performed at 45 kV and 650 μA . The integration time was set to 2 h. The data were azimuthally integrated with SAXS v.4.1.36 Bruker software (Bruker, USA). The distance distribution function was calculated with GNOM (ATSAS, EMBL, Germany), where R_{max} was set to 170 Å.

TEM analysis of the conformational state of THS:

10 nM THS was incubated for 30 min at 37° C in either (1) 5 mM EDTA or (2) 5 mM MgCl_2 , 1 mM ATP, 5 mM $\text{Al}(\text{NO}_3)_3$ and 30 mM NaF. Subsequently, TEM micrographs of the samples were made. From the micrographs THS particles were manually classified. For EDTA 622 particles and for ATP-AlFx 828 particles were classified.

Conjugation of HRP into THS:

THS was modified with a 200-fold excess of MTFB. To this end, 100 μl 14.1 μM THS was reacted with 100 μl 2.82 mM MTFB in Buffer A for 2.5 h at 37° C under gentle shaking. The product was purified and the buffer was exchanged to Buffer B by filter centrifugation (MWCO: 100 kDa). 71.8 μl 557 μM HRP (1 eq.) was reacted with 46 μl 8.7 mM HyNic (10 eq.) in Buffer A for 2h at RT under gentle shaking. Unbound HyNic was separated from the product by filter centrifugation (MWCO: 30 kDa) and the buffer was changed to Buffer B. A 25-fold excess of HRP-HyNic over THS-FB was used for the conjugation. Thus, 200 μl 7.1 μM THS-MTFB and 200 μl 200 μM HRP-HyNic were mixed and incubated for 14 h at RT under gentle shaking. Separation of THS-HRP from excess of HRP was carried out by SEC (HiPrep 16/60 Sephacryl S-200 column) in SEC Buffer. Chromatograms at 280 nm and 403 nm were recorded and the peaks were pooled and concentrated. The concentration of HRP was determined by measuring the absorbance at 403 nm, using a $\epsilon_{403 \text{ nm}} = 100'000 \text{ M}^{-1} \text{ cm}^{-1}$.²⁸⁸

ATPase activity of THS-HRP:

The ATPase activity of THS-HRP was measured by incubating different concentrations of THS-HRP (THS concentration: 0.02 μM , 0.05 μM , 0.1 μM and 0.2 μM) with 20 mM ATP in 30 mM Tris-HCl buffer pH 7.4, 100 mM KCl, 5 mM MgCl_2 . These reactions were incubated for 30 min at 37° C. The released phosphate was subsequently measured with an improved malachite green assay (QuantiChrom ATPase/GTPase Assay Kit, DATG-200, BioAssay Systems, USA). The data were analysed according the manufacturer's protocol.

HRP, HRP-HyNic and THS-HRP activity:

HRP activity of HRP, HRP-HyNic and THS-HRP was measured by incubating different concentrations of the samples in respect to HRP (0 nM, 5 nM, 10 nM and 20 nM) in assay buffer (30 mM Tris-HCl pH 7.4, 100 mM KCl, 5 mM MgCl_2 , 1 mM H_2O_2 and 1 mM ABTS) at 37° C. The change of absorbance at 420 nm was measured for 120 s with a SpectraMax M5^e (Molecular Device) plate reader. With the extinction coefficient of $\text{ABTS}^{+\bullet}$ $\epsilon_{420 \text{ nm, ABTS}} = 36'000 \text{ M}^{-1} \text{ cm}^{-1}$ ²⁸⁹ the oxidation rate of HRP was

calculated. The slope (\pm SD) of the change in concentration of ABTS^{••} was plotted against the HRP concentration.

HRP activity in THS upon different nucleotides:

ABTS assay: HRP activity of HRP and THS-HRP was measured by incubating different concentrations of THS-HRP (HRP concentration: 0 nM, 5 nM, 10 nM and 20 nM) with either (1) 1 mM ATP; (2) 1 mM ATP- γ -S; or (3) 1 mM ATP, 1 mM Al(NO₃)₃ and 6 mM NaF in assay buffer (30 mM Tris-HCl pH 7.4, 100 mM KCl, 5 mM MgCl₂, 1 mM H₂O₂ and 1 mM ABTS) at 37° C. The change of absorbance at 420 nm was measured for 120 s with a SpectraMax M5^e (Molecular Device) plate reader. With the extinction coefficient of ABTS^{••} $\epsilon_{420 \text{ nm, ABTS}} = 36'000 \text{ M}^{-1} \text{ cm}^{-1}$ ²⁸⁹ the oxidation rate of THS-HRP was calculated. The slope (\pm SD) of the change in concentration of ABTS^{••} was plotted against the HRP concentration.

DhRh6G assay: HRP activity of HRP and THS-HRP was measured by incubating different concentrations of THS-HRP (HRP concentration: 0 nM, 5 nM, 10 nM and 20 nM) with either (1) 1 mM ATP; (2) 1 mM ATP- γ -S; or (3) 1 mM ATP, 1 mM Al(NO₃)₃ and 6 mM NaF in assay buffer (30 mM Tris-HCl pH 7.4, 100 mM KCl, 5 mM MgCl₂, 500 μ M H₂O₂ and 500 μ M ABTS) at 37° C. The change of fluorescence excited at 520 nm and emitted at 555 nm was measured for 100 s with a SpectraMax M5^e (Molecular Device) plate reader. The slope (\pm SD) of the change fluorescence was plotted against the HRP concentration.

AuNP formation in THS-PAMAM:

The low gold concentration protocol to form AuNP was as follow: 10 μ l 550 μ M HAuCl₄ was added to 30 μ l 3.3 μ M PAMAM, THS or THS-PAMAM in 20 mM Tris pH 9, 200 mM NaCl, and incubated for 45 min. Afterwards 10 μ l 2.75 mM NaBH₄ was added and incubated for another 45 min. NaBH₄ solution was always prepared minutes before the experiment. To stop the reaction, the buffer was exchanged to PBS with centrifugal filters (MWCO: 3 kDa for PAMAM, MWCO: 100 kDa for THS-PAMAM) and to remove AuNP aggregates, the samples were filtered with syringe filters (0.45 μ m). For the high gold concentration protocol, ten-fold higher HAuCl₄ and NaBH₄ concentrations were used. In the repetitive protocol, the low gold concentration protocol was 5 times repeated including the filtration steps. TEM images of AuNP formed in THS-PAMAM were analysed. For the low gold concentration protocol 486 THS-PAMAM and 11 AuNP particles were analyzed, for the high gold concentration protocol 481 THS-PAMAM and 75 AuNP particles were analyzed and for the repetitive protocol 70 THS-PAMAM and 53 AuNP particles were analyzed. The diameters of AuNP were manually measured with ImageJ 1.48v (National Institutes of Health, USA).

PAMAM toxicity:

20'000 PC-3 cells were seeded in 96-well plates and incubated under normal growth conditions for 24 h. After this time, the old medium was removed and new medium with different PAMAM concentrations (3 μ M, 10 μ M, 30 μ M and 100 μ M) were added. The cells were further incubated for 24h and subsequently the cell viability was measured with a CCK-8 assay (as described in *siRNA delivery*).

Bibliography

1. F. Danhier, O. Feron and V. Pr eat, *Journal of Controlled Release*, 2010, **148**, 135-146.
2. D. Peer, J. M. Karp, S. Hong, O. C. Farokhzad, R. Margalit and R. Langer, *Nat. Nanotechnol.*, 2007, **2**, 751-760.
3. P. Ehrlich, *Pergamon, London*, 1960, 3.
4. P. Boisseau and B. Loubaton, *Comptes Rendus Physique*, 2011, **12**, 620-636.
5. V. P. Torchilin, *Nature Reviews Drug Discovery*, 2014, **13**, 813-827.
6. A. D. McNaught, A. Wilkinson and International Union of Pure and Applied Chemistry., *Compendium of chemical terminology : IUPAC recommendations*, Blackwell Science, Oxford Oxfordshire ; Malden, MA, 2nd edn., 1997.
7. R. A. Freitas, *Nanomedicine*, Landes Bioscience, Austin, TX, 1999.
8. T. M. Allen and P. R. Cullis, *Science*, 2004, **303**, 1818-1822.
9. R. A. Petros and J. M. DeSimone, *Nature Reviews Drug Discovery*, 2010, **9**, 615-627.
10. H. Soo Choi, W. Liu, P. Misra, E. Tanaka, J. P. Zimmer, B. Itty Ipe, M. G. Bawendi and J. V. Frangioni, *Nature Biotechnology*, 2007, **25**, 1165-1170.
11. Y. Matsumura and H. Maeda, *Cancer Research*, 1986, **46**, 6387-6392.
12. A. Albanese, P. S. Tang and W. C. W. Chan, *annual Review of Biomedical Engineering*, 2012, **14**, 1-16.
13. Y. H. Bae, *Journal of Controlled Release*, 2009, **133**, 2-3.
14. Y. H. Bae and K. Park, *Journal of Controlled Release*, 2011, **153**, 198-205.
15. H. Brooks, B. Lebleu and E. Viv es, *Advanced Drug Delivery Reviews*, 2005, **57**, 559-577.
16. E. Koren and V. P. Torchilin, *Trends in Molecular Medicine*, 2012, **18**, 385-393.
17. F. Milletti, *Drug Discovery Today*, 2012, **17**, 850-860.
18. A. MaHam, Z. Tang, H. Wu, J. Wang and Y. Lin, *Small*, 2009, **5**, 1706-1721.
19. Z. Drulis-Kawa and A. Dorotkiewicz-Jach, *International Journal of Pharmaceutics*, 2010, **387**, 187-198.
20. R. Kanasty, J. R. Dorkin, A. Vegas and D. Anderson, *Nature Materials*, 2013, **12**, 967-977.
21. G. Kaul and M. Amiji, *Pharmaceutical Research*, 2005, **22**, 951-961.
22. G. A. Koning and G. C. Krijger, *Anti-Cancer Agents in Medicinal Chemistry*, 2007, **7**, 425-440.
23. C. Nardin, J. Widmer, M. Winterhalter and W. Meier, *European Physical Journal E*, 2001, **4**, 403-410.
24. C. De Vocht, A. Ranquin, R. Willaert, J. A. Van Ginderachter, T. Vanhaecke, V. Rogiers, W. Vers ees, P. Van Gelder and J. Steyaert, *Journal of Controlled Release*, 2009, **137**, 246-254.
25. K. Langowska, C. G. Palivan and W. Meier, *Chemical Communications*, 2013, **49**, 128-130.
26. J. Liu, Y. Huang, A. Kumar, A. Tan, S. Jin, A. Mozhi and X.-J. Liang, *Biotechnology Advances*, 2014, **32**, 693-710.
27. B. Nandy, M. Santosh and P. K. Maiti, *Journal of Biosciences*, 2012, **37**, 457-474.
28. D. J. Phillips and M. I. Gibson, *Antioxidants & Redox Signaling*, 2013, **21**, 786-803.
29. A. Najer, D. L. Wu, D. Vasquez, C. G. Palivan and W. Meier, *Nanomedicine*, 2013, **8**, 425-447.
30. H.-I. Chang and M.-K. Yeh, *International Journal of Nanomedicine*, 2012, **7**, 49-60.
31. M. L. Immordino, F. Dosio and L. Cattel, *International Journal of Nanomedicine*, 2006, **1**, 297-315.
32. T. M. Allen and P. R. Cullis, *Advanced Drug Delivery Reviews*, 2013, **65**, 36-48.
33. B. M. Discher, D. A. Hammer, F. S. Bates and D. E. Discher, *Current Opinion in Colloid & Interface Science*, 2000, **5**, 125-131.
34. R. P. Brinkhuis, K. Stojanov, P. Laverman, J. Eilander, I. S. Zuhorn, F. P. J. T. Rutjes and J. C. M. van Hest, *Bioconjugate Chemistry*, 2012, **23**, 958-965.
35. M. Elsabahy and K. L. Wooley, *Chemical Society Reviews*, 2012, **41**, 2545-2561.
36. S. Venkataraman, J. L. Hedrick, Z. Y. Ong, C. Yang, P. L. R. Ee, P. T. Hammond and Y. Y. Yang, *Advanced Drug Delivery Reviews*, 2011, **63**, 1228-1246.

37. N. Larson and H. Ghandehari, *Chemistry of Materials*, 2012, **24**, 840-853.
38. G. Gunkel-Grabole, S. Sigg, M. Lomora, S. Lorcher, C. G. Palivan and W. P. Meier, *Biomaterials Science*, 2014, DOI: 10.1039/C4BM00230J.
39. F. M. Veronese and G. Pasut, *Drug Discovery Today*, 2005, **10**, 1451-1458.
40. T. Ishida, K. Atobe, X. Wang and H. Kiwada, *Journal of Controlled Release*, 2006, **115**, 251-258.
41. T. Ishida, M. Ichihara, X. Wang, K. Yamamoto, J. Kimura, E. Majima and H. Kiwada, *Journal of Controlled Release*, 2006, **112**, 15-25.
42. U. Kedar, P. Phutane, S. Shidhaye and V. Kadam, *Nanomedicine: Nanotechnology, Biology and Medicine*, 2010, **6**, 714-729.
43. H. Cho, I. Cheong, J. Lee and J. Kim, *Korean J. Chem. Eng.*, 2010, **27**, 731-740.
44. Z. Sezgin, N. Yuksel and T. Baykara, *European journal of pharmaceutics and biopharmaceutics : official journal of Arbeitsgemeinschaft fur Pharmazeutische Verfahrenstechnik e.V*, 2006, **64**, 261-268.
45. N. Nishiyama and K. Kataoka, *Pharmacology & Therapeutics*, 2006, **112**, 630-648.
46. N. Bayó-Puxan, M.-H. Dufresne, A. E. Felber, B. Castagner and J.-C. Leroux, *Journal of Controlled Release*, 2011, **156**, 118-127.
47. B. M. Discher, Y.-Y. Won, D. S. Ege, J. C.-M. Lee, F. S. Bates, D. E. Discher and D. A. Hammer, *Science*, 1999, **284**, 1143-1146.
48. W. Meier, *Chemical Society Reviews*, 2000, **29**, 295-303.
49. M. Antonietti and S. Forster, *Adv. Mater.*, 2003, **15**, 1323-1333.
50. K. Kita-Tokarczyk, J. Grumelard, T. Haefele and W. Meier, *Polymer*, 2005, **46**, 3540-3563.
51. F. C. Gaertner, R. Luxenhofer, B. Blechert, R. Jordan and M. Essler, *Journal of Controlled Release*, 2007, **119**, 291-300.
52. R. Hoogenboom, *Angewandte Chemie International Edition*, 2009, **48**, 7978-7994.
53. E. Cabane, X. Zhang, K. Langowska, C. Palivan and W. Meier, *Biointerphases*, 2012, **7**, 1-27.
54. J. R. Baker, *ASH Education Program Book*, 2009, **2009**, 708-719.
55. E. R. Gillies and J. M. J. Frechet, *Drug Discovery Today*, 2005, **10**, 35-43.
56. D. A. Tomalia, H. Baker, J. Dewald, M. Hall, G. Kallos, S. Martin, J. Roeck, J. Ryder and P. Smith, *Polymer Journal*, 1985, **17**, 117-132.
57. R. Esfand and D. A. Tomalia, *Drug Discovery Today*, 2001, **6**, 427-436.
58. U. Boas and P. M. H. Heegaard, *Chemical Society Reviews*, 2004, **33**, 43-63.
59. P. Kesharwani, K. Jain and N. K. Jain, *Prog. Polym. Sci.*, 2014, **39**, 268-307.
60. A. R. Menjoge, R. M. Kannan and D. A. Tomalia, *Drug Discovery Today*, 2010, **15**, 171-185.
61. S. Biswas and V. P. Torchilin, *Pharmaceutics*, 2013, **6**, 161-183.
62. N. M. Molino and S.-W. Wang, *Current Opinion in Biotechnology*, 2014, **28**, 75-82.
63. M. Uchida, M. T. Klem, M. Allen, P. Suci, M. Flenniken, E. Gillitzer, Z. Varpness, L. O. Liepold, M. Young and T. Douglas, *Adv. Mater.*, 2007, **19**, 1025-1042.
64. J. G. van den Boorn, M. Schlee, C. Coch and G. Hartmann, *Nature Biotechnology*, 2011, **29**, 325-326.
65. J. C. Ranford, A. R. M. Coates and B. Henderson, *Expert Reviews in Molecular Medicine*, 2000, **2**, 1-17.
66. P. A. Suci, Z. Varpness, E. Gillitzer, T. Douglas and M. Young, *Langmuir*, 2007, **23**, 12280-12286.
67. T. L. Schlick, Z. Ding, E. W. Kovacs and M. B. Francis, *Journal of the American Chemical Society*, 2005, **127**, 3718-3723.
68. A. A. Aljabali, S. Shukla, G. P. Lomonossoff, N. F. Steinmetz and D. J. Evans, *Molecular Pharmaceutics*, 2012, **10**, 3-10.
69. C. E. Ashley, E. C. Carnes, G. K. Phillips, P. N. Durfee, M. D. Buley, C. A. Lino, D. P. Padilla, B. Phillips, M. B. Carter, C. L. Willman, C. J. Brinker, J. d. C. Caldeira, B. Chackerian, W. Wharton and D. S. Peabody, *ACS Nano*, 2011, **5**, 5729-5745.
70. D. P. Patterson, P. E. Prevelige and T. Douglas, *ACS Nano*, 2012, **6**, 5000-5009.

71. L. Shan, S. Cui, C. Du, S. Wan, Z. Qian, S. Achilefu and Y. Gu, *Biomaterials*, 2012, **33**, 146-162.
72. S. J. Kaczmarczyk, K. Sitaraman, H. A. Young, S. H. Hughes and D. K. Chatterjee, *Proceedings of the National Academy of Sciences*, 2011, **108**, 16998-17003.
73. P. Suci, S. Kang, R. Gmür, T. Douglas and M. Young, *Antimicrobial Agents and Chemotherapy*, 2010, **54**, 2489-2496.
74. S. Lilavivat, D. Sardar, S. Jana, G. C. Thomas and K. J. Woycechowsky, *Journal of the American Chemical Society*, 2012, **134**, 13152-13155.
75. M. L. Flenniken, L. O. Liepold, B. E. Crowley, D. A. Willits, M. J. Young and T. Douglas, *Chemical Communications*, 2005, DOI: 10.1039/b413435d, 447-449.
76. R. Toita, M. Murata, K. Abe, S. Narahara, J. S. Piao, J.-H. Kang and M. Hashizume, *Chemical Communications*, 2013, **49**, 7442-7444.
77. A. MaHam, H. Wu, J. Wang, X. Kang, Y. Zhang and Y. Lin, *J. Mater. Chem.*, 2011, **21**, 8700-8708.
78. N. Bruns, K. Pustelny, L. M. Bergeron, T. A. Whitehead and D. S. Clark, *Angewandte Chemie International Edition*, 2009, **48**, 5666-5669.
79. S. Biswas, K. Kinbara, T. Niwa, H. Taguchi, N. Ishii, S. Watanabe, K. Miyata, K. Kataoka and T. Aida, *Nature Chemistry*, 2013, **5**, 613-620.
80. K. Renggli, P. Baumann, K. Langowska, O. Onaca, N. Bruns and W. Meier, *Adv. Funct. Mater.*, 2011, **21**, 1241-1259.
81. C. R. Kaiser, M. L. Flenniken, E. Gillitzer, A. L. Harmsen, A. G. Harmsen, M. A. Jutila, T. Douglas and M. J. Young, *International Journal of Nanomedicine*, 2007, **2**, 715-733.
82. C. S. Rae, I. Wei Khor, Q. Wang, G. Destito, M. J. Gonzalez, P. Singh, D. M. Thomas, M. N. Estrada, E. Powell, M. G. Finn and M. Manchester, *Virology*, 2005, **343**, 224-235.
83. J. D. Lewis, G. Destito, A. Zijlstra, M. J. Gonzalez, J. P. Quigley, M. Manchester and H. Stuhlmann, *Nature Medicine*, 2006, **12**, 354-360.
84. P. Singh, D. Prasuhn, R. M. Yeh, G. Destito, C. S. Rae, K. Osborn, M. G. Finn and M. Manchester, *Journal of Controlled Release*, 2007, **120**, 41-50.
85. T. Douglas and M. Young, *Science*, 2006, **312**, 873-875.
86. L. A. Lee, Z. W. Niu and Q. Wang, *Nano Res.*, 2009, **2**, 349-364.
87. Z. Zhen, W. Tang, H. Chen, X. Lin, T. Todd, G. Wang, T. Cowger, X. Chen and J. Xie, *ACS Nano*, 2013, **7**, 4830-4837.
88. M. Uchida, M. L. Flenniken, M. Allen, D. A. Willits, B. E. Crowley, S. Brumfield, A. F. Willis, L. Jackiw, M. Jutila, M. J. Young and T. Douglas, *Journal of the American Chemical Society*, 2006, **128**, 16626-16633.
89. N. Stephanopoulos, G. J. Tong, S. C. Hsiao and M. B. Francis, *ACS Nano*, 2010, **4**, 6014-6020.
90. M. J. Abedin, L. Liepold, P. Suci, M. Young and T. Douglas, *Journal of the American Chemical Society*, 2009, **131**, 4346-4354.
91. J. Lucon, S. Qazi, M. Uchida, G. J. Bedwell, B. LaFrance, P. E. Prevelige and T. Douglas, *Nature Chemistry*, 2012, **4**, 781-788.
92. R. Toita, M. Murata, K. Abe, S. Narahara, J. S. Piao, J.-H. Kang, K. Ohuchida and M. Hashizume, *International Journal of Nanomedicine*, 2013, **8**, 1989-1999.
93. L. Liepold, S. Anderson, D. Willits, L. Oltrogge, J. A. Frank, T. Douglas and M. Young, *Magnetic Resonance in Medicine*, 2007, **58**, 871-879.
94. P. D. Garimella, A. Datta, D. W. Romanini, K. N. Raymond and M. B. Francis, *Journal of the American Chemical Society*, 2011, **133**, 14704-14709.
95. G. J. Tong, S. C. Hsiao, Z. M. Carrico and M. B. Francis, *Journal of the American Chemical Society*, 2009, **131**, 11174-11178.
96. J. E. Glasgow, S. L. Capehart, M. B. Francis and D. Tullman-Ercek, *ACS Nano*, 2012, **6**, 8658-8664.
97. D. P. Patterson, B. Schwarz, R. S. Waters, T. Gedeon and T. Douglas, *ACS Chemical Biology*, 2013, **9**, 359-365.
98. R. Waehler, S. J. Russell and D. T. Curiel, *Nature Reviews Genetics*, 2007, **8**, 573-587.

99. K.-m. Choi, S.-H. Choi, H. Jeon, I.-S. Kim and H. J. Ahn, *ACS Nano*, 2011, **5**, 8690-8699.
100. B. Gallois, B. L. d'Estaintot, M.-A. Michaux, A. Dautant, T. Granier, G. Précigoux, J.-A. Soruco, F. Roland, O. Chavas-Alba, A. Herbas and R. R. Crichton, *Journal of Biological Inorganic Chemistry*, 1997, **2**, 360-367.
101. K. K. Kim, R. Kim and S.-H. Kim, *Nature*, 1998, **394**, 595-599.
102. F. Tama and C. L. Brooks, *Journal of Molecular Biology*, 2002, **318**, 733-747.
103. M. G. Klein, P. Zwart, S. C. Bagby, F. Cai, S. W. Chisholm, S. Heinhorst, G. C. Cannon and C. A. Kerfeld, *Journal of Molecular Biology*, 2009, **392**, 319-333.
104. S. Tanaka, M. R. Sawaya and T. O. Yeates, *Science*, 2010, **327**, 81-84.
105. L. Ditzel, J. Lowe, D. Stock, K. O. Stetter, H. Huber, R. Huber and S. Steinbacher, *Cell*, 1998, **93**, 125-138.
106. M. G. Bigotti, S. R. W. Bellamy and A. R. Clarke, *Journal of Molecular Biology*, 2006, **362**, 835-843.
107. A. L. Horwich, W. A. Fenton, E. Chapman and G. W. Farr, in *Annual Review of Cell and Developmental Biology*, 2007, vol. 23, pp. 115-145.
108. C. Dekker, K. R. Willison and W. R. Taylor, *Proteins-Structure Function and Bioinformatics*, 2011, **79**, 1172-1192.
109. Z. Lin and H. S. Rye, *Molecular Cell*, 2004, **16**, 23-34.
110. M. Klumpp, W. Baumeister and L.-O. Essen, *Cell*, 1997, **91**, 263-270.
111. M. Nitsch, M. Klumpp, A. Lupas and W. Baumeister, *Journal of Molecular Biology*, 1997, **267**, 142-149.
112. H. Kubota, G. Hynes and K. Willison, *European Journal of Biochemistry*, 1995, **230**, 3-16.
113. B. M. Phipps, A. Hoffmann, K. O. Stetter and W. Baumeister, *Embo Journal*, 1991, **10**, 1711-1722.
114. T. Waldmann, M. Nitsch, M. Klumpp and W. Baumeister, *Febs Letters*, 1995, **376**, 67-73.
115. M. Nitsch, J. Walz, D. Typke, M. Klumpp, L.-O. Essen and W. Baumeister, *Nature Structural & Molecular Biology*, 1998, **5**, 855-857.
116. N. R. Douglas, S. Reissmann, J. J. Zhang, B. Chen, J. Jakana, R. Kumar, W. Chiu and J. Frydman, *Cell*, 2011, **144**, 240-252.
117. D. K. Clare, S. Stagg, J. Quispe, G. W. Farr, A. L. Horwich and H. R. Saibil, *Structure*, 2008, **16**, 528-534.
118. C. Spiess, A. S. Meyer, S. Reissmann and J. Frydman, *Trends Cell Biol.*, 2004, **14**, 598-604.
119. H. Rommelaere, M. De Neve, R. Melki, J. Vandekerckhove and C. Ampe, *Biochemistry*, 1999, **38**, 3246-3257.
120. A. T. Large, M. D. Goldberg and P. A. Lund, *Biochemical Society Transaction*, 2009, **37**, 6.
121. A. Guagliardi, L. Cerchia and M. Rossi, *Journal of Biological Chemistry*, 1995, **270**, 28126-28132.
122. M. Furutani, T. Iida, T. Yoshida and T. Maruyama, *Journal of Biological Chemistry*, 1998, **273**, 28399-28407.
123. I. Gutsche, L. O. Essen and F. Baumeister, *Journal of Molecular Biology*, 1999, **293**, 295-312.
124. R. Iizuka, T. Yoshida, T. Maruyama, Y. Shomura, K. Miki and M. Yohda, *Biochemical and Biophysical Research Communications*, 2001, **289**, 1118-1124.
125. A. R. Kusmierczyk and J. Martin, *Biochemical Journal*, 2003, **371**, 669-673.
126. A. T. Large and P. A. Lund, *Frontiers in Bioscience*, 2009, **14**, 21.
127. G. Bosch, W. Baumeister and L.-O. Essen, *Journal of Molecular Biology*, 2000, **301**, 19-25.
128. I. Gutsche, J. Holzinger, M. Rossle, H. Heumann, W. Baumeister and R. P. May, *Current Biology*, 2000, **10**, 405-408.
129. R. Iizuka, T. Yoshida, Y. Shomura, K. Miki, T. Maruyama, M. Odaka and M. Yohda, *Journal of Biological Chemistry*, 2003, **278**, 44959-44965.
130. P. Gómez-Puertas, J. Martín-Benito, J. L. Carrascosa, K. R. Willison and J. M. Valpuesta, *Journal of Molecular Recognition*, 2004, **17**, 85-94.

131. S. Reissmann, C. Parnot, C. R. Booth, W. Chiu and J. Frydman, *Nature Structural & Molecular Biology*, 2007, **14**, 432-440.
132. H. Sekiguchi, A. Nakagawa, K. Moriya, K. Makabe, K. Ichiyanagi, S. Nozawa, T. Sato, S.-i. Adachi, K. Kuwajima, M. Yohda and Y. C. Sasaki, *PLoS One*, 2013, **8**, e64176.
133. M. G. Bigotti and A. R. Clarke, *Journal of Molecular Biology*, 2005, **348**, 13-26.
134. R. Iizuka, T. Yoshida, N. Ishii, T. Zako, K. Takahashi, K. Maki, T. Inobe, K. Kuwajima and M. Yohda, *Journal of Biological Chemistry*, 2005, **280**, 40375-40383.
135. R. C. Wilson and J. A. Doudna, *Annual Review of Biophysics*, 2013, **42**, 217-239.
136. J. Haasnoot, E. M. Westerhout and B. Berkhout, *Nature Biotechnology*, 2007, **25**, 1435-1443.
137. H. Cerutti and J. A. Casas-Mollano, *Curr Genet*, 2006, **50**, 81-99.
138. A. Fire, S. Xu, M. K. Montgomery, S. A. Kostas, S. E. Driver and C. C. Mello, *Nature*, 1998, **391**, 806-811.
139. D. Castanotto and J. J. Rossi, *Nature*, 2009, **457**, 426-433.
140. S. Akhtar and I. Benter, *Advanced Drug Delivery Reviews*, 2007, **59**, 164-182.
141. C. C. Mello and D. Conte, *Nature*, 2004, **431**, 338-342.
142. M. E. Davis, J. E. Zuckerman, C. H. J. Choi, D. Seligson, A. Tolcher, C. A. Alabi, Y. Yen, J. D. Heidel and A. Ribas, *Nature*, 2010, **464**, 1067-1070.
143. J. C. Burnett and J. J. Rossi, *Chemistry & Biology*, 2012, **19**, 60-71.
144. K. A. Whitehead, R. Langer and D. G. Anderson, *Nature Reviews Drug Discovery*, 2009, **8**, 129-138.
145. S. Akhtar and I. F. Benter, *Journal of Clinical Investigation*, 2007, **117**, 3623-3632.
146. J. Probst, S. Brechtel, B. Scheel, I. Hoerr, G. Jung, H.-G. Rammensee and S. Pascolo, *Genetic vaccines and therapy*, 2006, **4**, 4-4.
147. W. E. Rudzinski and T. M. Aminabhavi, *International Journal of Pharmaceutics*, 2010, **399**, 1-11.
148. A. D. Judge, V. Sood, J. R. Shaw, D. Fang, K. McClintock and I. MacLachlan, *Nature Biotechnology*, 2005, **23**, 457-462.
149. M. Gooding, L. P. Browne, F. M. Quinteiro and D. L. Selwood, *Chemical Biology & Drug Design*, 2012, **80**, 787-809.
150. J. de Jonge, M. Holtrop, J. Wilschut and A. Huckriede, *Gene Therapy*, 2005, **13**, 400-411.
151. J. W. Yoo, D. J. Irvine, D. E. Discher and S. Mitragotri, *Nature Reviews Drug Discovery*, 2011, **10**, 521-535.
152. J. Barquintero, H. Eixarch and M. Perez-Melgosa, *Gene Therapy*, 2004, **11**, S3-S9.
153. T. S. Zimmermann, A. C. H. Lee, A. Akinc, B. Bramlage, D. Bumcrot, M. N. Fedoruk, J. Harborth, J. A. Heyes, L. B. Jeffs, M. John, A. D. Judge, K. Lam, K. McClintock, L. V. Nechev, L. R. Palmer, T. Racie, I. Röhl, S. Seiffert, S. Shanmugam, V. Sood, J. Soutschek, I. Toudjarska, A. J. Wheat, E. Yaworski, W. Zedalis, V. Koteliansky, M. Manoharan, H.-P. Vornlocher and I. MacLachlan, *Nature*, 2006, **441**, 111-114.
154. T. W. Geisbert, L. E. Hensley, E. Kagan, E. Z. Yu, J. B. Geisbert, K. Daddario-DiCaprio, E. A. Fritz, P. B. Jahrling, K. McClintock, J. R. Phelps, A. C. H. Lee, A. Judge, L. B. Jeffs and I. MacLachlan, *The Journal of Infectious Diseases*, 2006, **193**, 1650-1657.
155. E. Wagner, *Accounts of Chemical Research*, 2011, **45**, 1005-1013.
156. D. J. Gary, N. Puri and Y. Y. Won, *Journal of Controlled Release*, 2007, **121**, 64-73.
157. F. Simeoni, M. Morris, F. Heitz and G. Divita, in *RNA Silencing*, ed. G. Carmichael, Humana Press, 2005, vol. 309, ch. 13, pp. 251-260.
158. T. Endoh and T. Ohtsuki, *Advanced Drug Delivery Reviews*, 2009, **61**, 704-709.
159. D. de Bruyn Ouboter, T. Schuster, V. Shanker, M. Heim and W. Meier, *Journal of Biomedical Materials Research Part A*, 2014, **102**, 1155-1163.
160. N. D. Sonawane, F. C. Szoka and A. S. Verkman, *Journal of Biological Chemistry*, 2003, **278**, 44826-44831.
161. D. Ouyang, H. Zhang, H. S. Parekh and S. C. Smith, *Biophysical Chemistry*, 2011, **158**, 126-133.

162. M. Videira, A. Arranja, D. Rafael and R. Gaspar, *Nanomedicine: Nanotechnology, Biology and Medicine*, 2014, **10**, 689-702.
163. E. Buhleier, W. Wehner and F. Vogtle, *Synthesis*, 1978, 155-158.
164. C. J. Hawker and J. M. J. Frechet, *Journal of the American Chemical Society*, 1990, **112**, 7638-7647.
165. P. M. H. Heegaard, U. Boas and N. S. Sorensen, *Bioconjugate Chemistry*, 2009, **21**, 405-418.
166. T. Schuster, M. Nussbaumer, P. Baumann, N. Bruns, W. Meier and A. Car, in *Subunit Vaccine Delivery*, eds. C. Foged, T. Rades, Y. Perrie and S. Hook, Springer New York, 2015, DOI: 10.1007/978-1-4939-1417-3_10, ch. 10, pp. 181-201.
167. S. Akhtar, B. Chandrasekhar, S. Attur, M. H. M. Yousif and I. F. Benter, *International Journal of Pharmaceutics*, 2013, **448**, 239-246.
168. J. C. Roberts, M. K. Bhargat and R. T. Zera, *Journal of Biomedical Materials Research*, 1996, **30**, 53-65.
169. R. Jevprasesphant, J. Penny, R. Jalal, D. Attwood, N. B. McKeown and A. D'Emanuele, *International Journal of Pharmaceutics*, 2003, **252**, 263-266.
170. S. P. Mukherjee and H. J. Byrne, *Nanomedicine*, 2013, **9**, 202-211.
171. L. B. Jensen, G. M. Pavan, M. R. Kasimova, S. Rutherford, A. Danani, H. M. Nielsen and C. Foged, *International Journal of Pharmaceutics*, 2011, **416**, 410-418.
172. T. Wang and T. Weil, *Chimica Oggi-Chemistry Today*, 2009, **27**, 6-10.
173. F. Alexis, E. Pridgen, L. K. Molnar and O. C. Farokhzad, *Molecular Pharmaceutics*, 2008, **5**, 505-515.
174. R. A. Sperling, P. Rivera Gil, F. Zhang, M. Zanella and W. J. Parak, *Chemical Society Reviews*, 2008, **37**, 1896-1908.
175. Y. Haba, C. Kojima, A. Harada, T. Ura, H. Horinaka and K. Kono, *Langmuir*, 2007, **23**, 5243-5246.
176. J. J. Lichty, J. L. Malecki, H. D. Agnew, D. J. Michelson-Horowitz and S. Tan, *Protein Expression and Purification*, 2005, **41**, 98-105.
177. K. Renggli, M. G. Nussbaumer, R. Urbani, T. Pfohl and N. Bruns, *Angewandte Chemie International Edition*, 2014, **53**, 1443-1447.
178. F. Heitz, M. C. Morris and G. Divita, *British Journal of Pharmacology*, 2009, **157**, 195-206.
179. A. T. Jones and E. J. Sayers, *Journal of Controlled Release*, 2012, **161**, 582-591.
180. N. Chanda, V. Kattumuri, R. Shukla, A. Zambre, K. Katti, A. Upendran, R. R. Kulkarni, P. Kan, G. M. Fent, S. W. Casteel, C. J. Smith, E. Boote, J. D. Robertson, C. Cutler, J. R. Lever, K. V. Katti and R. Kannan, *Proceedings of the National Academy of Sciences*, 2010, **107**, 8760-8765.
181. E. García Garayoa, D. Rüegg, P. Bläuenstein, M. Zwimpfer, I. U. Khan, V. Maes, A. Blanc, A. G. Beck-Sickinger, D. A. Tourwé and P. A. Schubiger, *Nuclear Medicine and Biology*, 2007, **34**, 17-28.
182. H. Yang, H. Cai, L. Wan, S. Liu, S. Li, J. Cheng and X. Lu, *PLoS One*, 2013, **8**, e57358.
183. C. Müller and R. Schibli, in *Molecular Imaging in Oncology*, eds. O. Schober and B. Riemann, Springer Berlin Heidelberg, 2013, vol. 187, ch. 2, pp. 65-105.
184. A. Martin, J. Hickey, A. Ablack, J. Lewis, L. Luyt and E. Gillies, *J Nanopart Res*, 2010, **12**, 1599-1608.
185. N. F. Steinmetz, A. L. Ablack, J. L. Hickey, J. Ablack, B. Manocha, J. S. Mymryk, L. G. Luyt and J. D. Lewis, *Small*, 2011, **7**, 1664-1672.
186. G. T. Hermanson, *Bioconjugate Techniques, 2nd Edition*, 2008.
187. G. Russell-Jones, K. McTavish, J. McEwan, J. Rice and D. Nowotnik, *Journal of Inorganic Biochemistry*, 2004, **98**, 1625-1633.
188. V. K. Yellepeddi, A. Kumar and S. Palakurthi, *Anticancer Research*, 2009, **29**, 2933-2943.
189. V. K. Yellepeddi, A. Kumar, D. M. Maher, S. C. Chauhan, K. K. Vangara and S. Palakurthi, *Anticancer Research*, 2011, **31**, 897-906.
190. A. Taheri, R. Dinarvand, F. Atyabi, F. Nouri, F. Ahadi, M. H. Ghahremani, S. N. Ostad, A. T. Borougeni and P. Mansoori, *Journal of Biomedical Nanotechnology*, 2011, **7**, 743-753.

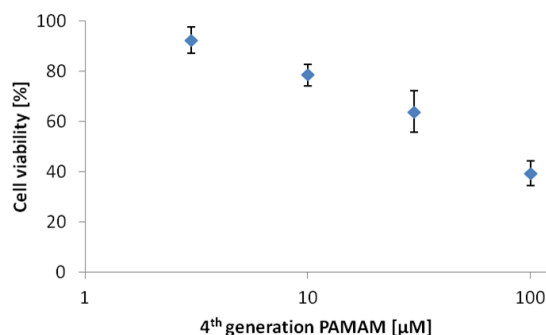
191. A. Taheri, R. Dinarvand, F. S. Nouri, M. R. Khorramizadeh, A. T. Borougeni, P. Mansoori and F. Atyabi, *International Journal of Nanomedicine*, 2011, **6**, 1863-1874.
192. S. Sabharanjak and S. Mayor, *Advanced Drug Delivery Reviews*, 2004, **56**, 1099-1109.
193. Y. Wang, X. Cao, R. Guo, M. Shen, M. Zhang, M. Zhu and X. Shi, *Polymer Chemistry*, 2011, **2**, 1754-1760.
194. G. Destito, R. Yeh, C. S. Rae, M. G. Finn and M. Manchester, *Chemistry & Biology*, 2007, **14**, 1152-1162.
195. M. Das, D. Mishra, T. K. Maiti, A. Basak and P. Pramanik, *Nanotechnology*, 2008, **19**, 415101.
196. S.-J. Yang, F.-H. Lin, K.-C. Tsai, M.-F. Wei, H.-M. Tsai, J.-M. Wong and M.-J. Shieh, *Bioconjugate Chemistry*, 2010, **21**, 679-689.
197. C. Sun, R. Sze and M. Zhang, *Journal of Biomedical Materials Research Part A*, 2006, **78A**, 550-557.
198. M. Huo, A. Zou, C. Yao, Y. Zhang, J. Zhou, J. Wang, Q. Zhu, J. Li and Q. Zhang, *Biomaterials*, 2012, **33**, 6393-6407.
199. C.-M. Huang, Y.-T. Wu and S.-T. Chen, *Chemistry & Biology*, 2000, **7**, 453-461.
200. J. Peng, X. Qi, Y. Chen, N. Ma, Z. Zhang, J. Xing, X. Zhu, Z. Li and Z. Wu, *Journal of Drug Targeting*, 2014, **22**, 428-438.
201. L.-C. Sun and D. H. Coy, *Current Drug Delivery*, 2011, **8**, 2-10.
202. M. Aumailley, M. Gurrath, G. Muller, J. Calvete, R. Timpl and H. Kessler, *Febs Letters*, 1991, **291**, 50-54.
203. K. Pollinger, R. Hennig, M. Breunig, J. Tessmar, A. Ohlmann, E. R. Tamm, R. Witzgall and A. Goepferich, *Small*, 2012, **8**, 3368-3375.
204. C. L. Waite and C. M. Roth, *Bioconjugate Chemistry*, 2009, **20**, 1908-1916.
205. X. Yang, H. Hong, J. J. Grailer, I. J. Rowland, A. Javadi, S. A. Hurley, Y. Xiao, Y. Yang, Y. Zhang, R. J. Nickles, W. Cai, D. A. Steeber and S. Gong, *Biomaterials*, 2011, **32**, 4151-4160.
206. K. Wang, T. L. Guan, D. A. Cheresh and G. R. Nemerow, *Journal of Virology*, 2000, **74**, 2731-2739.
207. N. Nitin, L. LaConte, W. Rhee and G. Bao, *Ann Biomed Eng*, 2009, **37**, 2018-2027.
208. L. Pan, Q. He, J. Liu, Y. Chen, M. Ma, L. Zhang and J. Shi, *Journal of the American Chemical Society*, 2012, **134**, 5722-5725.
209. S. M. Farkhani, A. Valizadeh, H. Karami, S. Mohammadi, N. Sohrabi and F. Badrzadeh, *Peptides*, 2014, **57**, 78-94.
210. J. Parenteau, R. Klinck, L. Good, Ü. Langel, R. J. Wellinger and S. A. Elela, *FEBS Lett.*, 2005, **579**, 4873-4878.
211. Y. Liu, M. Jones, C. M. Hingtgen, G. Bu, N. Laribee, R. E. Tanzi, R. D. Moir, A. Nath and J. J. He, *Nature Medicine*, 2000, **6**, 1380-1387.
212. F. Wang, Y. Wang, X. Zhang, W. Zhang, S. Guo and F. Jin, *Journal of Controlled Release*, 2014, **174**, 126-136.
213. J. S. Wadia, R. V. Stan and S. F. Dowdy, *Nature Medicine*, 2004, **10**, 310-315.
214. R. Binétruy-Tournaire, C. Demangel, B. Malavaud, R. Vassy, S. Rouyre, M. Kraemer, J. Plouët, C. Derbin, G. Perret and J. C. Mazié, *Embo Journal*, 2000, **19**, 1525-1533.
215. L. Albertazzi, M. Serresi, A. Albanese and F. Beltram, *Molecular Pharmaceutics*, 2010, **7**, 680-688.
216. S. Parimi, T. J. Barnes, D. F. Callen and C. A. Prestidge, *Biomacromolecules*, 2009, **11**, 382-389.
217. G. Li, Z. Hu, H. Yin, Y. Zhang, X. Huang, S. Wang and W. Li, *International Journal of Nanomedicine*, 2013, **8**, 1293-1306.
218. C. L. Waite, S. M. Sparks, K. E. Uhrich and C. M. Roth, *Bmc Biotechnology*, 2009, **9**.
219. V. P. Torchilin, T. S. Levchenko, R. Rammohan, N. Volodina, B. Papahadjopoulos-Sternberg and G. G. M. D'Souza, *Proceedings of the National Academy of Sciences*, 2003, **100**, 1972-1977.
220. J. K. Armstrong, R. B. Wenby, H. J. Meiselman and T. C. Fisher, *Biophys. J.*, 2004, **87**, 4259-4270.

221. J. H. Zhou, J. Y. Wu, N. Hafdi, J. P. Behr, P. Erbacher and L. Peng, *Chemical Communications*, 2006, DOI: 10.1039/b601381c, 2362-2364.
222. D. Huszar, M.-E. Theoclitou, J. Skolnik and R. Herbst, *Cancer Metastasis Rev*, 2009, **28**, 197-208.
223. E. J. Wojcik, R. S. Buckley, J. Richard, L. Liu, T. M. Huckaba and S. Kim, *Gene*, 2013, **531**, 133-149.
224. W. Hasan, K. Chu, A. Gullapalli, S. S. Dunn, E. M. Enlow, J. C. Luft, S. Tian, M. E. Napier, P. D. Pohlhaus, J. P. Rolland and J. M. DeSimone, *Nano Lett.*, 2011, **12**, 287-292.
225. Y. J. Kang, D. C. Park, H.-H. Shin, J. Park and S. Kang, *Biomacromolecules*, 2012, **13**, 4057-4064.
226. D. M. Ren, F. Kratz and S. W. Wang, *Small*, 2011, **7**, 1051-1060.
227. S. Doose, H. Neuweiler and M. Sauer, *ChemPhysChem*, 2005, **6**, 2277-2285.
228. N. Marmé and J.-P. Knemeyer, *Analytical and Bioanalytical Chemistry*, 2007, **388**, 1075-1085.
229. R. Abe, H. Ohashi, I. Iijima, M. Ihara, H. Takagi, T. Hohsaka and H. Ueda, *Journal of the American Chemical Society*, 2011, **133**, 17386-17394.
230. Y. Zhang, S. Yuan, R. Lu and A. Yu, *The Journal of Physical Chemistry B*, 2013, **117**, 7308-7316.
231. S. Banerjee and S. Mazumdar, *International Journal of Analytical Chemistry*, 2012, **2012**, 40.
232. J. M. Estrela, A. Ortega and E. Obrador, *Critical Reviews in Clinical Laboratory Sciences*, 2006, **43**, 143-181.
233. J. Yang, H. Chen, I. R. Vlahov, J.-X. Cheng and P. S. Low, *Proceedings of the National Academy of Sciences*, 2006, **103**, 13872-13877.
234. Y. Cong, G. F. Schröder, A. S. Meyer, J. Jakana, B. Ma, M. T. Dougherty, M. F. Schmid, S. Reissmann, M. Levitt, S. L. Ludtke, J. Frydman and W. Chiu, *Symmetry-free cryo-EM structures of the chaperonin TRiC along its ATPase-driven conformational cycle*, 2012.
235. D. Hoersch, S.-H. Roh, W. Chiu and T. Kortemme, *Nat. Nanotechnol.*, 2013, **8**, 928-932.
236. J. H. Pereira, C. Y. Ralston, N. R. Douglas, R. Kumar, T. Lopez, R. P. McAndrew, K. M. Knee, J. A. King, J. Frydman and P. D. Adams, *Mechanism of nucleotide sensing in group II chaperonins*, 2012.
237. A. S. Meyer, J. R. Gillespie, D. Walther, I. S. Millet, S. Doniach and J. Frydman, *Cell*, 2003, **113**, 369-381.
238. K. Zhang, L. Wang, Y. Liu, K.-Y. Chan, X. Pang, K. Schulten, Z. Dong and F. Sun, *Protein Cell*, 2013, **4**, 432-444.
239. D. I. Svergun and M. H. J. Koch, *Rep. Prog. Phys.*, 2003, **66**, 1735-1782.
240. C. D. Putnam, M. Hammel, G. L. Hura and J. A. Tainer, *Quarterly Reviews of Biophysics*, 2007, **40**, 191-285.
241. G. Schoehn, M. Hayes, M. Cliff, A. R. Clarke and H. R. Saibil, *Journal of Molecular Biology*, 2000, **301**, 323-332.
242. I. Gutsche, O. Mihalache, R. Hegerl, D. Typke and W. Baumeister, *Febs Letters*, 2000, **477**, 278-282.
243. S. A. Bode, I. J. Minten, R. J. M. Nolte and J. J. L. M. Cornelissen, *Nanoscale*, 2011, **3**, 2376-2389.
244. B. Maity, K. Fujita and T. Ueno, *Curr. Opin. Chem. Biol.*, 2015, **25**, 88-97.
245. S. Kang, M. Uchida, A. O'Neil, R. Li, P. E. Prevelige and T. Douglas, *Biomacromolecules*, 2010, **11**, 2804-2809.
246. M. Comellas-Aragones, H. Engelkamp, V. I. Claessen, N. Sommerdijk, A. E. Rowan, P. C. M. Christianen, J. C. Maan, B. J. M. Verduin, J. Cornelissen and R. J. M. Nolte, *Nat. Nanotechnol.*, 2007, **2**, 635-639.
247. I. J. Minten, V. I. Claessen, K. Blank, A. E. Rowan, R. J. M. Nolte and J. J. L. M. Cornelissen, *Chemical Science*, 2011, **2**, 358-362.
248. D. Cardinale, N. Carette and T. Michon, *Trends in Biotechnology*, 2012, **30**, 369-376.
249. N. C. Veitch, *Phytochemistry*, 2004, **65**, 249-259.
250. M. M. Tarpey and I. Fridovich, *Circulation Research*, 2001, **89**, 224-236.

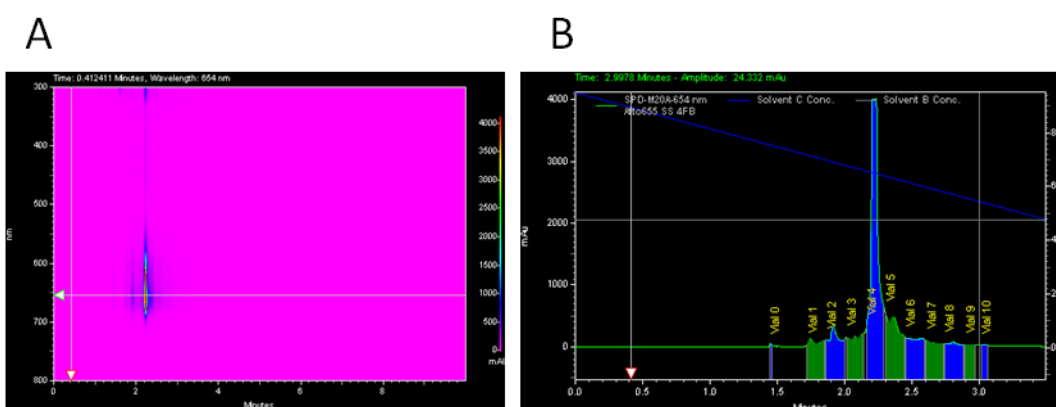
251. L. Edman, Z. Földes-Papp, S. Wennmalm and R. Rigler, *Chemical Physics*, 1999, **247**, 11-22.
252. W. Sun, J. J. Vallooran, A. Zabara and R. Mezzenga, *Nanoscale*, 2014, **6**, 6853-6859.
253. C. Winterbourn, in *Oxidative Stress and Redox Regulation*, eds. U. Jakob and D. Reichmann, Springer Netherlands, 2013, DOI: 10.1007/978-94-007-5787-5_2, ch. 2, pp. 43-58.
254. D.-M. Kong, J. Xu and H.-X. Shen, *Analytical Chemistry*, 2010, **82**, 6148-6153.
255. L. Stefan, F. Denat and D. Monchaud, *Nucleic Acids Research*, 2012, DOI: 10.1093/nar/gks581.
256. Y. Lin, Y. Huang, J. Ren and X. Qu, *NPG Asia Mater*, 2014, **6**, e114.
257. C. Kojima, Y. Watanabe, H. Hattori and T. Iida, *The Journal of Physical Chemistry C*, 2011, **115**, 19091-19095.
258. J. A. Barreto, W. O'Malley, M. Kubeil, B. Graham, H. Stephan and L. Spiccia, *Adv. Mater.*, 2011, **23**, H18-H40.
259. K. E. Sapsford, W. R. Algar, L. Berti, K. B. Gemmill, B. J. Casey, E. Oh, M. H. Stewart and I. L. Medintz, *Chemical Reviews*, 2013, **113**, 1904-2074.
260. L. W. Hoffman, G. G. Andersson, A. Sharma, S. R. Clarke and N. H. Voelcker, *Langmuir*, 2011, **27**, 6759-6767.
261. Y. Umeda, C. Kojima, A. Harada, H. Horinaka and K. Kono, *Bioconjugate Chemistry*, 2010, **21**, 1559-1564.
262. F. C. Meldrum, V. J. Wade, D. L. Nimmo, B. R. Heywood and S. Mann, *Nature*, 1991, **349**, 684-687.
263. M. Suzuki, M. Abe, T. Ueno, S. Abe, T. Goto, Y. Toda, T. Akita, Y. Yamada and Y. Watanabe, *Chemical Communications*, 2009, 4871-4873.
264. X. Liu, W. Wei, S. Huang, S.-S. Lin, X. Zhang, C. Zhang, Y. Du, G. Ma, M. Li, S. Mann and D. Ma, *Journal of Materials Chemistry B*, 2013, **1**, 3136-3143.
265. R. M. Crooks, M. Zhao, L. Sun, V. Chechik and L. K. Yeung, *Accounts of Chemical Research*, 2000, **34**, 181-190.
266. Y.-G. Kim, S.-K. Oh and R. M. Crooks, *Chemistry of Materials*, 2003, **16**, 167-172.
267. Y. Q. He, S. P. Liu, L. Kong and Z. F. Liu, *Spectrochimica Acta Part A: Molecular and Biomolecular Spectroscopy*, 2005, **61**, 2861-2866.
268. C. D. Paavola, S. L. Chan, Y. Li, K. M. Mazarella, R. A. McMillan and J. D. Trent, *Nanotechnology*, 2006, **17**, 1171-1176.
269. T. A. Whitehead, L. M. Bergeron and D. S. Clark, *Protein Engineering Design & Selection*, 2009, **22**, 607-613.
270. B. Zakeri and M. Howarth, *Journal of the American Chemical Society*, 2010, **132**, 4526-4527.
271. K. E. Thompson, C. J. Bashor, W. A. Lim and A. E. Keating, *ACS Synthetic Biology*, 2012, **1**, 118-129.
272. E. M. Sletten and C. R. Bertozzi, *Angewandte Chemie International Edition*, 2009, **48**, 6974-6998.
273. K. Lang and J. W. Chin, *Chemical Reviews*, 2014, **114**, 4764-4806.
274. M. Meng Lin, H.-H. Kim, H. Kim, M. Muhammed and D. Kyung Kim, *Nano reviews*, 2010, **1**.
275. Z. R. Stephen, F. M. Kievit and M. Zhang, *Materials Today*, 2011, **14**, 330-338.
276. S. D. Swanson, J. F. Kukowska-Latallo, A. K. Patri, C. Chen, S. Ge, Z. Cao, A. Kotlyar, A. T. East and J. R. Baker, *International Journal of Nanomedicine*, 2008, **3**, 201-210.
277. H. M. Ellerby, W. Arap, L. M. Ellerby, R. Kain, R. Andrusiak, G. D. Rio, S. Krajewski, C. R. Lombardo, R. Rao, E. Ruoslahti, D. E. Bredesen and R. Pasqualini, *Nature Medicine*, 1999, **5**, 1032-1038.
278. L. Agemy, D. Friedmann-Morvinski, V. R. Kotamraju, L. Roth, K. N. Sugahara, O. M. Girard, R. F. Mattrey, I. M. Verma and E. Ruoslahti, *Proceedings of the National Academy of Sciences*, 2011, **108**, 17450-17455.
279. J. Muenzer, J. E. Wraith, M. Beck, R. Giugliani, P. Harmatz, C. M. Eng, A. Vellodi, R. Martin, U. Ramaswami, M. Gucsavas-Calikoglu, S. Vijayaraghavan, S. Wendt, A. Puga, B. Ulbrich, M.

- Shinawi, M. Cleary, D. Piper, A. M. Conway and A. Kimura, *Genetics in Medicine*, 2006, **8**, 465-473.
280. R. Schiffmann, J. B. Kopp, H. A. Austin, S. Sabnis, D. F. Moore, T. Weibel, J. E. Balow and R. O. Brady, *Jama-Journal of the American Medical Association*, 2001, **285**, 2743-2749.
281. P. A. J. Muller and K. H. Vousden, *Nature Cell Biology*, 2013, **15**, 2-8.
282. K. T. Biegging, S. S. Mello and L. D. Attardi, *Nature Reviews Cancer*, 2014, **14**, 359-370.
283. D. Y. W. Ng, J. Fahrner, Y. Wu, K. Eisele, S. L. Kuan, H. Barth and T. Weil, *Advanced Healthcare Materials*, 2013, **2**, 1620-1629.
284. W. Jiskoot, T. W. Randolph, D. B. Volkin, C. R. Middaugh, C. Schöneich, G. Winter, W. Friess, D. J. A. Crommelin and J. F. Carpenter, *Journal of Pharmaceutical Sciences*, 2012, **101**, 946-954.
285. Y. Wu, D. Y. W. Ng, S. L. Kuan and T. Weil, *Biomaterials Science*, 2015, DOI: 10.1039/C4BM00270A.
286. U. K. Laemmli, *Nature*, 1970, **227**, 680-685.
287. J. Sambrook and D. Russell, *Molecular Cloning: A Laboratory Manual*, Cold Spring Harbor Laboratory Press, 2001.
288. A. A. A. Aljabali, J. E. Barclay, N. F. Steinmetz, G. P. Lomonosoff and D. J. Evans, *Nanoscale*, 2012, **4**, 5640-5645.
289. R. E. Childs and W. G. Bardsley, *Biochemical Journal*, 1975, **145**, 93-103.

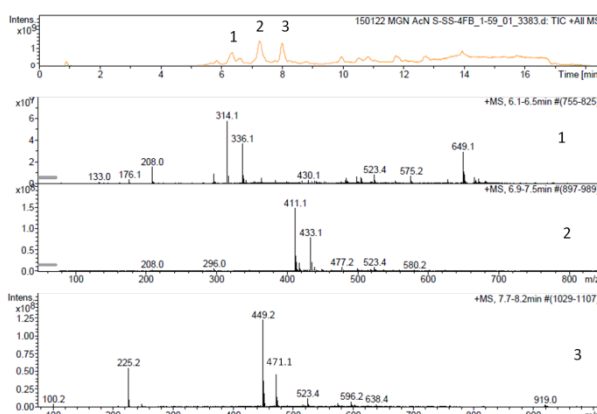
Appendix



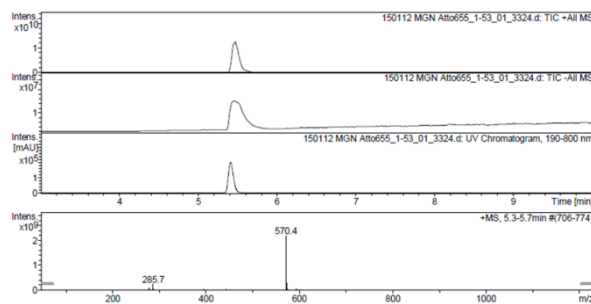
SI Fig. 8.1: Viability of PC-3 cells incubated with different amounts of 4th generation PAMAM for 24 h.



SI Fig. 9.1: (A) Whole spectrum of the HPLC chromatogram from the purification of Atto655-SS-FB. (B) Spectrum at 654 nm. The fraction Val 4 was further used.



SI Fig. 9.2: LC-MS of S-SS-4FB. Three main substances elute at 6.3 min (1), 7.3 min (2) and 8.0 min (3), respectively. The substance at 6.3 min is the hydrolyzed S-SS-4FB (314.1 m/z ($M+H$)⁺), the substance at 7.3 min is S-SS-4FB (411.1 m/z ($M+H$)⁺) and the substance at 8.0 min is most probable S-SS-4FB with a potassium ion (449.2 m/z ($M+K$)⁺). As seen from this LC-MS spectrum, S-SS-4FB is not so pure.



SI Fig. 9.3: LC-MS of Atto655-NH₂. Atto655-NH₂ eluted at around 5.4 min. Because the peak was so intense, the background peaks were not visible.

Curriculum vitae

Martin G. Nussbaumer

PhD student in Chemistry

MSc in Nanosciences, Major in Biology

Date of birth November 27, 1985

Citizen of Wallisellen ZH, Switzerland



EDUCATION

- 07/2010 - 02/2015 PhD student in the group of Prof. N. Bruns and Prof. W. Meier, Department of Chemistry, University of Basel
- 08/2008 - 06/2010 MSc in Nanosciences with Major in Biology, University of Basel
- 08/2005 - 08/2008 BSc in Nanosciences, University of Basel
- 07/2004 - 07/2005 Military service, rank of a lieutenant in nuclear, biological and chemical defense (NBC)
- 07/1998 - 06/2004 Grammar School in Köniz (Mathematics, Physics)

RESEARCH EXPERIENCE

- *The protein cage Thermosome as versatile delivery platform (2010 – 2015)*, PhD project in the group of Prof. N. Bruns and Prof. W. Meier, Department of Chemistry, University of Basel
- *Conjugation of Antibodies to Polymer Vesicles for targeted Drug Delivery Purposes (2010)*, master thesis in the group of Prof. W. Meier, Department of Chemistry, University of Basel
- *Synthesis and analysis of nucleotide-based amphiphilic diblockcopolymers (2010)*, project work in the group of Prof. Corinne Vebert and Prof. W. Meier, Department of Chemistry, University of Basel
- *N-terminal biotinylation of the RNA helicase YxiN (2009)*, project work in the group of Prof. D. Klostermeier, Biozentrum, University of Basel

RESEARCH INTERESTS

- Expression and purification of a chaperonin for targeted drug delivery; protein activity and stability tests
- Loading the chaperonin with different payloads (e.g. polymer, siRNA, dye, gold-nanoparticles) to enhance their stability
- Investigation of payload release
- Mammalian cell uptake studies of chaperonin modified with different targeting ligands

AWARDS

- Early Postdoc.Mobility from Swiss National Science Foundation
- Best Poster Award in physical chemistry of the Chemistry Department University of Basel, 2013
- 2012 SCNAT/SCS Chemistry Travel Award, 2012
- Distinction of best poster at International Nanoscience Conference, Baarlo, The Netherlands, August 2010

SKILLS and TECHNIQUES

Techniques

- Protein expression, purification, modification and characterization
- Gel electrophoresis, UV/VIS/IR-spectroscopy, FPLC, HPLC-MS, MALDI-TOF, TEM, AFM
- Mammalian and bacterial cell culture
- Flow cytometry, fluorescence microscopy and fluorescence correlation spectroscopy

Communication skills

Scientific writing (review, book chapter, several papers), presentation skills from academic talks, communication training (*Effective scientific communication I/II/III*)

Project Management

Organizer of the Science Slam Basel 2013 and 2014, course *Venture challenge - managing a start-up company* and troop leader in the Swiss Armed Forces

Teaching experience

Teaching assistant at the University of Basel for laboratory courses in physical chemistry, (2010 – 2014)

Languages

German - native, English - fluent (international experience), French - intermediate, Spanish - basic

Extracurricular activities

- Committee member of the PhD Chemistry Community (PCC) and organizer of the research seminar of the PCC (2012 – 2014)
- Founder and president of the football club FC Science United since September 2012
- Hobbies: Friends, Skiing, Football, Trekking, Travelling, former Boy Scout

Publications

- **Chaperonin-dendrimer conjugates for siRNA delivery.**
M.G. Nussbaumer, M. Rother, K. Renggli, M. Chami, N. Bruns; *submitted*.
- **Polymeric Particulates for Subunit Vaccine Delivery.**
T. Schuster, M.G. Nussbaumer, P. Baumann, N. Bruns, W. Meier, A. Car; *Subunit Vaccine Delivery*, **2015**, 181–201.
- **A Chaperonin as Protein Nanoreactor for Atom-Transfer Radical Polymerization.**
K. Renggli, M.G. Nussbaumer, R. Urbani, T. Pfohl, N. Bruns; *Angew. Chem. Int. Ed.*, **2014**, *53* (5), 1443-1447.
- **Fluorescent Protein Senses and Reports Mechanical Damage in Glass-Fiber-Reinforced Polymer Composites.** K. Makyła, C. Müller, S. Lörcher, T. Winkler, M.G. Nussbaumer, M. Eder, N. Bruns; *Adv. Mater.*, **2013**, *25* (19), 2701-2706
- **Polymer-protein core-shell hybrids for controlled siRNA delivery.** M.G. Nussbaumer, N. Bruns; *Polymer Preprints (American Chemical Society, Division of Polymer Chemistry)*, **2011**, *52* (2), 187-188.
- **Biocompatible Functionalization of Polymersome Surfaces: A new Approach to Surface Immobilization and Cell Targeting using Polymersomes.** S. Egli, M.G. Nussbaumer, V. Balasubramanian, M. Chami, N. Bruns, C. Palivan, W. Meier; *J. Am. Chem. Soc.*, **2011**, *133* (12), 4476-4483.

SELECTED ORAL PRESENTATIONS

- **Thermosome – a cage protein acting as a versatile delivery platform**
SCS Fall Meeting 2013, Lausanne, Switzerland, September 2013 .
- **Polymer-protein core-shell hybrids for controlled siRNA delivery**
Nanomaterials for Biomedical Technologies 2012 (DECHEMA), Frankfurt, Germany, March 2012.
- **Conjugation of Antibodies to Polymer Vesicles for Targeted Drug Delivery Purposes**
International Nanoscience Conference, Baarlo, The Netherlands, August 2010.

SELECTED POSTERS

- **Thermosome – a cage protein for targeted delivery of macromolecules**
M.G. Nussbaumer, N. Bruns; SCS Fall Meeting 2014, Zürich, Switzerland, September 2014.
- **How to use a protein cage as a multifunctional platform**
M.G. Nussbaumer, N. Bruns; *Rigi-Workshop 2013*, Rigi, Switzerland, January 2013.
- **Protein-polymer core-shell conjugates for controlled siRNA delivery**
M.G. Nussbaumer, M. Chami, A. Mascarin, T. Mindt, N. Bruns; *39th CRS annual meeting & exposition*, Québec, QC, Canada, July 2012.
- **Polymer-Protein Core-Shell Hybrids for Controlled siRNA Delivery**
M.G. Nussbaumer, A. Potenza, N. Bruns; *242nd American Chemical Society National Meeting & Exposition*, Denver, CO, USA, August 2011.
- **Conjugation of Antibodies to Polymer Vesicles for Targeted Drug Delivery Purposes**
M.G. Nussbaumer, S. Egli, W. Meier; *International Nanoscience Conference*, Baarlo, The Netherlands, August 2010.